

Crystallization of polyamide 11 under processing-
relevant cooling conditions and in presence of shear

Dissertation

zur Erlangung des Doktorgrades der Ingenieurwissenschaften
(Dr.-Ing.)

der

Naturwissenschaftlichen Fakultät II

Chemie, Physik und Mathematik

der Martin-Luther-Universität

Halle-Wittenberg

vorgelegt von

Katalee Jariyavidyanont

geb. am 06.08.1986 in Ubon Ratchathani, Thailand

Gutachter

1. Prof. Dr. René Androsch

2. Prof. Dr. Wenbing Hu

Datum der öffentlichen Verteidigung: 08.06.2022

Dedicated to my family.

CONTENTS

PREAMBLE	i
1. INTRODUCTION	1
1.1 Bio-based polyamide 11	1
1.2 Cooling rate and shear flow in polymer melt-processing	3
1.3 Crystallization at rapid cooling or high supercooling of the melt	6
1.3.1 General remarks about crystal nucleation	6
1.3.2 Kinetics of isothermal crystallization at different supercooling of the melt	6
1.3.3 Crystallization as a function of cooling rate	7
1.3.4 Effect of crystal nucleation on the semicrystalline morphology	8
1.3.5 Cooling-rate-/Supercooling-controlled crystal polymorphism	10
1.4 Shear-induced crystallization	12
1.5 State-of-the-art knowledge about the semicrystalline structure and crystallization of PA 11 at rapid-cooling conditions and in presence of shear	15
2. PROBLEM STATEMENT	17
3. AIMS AND STRATEGIES	18
4. RESULTS AND DISCUSSION	19
4.1 Experimental analysis of the lateral thermal inhomogeneity of a specific chip-calorimeter sensor	19
4.2 Nucleation-controlled dual semicrystalline morphology of polyamide 11	25
4.3 Crystal self-nucleation in polyamide 11	34
4.4 Crystal self-nucleation in polyamide 11 of different semicrystalline morphology	40
4.5 Kinetics of homogeneous crystal nucleation of polyamide 11 near the glass transition temperature	50
4.6 Shear-induced crystallization of polyamide 11	59
4.7 Thermal stability and nucleation efficacy of shear-induced point-like and shish-like crystallization precursors	70
5. CONCLUSIONS	77
References	80
List of abbreviations	88
List of figures and tables	89
Acknowledgements	91
Declaration of authorship	92
Curriculum Vitae	93

PREAMBLE

Polyamide 11 (PA 11) is a bio-based semicrystalline polymer which is used in high-performance engineering applications due to its balanced property profile including superior chemical resistance, excellent low-temperature impact strength, good thermal and dimensional stabilities. For semicrystalline polymers, in general, final properties depend on the morphology, including size, shape, fraction, orientation, structure, and perfection of crystals, and the structure of the surrounding amorphous phase. All these parameters can be tailored and balanced for various applications by the crystallization/processing conditions. In polymer-melt processing/forming such as extrusion or injection molding, the melt is often subjected to high cooling rates and shear deformation, which in addition can be a function of the local position in an extrudate or molded part. This, for example, frequently yields skin-core morphologies in injection molded components. Therefore, analysis of crystallization under processing-relevant cooling and shear conditions is of great importance for understanding the relationship between processing parameters, structure formation, and ultimate properties.

In this dissertation, a comprehensive evaluation of melt-crystallization of PA 11, focusing on processing-relevant rapid cooling and shear conditions was performed, allowing, in a wider view, tailoring processing routes for controlling the semicrystalline structure and with that final properties. In order to gain accurate and reliable information about the crystallization process under these conditions, sophisticated analysis and preparation techniques were used and developed. These include chip calorimetry, standalone and in combination with imaging techniques, an instrumented film preparation setup allowing fast cooling, or crystallization experiments in a rheometer. The observed results and their interpretation are presented in this dissertation in form of research publications, described in short below.

Publication (1) details the optimization of the handling of the used chip-calorimeter for crystallization at rapid cooling/high-melt supercooling experiments, from point of view of the lateral temperature distribution of the sensor, needed for obtaining accurate data on nanogram-scale samples.

Publications (2) to (5) present studies of quiescent-melt crystallization and the semicrystalline structure of PA 11. The effect of cooling rate, covering processing-relevant conditions, on the crystallization kinetics was analyzed by differential scanning calorimetry (DSC) and fast scanning chip calorimetry (FSC). The structure at the micro- and nanometer length-scales of PA 11 was investigated by polarized-light optical microscopy (POM), X-ray diffraction (XRD), and atomic force microscopy (AFM), providing, among others, guidelines to obtain qualitatively different semicrystalline morphologies as a function of crystallization conditions. In addition, self-nucleation was quantified for evaluation of melt memory effects as a function of the initial structure.

Publications (6) and (7) present analyses of shear-induced crystallization using a conventional parallel-plate rheometer. The crystallization kinetics after shearing the melt was evaluated by monitoring the evolution of the complex viscosity, serving for gaining knowledge about the critical specific work of flow above which additional crystal nuclei form. Furthermore, the thermal stability and nucleation efficacy of different types of shear-induced nuclei –point-like and shish-like precursors– were analyzed using hot-stage microscopy.

Since the worldwide interest for replacing petroleum-based polymers by environment-friendly bio-based polymers is growing, it is expected that the demand for using PA 11 is further increasing, thus requiring intensification of research for obtaining processing-structure-property relationships, for widening the product portfolio. The collected data and drawn conclusions about crystallization-controlled generation of different structures of fully bio-based PA 11 are therefore considered beneficial to optimize and tailor processing routes for specific applications.

1. INTRODUCTION

1.1 Bio-based polyamide 11

At present, the human society is experiencing a global environmental crisis. Main issues, related to polymer materials, are the use of non-renewable natural resources like crude oil and natural gas for their production, and the pollution of the environment by increasing greenhouse gas emission or generation of non-degradable plastic debris after their use. The public has become aware of this issue and increasingly pays attention to the use of environment-friendly bio-based polymers. This is mirrored by the continuously growing global capacity of their production, from around 3.8 million tons in 2019 to 4.2 million tons in 2020, and it is forecasted to increase further to 6.7 million tons in 2025.¹ For bio-based polyamides, there is expected an increase of the production volume by approximately 36 % until 2025.¹

Bio-based polyamide 11 (PA 11) is fully produced from short-term renewable castor oil. It has been commercialized for over 70 years and constantly developed to provide the market a wide range of grades for a variety of processing routes and applications.²⁻⁵ The timeline of history of PA 11 is presented in **Figure 1**. First PA 11 synthesis attempts date back to the late 1930s by Joseph Zeltner who was inspired by the synthesis of polyamide 66 (PA 66) by Wallace Hume Carothers. Successful synthesis of PA 11 was first achieved in the early 1940s by Michel Genas and Marcel Kastner who continued the research during the difficult times of World War II, leading to its commercialization in the late 1940s by the company Organico, under the trade name Rilsan[®]. Nowadays, the manufacture of bio-based PA 11 is carried out by Arkema in France, supplying over 30 grades to the market.^{3,4} The production plants are located in three major regions, in Europe (Serquigny, France), USA (Birdsboro, Pennsylvania), and Asia (Changshu, China).⁶ Furthermore, Arkema has announced a new plant in Singapore, scheduled to come on stream in 2022 to increase its global capacities by 50 %.⁷

The production steps to obtain bio-based PA 11 are illustrated, as a set of images, on the top of **Figure 2**. Castor seeds are collected from the castor plant and extracted to obtain their oil which is used to produce the 11- ω -aminoundecanoic-acid monomer (Amino 11), for subsequent condensation polymerization of PA 11. Besides its use for producing PA 11, castor oil is also a feedstock for many other industries such as manufacturing of soaps, lubricants, paints, and cosmetics, because it is a renewable natural resource, doesn't compete with food, and is inexpensive.^{8,9}

PA 11 is an aliphatic macromolecule with its repeating unit consisting of a rather long sequence of ten methylene groups and an amide group shown at the bottom of **Figure 2**. The long methylene sequence between the amide groups leads to a rather low density of hydrogen bonds between neighbored chains, causing a relatively low melting temperature (T_m) when comparing to other polyamides with higher density of hydrogen bonds such as polyamide 6 (PA 6) or PA 66.¹⁰⁻¹³ The long methylene sequence of PA 11 promotes excellent ductility and low-temperature impact strength down to -40 °C, low moisture absorption, and high dimensional stability.¹³ Furthermore, PA 11 exhibits good resistance to chemicals including low permeability to oxygen and hydrocarbons, and good thermal stability at high temperatures up to 150 °C. Therefore, it is used in many high-performance engineering applications such as flexible oil and gas pipes in on- and off-shore applications, fluid transfer lines and air brake

systems in automotive vehicles, electrical cable sheathing, electronic devices, coatings, sport goods, and medical devices.^{14–18}

Products of PA 11 typically are manufactured by melt-processing such as injection molding, extrusion, rotomolding, or 3D printing. In these technologies, the liquid melt is transferred/shaped into a solid part by vitrification and/or crystallization. The latter process often occurs at high supercooling of the melt and/or in presence of shear forces, which is not yet quantified for PA 11. Since the presence of crystals and the semicrystalline morphology are key parameters influencing the property profile, knowledge of the crystallization process, in particular under these conditions, is needed for understanding processing-structure relationships.

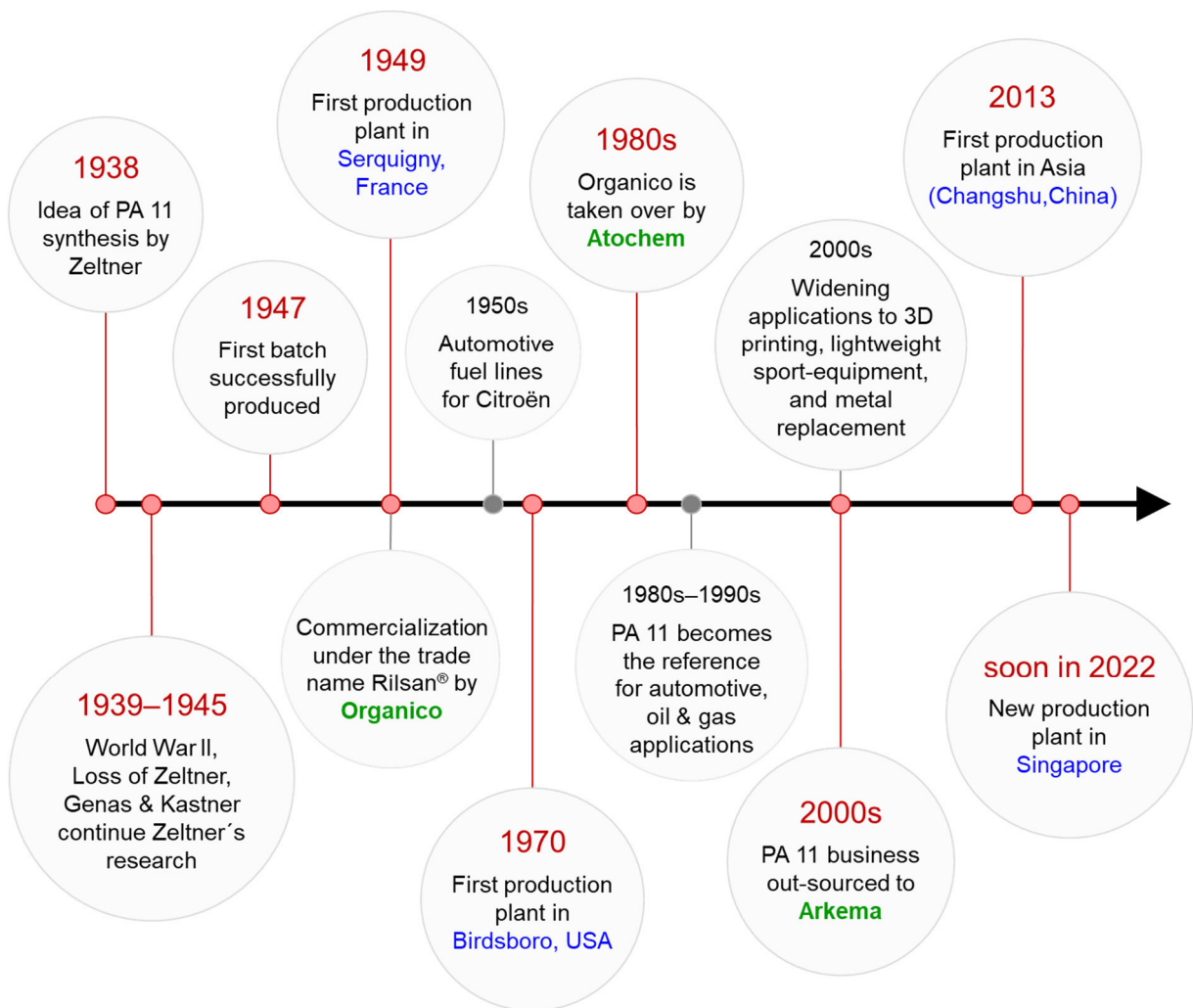


Figure 1: Timeline of history and development of Rilsan® PA 11.

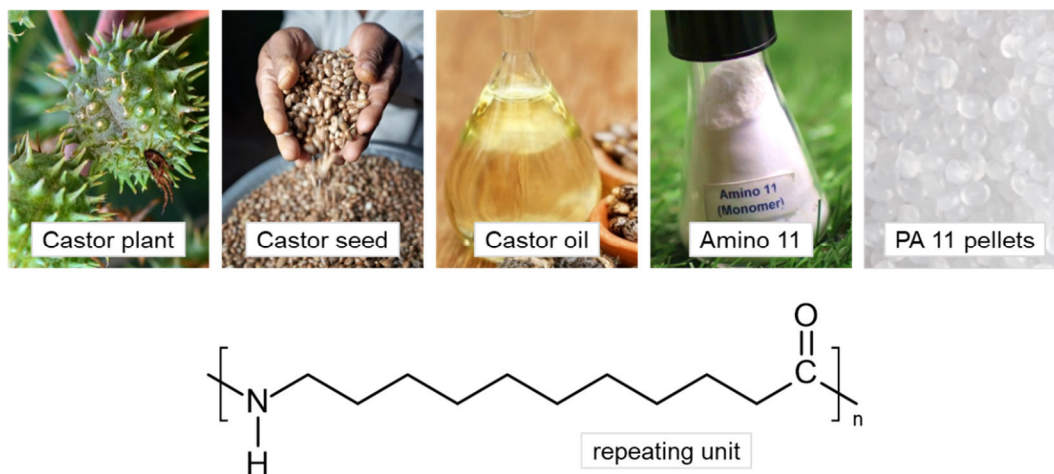


Figure 2: Production steps, from left to right, to obtain bio-based PA 11 (top) and repeating unit of the PA 11 macromolecule (bottom).^{2,14}

1.2 Cooling rate and shear flow in polymer melt-processing

Quantitative data about cooling rates and shear rates in polymer processing

Polymer products are generally manufactured by melt-processing. There are many types of plastic-manufacture technologies available for PA 11, among which extrusion and injection molding are most common, however, also rotomolding and 3D printing are applied.¹⁹ Extrusion is used for production of films, sheets, hoses, or pipes, while injection molding and 3D printing are suitable for fabrication of a wide variety of differently shaped parts. In many of these cases, the melt is subjected to shear forces and rather fast cooling, depending on the specific processing parameters including the part geometry. A prominent example demonstrating cooling and shear rates evident in the polymer melt-processing is isotactic polypropylene (iPP) which in the following will be further used as a comparative material throughout. **Figure 3** shows simulated shear-rate- (top) and temperature-distributions (bottom) of iPP as a function of time during filling the mold in an injection molding process, analyzed through the cross section of a tensile-test bar.²⁰ Different shear and cooling rates are observed over the entire cross-section of the component, indicated by different colors. Regarding the shear-rate simulation, high shear rate of about 10^3 s^{-1} is detected near the skin within one second during filling the mold whereas zero shear is observed in the core from the beginning until completion of the filling process. In case of the temperature distribution, the temperature of the melt of around $240 \text{ }^\circ\text{C}$ reduces within few seconds to close-to-the-mold-temperature at the skin, demonstrating the high cooling rate in this part of the component. In the center part, longer time for cooling the material is needed. Note that the reported data only hold for specific molding conditions.

Table 1 shows selected data about shear rates and cooling rates in different polymer melt-processing routes. Regarding shear rates, values may reach 10^1 to 10^3 s^{-1} during extrusion or, even higher, up to 10^4 s^{-1} in injection molding or 3D printing.^{21,22} Regarding cooling rates, up to several hundred K s^{-1} are reported.²³

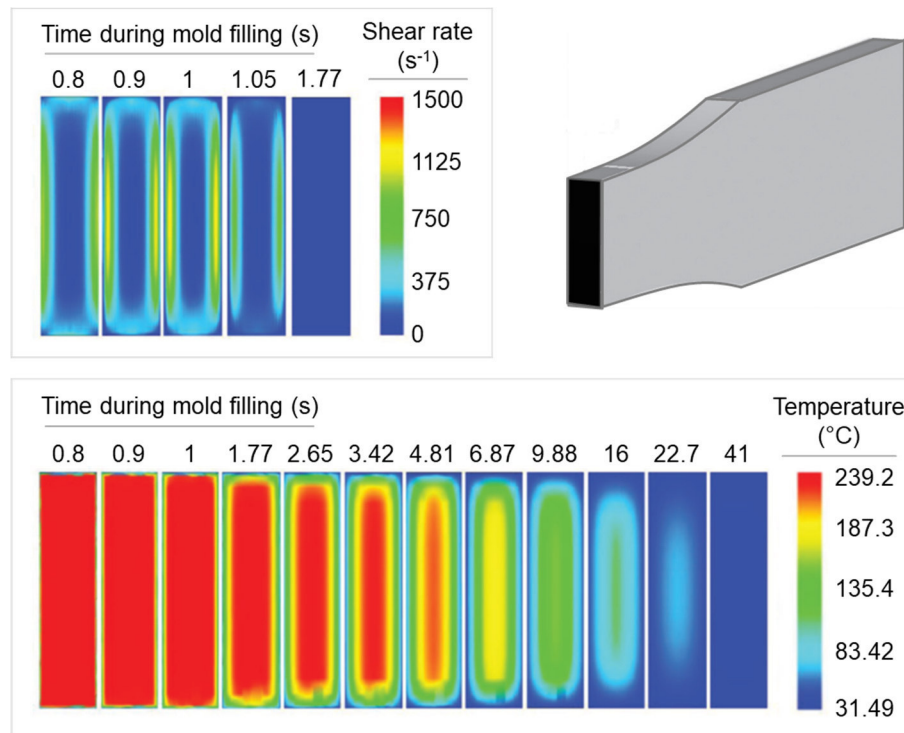


Figure 3: Simulated shear-rate distribution (top, left) and temperature distribution (bottom) over the cross section of a polypropylene tensile-test bar (top, right, black area), taken at the center of the bar.²⁰ The time scale starts after 0.8 s which corresponds the time of half mold filling; mold filling is completed after 1.77 s. Data adapted/reproduced from Ref. [20] with permission from Wiley.

Table 1: Examples of shear rates and cooling rates in melt processing of polymers using different manufacture technologies. The table serves for demonstration of the order of magnitude of cooling rates and shear rates only; detailed information about specific processing conditions, part geometries, etc. is available in the provided references.

Material	Shear rate (s^{-1})	Cooling rate ($K s^{-1}$)	Ref.
Injection molding		Skin/Core	
HDPE	-	130/30–50	[24,25]
PBT	up to 750	50/10	[26]
PA 11	-	100/10	[27]
iPP	375	600/ ≤ 10	[20]
Fused filament 3D printing			
PLA	27–7800	-	[22]
ABS	-	up to 180	[28]
PLA and ABS	949–1311	-	[29]
ABS	-	100	[30]
Extrusion		Skin/Core	
β -nucleated iPP	-	700/120	[23]
Blow film extrusion			
LLDPE	30–250	-	[31]
PET	45	-	[32]

Presence of cooling-rate and shear-rate gradients typically leads to development of so called skin-core morphologies.^{33–35} For example, in injection molding, the skin often shows a non-spherulitic structure, either being amorphous or containing only nanometer-sized ordered domains, because of rapid cooling and freezing the melt at the cold-mold wall. In contrast, slow cooling of the melt, evident in the core, allows formation of spherulites. Furthermore, a transition/shear zone, often observed between the skin and core regions, may form due to strong shear flow between the flowing melt and already frozen skin, leading to orientation of the macromolecules.^{33,35,36} The gradient structure, in consequence, influences the final properties.^{35,37–41} As an example, **Figure 4** shows the elastic modulus obtained by indentation analysis as a function of the relative position along the cross section of an injection-molded tensile bar of iPP, with the top POM image revealing the above described gradient structure at the millimeter-length scale. The three images below were obtained by atomic force microscopy (AFM), showing details of the morphologies at the micrometer-length scale observed at different positions along the cross section, as indicated. The hardness data reveal rather low values in the frozen skin containing small globular elements. In contrast, maximum hardness values are detected in the shear zone where a highly oriented fibrillar structure is observed. Intermediate hardness values are observed in the core region where a spherulitic superstructure developed. The hardness differences in the various regions of the molded part are caused by the different semicrystalline morphologies, which besides the shown AFM-structure, likely include gradients of crystallinity,³³ crystal size,³⁴ and orientation. Importantly, the skin-core morphology can be adjusted by variation of processing parameters, such as mold temperature, melt temperature, injection speed, or holding pressure, all affecting cooling and shearing conditions. Therefore, study of crystallization under rapid cooling conditions and in presence of shear flow is essential. In a broader perspective, knowledge of crystallization under such conditions is useful to understand and predict structure formation in polymer processing and, with that, to tailor final properties, by variation of processing parameters.^{33–35,42–44} Similar considerations hold for other processing routes.

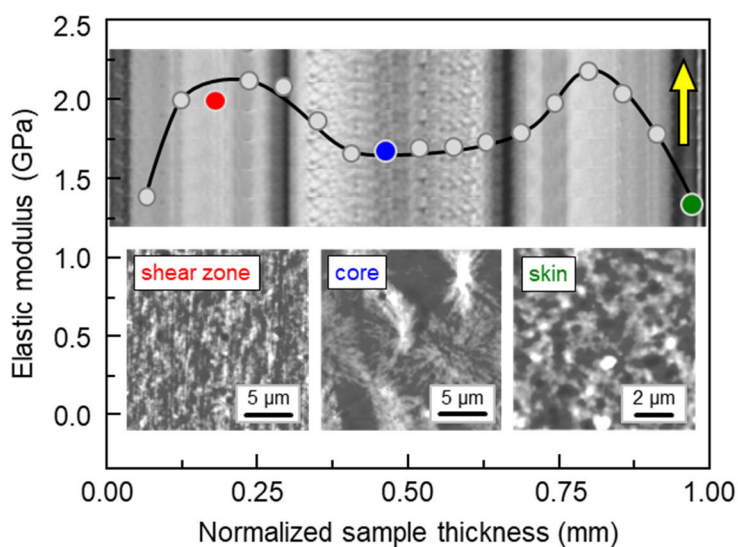


Figure 4: Elastic modulus as a function of the distance along the thickness of an injection-molded bar of iPP, shown with the top POM-image.³⁵ The flow direction is indicated by the yellow arrow. The three images at the bottom show the structure at different positions observed by AFM, reproduced from Ref. [45] with permission from AIP publishing.

1.3 Crystallization at rapid cooling or high supercooling of the melt

1.3.1 General remarks about crystal nucleation

Polymer crystallization involves crystal nucleation and growth. Nucleation can occur by two different mechanisms, which are homogeneous and heterogeneous nucleation. Homogeneous nucleation is the formation of primary nuclei in the bulk amorphous phase, due to density fluctuations. In contrast, heterogeneous nucleation occurs at pre-existing heterogeneities within the system, like impurities, surfaces, interfaces, nucleating agents, etc. Presence of such foreign surfaces leads to a reduction of the energy barrier for the formation of a stable nucleus. In addition, a special case of heterogeneous nucleation is nucleation based on so called self-seed, which, for example, maybe remnants of molten crystals, leaving a signature in the liquid phase.⁴⁶⁻⁴⁸ Because of the low interfacial energy between the self-seed nucleus and surrounding melt, self-nucleation may even be faster than heterogeneous nucleation on foreign surfaces.

Typically, heterogeneous nucleation is effective at high temperature or low supercooling of the melt while homogeneous nucleation is predominant at high supercooling only, because of the higher energy barrier to form a stable nucleus. This implies that during rather slow cooling the melt crystallization often occurs via heterogeneous nucleation unless it is outpaced by fast transfer of the melt into a highly supercooled state, where homogeneous nucleation is dominant. The different nucleation mechanisms, being predominant at various temperatures, can be identified by analysis of the crystallization kinetics and, in many cases, by observation of the nuclei number after completed crystallization.⁴⁹

1.3.2. Kinetics of isothermal crystallization at different supercooling of the melt

Differential scanning calorimetry (DSC) is widely used for analysis of the crystallization kinetics. However, due to the rather large size of the furnace and the corresponding large samples, high scanning rates and detection of fast processes are limited. Typically, DSC permits cooling and heating at rates up to few hundred K min⁻¹ only.⁵⁰ Furthermore, with the long instrumental time constant of, typically, several ten seconds,⁵¹ only slow transitions can be characterized regarding their kinetics.⁵² Hence, investigation of the kinetics of crystallization, particularly at processing-relevant cooling rates (see Table 1) and at high melt-supercooling, is impractical. Increasing the scanning rate to be several orders of magnitude higher than in case of conventional DSC, as well as decreasing the instrumental time constant down to milliseconds, is possible by decreasing the size/mass of both the calorimeter furnace and the sample,⁵³⁻⁵⁵ as is realized in fast scanning chip calorimeters (FSC). With such devices, quantitative information about the kinetics of crystallization in a wide range of temperatures or cooling rates, via heterogeneous and homogeneous nucleation, can be observed.

By using FSC, it was found that many polymers, though not all, show a bimodal temperature-dependence of the overall crystallization rate,⁵⁶⁻⁶⁰ revealing two crystallization-rate maxima at low and high supercooling of the melt, related to heterogeneous and homogeneous nucleation, respectively. **Figure 5** presents characteristic times of crystallization (being the inverse of the crystallization rate) obtained on isothermal crystallization of various iPP at different temperatures, using FSC (filled symbols) and DSC (open symbols).⁵⁹⁻⁶³ On lowering the temperature, or increasing the supercooling of the melt,

the characteristic crystallization time decreases because of the increase of the thermodynamic driving force for crystallization, reaches a minimum value, and begins to increase due to the lowering of the mobility of molecular chain segments. A further increase of the supercooling leads to a second low-temperature crystallization-time minimum, which has been suggested being related to a change of the nucleation mechanism,⁶⁴ from heterogeneous nucleation at high temperature to homogeneous nucleation at low temperature (here, for iPP, the cross-over temperature is around 50–60 °C). Finally, the crystallization time increases again due to the further decrease of the chain mobility when approaching the glass transition temperature (T_g) of around 0 °C, slowing down crystal growth. The blue-colored data refer to the pioneering study of C. Schick,⁶¹ while the other data sets (gray symbols) were obtained by different research groups,^{60,62,63} having used different iPP grades. These data exhibit a similar bimodal temperature-distribution of crystallization times, however, with slightly different cross-over temperatures, presumably due to a different heterogeneous nucleation kinetics. Since crystallization at high temperature is controlled by the activation energy for heterogeneous nucleation, shorter crystallization times (see gray downward arrow) probably are caused by presence of impurities or additives/nucleating agents; an additional factor may be the chemical architecture of the macromolecules (e.g. tacticity or molar mass and its distribution) as it affects the crystal growth rate, contributing to the measured characteristic crystallization time.^{60,61,65} In contrast, low-temperature crystallization via homogeneous nucleation below 55–60 °C seems less affected by the molecular characteristics and possible presence of additives.

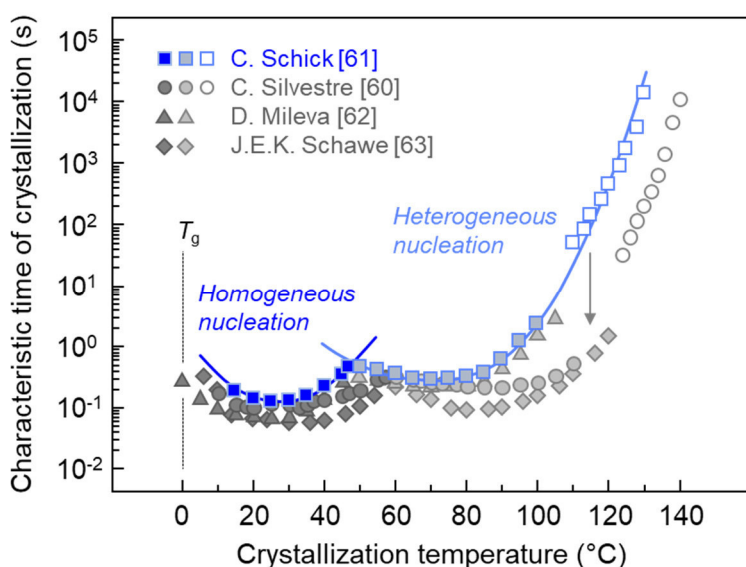


Figure 5: Characteristic time of crystallization of iPP in a wide range of temperatures between 0 and 140 °C, proceeding via heterogeneous (filled and unfilled symbols in light-blue and light-gray colors, at temperatures above about 55 °C) and homogeneous nucleation (dark-blue and dark-gray filled symbols), obtained by FSC (filled symbols) and DSC (unfilled symbols).^{60–63} The data were adapted from Ref. [60] with permission from Wiley and from Refs. [61] and [63] with permission from Springer.

1.3.3. Crystallization as a function of cooling rate

Crystallization in polymer melt-processing often occurs during rapid cooling, as shown in Table 1. Analysis of crystallization in a wide range of cooling rates can be obtained by a combination of DSC and FSC. **Figure 6** shows crystallization peak-temperatures of iPP as a function of the cooling rate, revealing crystallization at high and low supercooling of the melt. Melt-crystallization on slow cooling, at rates below 50 K s⁻¹ yields a high-temperature crystallization peak (light-blue symbols). Crystallization at high temperature proceeds via heterogeneous crystal nucleation which can be suppressed, leading to low-temperature

crystallization through homogeneous nucleation (dark-blue symbols) if cooling the melt at rates faster than 150 K s^{-1} . Two crystallization events, at high and low temperatures, are observed if the melt is cooled at rates between 50 and 150 K s^{-1} (gray-shaded area). Complete vitrification of the melt occurs if the melt is quenched to below T_g with a sufficiently higher rate of few hundred K s^{-1} .

Although fast cooling of the melt can suppress crystallization, the used cooling rate still may allow homogeneous crystal nucleation. Formation of such crystal nuclei during cooling can only be prevented if the used cooling rate is higher than the critical cooling rate for suppressing nucleation. **Table 2** provides information about critical cooling rates for suppression of both crystallization (crystal growth) and crystal nucleation for different homopolymers. According to the data provided in Table 1, in polymer melt-processing, cooling rates up to about $500\text{--}1000 \text{ K s}^{-1}$ are realistic. If the cooling rate is higher than the critical cooling rate for suppressing crystallization, complete vitrification of the melt occurs, to yield a glass at ambient temperature if the glass transition occurs at higher temperature. However, such cooling rates may still be too low to avoid homogeneous crystal nucleation during cooling (see for example the PA-6-data in Table 2). Such nuclei formed during cooling, or even at temperatures slightly below T_g may cause cold-crystallization on subsequent heating. Analysis of the cold-crystallization behavior as a function of the cooling rate or the conditions of annealing the glass, therefore, can yield information about the nucleation kinetics, applying Tammann's two-stage crystal nuclei development method.⁶⁶

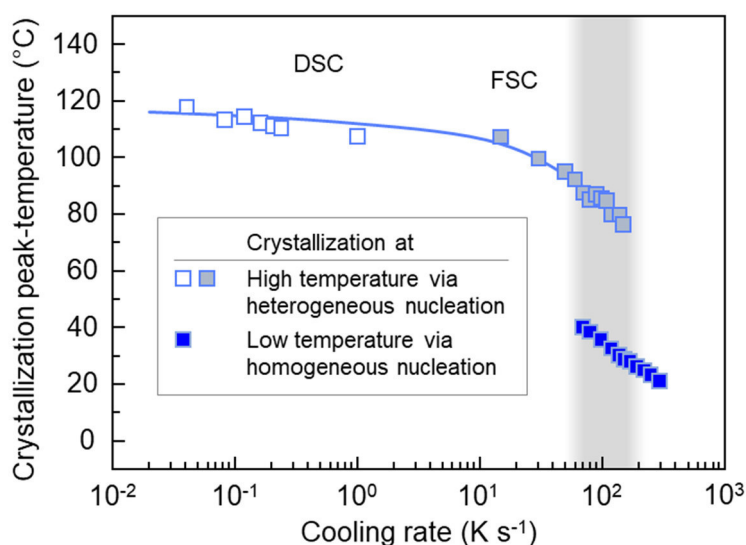


Figure 6: Crystallization peak-temperature of iPP as a function of cooling rate, obtained by DSC ($\leq 1 \text{ K s}^{-1}$, open squares) and by FSC ($> 10 \text{ K s}^{-1}$, filled squares).⁵⁵ Adapted with permission from F. De Santis, S. Adamovsky, G. Titomanlio, C. Schick. Scanning nanocalorimetry at high cooling rate of isotactic polypropylene. *Macromolecules* 2006, 39, 2562–2567. Copyright (2021) American Chemical Society.

1.3.4. Effect of crystal nucleation on the semicrystalline morphology

Crystallization via different nucleation mechanisms typically is connected with different nuclei densities, which can be quantified by microscopy. **Figure 7** shows AFM nanostructures of iPP,⁷⁴ PA 6,⁷⁵ and PA 66,⁵⁷ analyzed at room temperature after crystallization at high and low supercooling of the melt, shown with the top and bottom rows, respectively. Crystallization at low supercooling of the melt proceeds via space-filling spherulitic growth of laterally extended lamellae from only few heterogeneous nuclei (yellow circles). At high supercooling of the melt, in contrast, due to the largely increased number of nuclei by several orders of magnitude, lateral

Table 2: Examples of critical cooling rates for suppression of crystallization and homogeneous crystal nucleation.

Polymer	Critical cooling rate (in K s^{-1}) for suppression of		Ref.
	Crystallization	Crystal nucleation	
iPP	1000	-	[55]
PBT	2000	20,000	[67]
PCL	1000	20,000	[68]
PBN	6000	30,000	[69]
iPB-1	10	-	[70]
PA 6	150	>10,000	[71,72]
PLLA	0.50	50	[73]

growth of nuclei and formation of lamellae and spherulites are suppressed, and only numerous particle-like domains are observed.^{76,77} The large number of nuclei constrains the neighbored, amorphous structure, disabling grow of perfect crystals, and therefore often only conformationally disordered crystals or mesophases develop.⁷⁸ The difference in the number of nuclei active at low and high supercooling of the melt can be up to about 10 orders of magnitude.⁵⁶ For example, quantitative analysis of the nuclei density in poly(butylene terephthalate) (PBT) using microscopy revealed values of 10^6 and 10^{15} nuclei mm^{-3} for heterogeneous and homogenous nucleation on crystallization at low and high supercooling of the melt, respectively.⁵⁶

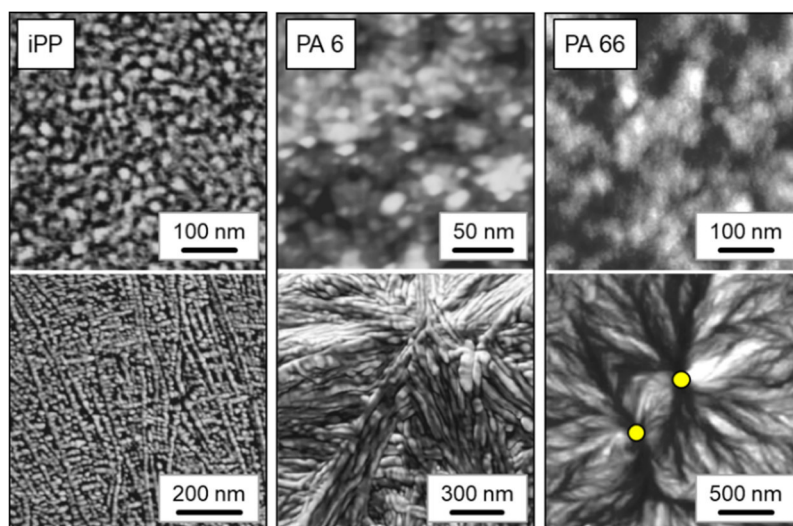


Figure 7: AFM images of iPP,⁷⁴ PA 6,⁷⁵ and PA 66,⁵⁷ (from left to right), obtained by crystallization at high (top row) and at low supercooling of the melt (bottom row). The yellow circles in the bottom-right image indicate two heterogeneous nuclei where the crystal growth started. Images of iPP were reprinted with permission from Q. Zia, D. Mileva, R. Androsch. Rigid Amorphous fraction in isotactic polypropylene. *Macromolecules* 2008, 41, 8095–8102. Copyright (2021) American Chemical Society; images of PA 6 were reprinted from D. Mileva, R. Androsch, E. Zhuravlev, C. Schick. Morphology of mesophase and crystals of polyamide 6 prepared in a fast scanning chip calorimeter. *Polymer* 2012, 53, 3994–4001, Copyright (2021), with permission from Elsevier; images of PA 66 were reprinted with permission from A.M. Gohn, A.M. Rhoades, N. Wonderling, T. Tighe, R. Androsch. The effect of supercooling of the melt on the semicrystalline morphology of PA 66. *Thermochim. Acta* 2017, 655, 313–318, Copyright (2021), with permission from Elsevier.

Melt-crystallization during polymer processing depends on the specific cooling conditions, and often occurs at various temperatures, at both low and high supercooling of the melt (see Figure 6). As a result, different semicrystalline morphologies develop and may affect ultimate properties. The cooling-rate dependence of the development of semicrystalline structures of iPP, as an example, is presented in **Figure 8**. Slow cooling of the melt at rates below 1 K s^{-1} to ambient temperature leads to formation of a space-filled spherulitic structure, originating from few nuclei. Increasing the cooling rate to be between 1 and 10 K s^{-1} leads to an increase of the nuclei density, yielding smaller spherulites. If the cooling rate is between 10 and 100 K s^{-1} , a two-fold spherulite-size distribution developed, represented by small spherulites and non-spherulitically distributed mesophase due to crystallization via both nucleation mechanisms; at first, at high temperature, via heterogeneous nucleation and later, at lower temperature, via homogeneous nucleation (see the gray-shaded area in Figure 6).^{56,79} Cooling the melt between 150 and 300 K s^{-1} causes non-spherulitic growth of mesophase. Quenching the iPP melt at rates faster than 500 K s^{-1} to below T_g of about $0 \text{ }^\circ\text{C}$ suppresses crystallization, however, subsequent annealing at ambient temperature also leads to formation of mesophase.

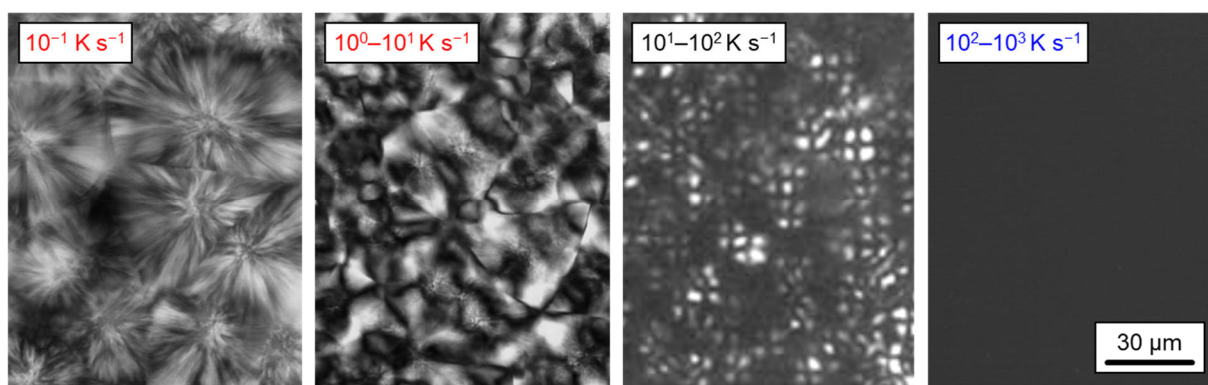


Figure 8: POM images of the structure of $100 \text{ }\mu\text{m}$ thick iPP films, prepared by cooling the melt at different rates, as indicated in each image.^{80,81} The scale bar of $30 \text{ }\mu\text{m}$ applies to all images. The first, second, and fourth image from the left were reprinted with permission from D. Mileva, Q. Zia, R. Androsch, H.-J. Radusch, S. Piccarolo. Mesophase formation in poly(propylene-ran-1-butene) by rapid cooling. *Polymer* 2009, 50, 5482–5489, Copyright (2021), with permission from Elsevier; the third image from the left was reproduced from Ref. [81] with permission from Wiley.

1.3.5. Cooling-rate-/Supercooling-controlled crystal polymorphism

Besides the tremendous increase of the nuclei density and a change of the semicrystalline superstructure upon increasing the supercooling of the melt, often there is observed formation of different crystal polymorphs. For example, **Figure 9** shows on the left-hand side the effect of cooling rate on melt-crystallization of iPP from point-of-view of the formation of different crystal polymorphs as analyzed by wide angle X-ray scattering (WAXS)⁸⁰ and on the right-hand side the projection of the basal planes of the unit cell of α -crystals and of mesophase.⁸² Slow cooling of the melt (red data) allows formation of the stable monoclinic α -crystal form with a well-defined layer-to-layer arrangement of left-handed and right-handed helices (see green arrows). In contrast, rapid cooling of the iPP melt at a rate higher than 100 K s^{-1} (blue data) leads to formation of a mesophase, also described as a conformationally disordered and defective crystal.^{79,80,83,84} The lateral arrangement of left-handed and right-handed helices in the

mesomorphic phase is random, leading, as a result, to a lower packing density when compared to the monoclinic structure. The scattering patterns obtained from samples cooled at rates between 50 and 80 K s⁻¹ (black data) show fading of the characteristic diffraction peaks of the α -form with gradually development of mesophase instead. In case of PA 6, a similar supercooling-controlled polymorphism is evident. Melt-crystallization at low supercooling allows formation of stable α -crystals while formation of a pseudo-hexagonal mesophase occurs at high supercooling.^{85,86} Such supercooling-controlled crystal polymorphism, that is, forming stable crystals at slow cooling or low melt-supercooling and disordered crystals/mesophases at fast cooling or high supercooling of the melt, is reported for other polymers too, as shown in **Table 3**. It should be noted that such supercooling-controlled crystal polymorphism is not a general phenomenon. For example, PBT shows no change of the crystal structure when crystallizing at different temperature.⁵⁶

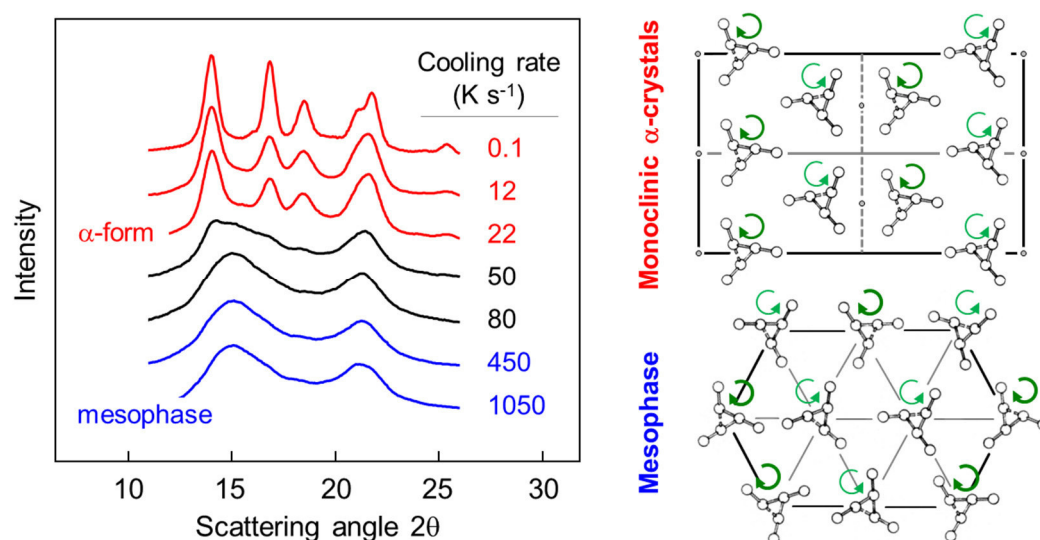


Figure 9: WAXS patterns of iPP, obtained from film samples prepared by cooling the melt at different rates⁸⁰ (left) and basal planes of the unit cell of monoclinic α -crystals and pseudo-hexagonal mesophase (right).⁸² The left figure was reprinted with permission from D. Mileva, Q. Zia, R. Androsch, H.-J. Radusch, S. Piccarolo. Mesophase formation in poly(propylene-ran-1-butene) by rapid cooling. *Polymer* 2009, 50, 5482–5489, Copyright (2021), with permission from Elsevier; the right figure was reproduced from Ref. [82] with permission from Wiley.

Table 3: Supercooling-controlled crystal polymorphism of various polymers.

Polymer	Crystal polymorphs forming at		Ref.
	Slow-cooling/low supercooling of the melt via heterogeneous nucleation	Fast-cooling/high supercooling of the melt via homogeneous nucleation	
iPP	Monoclinic α -crystal	Mesophase	[79,80,83]
PA 6	Monoclinic α -crystal	Pseudo-hexagonal γ -mesophase	[85]
PA 66	Triclinic α -crystal	Pseudo-hexagonal γ -mesophase	[57]
PA 11	Triclinic α -crystal	Pseudo-hexagonal δ' -mesophase	[58,87]
PA 12	Pseudo-hexagonal γ -crystal	Pseudo-hexagonal γ' -mesophase	[88,89]

1.4 Shear-induced crystallization

In polymer processing, often the melt is subjected to shear flow, as documented in Table 1, causing melt deformation, causing e.g. molecular orientation or stretching of chain segments. The deformed melt has a lower conformational entropy compared to the relaxed melt and hence leads to a reduction of the energy barrier for formation of nuclei.^{90–95} As a result, the nuclei density increases, and crystallization accelerates.^{90–95} In addition, crystallization of the deformed melt will affect the semicrystalline morphology, and with that ultimate properties, e.g. by preferred orientation of crystals. Therefore, study of shear-induced crystallization, also often termed flow-induced crystallization, is of great importance for understanding the relationship between melt-processing conditions and the resulting structure.

Shear-induced crystallization occurs if the shear rate ($\dot{\gamma}$) and shear time (t_s), given to the melt at a specific shear temperature (T_s), are higher than critical threshold values to allow formation of additional nuclei, and if nuclei are not destroyed by chain relaxation after cessation of shear.^{94–97} At a certain shear temperature, shear rate and shear time play a role to define a critical value for shear-induced crystallization. If shear conditions are severe enough to induce chain orientation or stretching, shear-induced additional point-like or shish-like nuclei, can be formed, respectively. The critical shear values where chains become oriented or stretched have been proposed by correlating shear rates and chain relaxation times.⁹⁷ Two characteristic relaxation times are important for controlling chain orientation and stretching, that are the reptation (τ_r) and Rouse times (τ_R), respectively. If shearing the melt at rates which are greater than the inverse value of the reptation relaxation time ($\dot{\gamma} > 1/\tau_r$), then occurs orientation of the chains, and shear-induced additional point-like nuclei form. When the shear rate increases to be higher than the inverse of the Rouse time ($\dot{\gamma} > 1/\tau_R$), then molecular chains are stretched, providing thread-like or shish-like nucleating sites. With this concept, three different flow regimes are established, demonstrated in **Figure 10**. POM images on the top illustrate the semicrystalline structures of iPP formed after crystallization in different regimes.⁹⁸ Shearing the melt at subcritical rates leads to crystallization as in the quiescent melt, specified as Regime I (black); the shear rate is too low to cause orientation of the melt. Thus, a spherulitic superstructure due to the low nuclei number is observed in this regime. If shearing the melt at rates which is higher than $1/\tau_r$, the crystallization induction-time gradually decreases (indicated as Regime II, in blue). In this Regime, a finer structure develops due to an increased number of point-like nuclei.^{99–101} This observation defines the critical shear-rate-value for shear-induced formation of additional point-like nuclei. Increasing the shear rate to values greater than $1/\tau_R$ leads to a further rapid reduction of the crystallization time, as shown with the red data (Regime III). Crystallization at such condition is characterized by shish-kebab formation; threadlike structures along the flow direction are called shishes, which assist growth of the lamellar crystals, called kebabs, perpendicular outward from the shishes.^{96,102–108} Hence, such shear rate is defined as the critical value for shear-induced formation of thread-like nuclei.

Similar effects hold for variation of the shear time, that is, shear-induced crystallization will only occur if the shear rate exceeds a minimum value.^{101,103} It was found that increasing further either shear rate or shear time such to exceed a critical threshold for nuclei saturation, where a maximum number of precursors is reached, the crystallization time becomes constant.^{99,109,110} Regarding the shear temperature, shearing the melt at higher temperature is connected with a

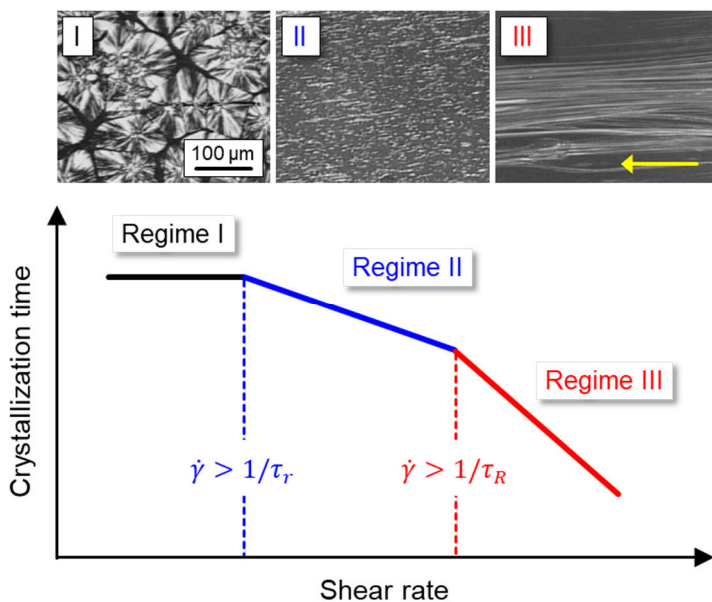


Figure 10: Crystallization time as a function of shear rate, allowing to distinguish three crystallization regimes: zero-shear or quiescent-melt crystallization (Regime I, black), shear-induced formation of point-like nuclei (Regime II, blue), and shear-induced formation of fibrillar structure (Regime III, red). The POM images on the top show iPP structures formed after crystallization in different regimes.⁹⁸ The flow direction is indicated with the yellow arrow.

decrease of the relaxation times, that is, polymer chains can quickly relax back to the stable random-coils conformation (isotropic melt) after prior orientation or stretch.¹¹¹ Therefore, higher shear rates are required for obtaining shear-induced precursors.

Variation of shear rate and shear time is commonly done to define the critical conditions for shear-induced crystallization, however, only being valid at a specific temperature. Alternatively, a single control parameter, describing at which conditions shear-induced crystallization occurs, can be defined with the specific work of flow (W),⁹⁰ as shown below with Eq. (1). In this equation, η is the viscosity averaged over the shear time (t_s). Since the viscosity, which is controlled by temperature, is included in this equation, the concept of the specific work of flow for determination of critical conditions for shear-induced crystallization describes the combined effects of shear rate, shear time, and shear temperature by a single quantity.

$$W = \int_{t_0}^{t_s} \eta \dot{\gamma}^2 dt = \eta \dot{\gamma}^2 t_s \quad (1)$$

The critical specific work of flow, above which shear-induced formation of additional point-like nuclei and thread-like precursors occurs, is available for various polymers, as listed in **Table 4**. A main advantage of using the work-concept, compared to plain information about critical shear rates or times, is the possibility to consider interconversion of shear rate, shear time, and viscosity with the latter controlled by the temperature. Nevertheless, these three parameters can only be interconvertible if the shear rate exceeds the critical threshold value for shear-induced formation of nuclei.¹⁰¹ Regarding the data of Table 4, it should be noted that the critical specific work of flow of a given polymer strongly depends on the chemical architecture, including molar masses and its distribution.

Table 4: Specific work of flow of various homopolymers.

Polymers	Critical specific work of flow (W_c) (in MPa) for generation of		Ref.
	Point-like nuclei	Shish-like nuclei	
iPP	7–8	25–70	[90,93,100,118]
LDPE	-	0.29–0.75	[96]
PEEK	1	-	[110]
PLLA	0.02–0.05	2.5	[101,106]
PA 66	0.05	-	[104]

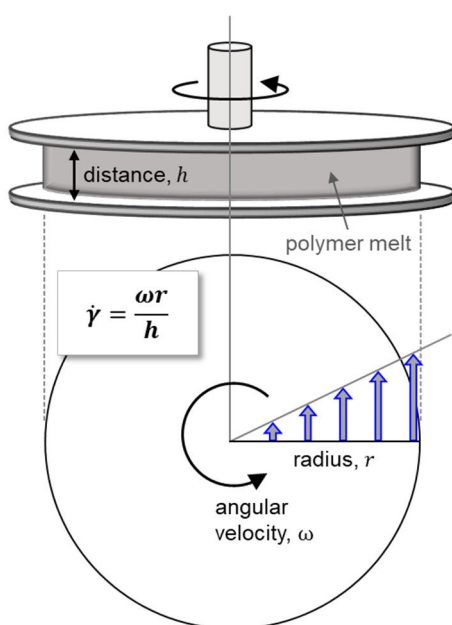


Figure 11: Sketch of the sample compartment of a parallel-plate rheometer (top). The lower part shows the increase of the shear rate with radius of the disc-like sample.

Shear-induced crystallization in many polymers has been studied using a conventional parallel-plate rheometer.^{104,106,112–116} **Figure 11** shows a sketch of such geometry where the bottom plate is fixed, and the top plate is rotating. When moving the upper plate and shearing the sample with a constant thickness (h), the angular velocity (ω) rises as a function of the radius of the sample (r) (see blue arrows). As such, the shear rate increases proportionally to the sample radius (see equation in the figure)¹¹⁷ and, in consequence, the specific work of flow increases correspondingly. Typically, the shear-induced crystallization experiment is performed by two steps; first, the melt is sheared at a predefined rate, time, and temperature, and secondly, the crystallization step is performed, generally at isothermal condition at a specific temperature. The kinetics of crystallization can be followed by the evolution of the shear modulus or the complex viscosity. As a function of shear rate and shear time, at a specific temperature, if there is shear-induced crystallization, the onset of the increase

of shear modulus or of the complex viscosity curves shifts to shorter time. The semicrystalline structure formed from the sheared melt can afterwards be inspected by microscopy, or other analysis-tools, often revealing a gradient structure along the radius of the sheared disk due to the shear gradient,^{106,119} as shown in **Figure 12** on an example of poly(L-lactic acid) (PLLA).¹⁰⁶ In the center, where the specific work of flow is zero, crystallization is incomplete in the pre-set crystallization time of 4 min, due to the low rate of the quiescent-melt crystallization. With increasing distance toward the edge of the disc, the specific work of flow increases. If the specific work of flow is above the critical value where shear-induced formation of additional point-like nuclei occurs, then a higher number of spherulites is observed due to an increase of the nuclei density, accelerating crystallization in this region.^{90,119} In case of alignment of nuclei, causing formation of so-called row-nucleated structures,^{120,121} smaller spherulites, or tiny point-like structures may form if the shear deformation further increases (see Regime II in Figure 10).¹⁰⁸ Furthermore, replacement of the row- and point-like structures by shish-kebabs is

observed if the shear deformation is much stronger, well above the critical specific work of flow for shear-induced formation of thread-like nuclei, as presented in Table 4.^{103,104,106,109}

Shear-induced shish-like precursors have been found to be more stable than the crystal nuclei leading to growth of spherulites.^{122,100,123–127} The dissolution of nuclei formed in the quiescent melt occurs typically 10–15 K above the melting temperatures of spherulitically grown lamellar crystals.^{48,128,129} Melting and annealing a sample a few Kelvin higher than the melting point of spherulitically grown crystals may preserve self-seed which can act like a nucleating agent accelerating subsequent crystallization on lowering the temperature. In case of sheared melts, shish-like precursors can survive at higher temperatures than self-seed based on lamellar crystals formed in the quiescent melt,^{100,113,123,126} and the lifetime of shish-like nuclei is rather long if heating to the temperatures below the equilibrium melting temperature.^{100,126} The stability of the sheared-induced crystallization precursors is related to the relaxation time of stretched chain segments in the deformed entanglement network. It was found that the sheared-induced precursors can be dissolved by annealing the melt at high temperatures for a short time or at low temperatures for longer time.^{100,126} With insufficient thermal conditions for chain relaxation, shish-based precursors will survive and, as a result, serve as nuclei enhancing subsequent crystallization.^{126,130} The nucleation efficiency of the sheared-induced precursors is found to depend on the shear deformation.^{126,130,131}

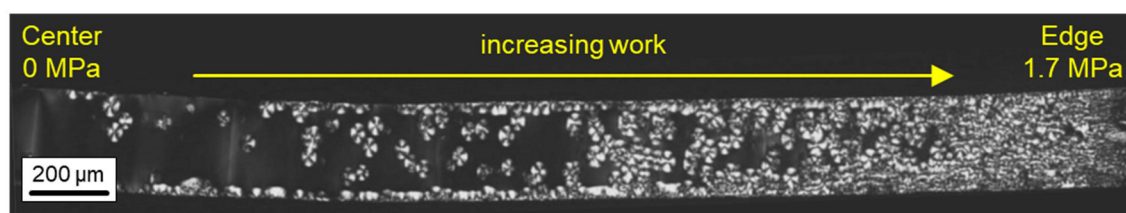


Figure 12: POM image showing the structure of a sheared PLLA disc ($\dot{\gamma} = 2.5 \text{ s}^{-1}$, $t_s = 10 \text{ s}$, $T_s = 135 \text{ }^\circ\text{C}$), crystallized at $135 \text{ }^\circ\text{C}$ for 4 min, along the radius, reproduced from Ref. [106] with permission from Wiley. The specific work of flow values indicated in the figure are obtained by calculation using Eq. (1), demonstrating a maximum specific work of flow at the edge of about 1.7 MPa.

1.5 State-of-the-art knowledge about the semicrystalline structure and crystallization of PA 11 at rapid-cooling conditions and in presence of shear

PA 11 is a crystallizable polymer, able to crystallize into different structures (polymorphism) which are controlled by the crystallization conditions.^{58,132–134} Regarding crystallization of the quiescent melt, **Figure 13** shows on the left-hand side a schematic diagram about the cooling-rate/supercooling-controlled crystal polymorphism and related semicrystalline morphologies in PA 11 with fast (red) and slow cooling routes (blue) presented in the left and right parts, respectively.²⁷ The right-hand side of the figure presents the basal planes of the unit cells of the pseudo-hexagonal δ' -crystal (top) and the triclinic α -crystal (bottom).¹³⁵ Slow cooling of the melt allows formation of pseudo-hexagonal δ -crystals via heterogeneous nucleation at low supercooling, which reversibly transform into triclinic α -crystals at the Brill-transition temperature (T_{Brill}).^{136,137} The α -form, typically, is of lamellar shape and organized within spherulites.⁵⁸ The basal plane of the unit cell of the α -crystal shows the arrangement of hydrogen bonds between adjacent chains, being aligned, indicated by the yellow color. In

contrast, fast cooling of the melt leads to non-spherulitic growth of pseudo-hexagonal δ' -crystals of nodular shape at high supercooling of the melt via homogeneous nucleation. The pseudo-hexagonal δ' -crystal is characterized by a random orientation of hydrogen bonds between neighbored chain segments. The δ' -mesophase is metastable at room temperature and irreversibly transforms into the stable δ/α -crystal modification upon heating.^{134,137} So far, quantitative information about cooling-rate-controlled nucleation and crystallization, and with that in relation to formation of specific morphologies in PA 11 is not available.

Shear-induced crystallization has been studied in several polyamides such as PA 6,¹¹⁶ PA 66,¹⁰⁴ and polyamide 12 (PA 12).¹³⁰ However, analyses of crystallization of the sheared melt of linear PA 11 are lacking; only a single work about the effect of shear on crystallization in case of a self-synthesized branched PA 11 is available.¹³⁸ The experimental results suggested that there is no shear-induced crystallization though a high shear rate up to 10 s^{-1} for 6 s was applied. The lack of knowledge of critical shear parameters, required to enhance crystallization during processing of PA 11 and to generate specific semicrystalline morphologies, is a main motivation of the research presented in this dissertation since such knowledge is required to establish a relation between processing parameters, structure formation, and properties.

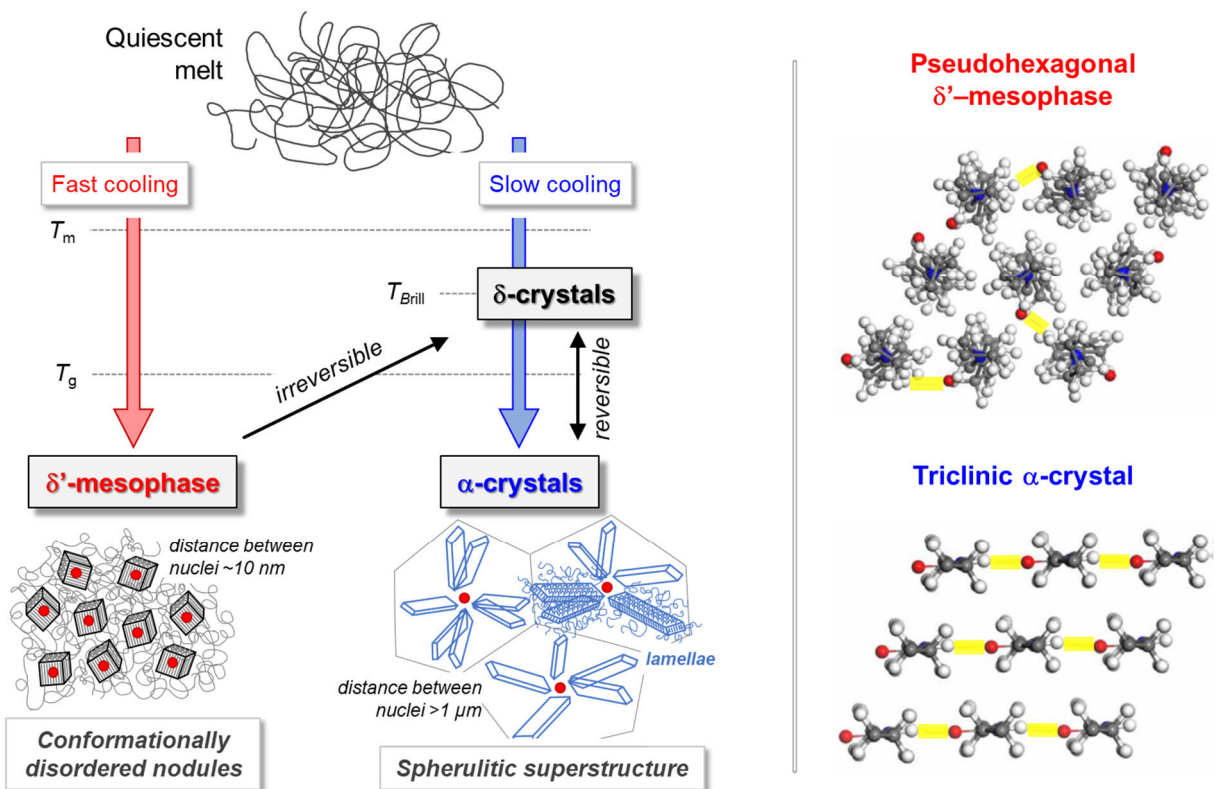


Figure 13: Schematic about the cooling-rate controlled crystal polymorphism and semicrystalline morphologies of PA 11 crystallized from the quiescent melt (left), with fast and slow cooling routes represented in the red and blue colors, respectively (reproduced from Ref. [27] with permission from Wiley). Basal planes of the unit cells of pseudo-hexagonal δ' -crystals (top) and the triclinic α -crystals (bottom) are shown in the right part of the figure.¹³⁵

2. PROBLEM STATEMENT

PA 11 is a semicrystalline bio-based polymer used in high-performance engineering applications. The properties of polymers, in general, are affected by the semicrystalline morphology including fraction, structure, size, shape, and perfection of crystals, and their organization in a superstructure, with all these parameters controlled by the crystallization/processing conditions. Crystallization during polymer melt-processing often occurs in presence of shear forces and at rapid-cooling conditions, with the resulting structures expected being different from the morphology obtained by crystallization during slow cooling and in absence of mechanical forces. In order to be able to tailor the structure and, consequently, properties, the crystallization behavior at such processing-relevant cooling conditions and in presence of shear conditions needs to be known.

Research of crystallization of PA 11 under processing-relevant conditions is limited. Few works provided initial information about the cooling-rate/supercooling dependence of the crystallization kinetics and the crystal polymorphism.^{58,87,139} However, a correlation between the supercooling of the melt and nucleation-controlled formation of specific morphologies has not been evaluated. Furthermore, quantitative information about the kinetics of homogeneous crystal nucleation is not available neither, being, among others, important for predicting the long-term behavior of this polymer at ambient temperature, that is, at a temperature slightly below the glass transition temperature. Knowledge about shear-induced crystallization of PA 11 is completely absent, disabling tailoring of processing routes towards adjustment of specific semicrystalline morphologies when developing during cooling an oriented melt.

3. AIMS AND STRATEGIES

Knowledge and understanding of the relationship between processing-condition-controlled crystallization and the resulting structure is of importance in determining ultimate polymer properties, however, is lacking for PA 11. The aim of this work is therefore to investigate the effect of processing-relevant cooling rates and shear conditions on the crystal nucleation and crystallization on one side and on the resulting semicrystalline morphology on the other side. A comprehensive overview about nucleation and crystallization pathways on solidification the quiescent and sheared melt of this important bio-based polymer will be provided.

To achieve the aim of the work, crystallization of the quiescent melt at different processing-relevant cooling rates will be analyzed. A sophisticated technique is required for such investigation, which is FSC. This method allows cooling the polymer at rates up to 100,000 K/s which is needed to evaluate the kinetics of homogeneous crystal nucleation in PA 11 at high melt-supercooling. Analysis of the temperature dependence of the nucleation rate is performed using Tammann's two-stage crystal nuclei development method. In addition, details of FSC instrumentation from point of view of assuring an optimum experimental setup are explored. Based on the gained knowledge about the nucleation and crystallization kinetics, a correlation with the structure formed at specific conditions will be established. Film samples will be prepared at various cooling conditions using different cooling media, and semicrystalline morphologies of such film samples will be inspected using POM, XRD, and AFM.

The effect of shear on the melt-crystallization and the morphology of PA 11 will be examined using a parallel-plate rheometer. Different shear rates for a fixed shear time will be applied to the samples, and the sheared melt will be crystallized at a selected temperature. Then, the crystallization kinetics will be followed by the evolution of the complex viscosity, to determine the critical conditions for flow-induced crystallization, followed by analysis of semicrystalline morphologies when the melt was sheared at different conditions. The concept of the specific work of flow will be applied here for the first time to PA 11, to propose the relationship between the shear conditions, the crystallization kinetics, and the final morphology.

Finally, the thermal stability and nucleation efficacy of self-nuclei based on molten crystals, formerly formed from both the quiescent and oriented melt, will be analyzed. It is an attempt to gain quantitative information about stability and nucleation efficacy of two types of shear-induced precursors; point-like and shish-like nuclei, using hot-stage microscopy. The results are expected to improve the understanding of memory effects in repeated processing.

In summary, with the knowledge and information of nucleation and crystallization under processing-relevant conditions, it is ultimately expected to contribute for better understanding and prediction of structure formation in polymer melt-processing of PA 11. Furthermore, as an additional benefit of this work, experimental tools and special-designed experiments can be applied for similar analyses of the polymers.

4. RESULTS AND DISCUSSION

The results and discussion part in this cumulative dissertation are presented as a series of research publications, introduced in short below, based on Graphical abstracts.

4.1 Experimental analysis of lateral thermal inhomogeneity of a specific chip-calorimeter sensor

Katalee Jariyavidyanont¹, Amir Abdelaziz², René Androsch¹, Christoph Schick^{2,3}

¹ Interdisciplinary Center for Transfer-oriented Research in Natural Sciences (IWE TFN), Martin Luther University Halle-Wittenberg, 06099 Halle/Saale, Germany.

² University of Rostock, Institute of Physics and Competence Center CALOR, Albert-Einstein-Str. 23–24, 18059 Rostock, Germany.

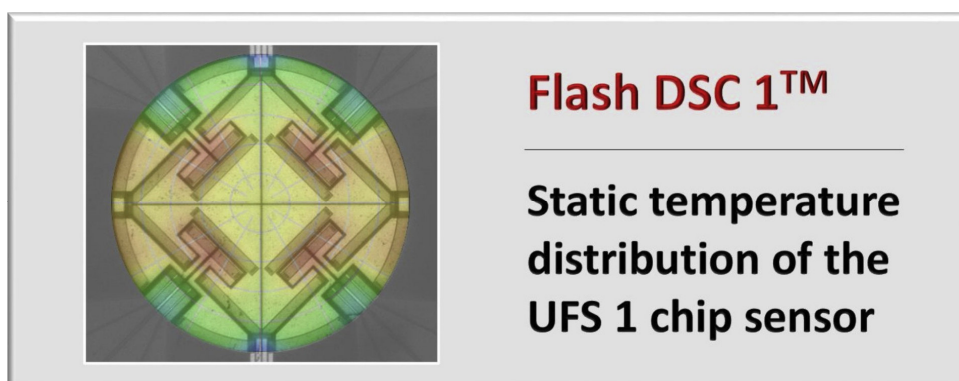
³ Kazan Federal University, 18 Kremlyovskaya Street, Kazan 420008, Russian Federation.

Thermochimica Acta 2019, 674, 95–99.

Research highlights

1. Quantitative information about crystal nucleation and crystallization at high supercooling of the melt requires the use of fast scanning chip calorimetry (FSC).
2. In-situ thermo-optical position-resolved analysis of melting of indium, isotropization of the 8OCB liquid crystal, and melting of PLLA suggests an inhomogeneous temperature distribution of the chip sensor UFS 1 due to existence of distinct hot- and cold-spots on the sensor heating area.
3. The central area of the sensor is recommended for placing samples, if precise measurement of transition temperatures is needed.

Graphical abstract





Experimental analysis of lateral thermal inhomogeneity of a specific chip-calorimeter sensor



Katalee Jariyavidyanont^a, Amir Abdelaziz^b, René Androsch^a, Christoph Schick^{b,c,*}

^a Interdisciplinary Center for Transfer-Oriented Research in Natural Sciences (IWE TFN), Martin Luther University Halle-Wittenberg, 06099, Halle/Saale, Germany

^b University of Rostock, Institute of Physics and Competence Center CALOR, Albert-Einstein-Str. 23–24, 18059 Rostock, Germany

^c Kazan Federal University, 18 Kremlyovskaya Street, Kazan 420008, Russian Federation

ARTICLE INFO

Keywords:

Fast scanning chip calorimetry (FSC)
Temperature distribution
Indium melting
Crystallization
Melting and isotropization

ABSTRACT

Fast scanning calorimetry (FSC) requires reliable temperature measurements and knowledge about the temperature distribution in the chip calorimeter sensor. Analysis of the melting temperature of indium placed at different positions on the sensor and thermo-optical analysis of the isotropization of 4,4'-octyloxy cyanobiphenyl (8OCB) liquid crystal allow estimation of the lateral temperature distribution of chip calorimeter sensors. The chip sensor UFS 1 (Flash DSC1™, Mettler Toledo, Switzerland) was chosen as an example but the procedures described also hold for other sensors. The data revealed on one side existence of distinct hot- and cold-spots and on the other side an area with a rather homogeneous temperature distribution. The latter, central area of the sensor is recommended for placing samples if precise measurement of transition temperatures are anticipated. The observed inhomogeneous temperature distribution over the total sensor area is confirmed by thermo-optical analysis of melting of poly (L-lactic acid) and crystallization of isotactic polypropylene, emphasizing the need for careful sample preparation/positioning in typical fast scanning chip calorimeter analyses.

1. Introduction

Fast scanning calorimetry (FSC) is an analytical tool for calorimetry-based thermal analysis of materials at conditions which cannot be achieved by conventional differential scanning calorimetry (DSC) [1]. These include in particular high cooling and heating rates, recording of heat-flow rate data at high sampling rate and with minimal instrumental lag, or the possibility of analysis of tiniest amount of samples. Such conditions are realized by chip-calorimeters, which were developed starting around the mid 1990ies [2,3], and which nowadays are available with a large variety of sizes and corresponding performance levels [4]. In case of the commercial Flash DSC1™, Mettler-Toledo (Switzerland) [5], which employs the Xensor Integration XI-400 chip (Mettler-Toledo UFS 1™) [4], operated in power-compensation differential mode, it is possible to heat and cool samples at rates up to few thousand K/s. The sensor time constant is around few milliseconds, allowing analysis of the kinetics of phase transitions with half-transition times of as low as about 10 ms [5]. Such performance is possible due to the low addenda heat capacity of the chip sensor, with heaters and thermometers integrated into a thin membrane, produced by MEMS. Typically, in case of the UFS 1 sensor, the sample mass is in between 10 and few hundred ng. However, there are much smaller and therefore

faster sensors available, requiring then samples of sub-ng mass, permitting calorimetric analyses at rates of temperature change up to 10⁶ K/s [6,7].

Reliable FSC measurements require detailed knowledge of the instrument characteristics including calibration procedures and sample-size effects. Information regarding the design, performance, and thermal lag, as well as initial, provider-side performed temperature calibration for the above-introduced UFS 1 sensor are available in the literature [8–11]. Of particular importance is the measurement of the temperature, as it is required as a rule in thermal analysis techniques. In a more general description of FSC instrumentation, details about temperature calibration are provided with emphasis placed on selection of calibrants, correction of thermal lags, temperature gradients in direction of the sample thickness as well as the lateral temperature profile in membrane-based calorimeters [12].

Thermal gradients in sample-thickness direction, from the bottom side of the sample, which is in contact with the sensor membrane containing the heaters and thermometers, to the upper surface of the sample, being surrounded by the gas acting a cooling medium, may span a temperature range of few Kelvin. This in particular is true for polymers, which exhibit a low thermal conductivity. In temperature-scanning experiments such large gradient typically is appreciated since

* Corresponding author at: University of Rostock, Institute of Physics and Competence Center CALOR, Albert-Einstein-Str. 23–24, 18059 Rostock, Germany.
E-mail address: christoph.schick@uni-rostock.de (C. Schick).

<https://doi.org/10.1016/j.tca.2019.02.016>

Received 18 January 2019; Received in revised form 25 February 2019; Accepted 26 February 2019

Available online 27 February 2019

0040-6031/© 2019 Elsevier B.V. All rights reserved.

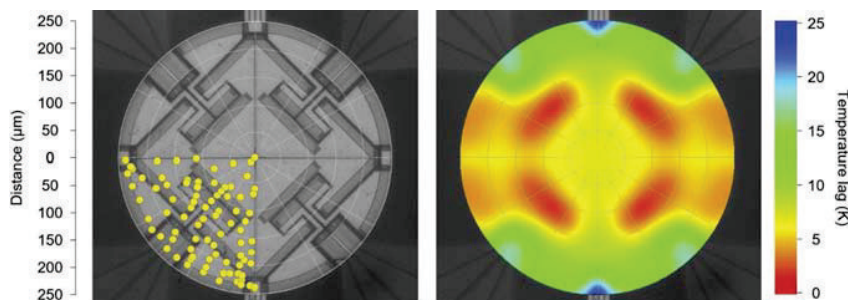


Fig. 1. Photograph of the Mettler-Toledo UFS 1 chip sensor, including the positioning of Indium for analysis of their apparent melting temperature. The spot size corresponds approximately the size of the sample (left). The set of measured melting temperatures, obtained on heating at 1000 K/s, was used to generate a contour plot using Origin 2015 (right).

thermal effects/transitions inherently often are rather broad due to structural inhomogeneity, however, since even at constant membrane temperature the sample is cooled on the upper surface by the surrounding gas a distinct static thermal gradient is observed [13–15].

Regarding the lateral temperature distribution on the sensor it was reported early [13] that even the heated area is small in chip calorimeters, the active sensor area is not homogeneously heated, in particular if containing two or even more resistive heater stripes. This was proven for specific sensors by infrared thermography and analytical modeling [16,17], and by watching the nematic–isotropic transition of the liquid crystal 8OCB [13], also used for temperature calibration of DSC instruments [18,19]. If the sensor is covered with a metal layer for the purpose of temperature homogenization, then local temperature differences at different sensor positions may be minimized [20,9]. However, since such additional metal layer adds to the addenda heat capacity of the sensor such a layer is counter-productive for achieving high scan rates. In contrast, for uncoated sensors, lateral temperature differences may reach 10 K, requiring then special care regarding placement of samples [8,13,21]. In particular, placing the sample on top of a heater, or outside of the heated area, is not recommended [12].

For the rather large commercial Mettler-Toledo UFS 1 XI-400 chip sensor detailed information about the lateral temperature distribution are not yet available. For this reason, several experimental approaches are introduced in the present study, which ultimately permits providing a recommendation about safe placement/positioning of samples if temperature-wise highly accurate data are needed.

2. Experimental

2.1. Materials

The temperature distribution of the Mettler-Toledo UFS 1 chip sensor was point-wise analyzed by placing Indium with a mass of around 1 ng at different positions on the heated area of the sensor, to subsequently be melted at rates of 10, 100, and 1000 K/s. We employed Indium from the Mettler-Toledo DSC-calibration set.

In a further experiment, the entire heatable area of the sensor was covered with the liquid crystalline material 8OCB (4,4'-octyloxycyanobiphenyl) ($C_{21}H_{25}NO$) from Merck KGaA (Germany) [22,23]. First, a thin film with a thickness of about 5 μm was prepared on a hot-stage, followed by cutting using scalpel/stereomicroscope, to fit the lateral dimension of the chip sensor. For evaluation of the static temperature distribution on the sensor, the isotropization of the nematic liquid crystalline phase at about 82 $^{\circ}\text{C}$ was followed on stepwise increase of the programmed temperature using an optical microscope.

The knowledge of the lateral temperature-distribution of the heatable area of the sensor, gained by the analysis of phase-transition temperatures of Indium and 8OCB-liquid crystals, ultimately was confirmed employing typical polymer samples. We used an extrusion-grade poly (L-lactic acid) (PLLA) homopolymer from Sulzer Chemtec Ltd. (Switzerland) for analysis of the position-dependent melting temperature, and a highly pure extrusion-grade isotactic polypropylene (iPP)

HC300BF from Borealis (Austria). The latter material contained a nucleating agent, added to assure reproducible crystallization in cooling experiments. The two polymer samples were subject of earlier crystallization studies [24–27], with more material-details reported therein. In both cases, PLLA and iPP, sample preparation included cutting thin sections with a thickness of about 10 μm using a SLEE microtome, followed by definition of the lateral sample size with a scalpel and stereomicroscope.

2.2. Instrumentation

We used a Flash DSC 1 chip calorimeter from Mettler-Toledo (Switzerland), operated with the sample support temperature set to 30 $^{\circ}\text{C}$. Sensors were conditioned and temperature-corrected according to the operating instructions of the instrument provider. Main reason for setting the sample-support temperature to 30 $^{\circ}\text{C}$ is non-required sub-ambient temperature operation, and the opportunity to use an external chip holder. The external chip holder (Functional Materials Rostock e.V., Germany) was connected to the FSC by wire-extension of the electrical pin-connectors of the main device. The advantage of the external chip holder is the possibility to place it onto the sample stage of a microscope, for in-situ observation of changes of structure of FSC samples during heating and cooling. We employed a Kern OPN-184 reflection mode polarized-light optical microscope (POM) equipped with a Leica camera for imaging.

3. Results and discussion

Fig. 1 shows at the left-hand side a photograph of the Mettler-Toledo UFS 1 chip sensor. The circular heatable area, symmetry wise, has two mirror planes, and its diameter is 500 μm . The yellow spots indicate the positioning of samples of Indium for analysis of their apparent melting temperature. Note that at any time only a single Indium sample was placed onto the sensor to (a) avoid disturbance of the individual melting processes by the endothermic heat flow of neighbored particles and (b) safely assign the recorded melting peak to a well-defined position on the sensor. Note furthermore that a single sample of Indium was used for several measurements at different positions. However, to assure that repeated melting and crystallization have no effect on the measured melting temperature, samples were replaced after an arbitrary number of uses. The indium samples were placed and moved on the sensor with the help of a 30 μm soft copper wire. The size of each yellow spot corresponds approximately the size of the sample. As such, there was observed a set of measured, by the chip sensor thermopile, apparent melting temperatures, obtained on heating at 1000 K/s, as a function of the position of the sample on the sensor. The latter was quantified by a virtual coordinative system, with its origin placed at the center of the heatable area of the sensor, using polar coordinates. In the example of Fig. 1, 88 positions of the indium sample were measured for obtaining the temperature distribution in a single quadrant of the sensor, which then allowed generation of a contour plot using the Origin 2015 software (right) [28]. The differences in the observed

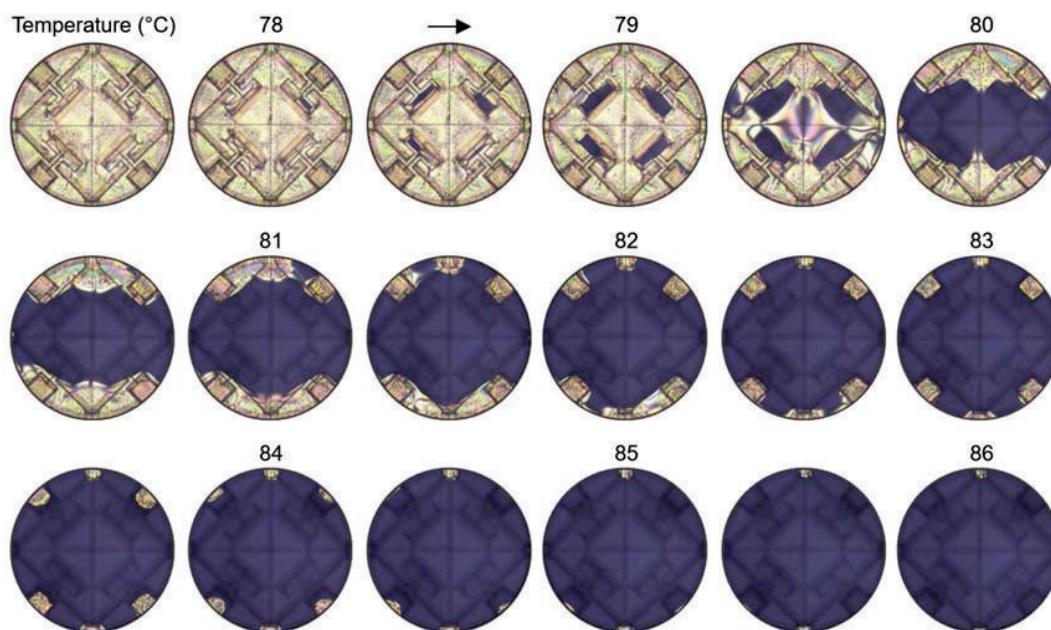


Fig. 2. POM photographs of the Mettler-Toledo UFS 1 chip sensor covered with a layer of 4,4'-octyloxycyanobiphenyl (80CB). The images were taken during heating the nematic liquid-crystalline phase to above the isotropization temperature at around 80 °C at a rate of 0.01 K/s, to be read line-wise from left to right and top to bottom. The temperature-difference between neighbored images is 0.5 K. The slight asymmetry between top and bottom parts of the images is probably caused by a thickness gradient of the sample.

melting temperatures are expressed as different colors (see scale bar to the right). Red color indicates the position of samples of indium which melted at the lowest recorded temperature, while melting of samples placed in yellow, green, and blue colored areas apparently melted at higher temperature. It is worth noting that the heating rate has an only minor effect on the observations. The apparent-melting-temperature distribution was measured using heating rates of 1, 10, 100, and 1000 K/s with only negligible heat-rate-caused thermal lags detected, being of the order of magnitude of 1 K in the analyzed heating-rate range. Accordingly, the color map in Fig. 1 represents the approximate static temperature distribution of the sensor at about 150 °C, when using a sample support temperature of 30 °C. As such, the sensor contains four strip-like heaters, assuring a rather homogeneous temperature field/band with a width of about 300 μm parallel to the horizontal mirror plane, in which the temperature deviation is lower than 5–7 K compared to the temperature on top of the heaters. The green and blue colored areas are significantly colder than the area of the central band, with the apparent-melting temperature deviation being 10 + K compared to the area on top of the heaters.

Fig. 2 shows a series of POM photographs of the UFS 1 chip sensor covered with a thin layer of 80CB, taken during heating the nematic liquid-crystalline phase to above the isotropization temperature at around 80 °C at a rate of 0.01 K/s. The slow heating rate was chosen to obtain the quasi-static temperature distribution and it does not allow to collect meaningful heat flow rate curves. The images need to be read line-wise from left to right, starting with the top row. The temperature-difference between two neighbored images is 0.5 K. The temperatures provided are the apparent temperatures measured by the thermopile, which is part of the chip sensor. At a measured temperature of 77.5 °C, the sample is liquid-crystalline, causing birefringence and bright appearance of the sample film between crossed polarizers (top left image). With increasing temperature, starting at around 78.5 °C, part of the film turns black/dark, if located on top of the heaters, indicating the transition of the nematic liquid crystal phase into the isotropic and non-

birefringent melt. On further heating, the melting continues along the horizontal mirror plane, leaving up to a temperature of about 80.5 °C not yet melted material in the top and bottom parts of the sensor. In addition, the analysis of the 80CB melting behavior in Fig. 2 confirm the existence of the cold point-like spots at the circumference of the sensor (see blue colored areas in Fig. 1). Here, the sample remained in the nematic liquid crystalline phase up to well above 84 °C.

According to the images recorded during isotropization of the M24 liquid crystalline phase on slow heating, there is an inhomogeneous temperature distribution at the surface of the UFS 1 chip sensor when heated to elevated temperature by its own heaters, similar as detected by the analysis of the position-dependent apparent melting temperature of indium (see Fig. 1). However, the absolute values of the local temperature differences are largely different in the experiments of the Figs. 1 and 2. Roughly, we observed that melting of indium occurs in a temperature window larger than 10 K, dependent on the positioning of the sample, while isotropization of the 80CB liquid crystal occurred within a temperature range of 3 K. We may speculate that the lower temperature differences between different sensor areas in case of the 80CB sample is caused by the lower absolute temperature (80 °C versus 156 °C in case of probing the temperature distribution by indium melting) and by lateral heat conduction through the sample, causing temperature homogenization.

In order to confirm the importance of the observation of an inhomogeneous temperature distribution on the surface of the UFS 1 chip sensor, typical polymer samples were analyzed regarding their melting and crystallization behaviors. Fig. 3 shows a square-like sample of PLLA with a thickness of about 10 μm on the sensor, with a fine-spherulitic semicrystalline morphology adjusted by crystal nucleation at 60 °C, which is close to the glass transition, followed by growth of α' -crystals at 90 °C. The sample was then heated at a rate of 1 K/s which first allows conversion of the α' - into α -crystals and then final melting. The images of Fig. 3 show that melting begins on top of the heaters, latest at around 160 °C, as there the sample turns black between crossed

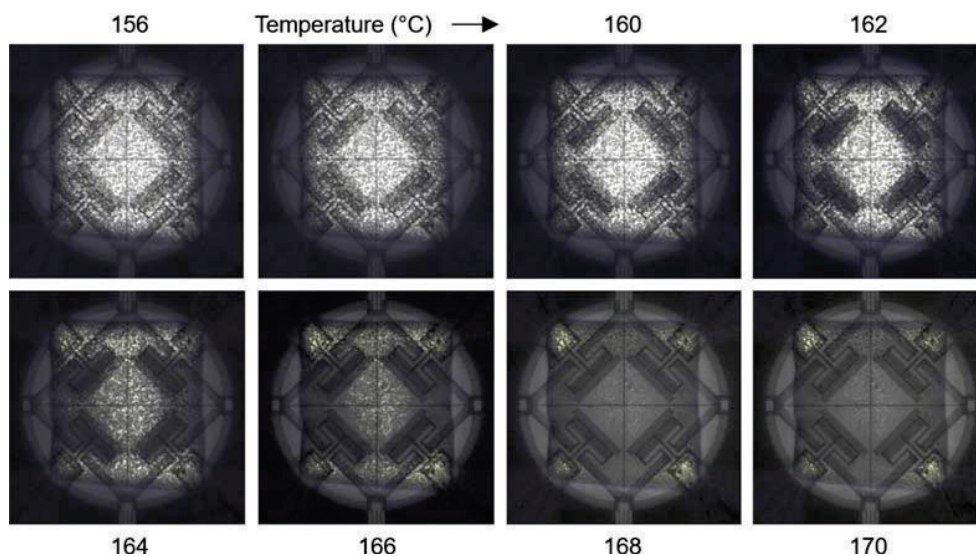


Fig. 3. POM photographs of the Mettler-Toledo UFS 1 chip sensor covered with a sample of PLLA with a thickness of about 10 μm . The images show the progress of melting in the various areas of the sensor during heating the semicrystalline sample at a rate of 1 K/s from 156 °C (top left) to 170 °C (right bottom).

polarizers first. As heating is continued, melting proceeds along the above described central band, with a clear delay in the central part of the sensor (see images at 166 °C). Only at distinctly increased temperature, stretching to 170 °C, or even higher, melting occurs in the top and bottom parts of the sensor as well as on top of the cold spots at the diagonals.

Since the morphology of a polymer depends on the cooling history/crystallization pathway, and since crystallization on the FSC sensor may proceed differently at different locations, the temperature distribution on cooling is also of interest. For this reason, the temperature inhomogeneity of the sensor was also measured in a cooling experiment, assuring that the initial structural state of the sample is not depending

on its position on the membrane. Fig. 4 shows a set of POM images of the sensor containing four samples of isotactic polypropylene located at different position. The positions of these samples were selected such to confirm the large temperature differences detected with the indium-melting experiment of Fig. 1 and 8OCB -isotropization experiment of Fig. 2. The images in Fig. 4 show the progress of crystallization during cooling the melt at a rate of 1 K/s, from 134 °C (top left) to 120 °C (right bottom), with all four samples having the same initial structure before begin of cooling. At 134 °C, all samples still are molten since appearing featureless and not showing any birefringence. With decreasing temperature, first, at 130 °C, the sample close to one of the cold spots (see blue colored areas in the right part of Fig. 1), turns bright, indicating

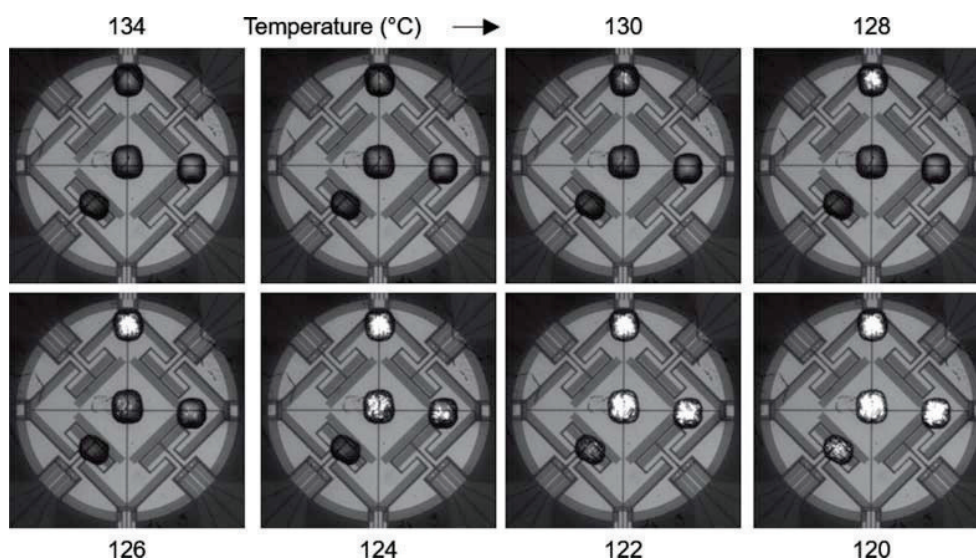


Fig. 4. POM photographs of the Mettler-Toledo UFS 1 chip sensor with four samples of isotactic polypropylene located at different position. The images show the progress of crystallization during cooling the melt at a rate of 1 K/s, from 134 °C (top left) to 120 °C (right bottom).

crystallization. At 126 °C, the two samples at the horizontal mirror plane show first formation of small spherulites, and only at an about 4 K lower temperature, at 122 °C, the sample placed directly on top of one of the heaters begins to crystallize. Worth emphasizing, the sample at the center of the sensor apparently begins to crystallize, roughly, at an about 4 K higher temperature than the sample paced on top of the heater, though not very far in position, and still well inside the heatable area.

4. Summary

This note is aimed to provide guidelines for correct sample placement on the UFS 1 chip sensor (Flash DSC 1, Mettler Toledo, Switzerland). Beside requirements regarding thermal gradients normal to the sensor caused by bad thermal contact between sample and chip sensor membrane, samples being too thick, cooling of the upper sample surface by the purge gas, etc., which are discussed in several publications, see e.g. [1] and references there in, lateral temperature inhomogeneity in the chip must be considered too.

Four independent ways to determine the lateral temperature profile in the active (heated) area of the chip sensor UFS 1 are discussed. (i) Placing a tiny piece of a metal or another material with well-defined melting temperature at different positions and measuring the apparent melting temperature. The obtained data allow construction of a temperature contour plot. (ii) Covering the sensor by a thin layer of a liquid crystal and observing the liquid crystalline (birefringent) to isotropic (non-birefringent) transition by polarized-light optical microscopy (POM). (iii) Following the lateral distribution of the melting transition of a semicrystalline polymer by POM. (iv) Observing the spatial development of birefringence during crystallization of a fast crystallizing polymer by POM. Method (i) is limited to continuous heating experiments since the melting peak of the calibrant is evaluated. Essentially the same holds for (iii) (heating) and (iv) (cooling) because (re)crystallization of the sample during extended isothermal stages must be avoided. In contrast, the nematic to isotropic transition of 8OCB does not show kinetics on the time scales of interest here. Consequently, method (ii) is applicable on heating, on cooling and under isothermal conditions. The latter allows investigation of the development of the temperature profile with extended periods of time, e.g. several hours.

The obtained results are summarized as follows: All four methods show a similar lateral temperature distribution in the chip sensor UFS 1 with hot spots on top of the heaters and cold spots at the periphery where the electrical connections enter the heated region. Temperature differences can reach 10 K between hot and cold spots, depending on the temperature difference between heated area and the ambient. Fortunately, in the central part of the heated area, surrounded by the heaters, all methods indicate an essentially flat temperature distribution with differences below 1 K. The lateral dimension of this area is about 150 μm and allows/suggests exclusive placement of the sample there.

For reliable fast scanning calorimetry employing the sensor UFS 1, the sample, fulfilling all other requirements, should be placed in the central square area of 150 \times 150 μm^2 and should not extend on top of the heaters (hot spots) and no sample should be placed near to the outer edge of the active area where cold spots are located.

Acknowledgements

AA acknowledges a stipendium from the government of Algeria. CS acknowledge financial support from the Ministry of Education and Science of the Russian Federation, grant 14.Y26.31.0019.

References

- [1] C. Schick, V. Mathot, *Fast Scanning Calorimetry*, Springer, 2016.
- [2] D.W. Denlinger, E.N. Abarra, K. Allen, P.W. Rooney, M.T. Messer, S.K. Watson, F. Hellman, Thin-film microcalorimeter for heat-capacity measurements from 1.5-K TO 800-K, *Rev. Sci. Instrum.* 65 (1994) 946–958.
- [3] S.L. Lai, G. Ramanath, L.H. Allen, P. Infante, Z. Ma, High-speed (10(4)-degrees-C/S) scanning microcalorimetry with monolayer sensitivity (*J/M(2)*), *Appl Phys. Lett.* 67 (1995) 1229–1231.
- [4] Detailed Technical Information about FSC Chips are Available by Xensor Integration®, (2017) <http://www.xensor.nl>.
- [5] V. Mathot, M. Pyda, T. Pijpers, G.V. Poel, E. Van de Kerkhof, S. Van Herwaarden, F. Van Herwaarden, A. Leenaers, The Flash DSC 1, a power compensation twin-type, chip-based fast scanning calorimeter (FSC): first findings on polymers, *Thermochim. Acta* 522 (2011) 36–45.
- [6] A.A. Minakov, C. Schick, Ultrafast thermal processing and nanocalorimetry at heating and cooling rates up to 1 MK/s, *Rev. Sci. Instrum.* (78) (2007) 073902.
- [7] E. Zhuravlev, V. Madhavi, A. Lustiger, R. Androsch, C. Schick, Crystallization of polyethylene at large undercooling, *ACS Macro Lett.* 5 (2016) 365–370.
- [8] G.V. Poel, D. Istrate, A. Magon, V. Mathot, Performance and calibration of the Flash DSC 1, a new, MEMS-based fast scanning calorimeter, *J. Therm Anal Calor* 110 (2012) 1533–1546.
- [9] S. Van Herwaarden, E. Iervolino, F. Van Herwaarden, T. Wijffels, A. Leenaers, V. Mathot, Design, performance and analysis of thermal lag of the UFS1 twin-calorimeter chip for fast scanning calorimetry using the Mettler-Toledo Flash DSC 1, *Thermochim. Acta* 522 (2011) 46–52.
- [10] E. Iervolino, A.W. Van Herwaarden, F.G. Van Herwaarden, E. Van de Kerkhof, P.P.W. Van Grinsven, A.C.H.L. Leenaers, V.B.F. Mathot, P.M. Sarro, Temperature calibration and electrical characterization of the differential scanning calorimeter chip UFS1 for the Mettler-Toledo Flash DSC 1, *Thermochim. Acta* 522 (2011) 53–59.
- [11] G.V. Poel, A. Sargsyan, V. Mathot, G.V. Assche, A. Wurm, C. Schick, A. Krumme, D. Zhou, Recommendation for Temperature Calibration of Fast Scanning Calorimeters (FsCs) for Sample Mass and Scan Rate, Beuth Verlag GmbH, Berlin, 2011.
- [12] C. Schick, R. Androsch, Fast scanning calorimetry, in: S. Vyazovkin, N. Koga, C. Schick (Eds.), *Handbook of Thermal Analysis and Calorimetry: Recent Advances, Techniques and Applications*, 2nd edition, Elsevier, 2018, pp. 47–102.
- [13] E. Zhuravlev, C. Schick, Fast scanning power compensated differential scanning nano-calorimeter: 1. The device, *Thermochim. Acta* 505 (2010) 1–13.
- [14] A. Toda, M. Konishi, An evaluation of thermal lags of fast-scan microchip DSC with polymer film samples, *Thermochim. Acta* 589 (2014) 262–269.
- [15] X. Monnier, A. Saiter, E. Dargent, Physical aging in PLA through standard DSC and fast scanning calorimetry investigations, *Thermochim. Acta* 648 (2017) 13–22.
- [16] A. Minakov, J. Morikawa, T. Hashimoto, H. Huth, C. Schick, Temperature distribution in a thin-film chip utilized for advanced nanocalorimetry, *Meas. Sci. Technol.* 17 (2006) 199–207.
- [17] A. Minakov, J. Morikawa, E. Zhuravlev, M. Ryu, A.W. van Herwaarden, C. Schick, High-speed dynamics of temperature distribution in ultrafast (up to 10⁸ K/s) chipnanocalorimeters, measured by infrared thermography of high resolution, *J. Appl. Phys.* 125 (5) (2019) 054501–054515.
- [18] S. Neuenfeld, C. Schick, Verifying the symmetry of differential scanning calorimeters concerning heating and cooling using liquid crystal secondary temperature standards, *Thermochim. Acta* 446 (2006) 55–65.
- [19] C. Schick, U. Jonsson, T. Vassilev, A. Minakov, J. Schawe, R. Scherrenberg, D. Lőrinczy, Applicability of 8OCB for temperature calibration of temperature modulated calorimeters, *Thermochim. Acta* 347 (2000) 53–61.
- [20] A.F. Lopeandia, J. Rodriguez-Viejo, M. Chacon, M.T. Clavaguera-Mora, F.J. Munoz, Heat transfer in symmetric U-shaped microreactors for thin film calorimetry, *J. Microchem. Microeng.* 16 (2006) 965–971.
- [21] C. Simon, M. Peterlechner, G. Wilde, Experimental determination of the nucleation rates of undercooled micron-sized liquid droplets based on fast chip calorimetry, *Thermochim. Acta* 603 (2015) 39–45.
- [22] C.W. Garland, G.B. Kasting, K.J. Lushington, High-resolution calorimetric study of the nematic–smectic-a transition in octyloxycyanobiphenyl (8OCB), *Phys. Rev. Lett.* 43 (1797) 1420–1423.
- [23] S.M. Sarge, G.W. Hoehne, H.K. Cammenga, W. Eysel, E. Gmelin, Temperature, heat and heat flow rate calibration of scanning calorimeters in the cooling mode, *Thermochim. Acta* 361 (2000) 1–20.
- [24] R. Androsch, M.L. Di Lorenzo, C. Schick, Crystal nucleation of random *l*/*d*-lactide copolymers, *Eur. Polym. J.* 75 (2016) 474–485.
- [25] M.L. Di Lorenzo, R. Androsch, Stability and reorganization of α' -crystals in random *l*/*d*-lactide copolymers, *Macromol. Chem. Phys.* 217 (2016) 1534–1538.
- [26] C. Sungkapreecha, N. Iqbal, A.M. Gohn, W.W. Focke, R. Androsch, Phase behavior of the polymer/drug system PLA/DEET, *Polymer* 126 (2017) 116–125.
- [27] A.M. Rhoades, N. Wonderling, A. Gohn, J. Williams, D. Mileva, M. Gahleitner, R. Androsch, Effect of cooling rate on crystal polymorphism in beta-nucleated isotactic polypropylene as revealed by a combined WAXS/FSC analysis, *Polymer* 90 (2016) 67–75.
- [28] Origin™, software documentation, <https://www.originlab.com/Origin>; assessed 20/12/2018.

4.2 Nucleation-controlled dual semicrystalline morphology of polyamide 11

Katalee Jariyavidyanont¹, Christoph Schick^{2,3}, René Androsch¹

¹ Interdisciplinary Center for Transfer-oriented Research in Natural Sciences (IWE TFN), Martin Luther University Halle-Wittenberg, Halle/Saale, Germany.

² Institute of Physics and Competence Center CALOR, University of Rostock, Germany.

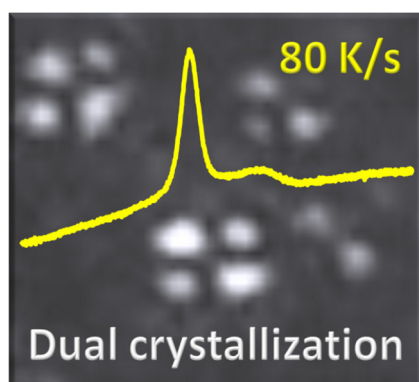
³ Department of Physical Chemistry, Kazan Federal University, Kazan, Russia.

Polymer International 2019, 68, 263–270, reproduced with permission from Wiley.

Research highlights

1. Quiescent-melt crystallization of PA 11 at processing-relevant cooling conditions was analyzed by FSC.
2. Different semicrystalline morphologies were generated by variation of nucleation pathways using a special film-preparation setup.
3. The correlation between cooling conditions and resulting semicrystalline morphologies was established.
4. A dual semicrystalline morphology was obtained when cooling the melt at rates between 20 and 200 K s⁻¹.

Graphical abstract



Nucleation-controlled dual semicrystalline morphology of polyamide 11

Katalee Jariyavidyanont,^a Christoph Schick^{b,c} and René Androsch^{a*}

Abstract

Crystallization of polyamide 11 at low supercooling of the melt proceeds via heterogeneous nucleation and spherulitic growth of lamellae, while at temperatures close to the glass transition homogeneous nucleation prevails, preventing spherulite formation and leading to formation of a large number of nanometer-sized mesophase domains. It is shown that spherulitic and non-spherulitic crystallization at low and high supercooling of the melt, respectively, can be enforced by tailoring the cooling conditions, causing a twofold semicrystalline morphology at ambient temperature. Analysis of non-isothermal crystallization as a function of the cooling rate, using fast scanning chip calorimetry, reveals that in the case of polyamide 11 such twofold semicrystalline morphology is predicted when cooling at rates between about 20 and 200 Ks⁻¹, since then two separate crystallization events are observed. The prediction has been confirmed by preparation of films crystallized during ballistic cooling at different rates which then were analyzed regarding their structure using optical microscopy, X-ray diffraction and calorimetry. The study is completed by discussion of implications of twofold non-isothermal crystallization for structure evolution in polymer processing, as well as by providing information that such behavior is not only typical for polyamide 11 but also for isotactic polypropylene or poly(butylene terephthalate) as two further examples.

© 2018 Society of Chemical Industry

Keywords: polyamide 11; nucleation; crystallization; semicrystalline morphology; fast scanning chip calorimetry

INTRODUCTION

For numerous polymers it has been shown that crystallization at low supercooling of the melt proceeds via a heterogeneous nucleation mechanism, while at high melt supercooling, at temperatures close to the glass transition, homogeneous nucleation prevails.^{1,2} The low-temperature homogeneous nucleation scheme may be realized in samples which do not contain heterogeneous nucleation sites and which therefore do not crystallize at high temperature, as may be the case in nanometer-sized droplets, finely dispersed blend components, thin films, etc.^{3–7} Regarding research about crystallization of polyamides (PAs), Mathot and co-workers performed pioneering experiments proving homogeneous nucleation in industrially relevant multicomponent systems containing small droplets.^{8–10} Bulk samples, including the majority of technical formulations/industrial polymers, often contain impurities or purposely added nucleation agents, which promote crystallization at high temperature via heterogeneous nucleation.^{11,12} In such samples, homogeneous nucleation at low temperature can only be enforced by rapid cooling, bypassing the temperature range of maximum growth rate without space-filling growth of crystals originating from heterogeneous nuclei.

Quantitative information about the temperature ranges of predominant heterogeneous and homogeneous crystal nucleation in recent years has been obtained by fast scanning chip calorimetry (FSC) which allows analysis of crystallization rates in a wide range of temperatures, often revealing a bimodal distribution due to the different nucleation mechanisms.^{1,2} In general, the crystallization rate increases with supercooling of the melt due to increasing thermodynamic driving force, passes through maximum and

then slows down because of hindered molecular transport processes. However, it was shown that at low temperature, often 50–70 K above the glass transition temperature T_g , the crystallization rate increases again to pass through a further maximum close to T_g . The assignment of the high- and low-temperature crystallization-rate maxima to the maximum growth rate of heterogeneously nucleated crystals and the maximum rate of homogeneous nucleation, respectively, was then further supported by analysis of nuclei densities¹³ and by linking the kinetics of the relaxation of glasses with that of nuclei formation;^{14–16} regarding the latter it was shown that glass relaxation and homogeneous nucleation are coupled, thus occurring on a similar length scale and independent of the presence of heterogeneous nucleation sites. Note that addition of heterogeneous nucleators into a given system only affects the kinetics of the high-temperature crystallization process, being outpaced by homogeneous nucleation at low temperature with its kinetics often not changing.^{17–19}

Most important in the context of this study is the effect of the nucleation mechanism on the development of the semicrystalline

* Correspondence to: R Androsch, Interdisciplinary Center for Transfer-oriented Research in Natural Sciences (IWE TFN), Martin Luther University Halle-Wittenberg, 06099 Halle/Saale, Germany.
E-mail: rene.androsch@iw.uni-halle.de

^a Interdisciplinary Center for Transfer-oriented Research in Natural Sciences (IWE TFN), Martin Luther University Halle-Wittenberg, Halle/Saale, Germany

^b Institute of Physics and Competence Center CALOR, University of Rostock, Rostock, Germany

^c Department of Physical Chemistry, Kazan Federal University, Kazan, Russia

morphology. Heterogeneous nucleation at high temperature, with distances between neighboring nuclei of several micrometers up to several hundred micrometers, typically leads to spherulitic growth of lamellar crystals.^{20,21} In contrast, crystallization at low temperature is connected with a tremendous increase of the nuclei density by several orders of magnitude,¹³ which then does not allow distinct lateral growth of nuclei/crystals due to space and mobility constraints, ultimately leading to a semicrystalline structure consisting of independently grown, small ordered domains embedded in the amorphous matrix without forming a higher order superstructure. Often, though not throughout, these small domains exhibit a mesomorphic structure, which in the case of PA 6 was characterized such that the chains are straight and nearly extended, and having equal distance to all neighbors, leading to a hexagonal symmetry. In addition, a smectic periodicity along the chain axis was proven with the detection of a meridional scattering peak in fiber pattern analysis.²²

Formation of such qualitatively different semicrystalline morphologies, that is, laterally extended lamellae separated by amorphous structures within spherulites on one side and approximately isometric domains distributed in an amorphous matrix on the other side, controlled by the degree of supercooling of the melt upon crystallization, has been proven for many polymers including isotactic polypropylene (iPP),^{23–25} poly(butylene terephthalate) (PBT),¹³ PA 6,^{26,27} PA 66,²⁸ as well as PA 11,²⁹ with the latter being the subject of the present work.

It is worthwhile noting that application-relevant properties are largely influenced by the different habit and arrangement of crystals, even if the crystallinity is similar; for example, non-spherulitic structures lead to higher ductility and reduced (visible) light scattering, compared to a spherulitically crystallized counterpart,^{30–36} justifying continuing research efforts for obtaining polymeric materials with tailored structures and properties. Moreover, in addition to effects related to the shearing of the melt, in industrial melt-processing of polymers, in particular injection molding, polymers may be subjected to a wide range cooling rates, often reaching few hundred kelvins per second in the skin layer while cooling slower in the central parts.^{37–39} Such high cooling rate in the skin may be sufficient to suppress crystal growth from heterogeneous nuclei, and related to the cooling-rate gradient along the cross-section it then causes a gradient of the semicrystalline morphology.^{39–41}

It was the aim of the work presented here to prove/disprove the concept of obtaining a nucleation-controlled twofold semicrystalline morphology by incomplete high-temperature crystallization, leaving then crystallizable amorphous structure for continuation of the crystallization process at lower temperature via homogeneous nucleation. As a result of such a nucleation pathway it is expected that isolated spherulites are embedded in a semicrystalline matrix containing isometric crystals. The study was performed using PA 11, as for this polymer it was shown that in a relatively narrow temperature range at around 110 °C, the few heterogeneous nuclei are outpaced at lower temperature by the rapidly increasing number of homogeneous nuclei with the consequences described above for the semicrystalline structure. Considering industrial processing, films were prepared by ballistic cooling of the melt at different rates, which then were analyzed regarding their structure. The crystallization history of the films was correlated with FSC cooling curves, with the latter providing an accurate prediction of cooling conditions needed to obtain a twofold semicrystalline morphology.

EXPERIMENTAL

Material

A heat- and light-stabilized, natural PA 11 extrusion grade Rilsan® BESNO TL from Arkema was used. The melt volume index of the polymer is 1 cm³/(10 min) (235 °C, 2.16 kg),⁴² and the number-average molar mass and polydispersity are 17.2 kg mol⁻¹ and around 2, respectively;⁴³ further material data are available in the literature.⁴² The material was delivered as pellet, and was used as received for FSC analysis of non-isothermal crystallization.

Film samples with a thickness of 220 ± 10 μm were prepared using a Lot QD hydraulic hot-press equipped with a thin-film maker accessory. The as-received pellets were first dried at 80 °C for a period of 24 h before compression molding at a temperature of 220 °C between thin Teflon layers. The Teflon–polymer–Teflon sandwich was then cooled using various cooling media including ice–water, room-temperature water, metal plates or ambient air, to obtain films with different structures. To precisely monitor the decrease of the temperature during cooling, a chromel–alumel μ-thermocouple from Omega with a wire diameter of 80 μm was placed with its front end inside the sample and connected to a fast temperature–time logger (OM-DAQXL-1-EU), permitting sampling of temperatures at a frequency up to 25 Hz. Temperature–time profiles were smoothed to allow calculation of the first derivative, that is, the cooling rate, which was then plotted as a function of temperature.

Instrumentation

Fast scanning chip calorimetry

FSC was employed for obtaining information about temperatures of crystallization as a function of the cooling rate, in order to identify the cooling-rate range in which multiple crystallization events occur. We used a power-compensation Mettler-Toledo Flash DSC 1, operated in combination with a Huber TC100 intracooler. The sample support temperature was kept constant at –90 °C and the sample environment was purged with dry nitrogen gas using a flow rate of 60 mL min⁻¹. The empty sensor was conditioned and temperature-corrected according to the instrument operating instructions before wetting the heatable area of the sample furnace with a thin layer of Wacker AK 60000 silicon oil, in order to improve the thermal contact between the sensor membrane and the sample. Specimens with a thickness of less than 15 μm and lateral width of about 50–100 μm were prepared and placed onto the membrane. The mass of the samples, roughly, was between 50 and 200 ng and was estimated from the change of the absolute sample heat capacity on complete vitrification of the supercooled melt and its comparison with the expected mass-specific heat capacity change of 0.38 J g⁻¹ K⁻¹.⁴⁴

The FSC cooling curves were evaluated regarding temperatures and enthalpies of crystallization. The asymmetry of the heat losses was obtained by recording the instrumental differential heat-flow rate in the presence of the sample on sufficiently slow cooling at a rate of 1 K s⁻¹. The curve was smoothed to remove the small latent heat contribution of the crystallization event of the material, and then subtracted from all curves recorded at the various cooling rates. The temperature of crystallization was defined as temperature of maximum heat-flow rate of the various crystallization events, and the enthalpy of crystallization was estimated by the peak area using a straight baseline for peak integration. While determination of the parameters of the observed fast low-temperature process was uncritical, temperatures and enthalpies of the slow high-temperature process, which

stretched over a rather wide temperature range, are considered as estimates only.

Further valuable information about instrumentation and application of FSC is available in the literature, authored by Mathot and co-workers, recognizing early the need to implement rapid-cooling polymer-crystallization research to advance/fit both academic and also industrial needs.^{45–49}

Differential scanning calorimetry

DSC was used for analysis of the crystallinity of films prepared by cooling the melt at different rates. In particular it was the aim to show that featureless appearance of rapidly cooled films in polarized light optical microscopy is not caused by absence of crystallization but due to the smallness of crystals. The measurements were done with a calibrated Mettler-Toledo heat-flux DSC 1 attached to a Huber TC100 intracooler. Samples with a mass of 5 mg were encapsulated in small 20 μL aluminum pans and heated from -20 to 220 $^{\circ}\text{C}$ at a rate of 10 K min^{-1} while purging the furnace with dry nitrogen gas at a rate of 60 mL min^{-1} . The crystallinity of the samples was determined by normalizing the measured enthalpy of melting with the bulk enthalpy of melting of 189 J g^{-1} .⁵⁰ The reproducibility was confirmed by repeating the measurement with a new sample taken from a different film of identical thermal history. In addition, DSC was employed for measurement of temperatures and enthalpies of crystallization at rates between 2 K min^{-1} (0.033 K s^{-1}) and 50 K min^{-1} (0.833 K s^{-1}), using the as-received pellets.

X-ray diffraction

XRD was used to gain information about the prevailing crystal polymorph in the various film samples of different thermal history. The XRD analyses were performed with a URD 63 diffractometer, using Ni-filtered $\text{Cu K}\alpha$ radiation with a wavelength of 0.15418 nm, and a scintillation counter for registration of the scattered X-rays. Data were collected in transmission mode.

Polarized-light optical microscopy (POM)

The semicrystalline structure of the PA 11 film samples of different crystallization history at the micrometer length scale was observed with a Leica DMRX optical microscope in transmission mode using crossed polarizers. A Slee CUT 5062 rotary microtome was employed to prepare thin sections with a thickness of 10 μm , representing the cross-section of 220 μm thick films. The thin sections were embedded in low-viscosity Type A Cargille immersion oil between glass cover slips, and imaged using a Motic 2300 CCD camera attached to the microscope. Annealing experiments were performed using a Linkam THMS600 hot stage.

RESULTS AND DISCUSSION

FSC analysis of non-isothermal crystallization of PA 11

In Fig. 1 are plotted FSC scans of PA 11, recorded during cooling of the melt at rates between 1000 and 10 K s^{-1} , and DSC scans obtained on cooling the melt at 0.833 K s^{-1} (50 K min^{-1}) and 0.167 K s^{-1} (10 K min^{-1}). Cooling at rates lower than 30 K s^{-1} leads to a single crystallization event at around 150 $^{\circ}\text{C}$ (red curves). As expected, the crystallization temperature decreases and the width of the transition increases with increasing cooling rate. If samples are cooled at rates between 30 and 100 K s^{-1} (gray curves) then the broad high-temperature crystallization process (dashed line)

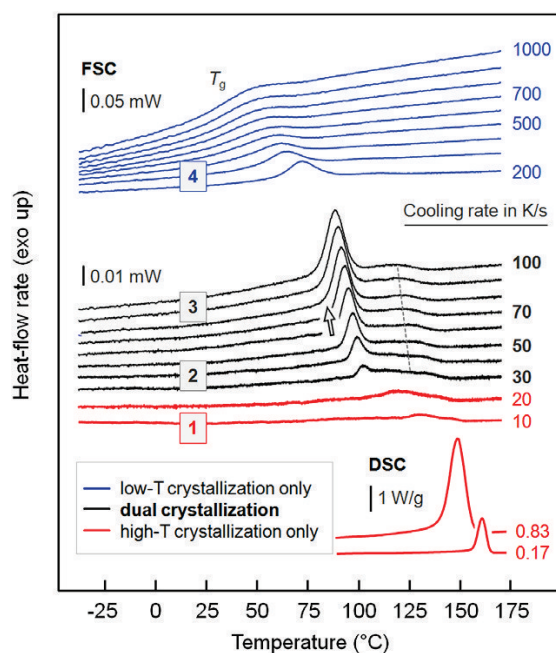


Figure 1. FSC curves recorded on cooling the melt at different rates between 10 (bottom curve) and 1000 K s^{-1} (top curve), and DSC curves obtained on cooling the melt at 0.833 K s^{-1} (50 K min^{-1}) and 0.167 K s^{-1} (10 K min^{-1}). Red, gray and blue coloring of curves is employed to distinguish cooling-rate ranges leading to high-temperature crystallization only, occurrence of two crystallization events and low-temperature crystallization only, respectively.

becomes superimposed by a sharp crystallization peak at temperatures lower than 100 $^{\circ}\text{C}$ (see arrow). It will be shown below that the appearance of the distinct low-temperature crystallization peak is coupled to incomplete high-temperature crystallization. With increasing cooling rate, crystallization at high temperature is increasingly suppressed and then the non-crystallized but crystallizable material orders at lower temperature. If the cooling rate is increased beyond 100 – 200 K s^{-1} then crystallization at temperatures higher than 100 $^{\circ}\text{C}$ is not visible and only the low-temperature crystallization process is detected (blue curves). This crystallization event, however, also fades with increasing cooling rate, and on cooling the melt at 1000 K s^{-1} to below T_g only negligible amount of the melt transforms into ordered structure.

Figure 2 provides quantitative information about temperatures (top part) and enthalpies (bottom part) of crystallization, plotted as a function of the cooling rate. Similar to Fig. 1, red, gray and blue coloring of data is employed to distinguish cooling-rate ranges leading to high-temperature crystallization only, occurrence of two crystallization events and low-temperature crystallization only, respectively. Most important is the observation that the low-temperature crystallization process on increasing the cooling rate beyond about 30 K s^{-1} is at the expense of the high-temperature crystallization process (see downward- and upward-directed arrows in the plot of transition enthalpies). At low cooling rate, as realized in DSC experiments, the enthalpy of crystallization is close to 50 J g^{-1} . Cooling faster than 30 K s^{-1} , however, does not allow completion of the high-temperature crystallization process, as is indicated with the sharp down-drop of the transition enthalpy. As the enthalpy of the high-temperature crystallization

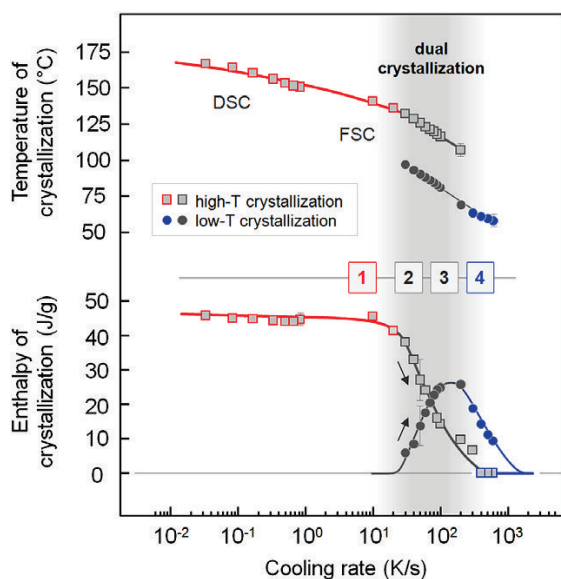


Figure 2. Temperature (top part) and enthalpy of crystallization of PA 11 as a function of the cooling rate. Data were obtained from FSC ($\geq 10 \text{ K s}^{-1}$) and DSC cooling experiments ($\leq 0.833 \text{ K s}^{-1}$). DSC data are averages of three independent measurements, with the standard deviation being similar to the data-point size. FSC experiments were performed five times, in order to prove reproducibility. Red, gray and blue coloring of data is employed to distinguish cooling-rate ranges leading to high-temperature crystallization only, occurrence of two crystallization events and low-temperature crystallization only, respectively.

process decreases, the enthalpy of the low-temperature transition increases, at least if the cooling rate is lower than $100\text{--}200 \text{ K s}^{-1}$; on cooling faster than 200 K s^{-1} also the low-temperature transition becomes suppressed. It is worth noting that the crystallinity of PA 11 is almost independent of the cooling rate below the critical value of a few hundred kelvins per second, which is in accord with a prior study of crystallization under rapid cooling conditions using a combination of FSC and XRD, performed by Mathot and co-workers.⁵¹

For morphological studies, film samples of different thermal history were prepared, attempting to mimic the cooling conditions which lead to the three different crystallization scenarios. By variation of the target temperature and the heat-transfer conditions in ballistic cooling experiments, indeed, it was possible to adjust cooling conditions as indicated with the boxed numbers 1 to 4 in Figs 1 and 2. However, before discussion of the semicrystalline morphology of films of different cooling history, we may emphasize with the FSC cooling scans in Fig. 3 that observation of two separate crystallization events during cooling is not a specific observation holding only for PA 11 but that it must be considered as a general phenomenon in non-isothermal crystallization of polymers if the cooling rate is high enough to hinder completion of the heterogeneously nucleated crystallization process at high temperature, and if the cooling rate is still low enough to allow formation and growth of homogeneous nuclei to crystals at lower temperature. In the case of iPP the high-temperature crystallization process cannot complete if the cooling rate exceeds $50\text{--}100 \text{ K s}^{-1}$, which then causes rapid formation of a mesophase around room temperature.^{52–54} Similarly, for PBT a critical cooling rate for suppression of the high-temperature crystallization

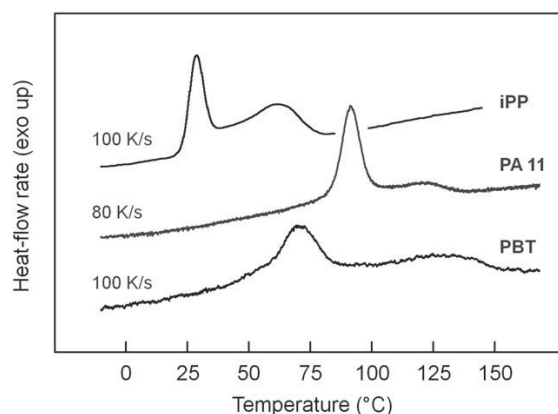


Figure 3. FSC curves obtained on cooling iPP, PA 11 and PBT at rates which lead to two crystallization events. Data obtained for iPP and PBT were taken from Poel *et al.*⁴⁹ and Androsch *et al.*,¹³ respectively. Note that scaling of the heat-flow rate axis is different for the individual curves.

process of about 30 K s^{-1} has been detected, causing then crystallization below 100 °C ;^{13,55} a further example is available in the literature, describing the crystallization behavior of PA 12.⁵⁶

Morphology of films of different cooling history

Films of different thermal history were prepared by compression molding, followed by ballistic cooling of the melt at different rates. Figure 4 shows with the gray data points and curves the temperature dependence of the cooling rate of different films, calculated from the experimentally observed temperature–time profiles; before differentiation, the temperature–time profiles were smoothed using a fast Fourier transform filter, as is custom in signal processing.^{57,58} For all samples there is a decrease in the cooling rate on the approach of the target temperature according to Newton's law of cooling.⁵⁹ For the slowest cooled sample (i) the cooling rate in the temperature range relevant for crystallization, that is, between about 160 and 50 °C , is less than 5 K s^{-1} , permitting crystallization at rather low supercooling of the melt close to 150 °C . Due to the large amount of heat released during the phase transformation, the cooling rate shows a minimum at the crystallization temperature. However, even if it were impossible to detect the transition temperature during cooling of the films with the embedded thermocouple, the FSC data of Figs 1 and 2 would provide such information, as is demonstrated with the red and blue data points and curves, representing crystallization temperatures associated with the high- and low-temperature crystallization processes, respectively. With regard to the film-cooling experiment (i), these data need to be read such that cooling at a rate of 5 K s^{-1} leads to crystallization at $140\text{--}150 \text{ °C}$, perfectly agreeing with the crystallization temperature detected with the thermocouple in the film sample. At this low rate, no further crystallization events were detected. Faster cooling at rates between about 10 and 100 K s^{-1} , as realized with the films (ii) and (iii), in contrast, does not allow completion of the high-temperature crystallization process at temperatures defined by the intersection with the FSC data shown in red. Therefore a low-temperature crystallization event is predicted with the blue FSC data points and also experimentally confirmed with the local minimum in the cooling-rate profile. Only if the cooling rate exceeds about 100 K s^{-1} , then the high-temperature crystallization process is fully suppressed and the melt transforms partially to an ordered phase at about 75 °C , close to T_g .

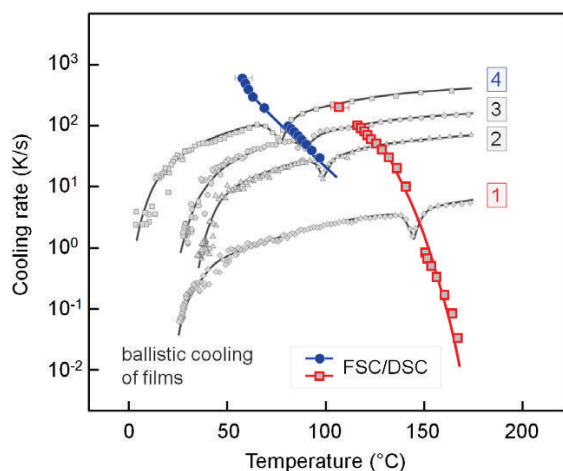


Figure 4. Cooling rate as a function of temperature during ballistic cooling of compression-molded films of PA 11 (gray data points and curves). Films associated with the curves labeled 1 to 4 were prepared using air, metal blocks pre-conditioned at 35 °C, metal blocks pre-conditioned at 25 °C and ice–water, respectively, as quenching media. The red squares and blue circles represent peak temperatures of crystallization of PA 11, measured as a function of cooling rate using FSC (see Fig. 2).

Figure 5 shows POM micrographs of the center part of the cross-section of the films of PA 11 of different cooling history, as shown with the cooling-rate profiles in Fig. 4. First of all, it may be noted that the film-thickness direction is parallel to the long, vertical edge of the images, representing a distance of about 130 μm , that is, almost two-thirds of the total thickness. Furthermore we may emphasize that the structures shown are representative for all regions of the cross-section, that is, there was no gradient structure observed. For slowly cooled PA 11 (left image labeled 1), which crystallized at about 150 °C, there is detected a space-filling spherulitic superstructure, with the spherulite size being 10–20 μm , being in accord with the literature;⁶⁰ at slow cooling there is sufficient time to grow spherulitic structures from the few heterogeneous nuclei until space filling stops further growth. If the cooling rate is increased to 10–50 K s^{-1} , as achieved with the cooling experiment 2 (see Fig. 4), then the spherulite size is reduced to values lower than 5 μm which is caused by insufficient time for growth of spherulites out of the most active heterogeneous nuclei and the increased number of activated heterogeneous nuclei when decreasing the crystallization temperature to about 130 °C (see Fig. 4); however, spherulitic crystallization seems incomplete in some parts of the film, pointing to the beginning of deterioration of the high-temperature crystallization process and causing continuation of crystallization at lower temperature (see cooling-rate minimum around 100 °C in curve 2 of Fig. 4). Incompletion of the high-temperature crystallization process is obvious if the cooling rate is further increased to around 100 K s^{-1} (curve 3 in Fig. 4) since then the POM micrograph shows only isolated spherulites with a size of 2–4 μm surrounded by non-spherulitic structure, and since both the cooling-rate profile in Fig. 4 and the FSC scans of Fig. 1 reveal negligible high-temperature crystallization. In that case a dual semicrystalline morphology is observed with spherulitically grown lamellar crystals on one side, and crystals formed at low temperature from homogeneous nuclei. Finally, if the cooling rate is further increased to values well above 100 K s^{-1} (see curve 4 in Fig. 4) then solidification of the melt occurs at

around 75 °C, with the crystals then arranged such that there cannot be observed a characteristic birefringence pattern in POM, that is, with the crystals not forming a higher-order superstructure as is the case with the coordinated, radial growth starting from few heterogeneous nuclei.

Proof of presence of non-spherulitic ordered structures

Featureless POM micrographs, as shown with the right image in Fig. 5, typically are indicative for completely amorphous samples. In order to provide information that a semicrystalline morphology is evident even in such case of a featureless appearance in POM, DSC and XRD analyses were performed, as well as a specific high-temperature annealing experiment, explained with Fig. 6. The main idea behind the annealing experiment is the assumption that the amorphous glassy structure formed on rapid cooling will crystallize upon heating the material to above T_g . Similarly, it could be expected that the isolated spherulites evident in image 3 of Fig. 5 continue to grow if the sample is heated to temperatures above 130 °C, that is, to a temperature where the high-temperature crystallization process is occurring. The left-hand image in Fig. 6 is a soft zoom of image 3 in Fig. 5, showing the isolated spherulites with a diameter of 2–3 μm , which formed within the high-temperature crystallization process. With the inset text in the top left corner is emphasized the question as to whether the black surrounding is a fully amorphous phase or containing crystals. The sample was then heated to 150 °C, that is, to well above T_g , and annealed for a period of 5 min. After cooling to ambient temperature the image shown to the right was captured. Obviously, heating the initial film to above T_g does not affect the morphology, as the spherulites do not continue to grow, clearly evidencing that the surrounding featureless structure is not a single devitrified amorphous phase but rather contains small crystals which likely even immobilize their local amorphous surrounding; note that it was found early that the presence of crystals in PA 11 leads to formation of a rigid amorphous fraction,^{61,62} similar as in PA 6.^{63,64} As such it is clear that annealing even well above T_g does not cause a change of the morphology at the micrometer length scale.

Further evidence that all films shown in Fig. 5, regardless their largely different morphology, exhibit similar level of crystallinity is provided with the DSC heating scans in the right plot of Fig. 7. The labeling of curves at their right-hand side is in accord with that of the cooling-rate profiles in Fig. 4 and image designation in Fig. 5. Independent of the largely different crystallization history, all samples show a melting peak close to 190 °C, which is attributed to crystal reorganization during rather slow heating at 10 K min^{-1} . Typically, polymer crystals melt around 10 K above the temperature of their formation (see for example recent crystal-reorganization studies performed on poly(ethylene terephthalate),⁶⁵ PBT⁶⁶ or PA 6⁶⁷); however, they tend to reorganize by melting which is followed by fast melt-recrystallization, occurring on a sub-second time scale.⁶⁸ Reorganization may in particular be evident if the zero-entropy production melting temperature of crystals of low metastability is well below the equilibrium melting temperature, leaving then after melting of the crystals a highly unstable melt. However, most important regarding the DSC curves in Fig. 7 is the observation that the enthalpy of melting of all films is around 50 J g^{-1} , which corresponds to a crystallinity of around 26% when using a bulk enthalpy of melting of 189 J g^{-1} for normalization.⁵⁰ In more clear words, the fully spherulitic structure obtained after rather slow cooling of the melt at a rate of 1–5 K s^{-1} and the non-spherulitic structure obtained after fast cooling of the

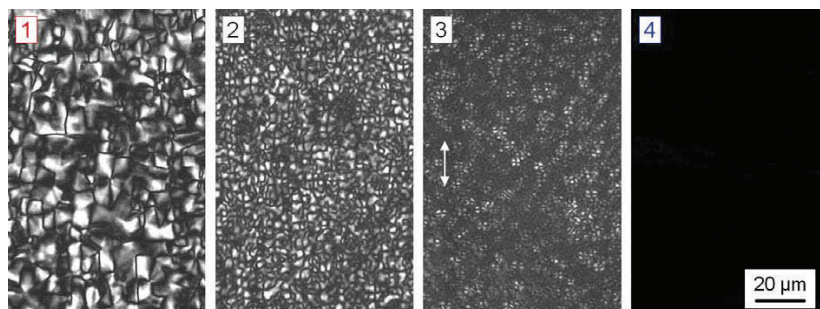


Figure 5. POM micrographs of the cross-section of films of PA 11 of different cooling history, as shown with the cooling-rate profiles in Fig. 4. The film-thickness direction is parallel to the long, vertical edge of the images, as is indicated with the double arrow in image 3.

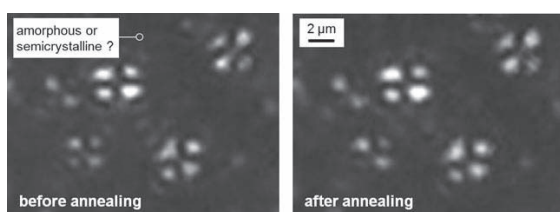


Figure 6. POM micrographs of part of the cross-section of a PA 11 film which was prepared by ballistic cooling at a rate close to 100 K s^{-1} (see cooling-rate profile 3 in Fig. 4), before annealing (left image) and after annealing for 5 min at 150°C (right image).

melt at $100\text{--}500 \text{ K s}^{-1}$, shown with the left and right images in Fig. 5, exhibit similar crystallinity.

The observation of independence of the enthalpy of melting, that is, of the crystallinity, of the cooling history seems in contradiction with the transition enthalpies shown in the bottom part of Fig. 2. There (in Fig. 2) for the fastest cooled film 4, a total transition enthalpy of at best $20\text{--}25 \text{ J g}^{-1}$ may be predicted. The crystallinity mismatch is explained with the temperature dependence of the cooling rate in the film-preparation experiment. For film 4, the cooling rate at high temperature was sufficient (about 200 K s^{-1}) to suppress high-temperature crystallization; however, this was then much slower in the temperature range of the low-temperature crystallization process (down to about 50 K s^{-1} close to T_g) compared to the constant cooling rate in the FSC device. It is therefore important to note that the transition enthalpies measured on linear cooling by FSC do not necessarily represent maximum achievable values. These can only be obtained within isothermal crystallization experiments, which, indeed, confirmed that the maximum achievable crystallinity is almost independent of the crystallization temperature in the case of PA 11.⁶⁹

Despite similar enthalpy-based crystallinity of the films of largely different semicrystalline morphology, the XRD patterns in the left plot of Fig. 7 reveal that the crystals forming in the high- and low-temperature crystallization processes, as indicated with the red and blue coloring of curves, respectively, have different symmetry and perfection. Crystallization at rather high temperature close to 150°C (red curve, cooling regime 1) leads to formation of the triclinic α -crystal polymorph, as is identified with the two characteristic peaks at 2θ around 20.4° and 22.5° , providing information about the unit cell dimension in cross-chain direction. Note that the angular position of these peaks, that is of the dimensions of the basal plane of the unit cell, defining the perfection and stability of crystals,⁷⁰ depends on the crystallization temperature;

crystallization at higher temperature would increase the distance between peaks, indicating an increased anisotropy in cross-chain direction, while crystallization at lower temperature leads to a decrease of their distance. For PA 11 it was found by systematic analysis of the XRD patterns of samples of well-defined isothermal crystallization history, using FSC for sample preparation, that these peaks are merged if the crystallization temperature is lower than 110°C .⁶⁹ In that case only rotational symmetry of the chains is evident, defining it as a mesophase, being a phenomenon holding for many PAs when rapidly cooled or crystallized at high melt supercooling.^{71–73} Such a situation is evident for film 4 (blue curve) which was rapidly cooled at a rate higher than 100 K s^{-1} , with the crystallization peak temperature observed at around 75°C . For films 2 and 3, which crystallized at both high and low temperatures, a mixture of both crystal types is expected, which, however, are not clearly identifiable in the corresponding X-ray patterns in Fig. 7, perhaps caused by line-broadening due to small crystal size. Since the XRD patterns of rapidly cooled PAs containing the mesophase only show a rather broad and halo-like peak, representing the lateral distance between chains, in Fig. 7 also the scattering curve of a fully amorphous sample is included,⁶⁹ for demonstration that the films 2–4 indeed contain ordered structures.

CONCLUSIONS

Melt crystallization of PA 11 is initiated by heterogeneous nuclei at temperatures higher than about 120°C , while homogeneous nucleation prevails at lower crystallization temperatures.²⁹ Related to the largely different nuclei density, different semicrystalline morphologies develop above and below the crossover temperature. The rather low number of heterogeneous nuclei on high-temperature crystallization allows extended lateral growth of crystals forming spherulites if the sample stays for sufficiently long time near the temperature of maximum growth rate. Due to the much larger number of homogeneous nuclei developing below about 120°C , crystals remain small and cannot form a high-order superstructure. While isothermal crystallization in the high- and low-temperature nucleation schemes can be completed by appropriate extending the crystallization time, in non-isothermal crystallization processes the slow, high-temperature spherulitic crystallization may not be completed if the cooling rate is too fast. In such a case, in the remaining amorphous phase crystalline structures can still form at lower temperature, since there the nucleation rate is drastically increased. In calorimetry, when cooling at rates between 20 and 200 K s^{-1} , two crystallization events/peaks are then detected, suggesting a twofold crystallization. It was

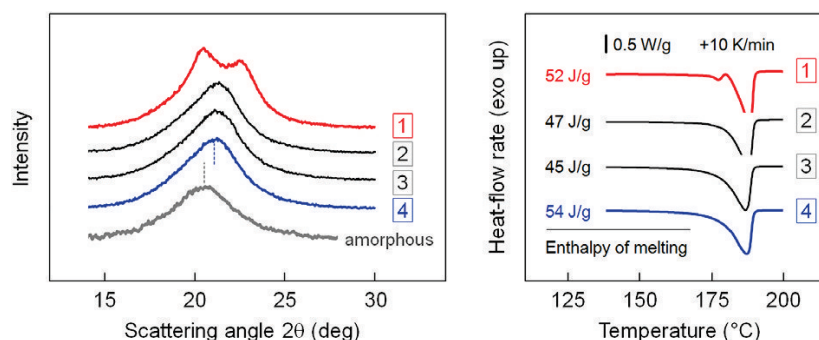


Figure 7. XRD patterns (left) and DSC heating scans (right) of PA 11 films of different thermal history as described with the cooling-rate profiles of Fig. 4. Red and blue colored curves, labeled 1 and 4, respectively, indicate exclusive crystallization in the high- and low-temperature range, respectively. The XRD curve of fully amorphous PA 11 (gray), measured in an independent study,⁶⁷ is included for illustration that films 2–4 contain ordered structures.

successfully proven that then a dual semicrystalline morphology is developing, containing spherulitically grown lamella at high temperature and non-spherulitically distributed mesophase domains, formed at lower temperature. More precisely, (i) cooling the melt slower than 20 K s^{-1} leads to a space-filled spherulitic structure, (ii) cooling at a rate between 20 and 200 K s^{-1} leads to a dual semicrystalline morphology, (iii) cooling faster than 100 K s^{-1} causes formation of a fully non-spherulitic structure and (iv) cooling at rates above 1000 K s^{-1} eventually yields fully non-crystalline amorphous states.

While the cooling-rate range to observe a dual semicrystalline morphology seems rather narrow, covering only one order of magnitude, observation of such structures is common in polymer processing. In injection molding, cooling-rate gradients from several hundred kelvins per second in the skin layer to values less than 1 K s^{-1} in the core are typical, causing then solidification at different temperatures in the various layers across the thickness, and formation of a correspondingly wide spectrum of morphologies, from amorphous to completely non-spherulitic semicrystalline to space-filled spherulitic semicrystalline, and all intermediate stages in between.

ACKNOWLEDGEMENTS

KJ and RA are grateful for support by the European Structural and Investment Funds, and CS acknowledges financial support from the Ministry of Education and Science of the Russian Federation, grant 14.Y26.31.0019. The authors express their respect for the achievements of Vincent Mathot in the field of thermal analysis of crystallizable polymers, and acknowledge the many inspiring discussions over more than two decades (RA, CS), as well as the many new ideas brought into the community, always challenging old and well-established routes.

REFERENCES

- Androsch R and Schick C, *Adv Polym Sci* **276**:257–288 (2015).
- Schick C, Androsch R and Schmelzer JWP, *J Phys: Condensed Matter* **29**:453002 35 pp. (2017).
- Gornick F, Ross GS and Frolen LJ, *J Polym Sci Polym Symp* **18**:79–91 (1967).
- Koutsky JA, Walton AG and Baer E, *J Appl Phys* **38**:1832–1839 (1967).
- Jin Y, Hiltner A and Baer E, *J Polym Sci Polym Phys* **45**:1138–1151 (2007).
- Santana OO and Müller AJ, *Polym Bull* **32**:471–477 (1994).
- Arnal ML, Müller AJ, Maiti P and Hikosaka M, *Macromol Chem Phys* **201**:2493–2504 (2000).
- Tol RT, Mathot VBF, Reynaers H, Goderis B and Groeninckx G, *Polymer* **46**:2966–2977 (2005).
- Tol RT, Minakov AA, Adamovsky SA, Mathot VBF and Schick C, *Polymer* **47**:2172–2178 (2006).
- Sánchez MS, Mathot V, Poel GV, Groeninckx G and Bruls W, *J Polym Sci Polym Phys* **44**:815–825 (2006).
- Binsbergen FL, *J Polym Sci Polym Symp* **59**:11–29 (1977).
- Gahleitner M, Grein C, Kheirandish S and Wolfschwenger J, *Int Polym Proc* **26**:2–20 (2011).
- Androsch R, Rhoades AM, Stolte I and Schick C, *Eur Polym J* **66**:180–189 (2015).
- Androsch R, Schick C and Schmelzer JWP, *Eur Polym J* **53**:100–108 (2014).
- Angell CA, MacFarlane DR and Oguni M, *Ann NY Acad Sci* **484**:241–247 (1986).
- Androsch R and Schick C, *J Phys Chem B* **120**:4522–4528 (2016).
- Zhuravlev E, Wurm A, Pötschke P, Androsch R, Schmelzer JWP and Schick C, *Eur Polym J* **52**:1–11 (2014).
- Wurm A, Herrmann A, Cornelius M, Zhuravlev E, Pospiech D, Nicula R et al., *Macromol Mater Eng* **300**:637–649 (2015).
- Mollova A, Androsch R, Mileva D, Gahleitner M and Funari SS, *Eur Polym J* **49**:1057–1065 (2013).
- Keith HD and Padden FJ Jr, *J Appl Phys* **34**:2409–2421 (1963).
- Keller A, *J Polym Sci* **17**:291–308 (1955); Keller A, *J Polym Sci* **17**:351–364 (1955); Keller A and Waring JRS, *J Polym Sci* **17**:447–472 (1955).
- Auriemma F, Petraccone V, Parravicini L and Corradini P, *Macromolecules* **30**:7554–7559 (1997).
- Hsu CC, Geil PH, Miyaji H and Asai K, *J Polym Sci Polym Phys* **24**:2379–2401 (1986).
- Ogawa T, Miyaji H and Asai K, *J Phys Soc Jpn* **54**:3668–3670 (1985).
- Zia Q, Androsch R, Radusch HJ and Piccarolo S, *Polymer* **47**:8163–8172 (2006).
- Mileva D, Androsch R, Zhuravlev E and Schick C, *Polymer* **53**:3994–4001 (2012).
- Mileva D, Kolesov I and Androsch R, *Colloid Polym Sci* **290**:971–978 (2012).
- Gohn AM, Rhoades AM, Wonderling N, Tighe T and Androsch R, *Thermochim Acta* **655**:313–318 (2017).
- Mollova A, Androsch R, Mileva D, Schick C and Benhamida A, *Macromolecules* **46**:828–835 (2013).
- Starkweather HW and Brooks RE, *J Appl Polym Sci* **1**:236–239 (1959).
- Way JL, Atkinson JR and Nutting J, *J Mater Sci* **9**:293–299 (1974).
- Perkins WG, *Polym Eng Sci* **39**:2445–2460 (1999).
- Zia Q, Radusch HJ and Androsch R, *Polym Bull* **63**:755–771 (2009).
- Mileva D, Androsch R and Radusch HJ, *Polym Bull* **62**:561–571 (2009).
- Kolesov I, Mileva D and Androsch R, *Polym Bull* **71**:581–593 (2014).
- Menyhárd A, Gahleitner M, Varga J, Bernreiter K, Jääskeläinen P, Øysæd H et al., *Eur Polym J* **45**:3138–3148 (2009).
- Rhoades A, Williams JL, Wonderling N, Androsch R and Guo J, *J Therm Anal Calorim* **127**:939–946 (2017).
- Russell DP and Beaumont PWR, *J Mater Sci* **15**:197–207 (1980).

- 39 Jariyavidyanont K, Williams JL, Rhoades AM, Kühnert I, Focke W and Androsch R, *Polym Eng Sci* (2017). Available: <https://doi.org/10.1002/pen.24665> [18 May 2018].
- 40 Trotignon JP and Verdu J, *J Appl Polym Sci* **34**:1–18 (1987).
- 41 Drummer D and Meister S, *Int J Polym Sci* **2014**:8, Article ID 718926 (2014). Available <https://doi.org/10.1155/2014/718926>.
- 42 Rilsan BESNO TL Product Information. <https://www.extremematerials-arkema.com/en/materials-database/> [2 August 2018].
- 43 Fornes TD and Paul DR, *Macromolecules* **37**:7698–7709 (2004).
- 44 Nylon 11 (NYLON11) Heat Capacity, Enthalpy, Entropy, Gibbs Energy: Datasheet from "The Advanced Thermal Analysis System (ATHAS) Databank – Polymer Thermodynamics" Release 2014 in SpringerMaterials. Available: http://materials.springer.com/polymerthermodynamics/docs/athas_0022 [16 May 2018].
- 45 Mathot VBF, *Thermochim Acta* **355**:1–33 (2000).
- 46 Mathot V, Pyda M, Pijpers T, Poel GV, Van de Kerkhof E, Van Herwaarden S et al., *Thermochim Acta* **522**:36–45 (2011).
- 47 Van Herwaarden S, Iervolino E, Van Herwaarden F, Wijffels T, Leenaers A and Mathot V, *Thermochim Acta* **522**:46–52 (2011).
- 48 Iervolino E, Van Herwaarden AW, Van Herwaarden FG, Van de Kerkhof E, Van Grinsven PPW, Leenaers ACHI et al., *Thermochim Acta* **522**:53–59 (2011).
- 49 Poel GV, Istrate D, Magon A and Mathot V, *J Therm Anal Calorim* **110**:1533–1546 (2012).
- 50 Zhang Q, Mo Z, Liu S and Zhang H, *Macromolecules* **33**:5999–6005 (2000).
- 51 Baeten D, Mathot VBF, Pijpers T, Verkinderen O, Portale G, Van Puyvelde P et al., *Macromol Rapid Commun* **36**:1184–1191 (2015).
- 52 Mileva D, Androsch R, Cavallo D and Alfonso GC, *Eur Polym J* **48**:1082–1092 (2012).
- 53 De Santis F, Adamovsky S, Titomanlio G and Schick C, *Macromolecules* **39**:2562–2567 (2006).
- 54 Van Drongelen M, Meijer-Visser T, Cavallo D, Portale G, Poel GV and Androsch R, *Thermochim Acta* **563**:33–37 (2013).
- 55 Schawe JE, *J Therm Anal Calorim* **116**:1165–1173 (2014).
- 56 Fischer C, Seefried A and Drummer D, *Polym Eng Sci* **57**:450–457 (2017).
- 57 Woltring HJ, *Hum Movement Sci* **4**:229–245 (1985).
- 58 Hatze H, *J Biomech* **14**:13–18 (1981).
- 59 Newton I, *Philos Trans* **22**:824–829 (1701). English translation in: Newton I. *Philos Trans R Soc Lond, Abridged*, **4**:572–575 (1809).
- 60 Magill JH, *J Polym Sci Polym Phys* **7**:123–142 (1969).
- 61 Wunderlich B, *Prog Polym Sci* **28**:383–450 (2003).
- 62 Xenopoulos A and Wunderlich B, *J Polym Sci Polym Phys* **28**:2271–2290 (1990).
- 63 Kolesov I and Androsch R, *Polymer* **53**:4770–4777 (2012).
- 64 Chen H and Cebe P, *J Therm Anal Calorim* **89**:417–425 (2007).
- 65 Minakov AA, Mordvintsev DA and Schick C, *Polymer* **45**:3755–3763 (2004).
- 66 Jariyavidyanont K, Androsch R and Schick C, *Polymer* **124**:274–283 (2017).
- 67 Furushima Y, Nakada M, Ishikiriyama K, Toda A, Androsch R, Zhuravlev E et al., *J Polym Sci Polym Phys* **54**:2126–2138 (2016).
- 68 Androsch R, Schick C and Di Lorenzo ML, *Macromol Chem Phys* **215**:1134–1139 (2014).
- 69 Rhoades AM, Wonderling N, Schick C and Androsch R, *Polymer* **106**:29–34 (2016).
- 70 Hiramami M, *J Macromol Sci Phys* **B23**:397–414 (1984).
- 71 Schmidt GF and Stuart HA, *Z Naturforsch* **13**:222–225 (1958).
- 72 Ziabicki A, *Koll Z Z Polym* **167**:132–141 (1959).
- 73 Androsch R, Stolp M and Radusch HJ, *Acta Polym* **47**:99–104 (1996).

4.3 Crystal self-nucleation in polyamide 11

Katalee Jariyavidyanont¹, Andreas Janke², René Androsch¹

¹ Interdisciplinary Center for Transfer-oriented Research in Natural Sciences, Martin Luther University Halle-Wittenberg, 06099, Halle/Saale, Germany.

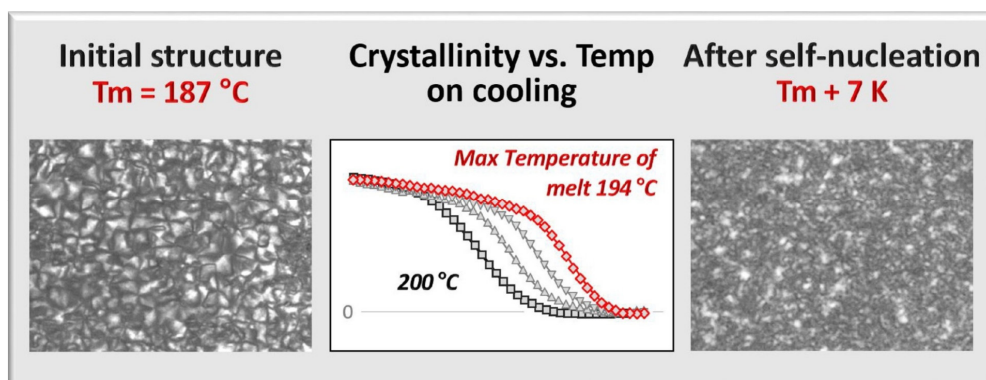
² Leibniz-Institut für Polymerforschung Dresden e.V., Hohe Str. 6, 01069, Dresden, Germany.

Thermochimica Acta 2019, 677, 139–143.

Research highlights

1. The thermal stability of self-seed based on spherulitically grown lamellar crystals was analyzed using hot-stage microscopy.
2. The presence of self-seed causes acceleration of crystallization and formation of a finer spherulitic structure.
3. The self-seed was stable up to about 10 K higher than the melting temperature of the lamellar crystals.

Graphical abstract





Contents lists available at ScienceDirect

Thermochimica Acta

journal homepage: www.elsevier.com/locate/tca

Crystal self-nucleation in polyamide 11

Katalee Jariyavidyanont^a, Andreas Janke^b, René Androsch^{a,*}

^a Interdisciplinary Center for Transfer-oriented Research in Natural Sciences, Martin Luther University Halle-Wittenberg, 06099, Halle/Saale, Germany

^b Leibniz-Institut für Polymerforschung Dresden e.V., Hohe Str. 6, 01069, Dresden, Germany

ARTICLE INFO

Keywords:

Crystal self-nucleation
Crystallization
Polyamide 11 (PA 11)
Nuclei density
Superstructure

ABSTRACT

Self-nucleation of crystallization of polyamide 11 (PA 11) has been studied by thermo-optical microscopy. Spherulitically arranged lamellar crystals with a melting peak temperature of 187 °C formed via heterogeneous nucleation on slow cooling the equilibrium melt and subsequent reorganization on slow heating. As a function of the maximum temperature of the melt after their complete melting, subsequent non-isothermal crystallization accelerates, caused by presence of self-nuclei. The number of self-nuclei decreases with increasing temperature of the melt and approaches zero at a temperature about 13 K higher than the melting temperature of the initially present crystals. Crystallization of the melt containing self-seed leads to formation of a distinctly finer spherulitic morphology than melt-crystallization in absence of self-seed at identical conditions.

1. Introduction

Crystallization of polymers requires nucleation to overcome the energy barrier for the creation of a stable interface between the melt and the crystal nucleus. Nucleation mechanisms include homogeneous and heterogeneous nucleation, associated with stochastic formation of crystal nuclei in the bulk or nucleation at existing surfaces or other heterogeneities, respectively. At low supercooling of the melt, typically heterogeneous nucleation is dominant while homogeneous nucleation prevails at high supercooling of the melt, at temperatures around the glass transition [1–4]. A special case of crystal nucleation is so-called self-nucleation which is a term denoted to nucleation at remnants of crystals of the own species, also called self-seed [4–6]. Such self-seed may be evident in the melt when crystals do not adopt the structure of the relaxed melt after their melting. In presence of self-seed, crystallization on subsequent slow cooling occurs faster than in case of their absence, and due to the higher number of nuclei, typically, a finer superstructure develops [6–8]. Self-nucleation on cooling may not be confused with melting and melt-recrystallization which is a term denoting a process involving melting of crystals of low stability and fast recrystallization of the unstable but also not completely disordered melt at identical or higher temperature [9–12]. Rather than, self-seed generation is a process connected with global melting of crystals though not yielding a melt of maximum entropy in the formerly ordered volume. Often, the temperature-ranges in which melting and melt-recrystallization on one side and in which self-seed survival on the other side are evident, are denoted as domain III and domain II self-

nucleation-temperature ranges, respectively [6–8].

Self-seed experiments typically are performed such to obtain first a relaxed melt by heating the polymer to above the equilibrium melting temperature, followed by formation of a semicrystalline reference-state, typically by slow cooling, yielding a spherulitic superstructure of crystal lamellae. Subsequently, these crystals are heated to different temperatures above their melting point. Potential self-seed left is then analyzed by monitoring the crystallization temperature on cooling as a function of the maximum temperature of the melt prior cooling. Typically, the self-seed concentration decreases with increasing maximum temperature of the melt [6–8].

Self-nucleation was observed in various polyamides (PA) including PA 66 [13] and PA 6 [14–17], however, is not reported yet for PA 11. For this reason, in the present work an attempt is made to provide information whether self-nucleation is evident also in PA 11. However, in advance to earlier reports about self-seeding, it is our long-term goal to prove/disprove a link between the initial semicrystalline morphology before melting of crystals on one side and the self-seed concentration on the other side. PA 11 is polymorphic, that is, as a function of the crystallization conditions different crystal forms develop. Typically, at rather low supercooling of the melt, triclinic α -crystals of lamellar shape grow spherulitically while at high supercooling of the melt a pseudo-hexagonal nodular mesophase forms, likely related to different mechanisms of crystal nucleation at high and low temperatures [18–21]. The temperature ranges of pre-dominant heterogeneous and homogenous crystal nucleation of PA 11 have been identified by fast scanning chip calorimetry (FSC), with main conceptual ideas about

* Corresponding author.

E-mail address: rene.androsch@iw.uni-halle.de (R. Androsch).

<https://doi.org/10.1016/j.tca.2019.02.006>

Received 29 December 2018; Received in revised form 30 January 2019; Accepted 8 February 2019
0040-6031/ © 2019 Elsevier B.V. All rights reserved.

both instrumentation [22,23] and polymer crystallization physics/nucleation mechanisms [24,25] provided by Christoph Schick, to whom this work and special issue is dedicated. Clearly, his contributions directed to the development/improvement of FSC and his ideas in the fields of formation, reorganization and melting of polymer crystals, and of relaxation phenomena in polymer glasses inspired our own research for many years, including the self-nucleation work presented here. In this initial PA-11-self-nucleation study, we provide first information that self-nuclei indeed can be produced in PA 11, however, with emphasis placed on crystal lamellae formed via heterogeneous nucleation at rather low supercooling of the melt.

2. Experimental

2.1. Material and preparation

We employed a high-viscosity, heat- and light-stabilized, natural-color PA 11 extrusion grade Rilsan BESNO TL from Arkema with a melt volume index of $1 \text{ cm}^3 (10 \text{ min})^{-1}$ (235 °C, 2.16 kg) [26]. The number-average molar mass and polydispersity were 17.2 kg mol^{-1} and around 2.0, respectively [27]. The material was available in form of pellets, used to prepare sections with a thickness of $10 \mu\text{m}$ on a SLEE microtome equipped with a tungsten carbide knife. These sections were later on used for preparation of spherulitically grown lamellar crystals.

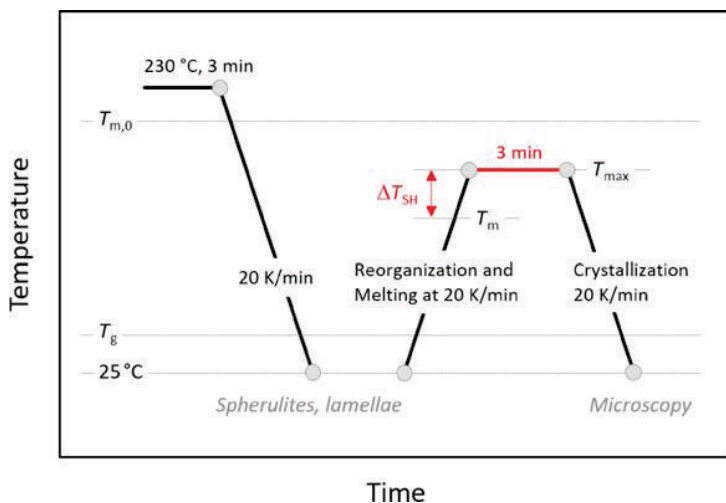


Fig. 1. Temperature-time protocol for analysis of self-nucleation in PA 11 using hot-stage POM. The gray horizontal lines denoted $T_{m,0}$ and T_g indicate the approximate position of the equilibrium melting temperature and glass transition temperature, respectively. Note that linear cooling at 20 K min^{-1} was possible to only about 45 °C , due to insufficient cooling capacity of the used hot-stage.

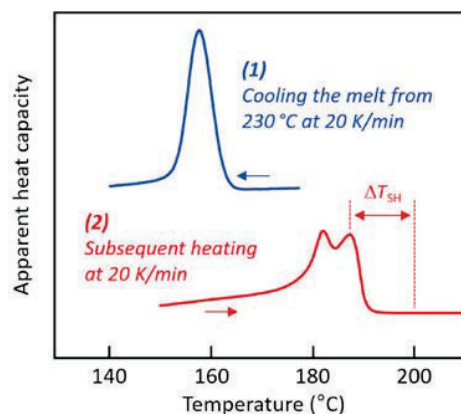
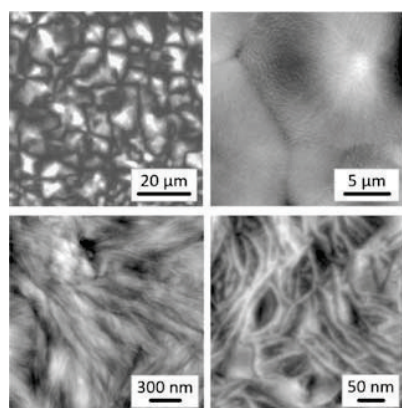


Fig. 2. Left: Micro- and nanometer length-scale structure of PA 11 crystallized on cooling the equilibrium melt at 20 K min^{-1} . Right: DSC cooling scan (blue), recorded for monitoring formation of the reference structure (see left images), and subsequent heating scan (red), recorded for gaining information about the melting temperature.

(Bruker, USA) with a nominal spring constant of 0.7 N m^{-1} and tip radius of 2 nm , and the set point was 0.02 V A section with a thickness of $50 \mu\text{m}$, cut from a pellet, was placed on a round coverslip, heated to $230 \text{ }^\circ\text{C}$, and then slowly cooled to $45 \text{ }^\circ\text{C}$ at a rate of 20 K min^{-1} using a Linkam THMS 600 hot-stage. Note that the surface of the samples was uncovered during crystallization.

3. Results and discussion

Fig. 1 shows the temperature-time protocol used for analysis of self-nucleation in PA 11 using hot-stage POM. First, semicrystalline PA 11 samples containing lamellae and spherulites were prepared by cooling the equilibrium melt from 230 to $25 \text{ }^\circ\text{C}$ at 20 K min^{-1} . Then these samples were heated at 20 K min^{-1} to different maximum temperatures (T_{max}) above the melting temperature (T_{m}), in order to evaluate survival of self-seed as a function of the temperature difference ΔT_{SH} ($= T_{\text{max}} - T_{\text{m}}$). In the following, the term “superheating” (SH) denotes the particular melt state at temperatures above T_{m} . Survival of self-seed in molten samples was evaluated by analysis of the kinetics of non-isothermal crystallization and of the POM structure, with the latter providing information about the nuclei density.

The left part of Fig. 2 shows POM and AFM images illustrating the structure of PA 11 melt-crystallized on cooling at 20 K min^{-1} at both the micrometer- and nanometer-length scales. The top left POM image reveals space-filling spherulitic crystal growth with a maximum size of spherulites of around $20 \mu\text{m}$. Spherulite formation is also detected by AFM (see top right image), confirming their size. The bottom two

images show the expected lamellar morphology of the crystals, grown parallel to the radius of the spherulites, with their thickness being $5\text{--}10 \text{ nm}$.

The right part of Fig. 2 shows in the upper part a DSC cooling scan (blue), which was recorded during the formation of the reference structure (see left images), before performing the self-nucleation experiments. As such, cooling the equilibrium melt from $230 \text{ }^\circ\text{C}$ to $25 \text{ }^\circ\text{C}$ at a rate of 20 K min^{-1} leads to crystallization at a temperature slightly lower than $160 \text{ }^\circ\text{C}$, yielding a crystallinity of close to 30% . The red curve represents the subsequently recorded DSC heating scan, for gaining information about the melting temperature of crystals. The heating rate was 20 K min^{-1} , with such slow heating allowing re-organization of the initially formed crystals, as indicated by the typical double melting behavior. As recently proven on the examples of poly (butylene terephthalate) (PBT) [11] or PA 66 [30], crystal re-organization is kinetically controlled involving melting of unstable crystals and fast melt-recrystallization producing crystals of higher stability. The maximum stability depends on the heating rate, which in case of heating at 20 K min^{-1} yields a melting temperature of close to $187 \text{ }^\circ\text{C}$. Referring to Fig. 1, the superheating-term ΔT_{SH} is indicated with the horizontal double arrow.

Fig. 3 shows the POM microstructure of PA 11 crystallized from the melt containing different amount of self-seed, with the self-seed concentration controlled by the maximum temperature of melt T_{max} (see Fig. 1), before cooling at 20 K min^{-1} . The maximum temperature of the melt is indicated in each image and was varied from 194 to $200 \text{ }^\circ\text{C}$, corresponding to a superheating of the melt ΔT_{SH} above the melting

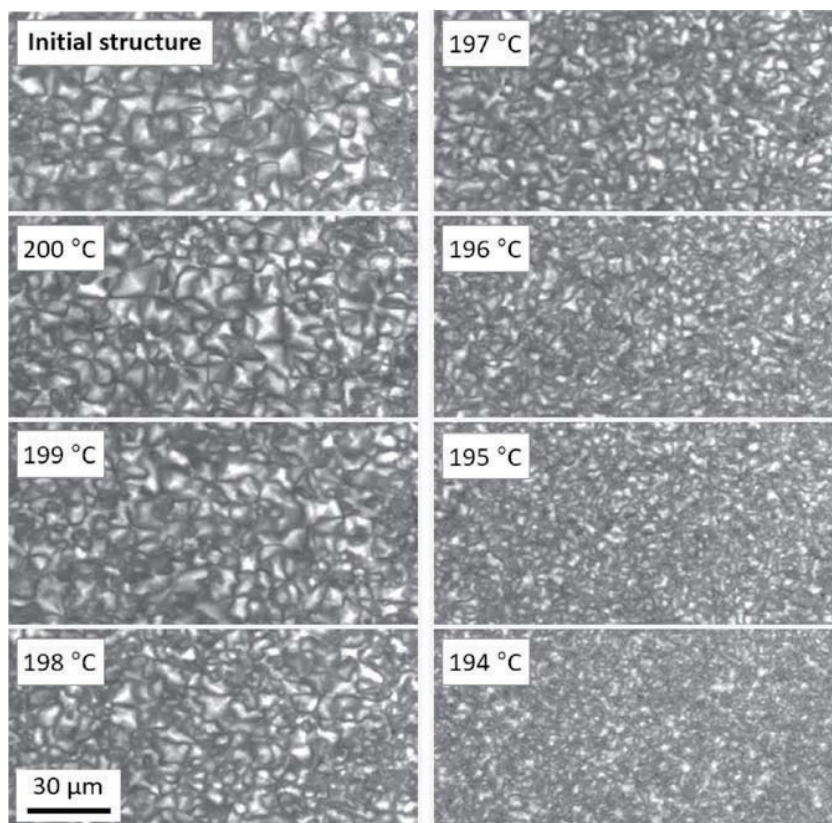


Fig. 3. Microstructure of PA 11 formed on non-isothermal melt-crystallization at 20 K min^{-1} . The maximum temperature of the melt (T_{max} , see Fig. 1) is shown in each image, and the melt-residence time was 3 min . The top left image shows the initial structure before heating, obtained on cooling the equilibrium melt from $230 \text{ }^\circ\text{C}$ at 20 K min^{-1} .

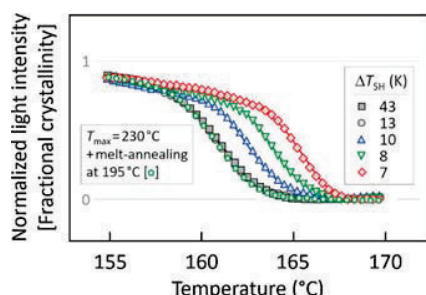


Fig. 4. Normalized crystallinity as a function of temperature as measured by the light intensity of POM images collected during cooling PA 11 from different maximum temperatures of the melt. Normalization is based on the intensity values obtained at 175 °C (0) and 145 °C (1). In an additional crystallization experiment, explained below with Fig. 5, the equilibrium melt was subject to an additional annealing step at 195 °C (small green pentagon symbols).

peak temperature of 187 °C of 7 to 13 K, respectively. Note that lower superheating did not allow complete melting of crystals but only partial melting and melt-recrystallization, with such conditions excluded in the present study. In other words, complete melting of all crystals is considered being pre-requisite for analysis of self-nucleation.

The images of Fig. 3 reveal information that distinct self-nucleation is observed in PA 11. The top left image was obtained on a sample crystallized on cooling the melt which before was heated to above the equilibrium melting temperature and which therefore does not contain self-nuclei, representing the reference state defined with the images in Fig. 2. The nuclei density is rather low and the spherulites correspondingly large. However, if after complete melting of crystals with a melting peak temperature of 187 °C the melt is not heated to above 198 °C then a distinctly finer spherulitic morphology is detected, indicating an increased number of self-seed nuclei. With increasing superheating of the melt (ΔT_{SH}), the self-seed concentration obviously decreases as the spherulite size systematically increases when heating the melt to increasingly higher temperature.

The increase of the self-seed concentration does not only lead to a different semicrystalline morphology, as demonstrated by Fig. 3, but also causes an increase of the overall crystallization rate. Fig. 4 shows the evolution of an equivalent of the crystallinity of PA 11 as a function of temperature, as measured by the light intensity of POM images. With

decreasing maximum temperature of the melt, T_{max} , or superheating above the melting temperature, ΔT_{SH} , the crystallization temperature systematically increases. However, consistent with the investigation of the resulting microstructure (Fig. 3), acceleration of crystallization is only observed if ΔT_{SH} is lower than 13 K (see gray circles and black squares in Fig. 4). At such high superheating of the melt, obviously, all crystal remnants/self-seed are melted or not effective anymore to enhance crystallization on subsequent cooling.

To confirm the above observations, an additional crystallization experiment was designed to rule out that the fine spherulitic morphology observed at low superheating of the melt above T_m is caused by different, non-self-seed type crystal nuclei. Note that classical theories of nucleation and crystallization also predict increased nuclei density with increasing supercooling of the melt to below the equilibrium melting temperature $T_{m,0}$ since the critical nucleus size is decreasing with decreasing temperature [4,31]. Fig. 5 shows in the top part temperature-time profiles for analysis of the effect of a high-temperature annealing step at 195 °C on non-isothermal melt-crystallization. Assuming that equilibration of the melt is assured by heating semicrystalline PA 11 to 230 °C, with the additional annealing step at 195 °C on cooling it may be confirmed that there is no formation of supercritical-size nuclei in the relaxed though supercooled melt. Such nuclei then also could cause such fine-spherulitic structures as obtained after heating semicrystalline PA 11 to temperatures only slightly higher than the melting temperature of crystals. However, the POM images shown in the lower part of Fig. 5 demonstrate that (a) all self-seed is destroyed upon heating to 230 °C, and (b) that annealing the supercooled but initially equilibrated melt at 195 °C for a period 3 min does not lead to formation of additional crystal nuclei, compared to those forming on continuous cooling. For comparison, the inset in the right micrograph shows again the structure which was obtained after heating the reference sample to a maximum temperature of 195 °C, leaving self-seed after melting of the crystals at 187 °C. In agreement with the analysis of the semicrystalline morphology/POM structure, the crystallization kinetics is also unaffected by the additional melt-annealing step, as shown with the green pentagon symbols in Fig. 4.

4. Conclusions

With this communication, we provided first evidence of self-nucleation of crystallization in the specific case of PA 11. In case of spherulitically grown lamellar crystals melting at a temperature close to

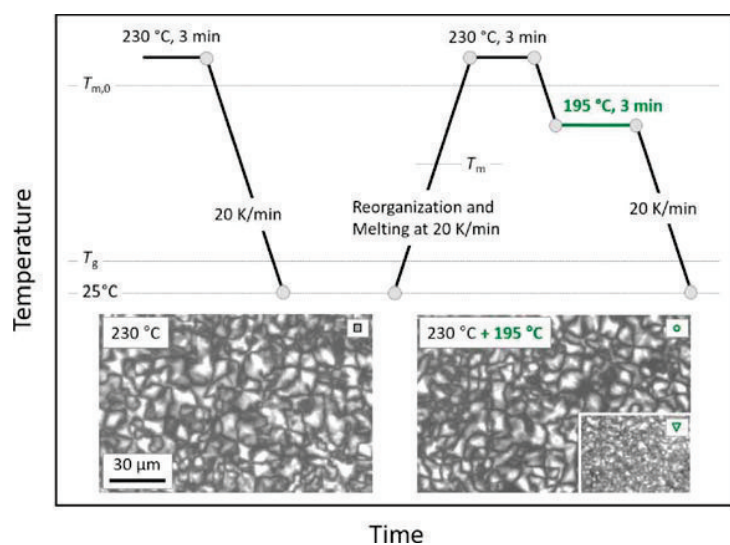


Fig. 5. Top: Temperature-time profiles for analysis of the effect of a high-temperature annealing step at 195 °C on non-isothermal melt-crystallization. Bottom: POM-images obtained after cooling the equilibrium melt of PA 11 at a rate of 20 K min^{-1} , without (left image) and with (right image) an additional annealing step at 195 °C. The inset in the right image shows the structure obtained after cooling the melt at 20 K min^{-1} , using self-seed which survived heating to 195 °C. The symbols in the top right corner of each image provide a link the crystallization kinetics shown in Fig. 4.

190 °C, self-seed is stable up to a temperature of 200 °C for the selected residence time of three minutes. With decreasing maximum temperature of the melt above the melting temperature of the initially present crystals, the self-seed concentration increases. Consequently, on subsequent non-isothermal melt-crystallization, crystallization is faster and the spherulitic superstructure is distinctly finer, compared to the structure after crystallization of the relaxed melt not containing self-seed.

We consider the data and results presented here as a pre-requisite for an in-depth study about the effect of the initial semicrystalline morphology on the stability of self-seed. As far as we are aware, such investigation is still lacking which also may be attributed to the need of using sophisticated tools like fast scanning chip calorimetry to (a) prepare crystals of largely different stability and morphology, and (b) allow their complete melting without prior reorganization/stabilization. Main ideas regarding such research evolved through the long-lasting collaboration with Christoph Schick, as documented e.g. in [12,32], focusing on the topic of fast melt-recrystallization of the unstable but self-seed containing melt of poly (L-lactic acid).

Acknowledgments

KJ and RA are grateful for support by the European Social Fund (ESF).

References

- [1] M.I. Vesselinov, *Crystal Growth for Beginners: Fundamentals of Nucleation, Crystal Growth and Epitaxy*, World scientific, New Jersey, 2016.
- [2] C. Schick, R. Androsch, J.W.P. Schmelzer, Homogeneous crystal nucleation in polymers, *J. Phys. Condens. Matter* 29 (2017) 453002 (35).
- [3] R. Androsch, C. Schick, Crystal nucleation of polymers at high supercooling of the melt, *Adv. Polym. Sci.* 276 (2017) 257–288.
- [4] B. Wunderlich, *Macromolecular physics, Crystal Nucleation, Growth, Annealing vol 2*, Academic Press, New York, 1976.
- [5] D.J. Blundell, A. Keller, A.J. Kovacs, A new self-nucleation phenomenon and its application to the growing of polymer crystals from solution, *J. Polym. Sci. Polym. Lett.* 4 (1966) 481–486.
- [6] R.M. Michell, A. Mugica, M. Zubitur, A.J. Müller, Self-nucleation of crystalline phases within homopolymers, polymer blends, copolymers, and nanocomposites, *Adv. Polym. Sci.* 276 (2017) 215–256.
- [7] B. Fillon, J.C. Wittmann, B. Lotz, A. Thierry, Self-nucleation and recrystallization of isotactic polypropylene (α phase) investigated by differential scanning calorimetry, *J. Polym. Sci. Polym. Phys.* 31 (1993) 1383–1393.
- [8] B. Fillon, B. Lotz, A. Thierry, J.C. Wittmann, Self-nucleation and enhanced nucleation of polymers. Definition of a convenient calorimetric “efficiency scale” and evaluation of nucleating additives in isotactic polypropylene (α phase), *J. Polym. Sci. Polym. Phys.* 31 (1993) 1395–1405.
- [9] D.J. Blundell, On the interpretation of multiple melting peaks in poly (ether ether ketone), *Polymer* 28 (1987) 2248–2251.
- [10] A.A. Minakov, D.A. Mordvintsev, C. Schick, Melting and reorganization of poly (ethylene terephthalate) on fast heating (1000 K/s), *Polymer* 45 (2004) 3755–3763.
- [11] K. Jariyavidyanont, R. Androsch, C. Schick, Crystal reorganization of poly (butylene terephthalate), *Polymer* 124 (2017) 274–283.
- [12] R. Androsch, E. Zhuravlev, C. Schick, Solid-state reorganization, melting and melt-recrystallization of conformationally disordered crystals (α' -phase) of poly (L-lactic acid), *Polymer* 55 (2014) 4932–4941.
- [13] J.V. McLaren, A kinetic study of the isothermal spherulitic crystallization of poly-hexamethylene adipamide, *Polymer* 4 (1963) 175–189.
- [14] J.H. Magill, Melting behaviour and spherulitic crystallization of polycapromide (nylon 6), *Polymer* 3 (1962) 43–51.
- [15] E. Turska, S. Gogolewski, Study on crystallization of nylon 6 (polycapramide). III. Effect of “crystalline memory” on crystallization kinetics, *J. Appl. Polym. Sci.* 19 (1975) 637–644.
- [16] N. Avramova, S. Fakirov, I. Avramov, Cumulative “memory” effect in nylon-6, *J. Polym. Sci. Polym. Phys.* 22 (1984) 311–313.
- [17] H. Li, R. Guo, Y. Liu, S. Liu, E. Proniewicz, L.M. Proniewicz, Y. Zhao, Y. Xu, J. Wu, Self-nucleation-induced nonisothermal crystallization of nylon 6 from the melt, *J. Appl. Polym. Sci.* 132 (2015) 42413.
- [18] L.J. Mathias, D.G. Powell, J.P. Autran, R.S. Porter, ^{15}N NMR characterization of multiple crystal forms and phase transitions in polyundecanamide (Nylon 11), *Macromolecules* 23 (1990) 963–967.
- [19] G.F. Schmidt, H.A. Stuart, Gitterstrukturen mit räumlichen Wasserstoffbrückensystemen und Gitterumwandlungen bei Polyamiden, *Z. Z. Naturforsch.* 13 (1958) 222–225.
- [20] A. Mollova, R. Androsch, D. Mileva, C. Schick, A. Benhamida, Effect of supercooling on crystallization of polyamide 11, *Macromolecules* 46 (2013) 828–835.
- [21] A.M. Rhoades, N. Wonderling, C. Schick, R. Androsch, Supercooling-controlled heterogeneous and homogenous crystal nucleation of polyamide 11 and its effect onto the crystal/mesophase polymorphism, *Polymer* 106 (2016) 29–34.
- [22] A.A. Minakov, C. Schick, Ultrafast thermal processing and nanocalorimetry at heating and cooling rates up to 1 MK/ s, *Rev. Sci. Instr.* 78 (2007) 073902.
- [23] C. Schick, V. Mathot, *Fast Scanning Calorimetry*, Springer, 2016.
- [24] A. Toda, R. Androsch, C. Schick, Insights into polymer crystallization and melting from fast scanning chip calorimetry, *Polymer* 91 (2016) 239–263.
- [25] C. Schick, R. Androsch, New insights into polymer crystallization by fast scanning chip calorimetry, *Fast Scanning Calorimetry*, Springer, Cham, 2016, pp. 463–535.
- [26] Rilsan BESNO TL Product Information, (2019) Assessed 08/02/2018 <https://www.extremematerials-arkema.com/en/materials-database/>.
- [27] T.D. Fornes, D.R. Paul, Structure and properties of nanocomposites based on Nylon-11 and -12 compared with those based on Nylon-6, *Macromolecules* 37 (2004) 7698–7709.
- [28] C.A. Schneider, W.S. Rasband, K.W. Eliceiri, NIH Image to ImageJ: 25 years of image analysis, *Nat. Methods* 9 (2012) 671–675.
- [29] Q. Zhang, Z. Mo, S. Liu, H. Zhang, Influence of annealing on structure of Nylon 11, *Macromolecules* 33 (2000) 5999–6005.
- [30] Y. Furushima, M. Nakada, K. Ishikiriyama, A. Toda, R. Androsch, E. Zhuravlev, C. Schick, Two crystal populations with different melting/reorganization kinetics of isothermally crystallized polyamide 6, *J. Polym. Sci. Polym. Phys.* 54 (2016) 2126–2138.
- [31] J.D. Hoffman, G.T. Davis, J.I. Lauritzen, Jr, The rate of crystallization of linear polymers with chain folding, in: N.B. Hannay (Ed.), *Treatise on Solid State Chemistry*, vol. 3, Plenum Press, New York, London, 1976.
- [32] R. Androsch, C. Schick, M.L. Di Lorenzo, Melting of conformationally disordered crystals (α' -phase) of poly (L-lactic acid), *Macromol. Chem. Phys.* 215 (2014) 1134–1139.

4.4 Crystal self-nucleation in polyamide 11 of different semicrystalline morphology

Katalee Jariyavidyanont¹, Andreas Janke², René Androsch¹

¹ Interdisciplinary Center for Transfer-oriented Research in Natural Sciences, Martin Luther University Halle-Wittenberg, 06099 Halle/Saale, Germany.

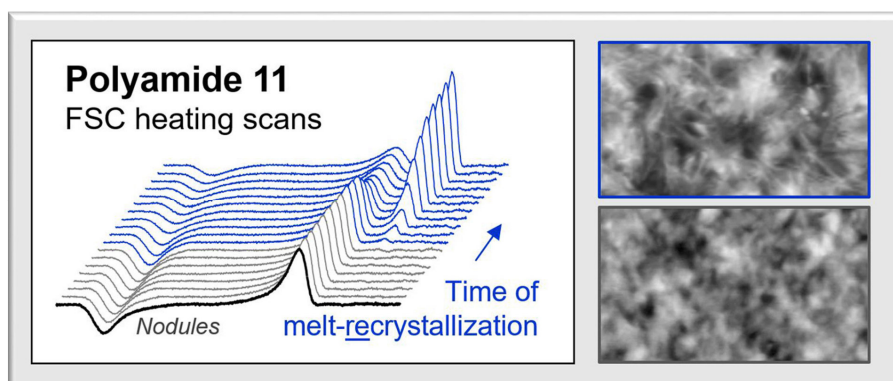
² Leibniz-Institut für Polymerforschung Dresden e.V., Hohe Str. 6, 01069 Dresden, Germany.

Polymer 2019, 184, 121864.

Research highlights

1. The kinetics of melt-recrystallization and the stability of self-nuclei of PA 11 initially containing either nodular or lamellar crystals was investigated by FSC, POM, and AFM.
2. A nodular mesophase with a high surface-to-volume ratio, formed from a large number of nuclei, on one side, and spherulitically grown lamellae, on the other side, were prepared on FSC sensors.
3. The higher survival-potential and melt-recrystallization rate of self-nuclei in PA 11 initially containing the nodular mesophase is caused by the strong coupling of the nodules to the surrounding amorphous structure and their larger number.

Graphical abstract





Contents lists available at ScienceDirect

Polymer

journal homepage: <http://www.elsevier.com/locate/polymer>

Crystal self-nucleation in polyamide 11 of different semicrystalline morphology

Katalee Jariyavidyanont^a, Andreas Janke^b, René Androsch^{a,*}

^a Interdisciplinary Center for Transfer-oriented Research in Natural Sciences, Martin Luther University Halle-Wittenberg, 06099 Halle/Saale, Germany

^b Leibniz-Institut für Polymerforschung Dresden e.V, Hohe Str. 6, 01069 Dresden, Germany

ARTICLE INFO

Keywords:

Crystal nucleation
Self-nucleation
Crystallization
Polyamide 11

ABSTRACT

Self-nuclei supported recrystallization of the crystal-free melt of polyamide 11 (PA 11) of qualitatively different initial semicrystalline morphology, either containing nodular crystals or spherulitically grown lamellar crystals, has been investigated by fast scanning chip calorimetry, optical microscopy and atomic force microscopy. Melt-recrystallization of PA 11 initially containing a large number of nodules of high surface-to-volume ratio and strong coupling to the surrounding amorphous structure, as confirmed with the detection of significant amount of rigid amorphous fraction, is distinctly faster than melt-recrystallization of PA 11 initially containing lamellae and spherulites, caused by a lower number of self-nuclei in the latter system. Moreover, the temperature range of survival of self-nuclei above the respective melting temperature of nodular and lamellar crystals is larger for PA 11 initially containing nodules. The melt-residence time, within the assessable time-range before onset of melt-recrystallization, has no effect on the self-nuclei number. Enhanced self-nucleation in PA 11 containing nodules, compared to spherulitically crystallized PA 11, is suggested being caused by the distinctly larger initial number of individually grown crystals. A possible effect of the rigid amorphous fraction, forming during nodular crystallization, on hindering relaxation of the melt is discussed.

1. Introduction

Polyamide 11 (PA 11) is a bio-based engineering thermoplastic produced from short-term renewable castor oil. It shows good chemical resistance, excellent impact and abrasion properties, and low moisture absorption compared to PA 6 or PA 66 [1–3]. In addition, it is characterized by a balanced thermal and mechanical behavior. For these reasons, PA 11 is used for various high-performance engineering applications such as flexible tubes or pipelines in offshore oilfields, hydraulic/pneumatic hoses, cable sheathing, automotive tubing, for sport goods, and for applications in the medical area [1–3].

PA 11 is a semicrystalline polymer with a maximum crystallinity of about 40% [4]. It exhibits different crystal structures controlled by the crystallization conditions [4–9]. Melt-crystallization of PA 11 on cooling slower than about 300 K/s leads to development of pseudo-hexagonal δ -crystals at low supercooling of the melt [8] which reversibly transform into triclinic α -crystals at the Brill-transition temperature of about 100 °C [10–12]. The equilibrium melting temperature ($T_{m,0}$) of the α -crystals is reported being 203 [4] or 220 °C [13], and the bulk enthalpy of fusion is between 189 and 244 J/g [4,13,14]. The

δ/α -crystals which form via heterogeneous nucleation at low supercooling of the melt typically exhibit a chain folded lamellar morphology and are organized within spherulites [8,15]. In contrast, fast cooling of the melt at rates between 200 and 500 K/s leads to non-spherulitic growth of pseudo-hexagonal δ' -crystals of nodular shape [8], initially classified as a hexagonal smectic mesomorphic form [5]; for this reason, in the present paper, δ' -crystals are also termed mesophase. Based on detailed analyses of the crystallization kinetics and nuclei density it is assumed that the mesophase forms via homogeneous nucleation [8, 16–18]. Crystallization is suppressed when quenching the melt with a rate higher than about 500 K/s [8] to below the glass transition temperature (T_g) of about 45 °C [13]. Analysis of the rate of isothermal crystallization reveals a bimodal temperature-dependence associated with a transition from heterogeneous nucleation at low supercooling of the melt to homogeneous nucleation at high supercooling [8,9]. Two crystallization-rate maxima are observed at around 120 and 65 °C [9], with the high-temperature maximum depending on the presence of heterogeneous nucleators [9,19]. Within the wide spectrum of crystallizable polymers, PA 11 may be classified as intermediate-fast crystallizing, with the minimum crystallization half-time being of the order of

* Corresponding author.

E-mail address: rene.androsch@iw.uni-halle.de (R. Androsch).

<https://doi.org/10.1016/j.polymer.2019.121864>

Received 21 August 2019; Received in revised form 27 September 2019; Accepted 4 October 2019

Available online 7 October 2019

0032-3861/© 2019 Elsevier Ltd. All rights reserved.

magnitude of 0.1 s.

Besides homogeneous and heterogeneous nucleation, there is a special nucleation process called self-nucleation [20–22]. When crystals are heated to above their melting temperature (T_m) but to below $T_{m,0}$, incomplete isotropization of the melt may occur. In such a case, remnants of crystals are preserved in the melt, serving as self-seed and accelerate subsequent crystallization. Alternatively, melt-memory effects have been associated with the time-dependent change of the entanglement density after crystal melting [23,24]. Worth noting that melt-recrystallization may also occur on heating which then often is called crystal reorganization [25–28], as long as the melt is in a super-cooled state. However, self-nucleation experiments are commonly performed on cooling, often using differential scanning calorimetry (DSC) and polarized-light optical microscopy (POM) [21,22,29,30].

Earlier studies proved that self-nucleation is evident also in polyamides including PA 6 [31–33], PA 1212 [34], and PA 11 [35]. Self-nucleation in PA 11 initially containing spherulitically grown lamellar crystals was detected by the changed kinetics of non-isothermal melt-recrystallization using a thermo-optical microscopic technique [35]. The initial structure was heated to different maximum temperatures (T_{max}) between T_m and $T_{m,0}$, and subsequently self-nucleation was analyzed by monitoring the crystallization temperature (T_c) on cooling as a function of T_{max} . In addition, self-nuclei were identified by evaluation of the nuclei/spherulite density after melt-recrystallization using POM. In presence of self-nuclei, T_c shifted to higher temperature with decreasing T_{max} . Simultaneously, the POM microstructure confirmed the presence of self-nuclei in the melt since a larger number of smaller spherulites after recrystallization was observed, compared to the structure obtained after crystallization of a fully relaxed melt. The number of self-nuclei decreased with increasing temperature of the melt and approached zero at a temperature about 10 K higher than T_m of the initial structure. It is important noting that T_m was obtained on heating at 20 K/min, implying that the initial structure may have been subject of crystal reorganization, being a general phenomenon limiting the establishment of correlations between initially present structures and high-temperature behaviors.

To our knowledge, the effect of different initial structure of a given polymer on the self-nuclei-concentration and -stability was hardly investigated. A dedicated study focused on the correlation of the initial crystallinity of a model ethylene 1-butene copolymer with 2.2 mol% ethyl branches with the self-nucleation behavior. A critical crystallinity level to observe a melt-memory effect on subsequent crystallization was determined. Moreover, a lower crystallinity threshold was identified when crystals formed on fast cooling rather than by slow crystallization. It was suggested that fast cooling allowed trapping of knots and loops around the crystals causing a lowering of the crystallinity threshold for

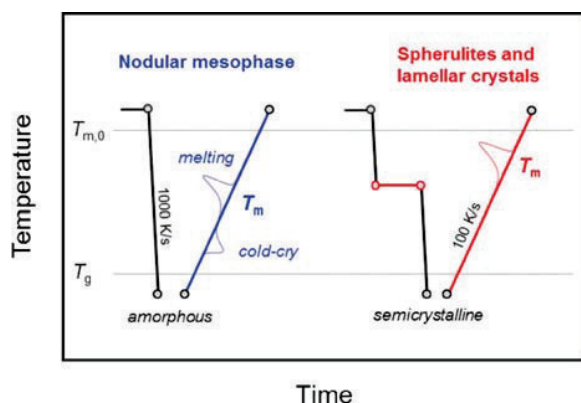


Fig. 1. Temperature-time profiles for preparation of PA 11 containing nodular mesophase (left) and spherulitically grown lamellar crystals (right).

self-nucleation [36].

Many polymers including PA 11 develop different semicrystalline morphologies as a function of the crystallization conditions and the nucleation path [18,37]. We assume that the semicrystalline morphology including the fraction, size, shape, and surface structure of crystals, as well as presence of non-equilibrium melt influence the concentration and stability of self-nuclei, and therefore the structure after melt-recrystallization. In this work, we intend to provide new insight about such link. Therefore, self-nucleation in PA 11 of different initial structure, as achieved by crystallization along different nucleation pathways, is analyzed in the present work. Due to the limitation of scanning rates in a DSC, fast scanning chip calorimetry (FSC) was used to prepare two qualitative different semicrystalline morphologies. Folded-chain lamellae in a spherulitic superstructure on one side, and mesomorphic nodules on the other side were formed via heterogeneous and homogeneous nucleation, respectively, and then the kinetics of isothermal and non-isothermal melt-recrystallization was analyzed as a function of T_{max} . The presence of self-nuclei based on those initial semicrystalline morphologies was confirmed by the final structure after recrystallization by means of both optical and atomic force microscopy (AFM).

2. Experimental

2.1. Material

Bio-based natural PA 11 Rilsan® BESNO-TL from Arkema was used. It is an extrusion grade of high viscosity containing heat and light stabilizers. The melt volume index is 1 cm³/10 min (235 °C, 2.16 kg) [38], and the molar mass and polydispersity are about 17.2 kg/mol and 2, respectively [39]. The material was delivered in the form of pellets.

2.2. Instrumentation

2.2.1. Fast scanning chip calorimetry (FSC)

FSC was used to investigate the kinetics of melt-recrystallization and the stability of self-nuclei. In addition, FSC served for preparation of samples of different initial semicrystalline morphology. A power compensation Mettler-Toledo Flash DSC 1 connected to a Huber TC 100 intracooler was employed in this work. The furnace was purged with dry nitrogen gas at a flow rate of 60 mL/min and the sample-support temperature was set constant at −90 °C. The empty UFS 1 sensor was conditioned and temperature-corrected according to the instrument operating instructions before placing the sample onto the chip membrane. Samples for FSC analysis were prepared from the as-received granules using a Slee rotary microtome CUT 4062 equipped with a tungsten carbide knife to obtain thin sections with a thickness of about 10 μm. The sections were subsequently reduced in their lateral size to 50–100 μm under a stereomicroscope using a scalpel for analysis of the kinetics of isothermal melt-recrystallization. Samples with a larger lateral width of 100–150 μm were prepared for analysis of the kinetics of non-isothermal melt-recrystallization, as these larger samples were also used for observation of the final structure after recrystallization by microscopy, both POM and AFM.

2.2.2. Polarized-light optical microscopy (POM)

The semicrystalline morphology of FSC samples at the micrometer length-scale, before and after melt-recrystallization, was observed by a reflection-mode Kern OPN-184 polarized-light optical microscope, with the sample located between crossed polarizers. The images were taken with an imaging source digital camera DFK 33UX252.

2.3. Atomic force microscopy (AFM)

Analysis of the nanometer length-scale structures of FSC samples before and after melt-recrystallization was performed with a Dimension

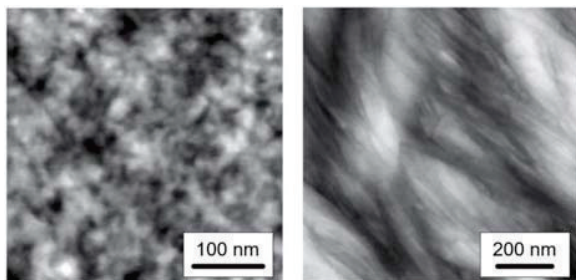


Fig. 2. AFM height-images of PA 11 containing either a nodular mesophase (left) or lamellar crystals (right).

FASTSCAN (Bruker-Nano, USA) operated in peak force tapping mode. Silicon nitride sensors SCANASYST-FLUID+ (Bruker, USA) with a nominal spring constant of 0.7 N/m and a tip radius of 2 nm were used, and the set point was 0.02 V. Prior AFM analysis, the chip membrane hosting the samples was separated from the surrounding ceramic frame of the UFS 1 sensor and placed on a glass slide using double-sided tape, in order to allow the cantilever and tip approaching the sample surface.

3. Results and discussion

3.1. Semicrystalline morphology of PA 11 crystallized along different nucleation pathways

Fig. 1 shows the temperature-time profile for preparation of PA 11 containing nodular mesophase (left) and spherulitically grown lamellar crystals (right). In the case of preparation of nodular mesophase domains, the melt was quenched with a cooling rate of 1000 K/s to below T_g to obtain a fully amorphous sample. Then, the amorphous phase was heated with a rate of 100 K/s to permit formation of the nodular mesophase by cold-crystallization at about 60 °C. In order to illustrate structure formation on heating, the heating ramp is schematically superimposed with an FSC heating scan showing cold-crystallization at a temperature slightly higher than T_g , followed by melting at rather low temperature. Spherulitically grown lamellae were prepared by isothermal crystallization at low supercooling of the melt at a temperature of 150 °C. Subsequent heating reveals that the crystals formed at 150 °C exhibit higher thermal stability than the mesophase domains as indicated with the schematically shown melting peak at a higher

temperature than in case of the mesophase.

The different semicrystalline morphologies were confirmed by AFM. Fig. 2 shows AFM height-images of PA 11 containing either nodular mesophase formed during isothermal cold-crystallization at 60 °C for 10 s (left), or spherulitically grown lamellar crystals developed by isothermal crystallization at 150 °C for 15 s (right). The mesophase nodules exhibit a size of 10–20 nm and are not arranged in a high-order superstructure, confirming their individual appearance/growth from numerous nuclei and a homogeneous nucleation mechanism as observed for many polymers including isotactic polypropylene [40], poly (butylene terephthalate) [41], PA 6 [42], or PA 66 [43]. Crystallization at 150 °C, in contrast, led to growth of lath-like lamellae with a thickness of about 10 nm and a length of several hundred nanometers.

3.2. Experimental protocol for analysis of the kinetics of melt-recrystallization and the stability of self-nuclei

Fig. 3 shows temperature-time profiles for analysis of the kinetics of isothermal (left) and non-isothermal melt-recrystallization (right). Regarding the isothermal experiments, the samples of different initial structure were heated at 100 K/s to different T_{max} between their respective T_m and $T_{m,0}$, with the low heating rate selected to minimize thermal lag effects. For convenience, in order to benchmark T_{max} in relation to T_m , we introduced a new quantity ΔT_{SH} ($= T_{max} - T_m$), with SH standing for “superheating”. In the present work, nodular and lamellar crystals melt between 160 and 170 °C, with the only slightly higher value in case of lamellar crystals caused by distinct mesophase-reorganization during slow heating at 100 K/s. Important to note, reorganization of the mesophase on slow heating involves a transition into δ/α -crystals, however, does not affect the shape and superstructure, that is, the nodular morphology is preserved [8]. After heating, the melt was held at each T_{max} for different time between 0.01 and 10,000 s, to allow melt-recrystallization before quenching to below T_g and analysis of the progress of melt-recrystallization by evaluation of the crystallinity on subsequent heating at 100 K/s. The kinetics of melt-recrystallization is considered depending on the number of self-nuclei, thus providing information about their stability when varying T_{max} .

The measurement scheme for analysis of the kinetics of non-isothermal melt-recrystallization is shown on the right side of Fig. 3. The samples of different initial structure were heated at 100 K/s to different T_{max} , kept there for 0.01 s, which is short enough to suppress crystallization, and then slowly cooled at 10 K/s to below T_g . The cooling scans were evaluated regarding the crystallization-peak temperature, which is expected to increase with increasing amount of self-

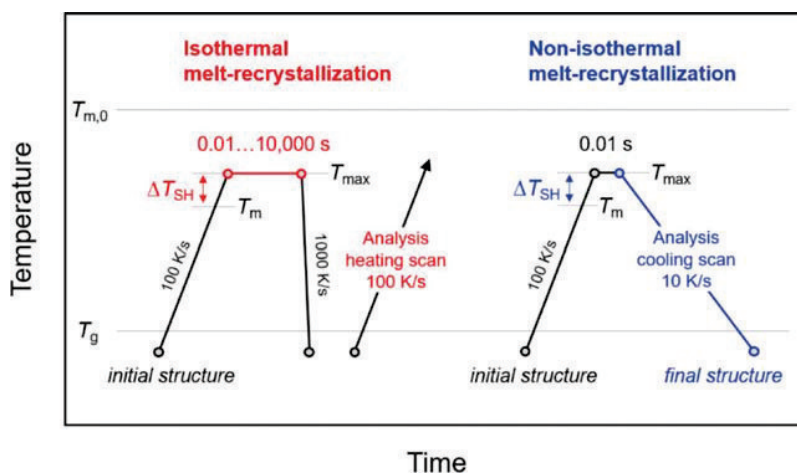


Fig. 3. Temperature-time profile for analysis of the kinetics of isothermal (left) and non-isothermal melt-recrystallization (right).

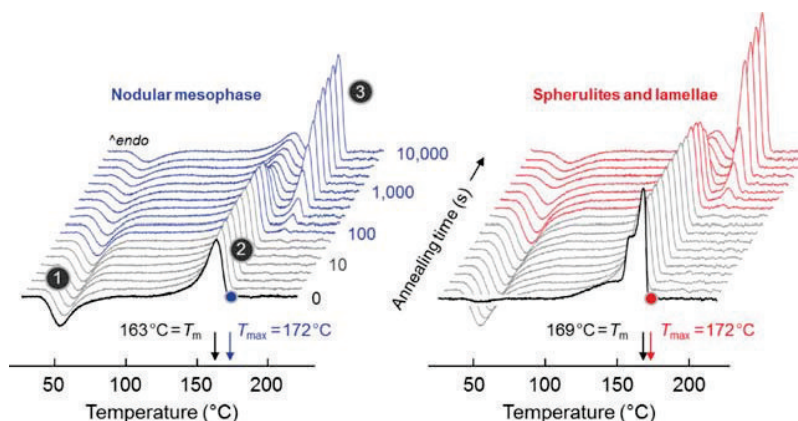


Fig. 4. Sets of FSC heating scans, heat-flow rate as a function of temperature, collected before (front curve) and after annealing the melt of PA 11 initially containing nodular mesophase (left) or lamellae and spherulites (right) for different periods of time up to 10,000 s at 172 °C (T_{max}) (see circles at the front curves).

nuclei. In addition, after cooling, the final structure was analyzed at room temperature by POM.

3.3. Kinetics of isothermal melt-recrystallization and stability of self-nuclei

Fig. 4, as an example, shows sets of FSC heating curves, heat-flow rate as a function of temperature, collected after annealing the melt of PA 11 which initially contained the nodular mesophase (left) or lamellar crystals and spherulites (right) for different time. In each set of data, the front black curve shows the melting behavior of the initial but reorganized crystals, either nodules or spherulitically grown lamellae, with the black vertical arrow indicating T_m . The temperature of annealing the melt, that is T_{max} , was 172 °C, indicated with blue or red circles and arrows at the temperature axis, and the annealing time was between 0.01 and 10,000 s. The numbers 1, 2, and 3 at selected curves indicate cold-crystallization, melting of crystals formed during heating by cold-crystallization and subsequent reorganization, and melting of crystals formed during annealing the melt by melt-recrystallization, respectively. Gray and blue/red coloring of curves is employed to distinguish annealing-time ranges before and during melt-recrystallization, respectively.

Regarding the data set shown to the left in Fig. 4, heating of initially fully amorphous PA 11 at a rate of 100 K/s leads to formation of the nodular mesophase at around 60 °C, with the corresponding cold-crystallization peak labeled '1'. The mesophase reorganizes during further heating to crystals, which finally melt in this particular experiment between 160 and 170 °C (see peak labeled '2'). If the crystal-free melt is subject of isothermal annealing at 172 °C (see blue circle at the front curve, or arrow at the temperature axis) for different time up to about 100 s, then subsequently recorded heating curves (gray), after prior freezing the structural state by fast cooling to below T_g , indicate absence of crystallization at the annealing temperature. An additional peak, labeled '3', representing melting of crystals formed during annealing the melt, is detected if the annealing time exceeds 100 s (blue curves). This peak increases in area with increasing annealing time, and allows quantification of the kinetics of melt-recrystallization. Simultaneously, with increasing fraction of crystals forming at 172 °C, cold-crystallization during subsequent heating is reduced.

In the case of the sample containing lamellar crystals, with the corresponding data set shown to the right in Fig. 4, the front curve obtained from the non-annealed sample shows two melting peaks due to reorganization of the initially at 150 °C formed lamellae. The high-temperature melting peak is detected close to 170 °C, and further heating to 172 °C leads to complete melting, as the subsequently

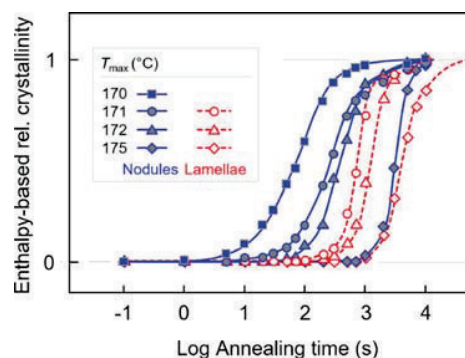


Fig. 5. Normalized enthalpy-based relative crystallinity as a function of the time of annealing/melt-recrystallization of PA 11 initially containing nodular mesophase (blue, filled symbols, solid lines) or lamellar crystals and spherulites (red, open symbols, dashed lines). The different symbols represent data obtained at different annealing temperatures, as indicated in the legend. (For interpretation of the references to color in this figure legend, the reader is referred to the Web version of this article.)

recorded heating scans confirm absence of crystals after freezing the structure by cooling to below T_g . Consequently there is observed cold-crystallization, and melting of crystals, formed from the mesophase, at 163 °C (see gray curves). A single melting peak is observed at any annealing time shorter than 100 s, and melt-recrystallization only starts on annealing longer than 300 s (red curves), as indicated with the observation of the melting peak at higher temperature.

Qualitative inspection of the example-data sets of Fig. 4 immediately provides important information that the initial semicrystalline morphology of PA 11 significantly affects the kinetics of melt-recrystallization at identical annealing temperature of the melt. Despite the temperature difference between T_{max} and T_m is larger in case of presence of nodular crystals ($\Delta T_{SH} = 9$ K), melt-recrystallization is distinctly faster than in case of the system initially containing lamellae and spherulites where ΔT_{SH} equals only 3 K.

Quantitatively, data sets as exemplarily shown in Fig. 4 were evaluated regarding the evolution of the crystallinity during the time of annealing the melt at T_{max} , by measuring the area under the peak labeled '3' in Fig. 4. Fig. 5 shows normalized relative crystallinities of PA 11 initially containing nodular mesophase (blue, filled symbols, solid lines) or lamellar crystals and spherulites (red, open symbols, dashed

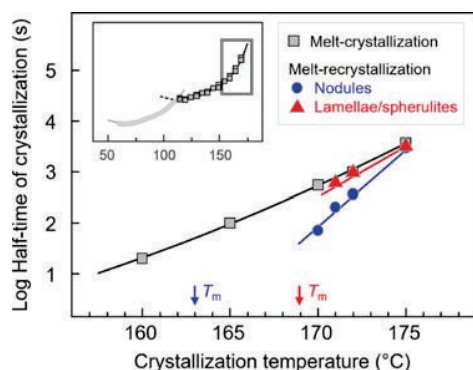


Fig. 6. Half-time of crystallization of the relaxed melt of PA 11 (black squares and inset) and of melt-recrystallization of PA 11 initially containing nodular mesophase (blue circles) or lamellae and spherulites (red triangles) as a function of temperature. The inset shows characteristic melt-crystallization times in a wider temperature range, taken from the literature [9], with the rectangle in the top right corner indicating the temperature window of melt-recrystallization experiments in the present work. The blue and red vertical arrows at the temperature axis mark temperatures of melting of nodular and lamellar crystals, respectively. (For interpretation of the references to color in this figure legend, the reader is referred to the Web version of this article.)

lines) as a function of the time of annealing/melt-recrystallization. The annealing process was performed at different T_{\max} of 170, 171, 172, and 175 °C, represented by squares, circles, triangles, and diamond symbols, respectively. Note that T_{\max} of 170 °C was too low to completely melt all lamellar crystals, that is, for that sample and condition data are not available. Normalization was done by dividing all transition enthalpies by the maximum obtained value of the respective sample, which contained either nodules or lamellae. In the case of PA 11 initially containing the nodular mesophase, melt-recrystallization at 7 K superheating ($T_{\max} = 170$ °C) (filled blue squares), started after about 5 s. With increasing ΔT_{SH} and T_{\max} , the onset of the melt-recrystallization process shifts to longer time, such that at $T_{\max} = 175$ °C melt-recrystallization only started after around 1000 s (blue diamond symbols). Most important, however, is the observation that melt-recrystallization of PA 11 initially containing lamellar crystals and spherulites is distinctly slower than in PA 11 initially containing nodular crystals. For example, melt-recrystallization of PA 11 initially containing nodules at 171 °C begins after about 10 s, while in case of the sample initially containing lamellae and spherulites a dwell time of about 100 s is needed to allow melt-crystallization (see blue and red circles). The kinetics of melt-recrystallization of PA 11 initially containing either nodular or lamellar crystals only becomes similar at $T_{\max} = 175$ °C (diamond symbols), indicating identical structures of the melt.

Fig. 6 shows half-times of primary crystallization of the relaxed melt of PA 11 (black squares) and of melt-recrystallization of PA 11 initially containing nodular mesophase (blue circles) or lamellar crystals and spherulites (red triangles), all as a function of temperature. The blue and red vertical arrows at the temperature axis indicate the melting temperatures of nodular and lamellar crystals at the given heating rate of 100 K/s, respectively, defining the low-temperature limit of melt-recrystallization experiments. The inset shows characteristic melt-crystallization times in a wider temperature range, collected in a different study [9], with the rectangle in the top right corner showing the temperature window of melt-recrystallization experiments in the present work. The data reveal that melt-recrystallization of the sample initially containing the nodular mesophase is significantly faster than crystallization of the relaxed melt. For example, at 170 °C, that is, at a superheating of the melt of 7 K above the melting temperature of the nodular crystals, the half-time of melt-recrystallization is around 70 s

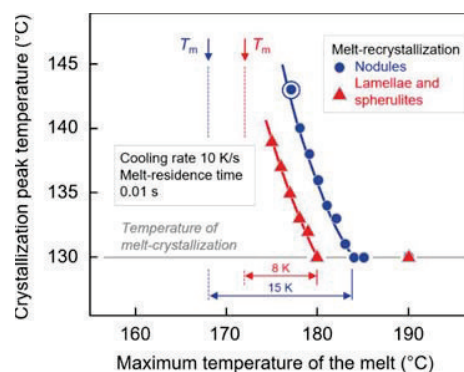


Fig. 7. Crystallization peak temperatures of PA 11 initially containing nodular mesophase (blue circles) or lamellae and spherulites (red triangles) as a function of the maximum temperature of the melt. The gray horizontal line represents the crystallization peak temperature of the relaxed melt, and the vertical arrows in the upper part indicate temperatures of melting of nodular and lamellar crystals at the used heating rate of 100 K/s. Crystallization temperatures were obtained on cooling the melt at 10 K/s. (For interpretation of the references to color in this figure legend, the reader is referred to the Web version of this article.)

while it is around 600 s in case of melt-crystallization. In contrast, melt-recrystallization of the sample initially containing lamellae and spherulites at 171 °C, which corresponds a superheating of 2 K, is only slightly faster than the crystallization of the relaxed melt. As expected, with increasing crystallization temperature in the analyzed temperature range, the half-times of crystallization increase, however, with the temperature-dependence/slope being different for the various samples. Most important, the crystallization half-times of all samples become similar if the crystallization temperature exceeds 175 °C, though the nodular sample still seems crystallizing slightly faster at this temperature, compared to samples containing lamellae and spherulites.

3.4. Non-isothermal melt-recrystallization of PA 11 of different initial structure

The effects of the initial semicrystalline morphology of PA 11 and superheating the melt to different maximum temperatures after complete melting of all crystals on non-isothermal melt-recrystallization were evaluated by analysis of the temperature of crystallization on cooling the melt at a rate of 10 K/s. In these experiments, samples with a larger lateral size than in case of analysis of the kinetics of isothermal melt-recrystallization, described above, were used for the purpose of subsequent POM imaging. Due to the larger sample size, and correspondingly changed instrumental thermal lag [44,45], slightly increased melting temperatures of about 168 °C and 172 °C were obtained for the systems containing nodular and lamellar crystals, respectively, compared to the samples used for isothermal experiments. Fig. 7 shows crystallization temperatures of PA 11 initially containing either the nodular mesophase (blue circles) or lamellar crystals and spherulites (red triangles) as a function of the maximum temperature of the melt. Non-isothermal crystallization of the relaxed melt, when cooled from 220 °C at the same rate of 10 K/s, is detected at 130 °C, represented with the gray horizontal line; detailed analyses of the dependence of the crystallization temperature on the cooling rate are reported elsewhere [8,46]. The melting-peak temperatures of nodular and lamellar crystals are indicated with the blue and red vertical arrows and dashed lines, respectively. The data of Fig. 7 show that non-isothermal melt-recrystallization of PA 11 initially containing nodular or lamellar crystals occurs at higher temperature than in case of crystallization of the relaxed melt when the maximum temperature after complete

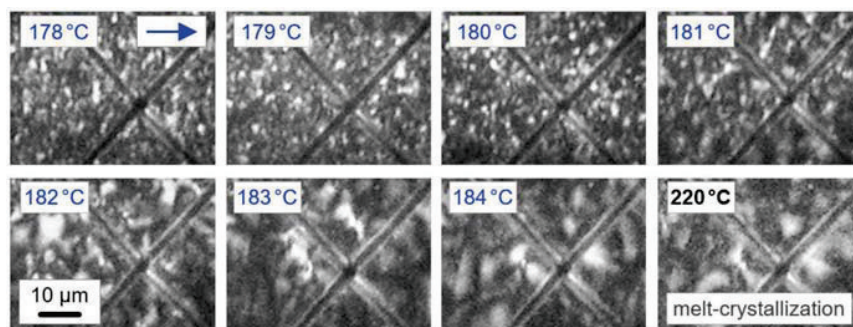


Fig. 8. POM micrographs of the structure of PA 11 formed on non-isothermal melt-recrystallization on cooling at 10 K/s. The maximum temperature of the melt is indicated in each image. The samples initially contained nodular crystals, which melted on heating at 100 K/s. The melt-residence time before cooling was 0.01 s. The arrow indicates the reading-sequence of images when evaluating the effect of increasing maximum temperature of the melt before cooling.

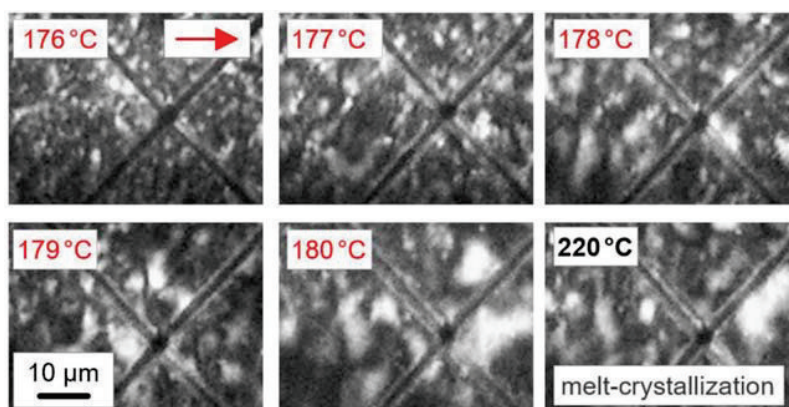


Fig. 9. POM micrographs of the structure of PA 11 formed on non-isothermal melt-recrystallization on cooling at 10 K/s. The maximum temperature of the melt is indicated in each image. The samples initially contained lamellar crystals and spherulites, which melted on heating at 100 K/s. The melt-residence time before cooling was 0.01 s. The arrow indicates the reading-sequence of images when evaluating the effect of increasing maximum temperature of the melt before cooling.

melting of the nodules and lamellae does not exceed 183 and 179 °C, respectively. In other words, distinct self-nucleation effects on non-isothermal crystallization during cooling are observed in a temperature window between T_m and T_m+15 K for PA 11 initially containing nodules and T_m and T_m+7 K for PA 11 initially containing lamella and spherulites. These temperature ranges are emphasized with the blue and red horizontal double arrows at the temperature axis. Within these temperature ranges, the crystallization temperatures increase with decreasing superheating ΔT_{SH} or T_{max} , to reach for the samples initially containing nodular or lamellar crystals maximum values 13 and 9 K higher than observed in case of melt-crystallization, respectively. As already observed in isothermal melt-recrystallization experiments (see Fig. 6), initial presence of nodular crystals leads to larger effects than initial presence of lamellae and spherulites, regarding both the width of the temperature range of self-nuclei survival as well as the absolute number of self-nuclei, with the latter assumed being proportional to the increase of the crystallization temperature. Note that observation of further data points at rather low superheating of the melt above T_m was impossible since only partial melting, paralleled by melt-recrystallization, occurred. Such conditions were excluded in this work.

3.5. POM structure of non-isothermally melt-recrystallized PA 11 of different initial morphology

Figs. 8 and 9 show POM micrographs of FSC samples of PA 11 which were non-isothermally melt-recrystallized on cooling at a rate of 10 K/s. Fig. 8 shows images of a sample which contained nodular crystals, while Fig. 9 shows images of a sample which initially contained lamellae and spherulites. The various images in each Figure provide information about the effect of the maximum temperature of the melt before cooling and melt-recrystallization, with T_{max} shown in each image. The arrow in the top left micrograph of each Figure indicates the reading-sequence when evaluating the effect of increasing T_{max} . As such, Figs. 8 and 9 complete the two data sets of Fig. 7, in which the corresponding dependence of the crystallization temperature on T_{max} was shown.

As a reference, the bottom-right image in Figs. 8 and 9 represents the structure after crystallization of the relaxed melt, free of self-nuclei. Rather large spherulites/domains of crystals of identical orientation with a size of the order of magnitude of 10 μm are visible, which is typical for PA 11. However, consistent with the results of Fig. 7, low superheating of the melt above the respective melting temperature of nodules and lamellae, before melt-recrystallization during cooling, causes the formation of a much finer structure due to the presence of self-nuclei. Parallel to the observation of a decrease of the crystallization temperature with increasing T_{max} in Fig. 7, the POM images reveal complete absence and destruction of self-nuclei at around 184 °C and

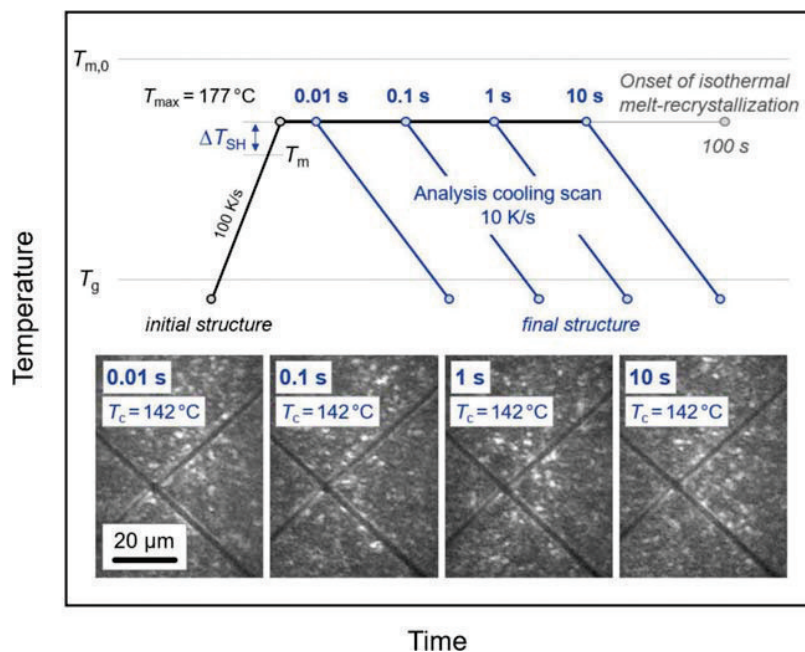


Fig. 10. Thermal protocol for analysis of the effect of the time of annealing the melt of PA 11 on the number of self-nuclei (top part). POM micrographs of the structure of PA 11 formed on non-isothermal melt-recrystallization on cooling at 10 K/s, after exposing the melt to different annealing time of 0.01, 0.1, 1, and 10 s (bottom part, from left to right, respectively). The performed example-experiment was done employing PA 11 initially containing nodules, which melted at 168 °C at the selected heating rate of 100 K/s; T_{\max} was 177 °C.

180 °C for the systems initially containing nodules and lamellae, respectively. Even the gradual decrease of the number of self-nuclei with increasing maximum temperature of the melt is detected by systematic coarsening of the POM structure.

3.6. Effect of melt-residence time on number of self-nuclei

Analyses of the kinetics of melt-recrystallization as a function of the maximum temperature of the melt after complete melting of either nodules or lamellae proved consistently that the stability limit of the most stable self-nuclei is about 12–15 K and less than 8 K above the respective melting temperature of the various crystals, respectively. A large fraction of self-nuclei, however, disappears already below the maximum stability-limit, as is indicated with the continuous slowing down of the crystallization rate and coarsening of the POM structure with increasing T_{\max} . Information about the effect of the melt-residence time on the number of self-nuclei is not gained from the experiments described above. Prior work about self-nucleation in iPP and PCL [21, 30] suggested that there is an only minor effect of time such that the number of self-nuclei slightly reduces on long-term annealing of the melt at the time scale of minutes and hours. For PA 11 of the present study, a thermal protocol as shown in the upper part of Fig. 10 was used to exemplarily evaluate the effect of time of annealing the melt containing self-nuclei. The specific pre-selected sample initially contained nodules which melted on heating at 100 K/s at 168 °C (see blue vertical arrow in Fig. 7). A superheating of 9 K, or T_{\max} of 177 °C was chosen, assuring presence of a high number of self-nuclei (see circled blue data point in Fig. 7). The melt was then annealed for different periods of time of 0.01, 0.1, 1, and 10 s before melt-recrystallization on cooling at 10 K/s. It is important noting that an extension of the annealing time would allow isothermal melt-recrystallization, beginning after about 100 s (see gray circle in Fig. 10), limiting the time-range for analysis of the nuclei number. After cooling the melt at 10 K/s to room temperature, the POM structure was evaluated permitting conclusions whether the melt-residence time affects the nuclei number, shown in the lower part of Fig. 10. The images taken after annealing the melt at 177 °C for 0.01, 0.1, 1, and 10 s before cooling (from left to right) are indifferent and

demonstrate that the number of self-nuclei obviously is not a function of the annealing time. Additional analysis of the crystallization-peak temperature revealed a value of 142 °C, independent on the melt-residence time. As such, it is concluded that the number of self-nuclei is mainly controlled by the temperature, and that the temperature-controlled destruction of self-nuclei proceeds at a time scale faster than 0.01 s.

3.7. Crystal morphology of melt-recrystallized PA 11 initially containing nodules or lamellae and spherulites

The AFM images of Fig. 2 provided information that cold-crystallization around 60 °C led to formation of nodules while isothermal melt-crystallization at 150 °C yielded formation of lamellae and spherulites. The observation of such qualitatively different crystal morphologies is caused by different mechanisms of crystal nucleation and the much higher nuclei density when crystallizing PA 11 at high supercooling of the melt. Regardless of the different initial crystal morphology, melt-recrystallization is faster than melt-crystallization at identical conditions, at least when the melt of initially semicrystalline PA 11 was not heated to above a critical temperature. In case of PA 11 initially containing lamellae and spherulites, the concentration of self-nuclei is distinctly higher than the density of nuclei which led to formation of the initial structure. This observation is in agreement with early self-nucleation studies [21,22], and confirms that intra-spherulitic structural features in the initial structure act as nucleation points on melt-recrystallization, as demonstrated by specific self-nucleation experiments on isotactic polystyrene [47].

For the system initially containing nodules, though the melt-recrystallization rate due to presence of self-nuclei between T_m and $T_m + 12$ K is higher than the rate of melt-crystallization, we observed that the self-nuclei concentration is much lower than the initial number of nodules/homogeneous crystal nuclei. This conclusion is derived from the detection of spherulitic structures/birefringent domains in POM after melt-recrystallization in presence of self-nuclei (see Fig. 8, POM images after exposing the melt to temperatures between 178 and 180 °C), but not before, in the initial state (see Fig. 5 in Ref. [46]). To

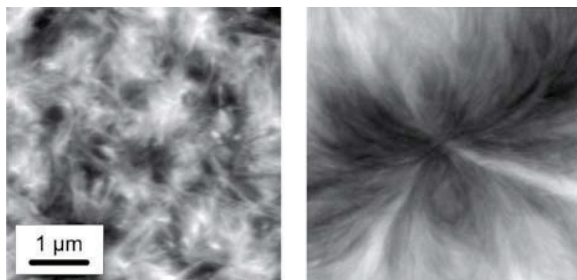


Fig. 11. AFM height images of PA 11 melt-recrystallized in presence of self-nuclei. The left image was taken on a sample which initially contained nodules, while the right image was taken on a sample which initially contained lamellae.

confirm the lower number of self-nuclei compared to the number of nuclei which led to the initial structure shown to the left of Fig. 2, AFM imaging after melt-recrystallization was performed.

Fig. 11 shows with the left image the morphology of melt-recrystallized PA 11 which initially contained nodules, and with the right image, for comparison, the morphology of melt-recrystallized PA 11 which initially contained lamellae. For the system initially containing lamellae and spherulites, qualitatively similar structures are observed before and after melt-crystallization in presence of self-nuclei (see right images in Figs. 2 and 11). In case of the initially nodular sample, due to the destruction of numerous homogeneous nuclei present at the cold-crystallization temperature of 60 °C on melting the nodules, after melt-recrystallization crystals of lamellar shape are observed. These lamellae are much shorter than on crystallization of the relaxed melt but form clusters, or small spherulite-like structures, detectable by POM.

4. Conclusions

Self-nuclei supported recrystallization of the crystal-free melt of PA 11 of qualitatively different initial semicrystalline morphology, either containing nodular crystals or spherulitically grown lamellar crystals, has been investigated for the first time. Nodular crystals were formed at high supercooling of the relaxed melt from a large number of homogeneous crystal nuclei while spherulites and lamellae were formed at low supercooling of the melt from a much lower number of heterogeneous nuclei. Though the temperatures of crystallization the relaxed melt to obtain samples of different semicrystalline morphology, that is, nodules grown from a large number of homogeneous nuclei and lamellae and spherulites grown from few heterogeneous nuclei, were largely different (60 °C and 150 °C, respectively), heating at 100 K/s allowed reorganization of both nodules and lamellae leading to similar melting temperatures without changing the semicrystalline morphology in terms of the crystal shape and surface-to-volume ratio. As such it was possible to analyze the melt-recrystallization behavior of PA 11 crystals of similar melting temperature but different habit and superstructure, grown from a largely different number of primary crystal nuclei.

The study of the melt-recrystallization behavior included the analysis of its kinetics, and the determination of the stability and number of self-nuclei. At identical difference between the melting temperature of nodules and lamellae on one side and melt-annealing temperature on the other side, melt-recrystallization of PA 11 initially containing nodules is much faster than melt-recrystallization of PA 11 initially containing lamellae and spherulites. This observation proves a distinct signature/memory of the initial semicrystalline morphology on melt-recrystallization such that the initially higher number of independently grown nodules, compared to spherulitically grown lamellae, leads to a higher number of self-nuclei. Besides the higher number of nodular crystals compared to lamellae, which we consider being the

main reason for enhanced self-nucleation, we furthermore suggest that enhanced coupling of nodular crystals with the surrounding amorphous phase contributes to the experimental observation. The small nodular crystals exhibit a much larger specific crystal surface area than laterally extended lamellae, which obviously stabilize crystal remnants and hinder fast isotropization of the melt. Strong covalent coupling of the initial nodular mesophase to the amorphous surrounding is detected by a large rigid amorphous fraction [48], though information whether reorganization during heating leads to a change of the surface structure is not yet available.

Compared to the number of primary homogeneous crystal nuclei on initial formation of nodules from the relaxed melt, the number of self-nuclei after their melting is lower, as proven by their growth to short lamellae and formation of domains visible in optical microscopy, which only is possible if nuclei are sufficiently distant. In turn, the number of self-nuclei in PA 11 initially containing lamellae and spherulites is higher than the number of heterogeneous nuclei which led to the initial formation of the spherulitic semicrystalline morphology, that is, intra-spherulitic structural features serve as self-nuclei.

Acknowledgments

KJ and RA are grateful for support by the European Social Funds.

References

- [1] Arkema, Rilsan® polyamide 11 resins. <https://www.extremematerials-arkema.com/en/product-families/rilsan-polyamide-11-family/>. (Accessed 15 May 2019).
- [2] W. Romão, E.V.R. Castro, E.A.S. Filho, R.C.L. Guimarães, A.L.N. Silva, S.C. S. Teixeira, M.A. de Paoli, G.L. de Sena, Ageing of polyamide 11 used in the manufacture of flexible piping. *J. Appl. Polym. Sci.* 114 (2009) 1777–1783.
- [3] K.A.A. Halim, J.B. Farrell, J.E. Kennedy, Preparation and characterisation of polyamide 11/montmorillonite (MMT) nanocomposites for use in angioplasty balloon applications. *Mater. Chem. Phys.* 143 (2013) 336–348.
- [4] Q. Zhang, Z. Mo, S. Liu, H. Zhang, Influence of annealing on structure of Nylon 11. *Macromolecules* 33 (2000) 5999–6005.
- [5] G.F. Schmidt, H.A. Stuart, Gitterstrukturen mit räumlichen Wasserstoffbrückensystemen und Gitterumwandlungen bei Polyamiden. *Z. Naturforschung A* 13 (1958) 222–225.
- [6] Q. Zhang, Z. Mo, H. Zhang, S. Liu, S.Z.D. Cheng, Crystal transitions of Nylon 11 under drawing and annealing. *Polymer* 42 (2001) 5543–5547.
- [7] S.S. Nair, C. Ramesh, K. Tashiro, Polymorphism in nylon-11: characterization using HTWAXS and HTFTIR. *Macromol. Symp.* 242 (2006) 216–226.
- [8] A. Mollova, R. Androsch, D. Mileva, C. Schick, A. Benhamida, Effect of supercooling on crystallization of polyamide 11. *Macromolecules* 46 (2013) 828–835.
- [9] A.M. Rhoades, N. Wonderling, C. Schick, R. Androsch, Supercooling-controlled heterogeneous and homogenous crystal nucleation of polyamide 11 and its effect onto the crystal/mesophase polymorphism. *Polymer* 106 (2016) 29–34.
- [10] R. Brill, Beziehungen zwischen Wasserstoffbindung und einigen Eigenschaften von Polyamiden. *Macromol. Chem. Phys.* 18 (1956) 294–309.
- [11] H.J. Radusch, M. Stolp, R. Androsch, Structure and temperature-induced structural changes of various polyamides. *Polymer* 35 (1994) 3568–3571.
- [12] J. Pepin, V. Miri, J.M. Lefebvre, New insights into the Brill transition in polyamide 11 and polyamide 6. *Macromolecules* 49 (2016) 564–573.
- [13] B. Wunderlich, The ATHAS database on heat capacities of polymers. *Pure Appl. Chem.* 67 (2009) 1019–1026.
- [14] M. Inoue, Studies on crystallization of high polymers by differential thermal analysis. *J. Polym. Sci.* 1 (1963) 2697–2709.
- [15] J.H. Magill, Formation of spherulites in polyamides. IV. Even-odd polyamides and poly(ω -aminocarboxylic acids). *J. Polym. Sci.* 7 (1969) 123–142.
- [16] K. Jariyavidyanont, W. Focke, R. Androsch, Thermal properties of biobased polyamide 11, in: M.L. Di Lorenzo, R. Androsch (Eds.), *Thermal Properties of Bio-Based Polymers*. *Adv. Polym. Sci.*, https://doi.org/10.1007/12_2019_47.
- [17] R. Androsch, C. Schick, Crystal nucleation of polymers at high supercooling of the melt, in: F. Auriemma, G.C. Alfonso, C. de Rosa (Eds.), *Polym. Cryst. I. Adv. Polym. Sci.*, Springer, 2015, pp. 257–288, 276.
- [18] A. Toda, R. Androsch, C. Schick, Insights into polymer crystallization and melting from fast scanning chip calorimetry. *Polymer* 91 (2016) 239–263.
- [19] I. Kolesov, R. Androsch, D. Mileva, W. Lebek, A. Benhamida, M. Kaci, W. Focke, Crystallization of a polyamide 11/organo-modified montmorillonite nanocomposite at rapid cooling. *Colloid Polym. Sci.* 291 (2013) 2541–2549.
- [20] D.J. Blundell, A. Keller, A.J. Kovacs, A new self-nucleation phenomenon and its application to the growing of polymer crystals from solution. *J. Polym. Sci. B* 4 (1966) 481–486.
- [21] B. Fillon, J.C. Wittmann, B. Lotz, A. Thierry, Self-nucleation and recrystallization of isotactic polypropylene (α phase) investigated by differential scanning calorimetry. *J. Polym. Sci. B* 31 (1993) 1383–1393.

- [22] R.M. Michell, A. Mugica, M. Zubitur, A.J. Müller, Self-nucleation of crystalline phases within homopolymers, polymer blends, copolymers, and nanocomposites, in: F. Auremma, G.C. Alfonso, C. de Rosa (Eds.), *Polym. Cryst. I. Adv. Polym. Sci.*, Springer, 2015, pp. 215–256, 276.
- [23] S. Yamazaki, M. Hikosaka, A. Toda, I. Wataoka, F. Gu, Role of entanglement in nucleation and 'melt relaxation' of polyethylene, *Polymer* 43 (2002) 6585–6593.
- [24] S. Yamazaki, F. Gu, K. Watanabe, K. Okada, A. Toda, M. Hikosaka, Two-step formation of entanglement from disentangled polymer melt detected by using nucleation rate, *Polymer* 47 (2006) 6422–6428.
- [25] A.A. Minakov, D.A. Mordvintsev, C. Schick, Melting and reorganization of poly (ethylene terephthalate) on fast heating (1000 K/s), *Polymer* 45 (2004) 3755–3763.
- [26] R. Androsch, E. Zhuravlev, C. Schick, Solid-state reorganization, melting and melt-recrystallization of conformationally disordered crystals (α' -phase) of poly (l-lactic acid), *Polymer* 55 (2014) 4932–4941.
- [27] Y. Furushima, S. Kumazawa, H. Umetsu, A. Toda, E. Zhuravlev, C. Schick, Melting and recrystallization kinetics of poly(butylene terephthalate), *Polymer* 109 (2017) 307–314.
- [28] K. Jariyavidyanont, R. Androsch, C. Schick, Crystal reorganization of poly (butylene terephthalate), *Polymer* 124 (2017) 274–283.
- [29] S. Schneider, X. Drujon, B. Lotz, J.C. Wittmann, Self-nucleation and enhanced nucleation of polyvinylidene fluoride (α -phase), *Polymer* 42 (2001) 8787–8798.
- [30] A.T. Lorenzo, M.L. Arnal, J.J. Sánchez, A.J. Müller, Effect of annealing time on the self-nucleation behavior of semicrystalline polymers, *J. Polym. Sci. B* 44 (2006) 1738–1750.
- [31] E. Turska, S. Gogolewski, Study on crystallization of nylon 6 (polycapramide). III. Effect of "crystalline memory" on crystallization kinetics, *J. Appl. Polym. Sci.* 19 (1975) 637–644.
- [32] H. Li, R. Guo, Y. Liu, S. Liu, E. Proniewicz, L.M. Proniewicz, Y. Zhao, Y. Xu, J. Wu, Self-nucleation-induced nonisothermal crystallization of nylon 6 from the melt, *J. Appl. Polym. Sci.* 132 (2015), <https://doi.org/10.1002/app.42413>.
- [33] D.S. Homminga, B. Goderis, V.B.F. Mathot, G. Groeninckx, Crystallization behavior of polymer/montmorillonite nanocomposites. Part III. Polyamide-6/montmorillonite nanocomposites, influence of matrix molecular weight, and of montmorillonite type and concentration, *Polymer* 47 (2006) 1630–1639.
- [34] J. Song, Q. Chen, M. Ren, X. Sun, H. Zhang, H. Zhang, Z. Mo, Effect of partial melting on the crystallization kinetics of nylon-1212, *J. Polym. Sci. B* 43 (2005) 3222–3230.
- [35] K. Jariyavidyanont, A. Janke, R. Androsch, Crystal self-nucleation in polyamide 11, *Thermochim. Acta* 677 (2019) 139–143.
- [36] X. Chen, A. Mamun, R.G. Alamo, Effect of level of crystallinity on melt memory above the equilibrium melting temperature in a random ethylene 1-butene copolymer, *Macromol. Chem. Phys.* 216 (2015) 1220–1226.
- [37] C. Schick, R. Androsch, Nucleation-controlled semicrystalline morphology of bulk polymers, *Polym. Cryst. 1* (2018), <https://doi.org/10.1002/pcr2.10036>.
- [38] Arkema, Materials database. <https://www.extremematerials-arkema.com/en/materials-database/products/datasheet/Rilsan%C2%AE%20BESNO%20TL>. (Accessed 15 May 2019).
- [39] T.D. Fornes, D.R. Paul, Structure and properties of nanocomposites based on nylon-11 and -12 compared with those based on nylon-6, *Macromolecules* 37 (2004) 7698–7709.
- [40] Q. Zia, R. Androsch, H.J. Radusch, E. Ingolić, Crystal morphology of rapidly cooled isotactic polypropylene: a comparative study by TEM and AFM, *Polym. Bull.* 60 (2008) 791–798.
- [41] R. Androsch, A.M. Rhoades, I. Stolte, C. Schick, Density of heterogeneous and homogeneous crystal nuclei in poly(butylene terephthalate), *Eur. Polym. J.* 66 (2015) 180–189.
- [42] D. Mileva, I. Kolesov, R. Androsch, Morphology of cold-crystallized polyamide 6, *Colloid Polym. Sci.* 290 (2012) 971–978.
- [43] A.M. Gohn, A.M. Rhoades, N. Wonderling, T. Tighe, R. Androsch, The effect of supercooling of the melt on the semicrystalline morphology of PA 66, *Thermochim. Acta* 655 (2017) 313–318.
- [44] S. van Herwaarden, E. Iervolino, F. van Herwaarden, T. Wijffels, A. Leenaers, V. Mathot, Design, performance and analysis of thermal lag of the UFS1 twin-calorimeter chip for fast scanning calorimetry using the Mettler-Toledo Flash DSC 1, *Thermochim. Acta* 522 (2011) 46–52.
- [45] A. Toda, M. Konishi, An evaluation of thermal lags of fast-scan microchip DSC with polymer film samples, *Thermochim. Acta* 589 (2014) 262–269.
- [46] K. Jariyavidyanont, C. Schick, R. Androsch, Nucleation-controlled dual semicrystalline morphology of polyamide 11, *Polym. Int.* 68 (2019) 263–270.
- [47] A. Mamun, S. Umamoto, N. Okui, N. Ishihara, Self-seeding effect on primary nucleation of isotactic polystyrene, *Macromolecules* 40 (2007) 6296–6303.
- [48] R. Androsch, K. Jariyavidyanont, C. Schick, Enthalpy relaxation of polyamide 11 of different morphology far below the glass transition temperature, *Entropy* 21 (2019) 984. <https://doi.org/10.3390/e21100984>.

4.5 Kinetics of homogeneous crystal nucleation of polyamide 11 near the glass transition temperature

Katalee Jariyavidyanont¹, Evgeny Zhuravlev², Christoph Schick^{2,3}, René Androsch¹

¹ Interdisciplinary Center for Transfer-oriented Research in Natural Sciences, Martin Luther University Halle-Wittenberg, Halle/Saale, Germany.

² Institute of Physics, University of Rostock, Rostock, Germany.

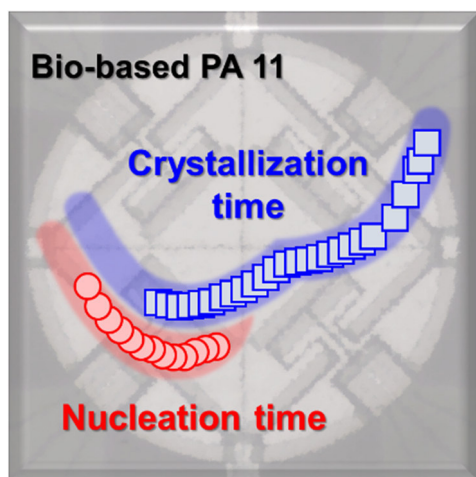
³ Department of Physical Chemistry, Kazan Federal University, Kazan, Russia.

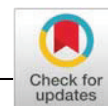
Polymer Crystallization 2020, 4, e10149, reproduced with permission from Wiley.

Research highlights

1. The rate of homogeneous crystal nucleation of PA 11 was analyzed using FSC and Tammann's two-stage crystal nuclei development method.
2. The critical cooling rates for suppressing crystallization and nucleation are around 1000 and 30,000 K s⁻¹, respectively.
3. Crystal nucleation is fastest at around 60 °C and begins after few milliseconds, which is about one order of magnitude shorter than the time of first observation of crystals or mesophase.

Graphical abstract





Kinetics of homogeneous crystal nucleation of polyamide 11 near the glass transition temperature

Katalee Jariyavidyanont¹ | Evgeny Zhuravlev² | Christoph Schick^{2,3} | René Androsch¹

¹Interdisciplinary Center for Transfer-oriented Research in Natural Sciences, Martin Luther University Halle-Wittenberg, Halle/Saale, Germany

²Institute of Physics, University of Rostock, Rostock, Germany

³Department of Physical Chemistry, Kazan Federal University, Kazan, Russia

Correspondence

Katalee Jariyavidyanont and René Androsch, Interdisciplinary Center for Transfer-oriented Research in Natural Sciences, Martin Luther University Halle-Wittenberg, 06099 Halle/Saale, Germany.

Email: katalee.jariyavidyanont@iw.uni-halle.de (K. J.) and rene.androsch@iw.uni-halle.de (R. A.)

Funding information

European Social Fund; Ministry of Education and Science of the Russian Federation, Grant/Award Number: 14.Y26.31.0019

Abstract

In this work, the kinetics of formation of homogeneous crystal nuclei of polyamide 11 (PA 11) near the glass transition temperature (T_g), which is slightly above ambient temperature, has been analyzed using fast scanning chip calorimetry (FSC), employing Tammann's two-stage crystal nuclei development method with non-isothermal and isothermal nucleation and growth stages. The critical cooling rate above which formation of an ordered phase (crystals or mesophase) is suppressed is around 1000 K/s. Formation of nuclei, in contrast, can only be prevented by cooling the melt faster than about 30,000 K/s to far below T_g . The temperature of fastest formation of crystal nuclei is about 10–15 K higher than T_g , with first detection of nuclei within less than a millisecond. As such, the onset-time of nuclei formation is about one order of magnitude shorter than the time of first observation of crystals/mesophase. Furthermore, annealing experiments performed below T_g revealed glass-crystallization, with the stability of the formed ordered phase limited to temperatures near T_g . Since rapid cooling and solidification of the melt of PA 11 at low temperatures often occurs in processing of this material, this work provides new insights into processing-controlled structure formation, eventually being beneficial for tailoring the property profile.

KEYWORDS

crystal nucleation, crystallization, fast scanning chip calorimetry, polyamide 11

1 | INTRODUCTION

Polyamide 11 (PA 11) is an environment-friendly polymer since it is derived from short-term renewable castor oil. It has been commercialized more than 70 years ago under the trade name RILSAN and nowadays various grades are available to the markets for a wide range of applications.^{1,2} It shows excellent impact resistance at room temperature as well as at very low temperature up to -40 °C, good dimensional stability due to low-moisture absorption, and good chemical and abrasion resistance.³ Thus, it is used for high-performance engineering applications such as in off- and on-shore oil and gas industries, automotive industry, for electrical and electronic components, tubing and coatings.³

PA 11 is a semicrystalline polymer with its property profile controlled by the semicrystalline morphology, including crystallinity, and structure, size, shape, and higher order organization of crystals. These parameters of the morphology depend on the crystallization conditions, particularly the supercooling of the melt before crystallization. Typically, crystallization at low and high supercooling of the melt proceeds via heterogeneous and homogeneous nucleation, respectively, with drastic consequences on morphology and properties.^{4–8} For many polymers including PA 11, it has been shown that crystallization at low supercooling of the melt allows for spherulitic growth of lamellae due to the rather low number of heterogeneous nuclei. In contrast, at high supercooling of the melt, the large number of homogeneous nuclei often causes formation of non-isothermal crystals.⁹ Quantitative

information about temperature ranges of predominant heterogeneous and homogeneous nucleation was gained by fast scanning chip calorimetry (FSC).^{10–13} Similar as for many other crystallizable polymers, such as isotactic polypropylene (iPP),^{10,14,15} poly(ϵ -caprolactone) (PCL),¹⁶ polyamide 66 (PA 66),^{17,18} or poly(butylene terephthalate) (PBT),^{19–21} FSC revealed a bimodal temperature-dependence of the overall crystallization rate indicative of different nucleation mechanisms, in particular if FSC is combined with microscopy.^{22–24} However, quantitative data about the kinetics of homogeneous nucleation cannot be gained by simple analysis of crystallization rates requiring more sophisticated approaches like Tammann's two-stage nuclei development method.^{25,26} The reason is the impossibility of direct detection of nuclei. Tammann's nuclei development method implies formation of homogeneous nuclei at high supercooling of the melt, or in the glass, and their development to crystals at higher temperatures. This scheme, so far, has been applied for analysis of the kinetics of nuclei formation of PCL,^{16,27} poly(L-lactic acid) (PLLA),^{28–30} poly(ethylene terephthalate) (PET),³¹ poly(butylene isophthalate) (PBI),^{32,33} polyamide 66 (PA 66),^{34,35} or polyamide 6 (PA 6).³⁶ For PA 11, data are not available.

Regarding crystallization of PA 11, it was found that at low supercooling of the melt pseudo-hexagonal δ -crystals form, which reversibly transform into stable triclinic α -crystals at the Brill transition temperature of about 100 °C.^{37–40} In contrast, metastable pseudo-hexagonal δ' -crystals are obtained at high supercooling of the melt.⁴¹ As mentioned above, the crystallization rate of PA 11 shows a bimodal temperature-dependence with a cross-over temperature between the two nucleation mechanisms at about 110 °C and high- and low-temperature crystallization rate maxima, corresponding to characteristic crystallization times of about 1 and 0.05 s, at around 120 and 65 °C, respectively.³⁹ In case of non-isothermal crystallization, high-temperature crystallization fades on cooling faster than few 10 K/s, allowing for low-temperature mesophase formation (δ' -crystals) if the cooling rate does not exceed 600 K/s.⁴² It should be noted that the cross-over temperature and high-temperature maximum of the crystallization rate, as well as the cooling rate at which high-temperature crystallization diminishes, depend on heterogeneous nucleating agents or additives; the above-reported values hold for the specific PA 11 grade used in the present work. If the cooling rate is faster than about 1000 K/s, the melt completely vitrifies at the glass transition temperature (T_g) of around 45 °C.

Information about possible nuclei formation on cooling faster than 1000 K/s is not available. However, a cold-crystallization peak is typically observed when heating the glassy and crystal-free sample to above T_g ,^{43,44} indicative of nuclei formation during prior cooling and/or annealing the glass, which is not quantified yet. Such thermal profiles, that is, fast cooling of the melt followed by annealing the glass slightly below T_g is often observed in industrial processing of this material, for example injection molding. Here, depending on the component geometry/wall thickness and molding parameters, cooling rates up to several 100 K/s may be observed,^{45–47} perhaps suppressing crystallization but permitting formation of nuclei which might grow to crystals over long time, causing, for example, aging/

change of properties.^{48,49} Classical enthalpy relaxation of the glass has been treated in a separate study⁴⁴ and crystal formation below T_g has been proven for another representative of the polyamide family, namely PA 6.³⁶

Therefore, in this work, we attempt obtaining rates of homogeneous nucleation for PA 11 at temperatures near T_g by using Tammann's nuclei development method. In the first part, non-isothermal experiments are described, serving for determination of critical cooling and heating rates for suppressing both formation of nuclei and crystals. In the second part, isothermal experiments are presented for observation of nucleation rates at temperatures around T_g . We employed two different fast scanning chip calorimeters, for performing scanning experiments covering rates of temperature change from 10 to 100,000 K/s.

2 | EXPERIMENTAL

2.1 | Material

Bio-based PA 11 RILSAN BESNO-TL (Arkema, France) was used in this work. It is a natural grade containing heat and light stabilizers, and lubricant, and is designed for processing by extrusion.⁵⁰ The melt-flow volume index, mass-average molar mass, and polydispersity are 1 cm³/10 min (235 °C, 2.16 kg),⁵⁰ 17.2 kg/mol, and 2,⁵¹ respectively.

2.2 | Fast scanning chip calorimetry

Non-isothermal and isothermal experiments for analysis of critical cooling and heating rates for nuclei formation, and of the crystal nucleation rate of PA 11 were performed using a fast scanning chip calorimeter Flash DSC 1 (Mettler-Toledo, Switzerland) and a home-made super-fast scanning nano-calorimeter (Functional Materials Rosstock e.V., Germany).

The Flash DSC 1, using a UFS 1 chip sensor, was connected to a Huber TC100 intracooler. The furnace was purged with nitrogen gas at a flow rate of 40 ml/min to avoid sample degradation. The sensor was conditioned and temperature-corrected according to the instrument operating instructions before loading a specimen. The as-received pellets were prepared using a Slee rotary microtome to obtain thin sections with a thickness about 10 μ m, and afterwards a scalpel and a stereomicroscope were used to cut the thin sections to obtain smaller specimens with a lateral size of about 50–100 μ m and a typical mass between 10 and 100 ng. Before loading a specimen on the central part of the heatable area of the chip sensor where a homogeneous temperature profile is expected,⁵² a thin layer of silicon oil was applied. This was followed by adding a thin gold leaf to reduce the effects of shrinkage and expansion of the specimen during repeated cooling and heating.⁵³ Furthermore, the use of the gold leaf facilitated easy removal of the specimen; therefore, the chip sensor was used for several specimens. The Mettler-Toledo Flash DSC 1 was employed for analyses using heating rates up to 10,000 K/s.

Super-fast scanning nano-calorimetry using a thin film chip sensor XI-395 (Xensor Integration, Netherlands) was employed in this work for higher scanning rates between 10,000 and 100,000 K/s. Details of the device and data treatment are reported elsewhere.^{54,55} A small piece of the polymer was manually cut from the pellet and placed directly onto the heatable area of the sensor. The masses of the samples were about 2 and 15 ng.

In addition, the kinetics of isothermal melt-crystallization of PA 11 at different temperature was investigated using the Flash DSC 1. The sample was melted by heating to 220 °C, held at this temperature for 0.5 s, and then cooled at a rate of 1000 K/s to crystallization temperatures between 50 and 150 °C. Peak-time of crystallization was collected from the crystallization-induced exothermic heat flow overtime. Detection of exothermic heat flow on crystallization at temperatures higher than 150 °C was difficult, therefore another approach to obtain information about crystallization kinetics was performed. The isothermal crystallization process was interrupted at predefined crystallization times, and then the fraction of formed crystals by their enthalpies of cold-crystallization and melting during subsequent heating was evaluated. The half-time of crystallization was estimated from the time needed to reach 50% relative crystallinity.

3 | RESULTS AND DISCUSSION

3.1 | Non-isothermal nucleation and crystallization experiments

Non-isothermal experiments were performed for obtaining critical cooling and heating rates for suppressing formation of crystals and nuclei, following the procedure described in Reference 16. The temperature–time profile is shown in Figure 1. The specimen was heated to 220 °C, which is above the equilibrium melting temperature ($T_{m,0}$) of PA 11,^{56,57} and equilibrated at this temperature for 0.5 s. Then, the melt was cooled at different rates between 10 and 100,000 K/s to below T_g , and subsequently the sample was heated at a fixed rate between 100 and 30,000 K/s. Enthalpies of cold-

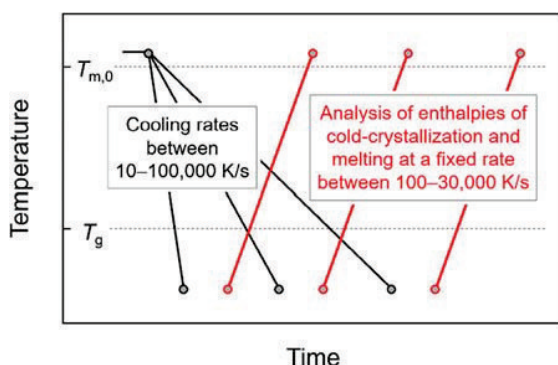


FIGURE 1 Temperature–time profile for obtaining critical cooling and heating rates for suppressing crystal and nuclei formation

crystallization and melting were analyzed from the heating scans in order to detect nuclei and crystal formation. Worth noting, similar experiments have been performed on different classes of materials including metallic glasses.⁵⁸

Figure 2 shows an example of FSC curves in apparent heat capacity units ($\text{mW}/[\text{K/s}] = \text{mJ}/\text{K}$) obtained during heating PA 11 at different rates of 5000 (top), 3000 (middle), and 1000 K/s (bottom), after cooling the melt at rates given in the legend. Curves associated to prior cooling between 10 and 100 K/s, 200 and 1000 K/s, and 2000 and 10,000 K/s are presented in red, green, and blue color, respectively. Regarding the experiment employing a heating rate of 1000 K/s (bottom set of curves), the heating scan of the sample quenched at 10,000 K/s (bold blue curve) shows a glass transition step at around 45 °C, a cold-crystallization peak at around 80 °C, and a single endothermic peak associated to melting of crystals formed during cold-crystallization at around 160 °C. The cold-crystallization enthalpy reduces on lowering the cooling rate, while the enthalpy of melting increases, indicating formation of crystals during cooling. The cold-crystallization peak disappears if the melt is cooled at rates lower than 200 K/s (red curves), and the endothermic peak on further heating is caused by melting of crystals formed during cooling.

Note that the shift of the melting-peak temperature to higher temperature on cooling at rates lower than 40 K/s (thin red curves) presumably/likely is caused by the increased crystallization temperature during cooling. With increasing heating rate (center and top sets of curves), the area of the cold-crystallization peak decreases due to reduced crystal growth and perhaps reduced number of nuclei forming during heating. It should be noted that the cold-crystallization and melting peaks become broader and shift to higher temperatures, compared to the heating scans obtained using a rate of 1000 K/s, because of instrumental thermal lag and/or the kinetics of melting.^{11,59} Again, the data of Figure 2 represent an example only, since

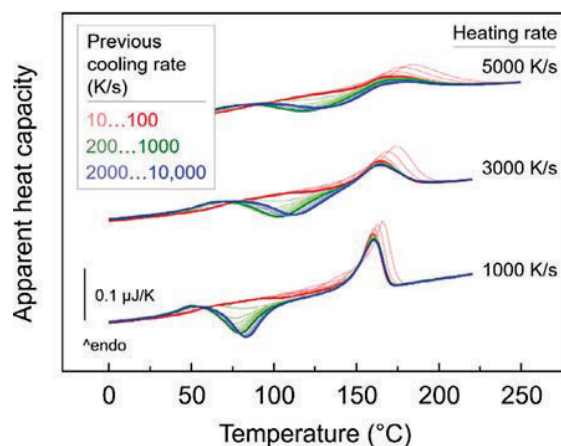


FIGURE 2 Apparent heat capacity as a function of temperature, obtained during heating PA 11 at rates of 5000 (top), 3000 (middle), and 1000 K/s (bottom), after cooling at different rates (Mettler-Toledo Flash DSC 1)

even higher cooling and heating rates up to 100,000 and 30,000 K/s, respectively, were applied to the samples using the super-fast nano-chip calorimeter, discussed below.

Figure 3 shows the total change of enthalpy (top part) and enthalpy of cold-crystallization (bottom part), obtained during heating PA 11 at rates between 100 and 50,000 K/s, as a function of the rate of prior cooling. The data collected by the Flash DSC 1 and the nano-chip calorimeter are presented by filled and open symbols, respectively. The total enthalpy change (filled and open squares) is equivalent to the enthalpy of crystallization during cooling and was obtained by integrating the FSC heating-curves covering the cold-crystallization and melting peaks. As expected, the total enthalpy change is independent on the heating rate. Crystallization at low supercooling of the melt at rates between 10 and 100 K/s leads to formation of crystals during cooling via heterogeneous nucleation^{38,42} and cold-crystallization on heating is not observed. On increasing the cooling rate (see gray arrow), melt-crystallization is gradually suppressed. Simultaneously, the enthalpy of cold-crystallization increases due to presence of increasing number of nuclei, which were not able to grow to crystals during cooling, regardless the heating rate (see black arrow). Formation of crystals during cooling, finally, is absent if the melt is cooled faster than 1000 K/s.

While the total change of enthalpy provides information about crystal formation during cooling, analysis of cold-crystallization permits gaining insight about nuclei formation. Heating of PA 11 slower than 50,000 to 100,000 K/s reveals a cold-crystallization peak as soon as crystallization is suppressed in the preceding cooling scan, starting at around 200 K/s. Heating faster than 50,000 K/s does not allow crystal growth, and cold-crystallization is therefore not observed, regardless presence of nuclei. If the heating rate is between 10,000

and 30,000 K/s, then with increasing cooling rate the cold-crystallization enthalpy first increases (up to a cooling rate of 1000 K/s) due to incomplete crystallization during cooling. Then, the cold-crystallization enthalpy decreases to almost zero at a cooling rate of about 50,000 K/s, due to the lowering of the number of nuclei forming during cooling. Note that there is detected minor cold-crystallization even on cooling faster than 50,000 K/s presumably due to presence of few heterogeneous nuclei (see for example open orange circles and dash line). Most important, the decrease of the cold-crystallization enthalpy when increasing the cooling rate from 1000 to 50,000 K/s reflects the kinetics of non-isothermal nuclei formation during cooling. In other words, cooling of PA 11 at rates as high as several 10,000 K/s still allows formation of homogeneous nuclei, increasing in number with decreasing cooling rate. If the heating rate is lower than 10,000 K/s, then the downturn of the enthalpy of cold-crystallization for samples cooled faster than 1000 K/s is much less pronounced and eventually completely absent (see e.g., data sets obtained at heating rates lower than 3000 K/s). The reason of this observation, we assume, is continued formation of homogeneous nuclei and crystal growth from both homogeneous and heterogeneous nuclei during rather slow heating. Note that we observed that with decreasing heating rate the cold-crystallization enthalpy increases to reach a maximum value of -40 J/g, which compares with the maximum enthalpy of crystallization of about $+40$ J/g after slow cooling.

Summarizing the data of Figure 3, it is concluded that the critical rates of cooling, below which crystallization on one side and homogeneous nucleation on the other side occur, are about 1000 and 30,000 K/s, respectively. In contrast, crystallization on heating even is allowed at higher rates than 1000 K/s due to nuclei formation below the cold-crystallization temperature. Crystallization on cooling faster

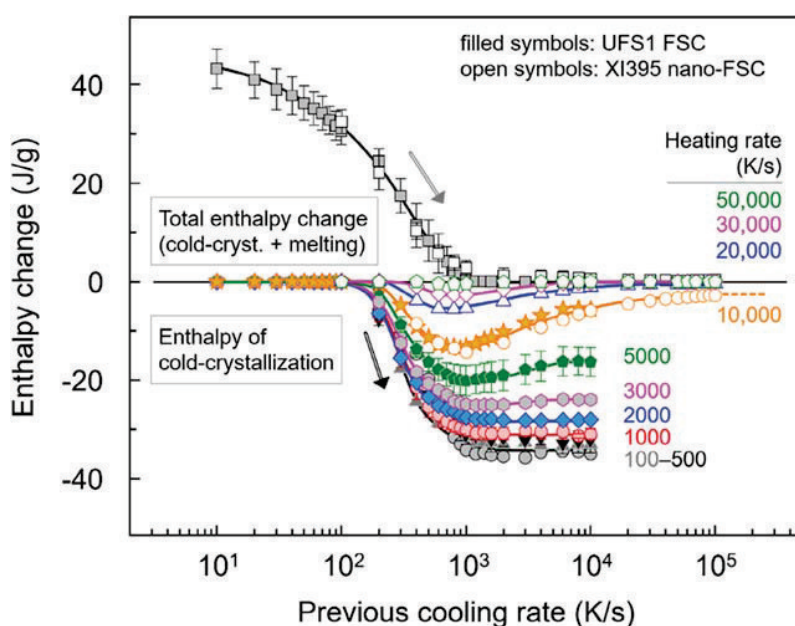


FIGURE 3 Total enthalpy change (top) and enthalpy of cold-crystallization (bottom) as a function of previous cooling rate (Mettler-Toledo Flash DSC 1 and the homemade super-fast scanning nano-calorimeter)

than 1000 K/s is suppressed since only heterogeneous nuclei can grow to crystals, which must be formed/present already at temperatures above the temperature of maximum crystal growth rate.

3.2 | Isothermal nucleation and crystallization experiments

Isothermal crystallization experiments were performed for analysis of the temperature-dependence of the characteristic time of crystal nucleation. Figure 4 shows the temperature–time protocol of the experiments. The melt was rapidly transferred from 220 °C to the annealing temperature using a cooling rate of 100,000 K/s to assure that there is no formation of both crystals and nuclei during cooling. Annealing was performed at temperatures between 17 and 77 °C, every 5 K, and the annealing time was between 0.1 ms and, depending on the annealing temperature, 200, 600, and 1000 s. After annealing, the sample was heated at a fixed rate of 20,000 K/s. Selection of the heating rate of 20,000 K/s is based on the FSC data shown in Figure 5, illustrating the effect of heating rate on nuclei formation during heating. Samples cooled at 100,000 K/s do not contain a detectable number of homogeneous crystal nuclei and consequently on heating at sufficiently high rate of 20,000 or 30,000 K/s, negligible cold-crystallization is detected. Slower heating at 10,000 K/s, in contrast, permits significant cold-crystallization on heating (see black curves in the corresponding data sets). Furthermore, the data prove that heating at 20,000 K/s is sufficiently fast to prevent additional nucleation during heating but still slow enough to allow crystallization, being a precondition for analysis of the nucleation rate according to Figure 4. The curves at 20,000 and 30,000 K/s confirm another precondition of the experiment, namely that the number of heterogeneous nuclei present in the particular sample is significantly smaller than the number of homogeneous nuclei. Otherwise, the cold-crystallization enthalpy would not tend to zero for the fastest

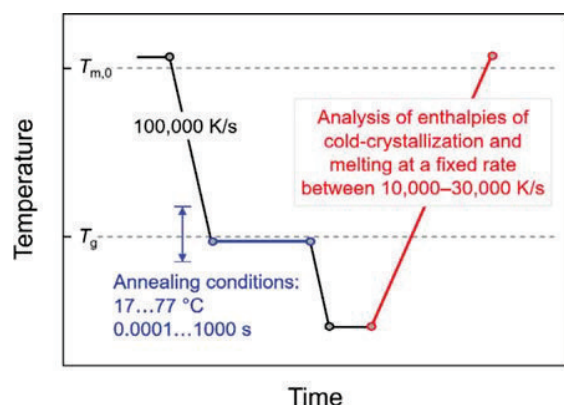


FIGURE 4 Temperature–time profile for analysis of the nucleation rate as a function of temperature. The horizontal dash lines indicate the approximate position of T_g and $T_{m,0}$

cooling rates. Finally, we preferred using a heating rate of 20,000 instead of 30,000 K/s since in the latter case crystal growth is more limited.

Figure 6 shows an example of FSC curves obtained during heating PA 11 at a rate of 20,000 K/s, after annealing for different times as indicated in the legend, at temperatures between 17 and 77 °C (top to bottom). Regarding the annealing experiment at 17 °C (top set of curves), zero annealing time (black curve) only shows negligible cold-crystallization and melting, perhaps due to presence of few heterogeneous nuclei. However, such negligible concentration of nuclei will not significantly influence the main results. For annealing times less than 1 s (gray curves), additional cold-crystallization and melting are not detected but an enthalpy recovery peak due to annealing of glassy PA 11, gradually increasing in size with annealing time. The cold-crystallization and the melting peaks slightly increase further in area if the annealing time is longer than 1 s (red curves). However, if the annealing time exceeds 6 s (blue curves), then the enthalpy recovery peak becomes superimposed by an additional sharp peak, presumably related to melting of small crystals formed at the annealing temperature, increasing in size and apparently shifting to higher temperature with annealing time. Melting of these tiny crystals leaves self-nuclei, which then recrystallize on further heating, causing exothermic heat flow and subsequent melting. Note that we did not observe in case of PA 11 such a distinct separation of enthalpy relaxation, crystal nucleation, and growth in the glassy state as observed, for example, in case of PA 6 or PCL.^{16,36}

With increasing annealing temperature, the low-temperature melting peak associated to melting of crystals formed during annealing obviously increases in size and shifts to higher temperature for a given annealing time. This result is expected since the melting temperature is controlled by the crystal size, which depends on the crystallization

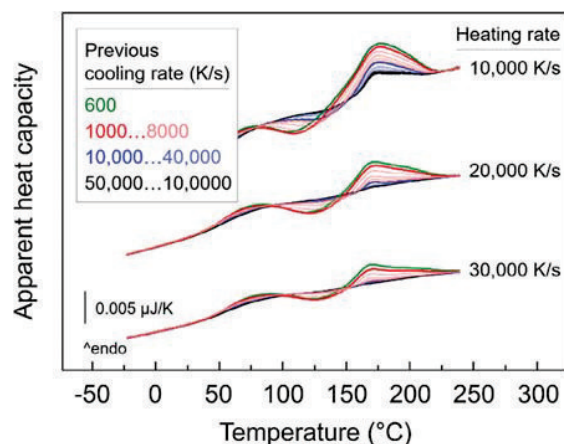


FIGURE 5 Apparent heat capacity as a function of temperature, obtained during heating PA 11 at rates of 10,000 (top), 20,000 (middle) and 30,000 K/s (bottom), after cooling at different rates as indicated in the legend. The data were collected using the chip nanocalorimeter

temperature. For a given annealing temperature, the low-temperature melting peak increases in temperature with annealing time due to the larger number of crystals (superposition of an endothermic and an exothermic peak, finally determining the peak shape) and/or the increase of their stability. In case melting at T_g is not observed, as it is true for short annealing times, subsequent cold-crystallization indicates isothermal formation of nuclei. If there is observed a low-temperature endothermic melting event slightly above T_g , then it is contiguously followed by an exothermic peak caused by recrystallization of the melt. Worthwhile noting that endothermic melting and exothermic recrystallization overlap such that analysis of enthalpy of cold-crystallization/melt-recrystallization is complicated. Exothermic cold-crystallization or melt-recrystallization finally is followed by a broad endothermic melting event of the crystals formed by recrystallization at around 175 °C.

The FSC heating curves of Figure 6 were quantitatively evaluated regarding the total change of enthalpy and cold-crystallization enthalpy, shown with the top and bottom data sets in Figure 7, respectively, as a function of the annealing time. However, in this plot only data are considered for which the exothermic event during

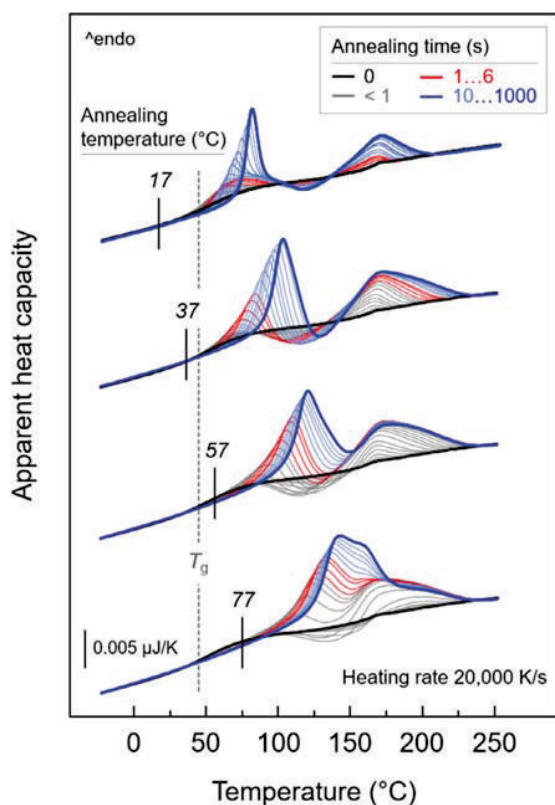


FIGURE 6 Apparent heat capacity as a function of temperature, obtained during heating PA 11 at a fixed rate of 20,000 K/s, after annealing between 17 and 77 °C (top to bottom) for different times. The dash-vertical line indicates T_g , as reported in the literature.⁵⁶

heating is unambiguously identified as cold-crystallization but not melt-recrystallization superimposed to prior low-temperature melting.

The latter is true for annealing experiments performed at temperatures lower than 47 °C. It is observed for the shown annealing conditions that the enthalpy of cold-crystallization begins to increase at a shorter annealing time than in case of the total change of enthalpy. For example, considering the data collected after annealing at 77 °C (blue stars), isothermal formation of nuclei starts at about 1 ms which causes on heating cold-crystallization. When the cold-crystallization enthalpy approaches its maximum value after annealing for about 40 ms, the total enthalpy change gradually increases, illustrating formation of crystals at the annealing temperature. The number of crystals increases if the annealing is continued, and as a result, cold-crystallization correspondingly reduces to vanish after annealing for about 0.1 s. In other words, after 0.1 s all nuclei grew to crystals during annealing, and the observed further increase of the crystallinity is related to secondary crystallization. Decreasing the annealing temperature allows for formation of a larger number of nuclei, as indicated with the higher maximum cold-crystallization enthalpy, beginning at even slightly shorter time than 1 ms. The trend does not hold for the annealing experiment at 47 °C (red circles) which, probably, is related to a dramatically reduced molecular mobility when approaching T_g , slowing down nucleation.

As a summary of the data of Figure 7, Figure 8 presents characteristic times of nucleation and crystallization of PA 11 as a function of temperature, indicated by red, and black/gray symbols, respectively. The characteristic crystallization times reveal a bimodal temperature-distribution associated to predominant heterogeneous (gray diamonds) and homogeneous (black squares) crystal nucleation at high and low temperatures, respectively. Characteristic times of

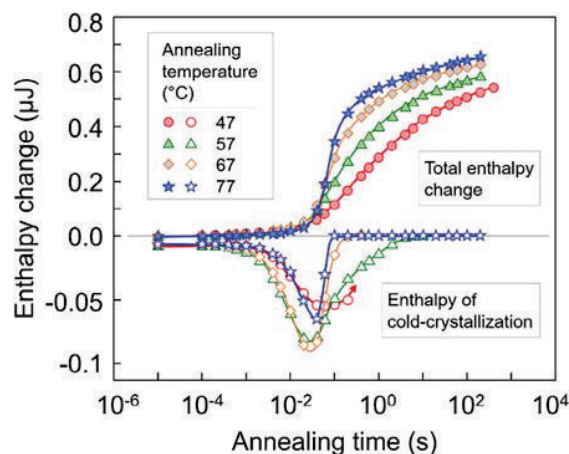
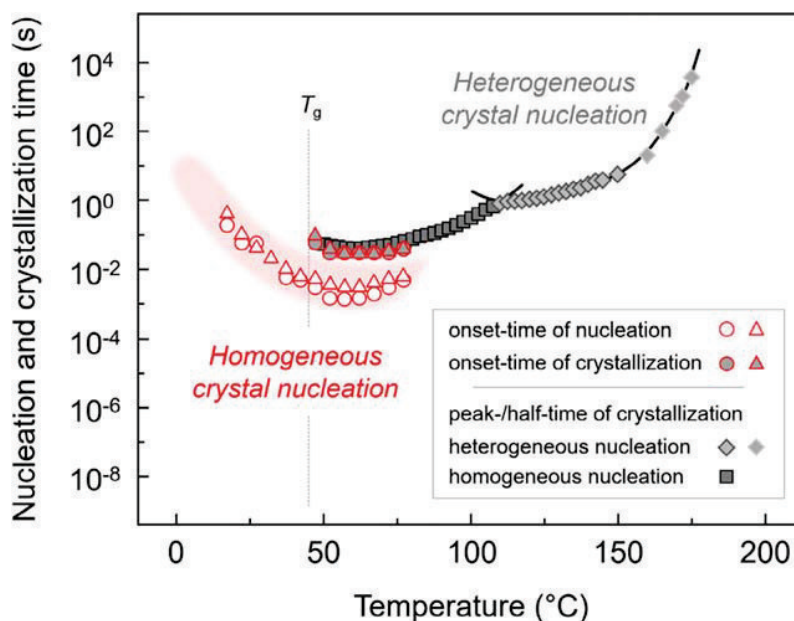


FIGURE 7 Enthalpy of cold-crystallization (bottom sets of data) and total enthalpy change (top sets of data), covering low-temperature melting, cold-crystallization or melt-recrystallization, and high-temperature melting, depending on the annealing temperature and time. The data were collected from the heating curves recorded at a fixed rate of 20,000 K/s

FIGURE 8 Characteristic time of nucleation (red symbols) and crystallization (black squares and gray diamonds) as a function of temperature. The data were evaluated from FSC heating scans recorded at rates of 20,000 (circles) and 30,000 K/s (triangles). The approximate position of T_g is indicated with the vertical dashed line



crystal nucleation were evaluated from FSC heating scans recorded at rates of 20,000 (circles) and 30,000 K/s (triangles) (see also Figure 4, red line), leading to similar results, as expected.

The data reveal that nucleation is fastest at around 60 °C, that is, at a temperature about 10–15 K higher than T_g . This generally expected behavior is also observed for other polymers such as PCL or PA 66 and other nonpolymeric materials, which similarly show the maximum rate of homogeneous nucleation at a temperature slightly above T_g .⁶⁰ The onset-time of nucleation, representing the begin of nucleation, is shown by the red-opened symbols and is about one order of magnitude shorter than the crystallization peak- or half-times. The gray-filled red-bordered symbols represent the time of the begin of crystallization, being close to the characteristic times of crystallization, proving the reliability of the data analysis performed here. Regarding the annealing experiments performed below T_g , only onset-times of nucleation are considered, due to above-described difficulties in data evaluation. Nevertheless, these glass-annealing experiments clearly proved nucleation and crystallization in the glass of PA 11.

4 | CONCLUSIONS

Crystallization and solidification of polymers including PA 11 in industrial processing often occurs at rapid cooling conditions, for example, in the skin layer of injection moldings. At such conditions, crystallization of PA 11 proceeds via homogeneous crystal nucleation leading to formation of a nodular mesophase surrounded by a rigid amorphous fraction. While morphological features of PA 11 processed at such conditions are well investigated, details about the kinetics of homogeneous crystal nucleation are not known. Such details, however, are

needed, for example, for judging the thermodynamic stability of fully vitrified PA 11, prepared on quenching the melt. Since the melt of PA 11 vitrifies at a temperature slightly above ambient, the glass is then highly unstable, being subject of enthalpy relaxation, crystal nucleation, and even crystal growth. As such, in the present work, the time scale of crystal nucleation at temperatures around the T_g is quantified, employing two different FSC, complementing each other regarding available scanning rate ranges from 10 to 100,000 K/s, and Tammann's two-stage nuclei development method. At a glance, crystal formation is suppressed when cooling the melt of PA 11 faster than 1000 K/s to below T_g , while crystal nucleation only becomes absent when cooling faster than 30,000 K/s. The temperature of fastest crystal nuclei formation is about 10–15 K higher than T_g , with first detection of nuclei within less than one millisecond. Annealing experiments performed below T_g revealed glass-crystallization, occurring at a timescale of few 100 s at room temperature. This result clearly proves that immediately after fast vitrification of the melt of PA 11, the sample is far from being metastable. In a broader context, the results agree with the observation on low molecular glass formers that nucleation and crystal growth at such deep supercooling is probably more controlled by local β -relaxation processes than by the α -relaxation (glass transition).^{61–64}

ACKNOWLEDGMENT

Katalee Jariyavidyanont and René Androsch acknowledge financial support by the European Structural and Investment Funds (ESF) and CS from the Ministry of Education and Science of the Russian Federation, grant 14.Y26.31.0019.

ORCID

Katalee Jariyavidyanont  <https://orcid.org/0000-0001-8240-126X>

REFERENCES

- [1] Arkema, Rilsan Polyamide 11 Resins, <https://www.extremematerials-arkema.com/en/product-families/rilsan-polyamide-11-family/> (accessed May 11, 2020).
- [2] M. Genas, *Angew. Chem.* **1962**, *74*, 535.
- [3] M. I. Kohan, M. I. Kohan, *Nylon Plastics Handbook*. Munich: Hanser/Gardner Publications, **1995**, p. 487.
- [4] D. P. Russell, P. W. R. Beaumont, *J. Mater. Sci.* **1980**, *15*, 197.
- [5] V. L. Carrubba, V. Brucato, S. Piccarolo, *Macromol. Symp.* **2002**, *180*, 43.
- [6] L. Shen, I. Y. Phang, T. Liu, *Polym. Test.* **2006**, *25*, 249.
- [7] Q. Zia, H.-J. Radusch, R. Androsch, *Polym. Bull.* **2009**, *63*, 755.
- [8] I. Kolesov, D. Mileva, R. Androsch, *Polym. Bull.* **2014**, *71*, 581.
- [9] C. Schick, R. Androsch, *Polym. Cryst.* **2018**, *1*, e10036.
- [10] F. De Santis, S. Adamovsky, G. Titomanlio, C. Schick, *Macromolecules* **2007**, *40*, 9026.
- [11] V. Mathot, M. Pyda, T. Pijpers, G. Vanden Poel, E. van de Kerkhof, S. van Herwaarden, F. van Herwaarden, A. Leenaers, *Thermochim. Acta* **2011**, *522*, 36.
- [12] A. Toda, R. Androsch, C. Schick, *Polymer* **2016**, *91*, 239.
- [13] Y. He, R. Luo, Z. Li, R. Lv, D. Zhou, S. Lim, X. Ren, H. Gao, W. Hu, *Macromol. Chem. Phys.* **2018**, *219*, 1700385.
- [14] C. Silvestre, S. Cimmino, D. Duraccio, C. Schick, *Macromol. Rapid Commun.* **2007**, *28*, 875.
- [15] J. E. K. Schawe, P. Pötschke, I. Alig, *Polymer* **2017**, *116*, 160.
- [16] E. Zhuravlev, J. W. P. Schmelzer, B. Wunderlich, C. Schick, *Polymer* **2011**, *52*, 1983.
- [17] A. M. Rhoades, J. L. Williams, R. Androsch, *Thermochim. Acta* **2015**, *603*, 103.
- [18] J. Faraj, N. Boyard, B. Pignon, J.-L. Bailleul, D. Delaunay, G. Orange, *Thermochim. Acta* **2016**, *624*, 27.
- [19] M. Pyda, E. Nowak-Pyda, J. Heeg, H. Huth, A. A. Minakov, M. L. Di Lorenzo, C. Schick, B. Wunderlich, *J. Polym. Sci., Part B: Polym. Phys.* **2006**, *44*, 1364.
- [20] R. Androsch, A. M. Rhoades, I. Stolte, C. Schick, *Eur. Polym. J.* **2015**, *66*, 180.
- [21] Y. Furushima, S. Kumazawa, H. Umetsu, A. Toda, E. Zhuravlev, A. Wurm, C. Schick, *J. Appl. Polym. Sci.* **2017**, *134*, 44739.
- [22] R. Androsch, M. L. Di Lorenzo, C. Schick, *Macromol. Chem. Phys.* **2018**, *219*, 1700479.
- [23] D. Mileva, R. Androsch, E. Zhuravlev, C. Schick, *Polymer* **2012**, *53*, 3994.
- [24] Y. Furushima, M. Nakada, A. Masuda, K. Okada, N. Iwata, M. Ohkura, *Polym. Cryst.* **2020**, *3*, e10102.
- [25] G. Tammann, *Z. für Phys. Chem.* **1898**, *25U*, 441.
- [26] G. Tammann, E. Jenckel, *Z. Anorg. Allg. Chem.* **1930**, *193*, 76.
- [27] E. Zhuravlev, J. W. P. Schmelzer, A. S. Abyzov, V. M. Fokin, R. Androsch, C. Schick, *Cryst. Growth Des.* **2015**, *15*, 786.
- [28] R. Androsch, M. L. Di Lorenzo, *Macromolecules* **2013**, *46*, 6048.
- [29] R. Androsch, M. L. Di Lorenzo, *Polymer* **2013**, *54*, 6882.
- [30] R. A. Andrianov, R. Androsch, R. Zhang, T. A. Mukhametzyanov, A. S. Abyzov, J. W. P. Schmelzer, C. Schick, *Polymer* **2020**, *196*, 122453.
- [31] R. Androsch, C. Schick, A. M. Rhoades, *Macromolecules* **2015**, *48*, 8082.
- [32] S. Quattrosoldi, R. Androsch, A. Janke, M. Soccio, N. Lotti, *Polymer* **2020**, *12*, 235.
- [33] S. Quattrosoldi, N. Lotti, M. Soccio, C. Schick, R. Androsch, *Polymer* **2020**, *12*, 1099.
- [34] R. Zhang, E. Zhuravlev, J. Schmelzer, R. Androsch, C. Schick, *Macromolecules* **2020**;53: 5560.
- [35] A. M. Anton, E. Zhuravlev, W. Kossack, R. Andrianov, C. Schick, F. Kremer, *Colloid Polym. Sci.* **2020**, *298*, 697. <https://doi.org/10.1007/s00396-020-04666-9>.
- [36] R. Androsch, C. Schick, J. W. P. Schmelzer, *Eur. Polym. J.* **2014**, *53*, 100.
- [37] R. Brill, *J. Für. Prakt. Chem.* **1942**, *161*, 49.
- [38] A. Mollova, R. Androsch, D. Mileva, C. Schick, A. Benhamida, *Macromolecules* **2013**, *46*, 828.
- [39] A. M. Rhoades, N. Wonderling, C. Schick, R. Androsch, *Polymer* **2016**, *106*, 29.
- [40] J. Pepin, V. Miri, J.-M. Lefebvre, *Macromolecules* **2016**, *49*, 564.
- [41] G. F. Schmidt, H. A. Stuart, *Z. für Naturforschung A* **1958**, *13*, 222.
- [42] K. Jariyavidyanont, C. Schick, R. Androsch, *Polym. Int.* **2019**, *68*, 263.
- [43] K. Jariyavidyanont, A. Janke, R. Androsch, *Polymer* **2019**, *184*, 121864.
- [44] R. Androsch, K. Jariyavidyanont, C. Schick, *Entropy* **2019**, *21*, 984.
- [45] A. M. Rhoades, J. L. Williams, N. Wonderling, R. Androsch, J. Guo, *J. Therm. Anal. Calorim.* **2017**, *127*, 939.
- [46] A. M. Gohn, A. M. Rhoades, D. Okonski, R. Androsch, *Macromol. Mater. Eng.* **2018**, *303*, 1800148.
- [47] K. Jariyavidyanont, J. L. Williams, A. M. Rhoades, I. Kühnert, W. Focke, R. Androsch, *Polym. Eng. Sci.* **2018**, *58*, 1053.
- [48] H. M. Naeem Iqbal, C. Sungkapreecha, R. Androsch, *Polym. Bull.* **2017**, *74*, 2565.
- [49] L. Cui, B. Imre, D. Tátraaljai, B. Pukánszky, *Polymer* **2020**, *186*, 122014.
- [50] Materials Database, Rilsan BESNO TL, <https://www.extremematerials-arkema.com/en/materials-database/products/datasheet/Rilsan%C2%AE%20BESNO%20TL> (accessed May 19, 2020).
- [51] T. D. Fornes, D. R. Paul, *Macromolecules* **2004**, *37*, 7698.
- [52] K. Jariyavidyanont, A. Abdelaziz, R. Androsch, C. Schick, *Thermochim. Acta* **2019**, *674*, 95.
- [53] A. Wurm, A. Herrmann, M. Cornelius, E. Zhuravlev, D. Pospiech, R. Nicula, C. Schick, *Macromol. Mater. Eng.* **2015**, *300*, 637.
- [54] E. Zhuravlev, C. Schick, *Thermochim. Acta* **2010**, *505*, 1.
- [55] E. Zhuravlev, C. Schick, *Thermochim. Acta* **2010**, *505*, 14.
- [56] Nylon 11 (NYLON11) Heat Capacity, Enthalpy, Entropy, Gibbs Energy, SpringerMaterials, http://materials.springer.com/polymerthermodynamics/docs/athas_0022 (accessed May 14, 2020).
- [57] Q. Zhang, Z. Mo, S. Liu, H. Zhang, *Macromolecules* **2000**, *33*, 5999.
- [58] J. E. K. Schawe, J. F. Löffler, *Nat. Commun.* **2019**, *10*, 1337.
- [59] R. S. Porter, *J. Polym. Sci. Polym. Lett. Ed.* **1980**, *18*, 824.
- [60] J. W. P. Schmelzer, A. S. Abyzov, V. M. Fokin, C. Schick, E. D. Zanolto, *J. Non-Cryst. Solids* **2015**, *429*, 24.
- [61] T. Hikima, M. Hanaya, M. Oguni, *J. Mol. Struct.* **1999**, *479*, 245.
- [62] T. Hikima, Y. Adachi, M. Hanaya, M. Oguni, *Phys. Rev. B* **1995**, *52*, 3900.
- [63] F. Paladi, M. Oguni, *J. Phys. Condens. Matter* **2003**, *15*, 3909.
- [64] S. Vyazovkin, I. Dranca, *J. Phys. Chem. B* **2007**, *111*, 7283.

How to cite this article: Jariyavidyanont K, Zhuravlev E, Schick C, Androsch R. Kinetics of homogeneous crystal nucleation of polyamide 11 near the glass transition temperature. *Polymer Crystallization*. 2020;e10149. <https://doi.org/10.1002/pcr2.10149>

4.6 Shear-induced crystallization of polyamide 11

Katalee Jariyavidyanont¹, Salvatore Mallardo², Pierfrancesco Cerruti², Maria Laura Di Lorenzo², Regine Boldt³, Alicyn M. Rhoades⁴, René Androsch¹

¹ Interdisciplinary Center for Transfer-oriented Research in Natural Sciences, Martin Luther University Halle-Wittenberg, 06099 Halle/Saale, Germany.

² Institute of Polymers, Composites and Biomaterials (CNR), Via Campi Flegrei, 34, 80078 Pozzuoli, Naples, Italy.

³ Leibniz-Institut für Polymerforschung Dresden e.V., Hohe Str. 6, 01069 Dresden, Germany.

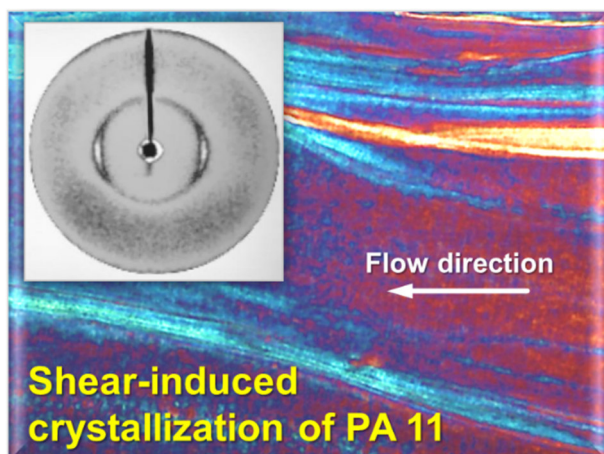
⁴ School of Engineering, Penn State Behrend, 4701 College Drive, Erie, PA 16563, USA.

Rheologica Acta 2021, 60, 231–240.

Research highlights

1. Shear-induced crystallization of PA 11 was studied using a parallel-plate rheometer and the semicrystalline morphology of the sheared disk was investigated by POM, XRD and AFM.
2. The sheared samples showed a gradient structure along the radius, from the center to the edge, including spherulites like in quiescent-melt crystallization, finer spherulites due to a larger number of nuclei generated by shear, and fibrillar structures, also induced by shear.
3. The critical shear rates, above which shear-induced formation of additional point-like and thread-like nuclei occur, are around 1 and 5–6 s⁻¹, respectively.
4. The critical specific work of flow for PA 11 is higher than in the case of PA 66, suggested to be attributed to the different chemical structure affecting the molecular-segment orientability and relaxation times.

Graphical abstract





Shear-induced crystallization of polyamide 11

Katalee Jariyavidyanont¹ · Salvatore Mallardo² · Pierfrancesco Cerruti² · Maria Laura Di Lorenzo² · Regine Boldt³ · Alicyn M. Rhoades⁴ · René Androsch¹

Received: 14 December 2020 / Revised: 4 February 2021 / Accepted: 20 February 2021
© The Author(s) 2021

Abstract

Shear-induced formation of crystal nuclei in polyamide 11 (PA 11) was studied using a conventional parallel-plate rheometer. Crystallization of PA 11 after shearing the melt at different rates for 60 s was followed by the evolution of the complex viscosity. The sheared samples showed in an optical microscope a gradient structure along the radius, due to the increasing shear rate from the center to the edge. The critical shear rate for shear-induced formation of nuclei was identified at the position where a distinct change of the semicrystalline superstructure is observed, being at around 1 to 2 s⁻¹. Below this threshold, a space-filled spherulitic superstructure developed as in quiescent-melt crystallization. Above this value, after shearing at rates between 1 and 5 s⁻¹, an increased number of point-like nuclei was detected, connected with formation of randomly oriented crystals. Shearing the melt at even higher rates led to a further increase of the nuclei number and growth of crystals oriented such that the chain axis is in parallel to the direction of flow. In addition, optical microscopy confirmed formation of long fibrillar structures after shearing at such condition. The critical specific work of flow of PA 11 was calculated to allow a comparison with that of polyamide 66 (PA 66). This comparison showed that in the case of PA 11 more work for shear-induced formation of nuclei is needed than in the case of PA 66, discussed in terms of the chemical structure of the repeat unit in the chains.

Keywords Polyamide 11 · Shear-induced nucleation/crystallization · Crystallization · Specific work of flow · Semicrystalline morphology

Introduction

Polyamide 11 (PA 11), produced by Arkema (trade name Rilsan[®]), is a bio-based polymer which is synthesized by polycondensation of ω -aminoundecanoic acid, extracted from castor oil (Genas 1962). It is an aliphatic polyamide

with its repeating unit consisting of a rather long sequence of ten methylene groups and an amide group. PA 11 is a crystallizable polymer exhibiting a rather low maximum crystallinity of less than 40% (Zhang et al. 2000). Due to its good chemical resistance, excellent impact properties, and good dimensional stability, it is considered a high-performance engineering polymer used in versatile applications such as automotive components, on-shore and off-shore oil pipelines, electronic components, gears, connectors, coating material, and diverse medical applications (Kohan 1995; Bello and Wood 2005; Halim et al. 2013). The properties, tailored for each of those applications, strongly depend on the semicrystalline structure, including fraction, size, shape, orientation, and perfection of crystals (Tordjeman et al. 2001; Azzurri et al. 2003; Dencheva et al. 2007; Kolesov et al. 2014). These parameters, in turn, are controlled by the crystallization and processing conditions (Jariyavidyanont et al. 2019).

Regarding quiescent-melt crystallization of PA 11 at processing-relevant cooling rates, the melt completely vitrifies

✉ Katalee Jariyavidyanont
katalee.jariyavidyanont@iw.uni-halle.de

✉ René Androsch
rene.androsch@iw.uni-halle.de

¹ Interdisciplinary Center for Transfer-oriented Research in Natural Sciences, Martin Luther University Halle-Wittenberg, 06099 Halle/Saale, Germany

² Institute of Polymers, Composites and Biomaterials (CNR), Via Campi Flegrei, 34, 80078 Pozzuoli, Naples, Italy

³ Leibniz-Institut für Polymerforschung Dresden e.V., Hohe Str. 6, 01069 Dresden, Germany

⁴ School of Engineering, Penn State Behrend, 4701 College Drive, Erie, PA 16563, USA

below the glass transition temperature (T_g) of about 45 °C on quenching at rates faster than about 1000 K s⁻¹ (Mollova et al. 2013; Jariyavidyanont et al. 2019), while cooling at lower rates allows crystallization/ordering. Formation of mesomorphic pseudohexagonal δ' -crystals is obtained at high supercooling of the melt slightly above T_g on cooling at rates between 200 and 500 K s⁻¹ (Schmidt and Stuart 1958; Rhoades et al. 2016). At such conditions, many crystal nuclei are active, hindering their lateral growth to lamellae and formation of spherulites. Instead, small ordered domains/nodules develop (Mollova et al. 2013; Schick and Androsch 2018). Cooling slower than 200 K s⁻¹ increasingly leads to high-temperature spherulitic crystallization of the melt, replacing the low-temperature ordering process. Finally, cooling at rates lower than 30 K s⁻¹ permits for the formation of a space-filled spherulitic structure by the growth of few nuclei at high temperature to lamellar pseudohexagonal δ -crystals (Mollova et al. 2013; Jariyavidyanont et al. 2019). These crystals convert reversibly on cooling to ambient temperature to triclinic α -crystals at the Brill-transition temperature at around 100 °C (Brill 1942; Pepin et al. 2016).

In polymer-manufacturing processes, crystallization often takes place in a non-quiescent highly supercooled melt due to high cooling rates and simultaneous presence of normal and shear forces/stress, causing deformation and/or orientation of the molecules (Somani et al. 2005; Ogino et al. 2006). Crystallization of PA 11 during injection molding and the resulting semicrystalline morphology were analyzed and correlated to the cooling-rate profile in the various regions of the molded part (Jariyavidyanont et al. 2018). Fast cooling at a rate of few hundred K s⁻¹ was predicted in the skin layer by simulation, and optical microscopy and X-ray analysis revealed formation of non-spherulitically grown α -crystals of low perfection. Toward the core, with increasing distance from the skin, the cooling rate decreased, allowing for formation of a spherulitic structure containing more perfect α -crystals.

An intermediate zone between the skin and core regions, often called a shear zone, is generally was observed as a result of shearing the melt during the filling process. Shear rates of the order of magnitude of 10³ s⁻¹ may be evident for a short period of time of around 1 s before crystallization, as simulated for a specific molding of isotactic polypropylene (Gohn et al. 2018). As a consequence, nucleation and crystallization are enhanced, as detected by an increase of the nuclei density, leading to a fine-spherulitic or non-spherulitic structure (Koscher and Fulchiron 2002; Janeschitz-Kriegl et al. 2003; Pantani et al. 2010; De Santis et al. 2016; Spoerer et al. 2020), due to the lower energy barrier for the formation of crystal nuclei (Coppola et al. 2001; Koscher and Fulchiron 2002; Lellinger et al. 2003). If the shear flow is strong enough (Hadinata et al. 2006; Mykhaylyk et al.

2008; Seo et al. 2018; Refaa et al. 2018; Iqbal et al. 2019), even oriented superstructures may form, like shish-kebab morphologies or aligned spherulites (Keller and Machin 1967; Zhang et al. 2005).

Regarding quantitative data on shear-induced crystallization of PA 11, we are aware of only a single study performed on branched molecules (Acierno and Puyvelde 2005). As far as we know, there exists no information about critical shearing conditions of PA 11 to promote shear-induced formation of nuclei, therefore being subject of the present work. Crystallization of PA 11 is followed via evolution of the complex viscosity collected during isothermal crystallization after shearing the melt at different rates, using a parallel-plate rheometer. The critical shear rate, defined as minimum shear rate applied to the sample to induce/enhance crystallization, was investigated and, after its compilation into a specific work of flow (W), compared with results of a similar study performed on polyamide 66 (PA 66) (Seo et al. 2018). The specific work of flow (Janeschitz-Kriegl et al. 2003) is calculated according to Eq. 1 and considers besides the shear rate ($\dot{\gamma}$) also the effects of shear time (t) and viscosity of the melt (η), depending on temperature and time of shear, on nuclei formation:

$$W = \int_{t_0}^{t_s} \eta(T, t) \dot{\gamma}^2 dt \quad (1)$$

Furthermore, besides correlating the shearing conditions with the kinetics of crystallization/nuclei formation, structural data including degree of crystallinity, crystal structure, and micrometer-scale superstructure were analyzed using differential scanning calorimetry (DSC), wide-angle X-ray scattering (WAXS), and polarized-light optical microscopy (POM), for interpretation of the effect of shear-induced crystallization on structure.

Experimental

Material and preparation

High-viscosity bio-based Rilsan[®] BESNO-TL PA 11, an extrusion grade containing heat and light stabilizers, was obtained from Arkema. The melt volume-flow rate, mass-average molar mass, and polydispersity are 1 cm³ (10 min)⁻¹ (235 °C, 2.16 kg) (Arkema 2020), 17.2 kg mol⁻¹, and 2, respectively (Fornes and Paul 2004). The material, delivered in the form of pellets, was dried at 80 °C for about 12 h before film compression molding. A pre-pressed film with a thickness of about 800 μ m was prepared by a Carver laboratory manual press at 220 °C using a maximum load of 2 t and then cut to obtain a circular disk with a diameter of about 16 mm for subsequent rheological analysis.

Rheological analysis

Shear-induced crystallization of PA 11 was investigated by using a Thermo Scientific HAAKE Rheostress6000 rheometer equipped with a closed temperature-controlled chamber and a 20-mm-diameter parallel-plate geometry setup. The chamber, purged with nitrogen gas at 20 mL min^{-1} , was heated to $220 \text{ }^\circ\text{C}$, equilibrated at this temperature for a few minutes, before adjusting the position of the upper shaft/plate by zero-gap setting. A 16-mm-diameter sample disk with a thickness of about $800 \text{ }\mu\text{m}$ was placed between the metal plates and equilibrated at $220 \text{ }^\circ\text{C}$ for 1 min. After that, the upper metal-plate was slowly lowered to the pre-defined gap distance of $500 \text{ }\mu\text{m}$, and the excess melt was trimmed from the outer edges of the plates. Note that the selected gap distance of $500 \text{ }\mu\text{m}$ was set according to the ISO 6721-10 standard, with the recommendation of the ratio $2r/h$ to be between 10 and 50 (r and h are the radius and gap distance, respectively) (Mezger 2006). Otherwise, if it is outside of the recommended range, there is risk of inhomogeneous deformation, secondary flow effects, transient behavior, and edge failure.

The shear and crystallization experiments were performed according to the protocol shown in Fig. 1. After trimming, the melt was kept at $220 \text{ }^\circ\text{C}$ for additional 2 min and then ballistically cooled at a rate of about $15\text{--}20 \text{ K min}^{-1}$ to the shear temperature of $190 \text{ }^\circ\text{C}$. Different shear rates, up to 10 s^{-1} , were applied to the sample for 60 s in all experiments. Note that the shear rate depends on the location in the disk, linearly increasing with the radius (Mezger 2006). In the following, shear rate information refers to the maximum shear rate at the edge of the plate ($r = 10 \text{ mm}$). After the shear step, the sample was cooled at a rate of 10 K min^{-1} to $180 \text{ }^\circ\text{C}$ and isothermally crystallized at this temperature for 1 h, allowing for completion of primary crystallization. The crystallization kinetics was monitored by the time dependence

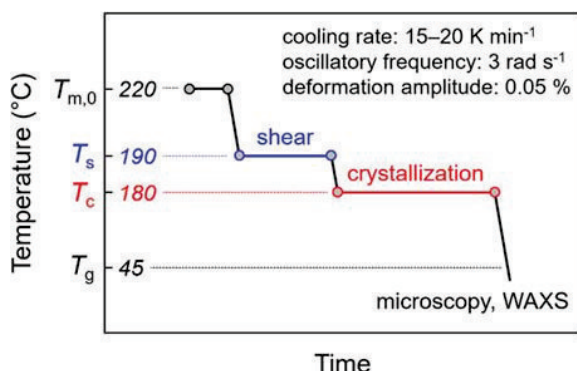


Fig. 1 Temperature and shear protocol for analysis of shear-induced crystallization of PA 11

of the complex viscosity, measured using an oscillatory frequency and deformation amplitude of 3 rad s^{-1} and 0.05% , respectively. For morphological and crystallinity analyses, Kapton[®] polyimide films, used as a non-adhesive layer, were glued on both metal plates before zero-gap setting. Shear and crystallization experiments for a given shear condition typically were performed at least two times (often up to four times) when using Kapton, being the preferred setup since allowing subsequent structure analysis. Since there was often observed a difference between program shear rate and true shear rate, error bars could not be obtained rather than an increased number of different shear-rate data. Experiments without using Kapton were performed only once, just for comparison with data obtained using Kapton-setup.

Differential scanning calorimetry

DSC was employed to investigate the crystallinity of a non-sheared sample and a sample crystallized after shearing the melt at a rate of about 7.6 s^{-1} . The samples with a mass of $5\text{--}10 \text{ mg}$ were taken near the center and edge of the disks and subsequently placed into $20 \text{ }\mu\text{L}$ aluminum pans. A heat-flux Mettler-Toledo DSC 1 in combination with a TC100 intracooler was used. The furnace was purged with nitrogen gas at a flow rate of 60 mL min^{-1} . The calibration of the instrument was checked by measurement of the temperature and enthalpy of melting of an indium standard. The crystallinity was estimated from the enthalpy of melting during heating using a rate of 20 K min^{-1} , with its calculation based on a value of the bulk enthalpy of melting of 189 J g^{-1} (Zhang et al. 2000).

Polarized-light optical microscopy

The microstructure of non-sheared and sheared PA 11, after completion of the crystallization step and cooling to room temperature, was analyzed by POM. Thin sections with a thickness of about $10 \text{ }\mu\text{m}$ were prepared using a SLEE-CUT-5062 rotary microtome. The sections were cut along the radius of the disks, from the center through the edge, that is, perpendicular to the flow direction. Then, thin sections were embedded in immersion oil between glass coverslips and observed with a Leica DMRX optical microscope in transmission mode using crossed polarizers. The images were captured by a Motic 2300 CCD camera attached to the microscope.

Wide-angle X-ray scattering

WAXS was used to investigate the crystal structure and orientation as a function of the radial position in the disks from the edge to the center. The analysis was performed at room temperature in transmission mode employing a Bruker D8

Discover X-ray diffractometer, equipped with an area detector, and using $\text{Cu K}\alpha$ radiation. The diameter of the circular beam was 0.5 mm and the exposure time was 30 min. The sample-to-detector distance was 149.7 mm.

Results and discussion

Figure 2 shows the evolution of the complex viscosity of PA 11 collected during isothermal crystallization at 180 °C for 1 h (see the red segment in Fig. 1). The data of the upper plot were obtained from the samples placed between the metal plates without using Kapton® films. The shear rates, as given in the legend, represent average values over the total shear time of 60 s. The bottom sets of data were obtained from the experiments using Kapton® films. In this case, the onset time of crystallization/increase of the viscosity is slightly delayed if compared to the data observed in experiments without using Kapton® (top data), as described below. Furthermore, in the lower plot, the upper plateau of the viscosity curves is not shown due to lack of reproducibility when samples exhibit high viscosity due to presence of crystals, in case of using Kapton® film. However, crystallization onset times are reproducible, since at this stage of the crystallization step, the viscosity is low, not leading to detrimental effects

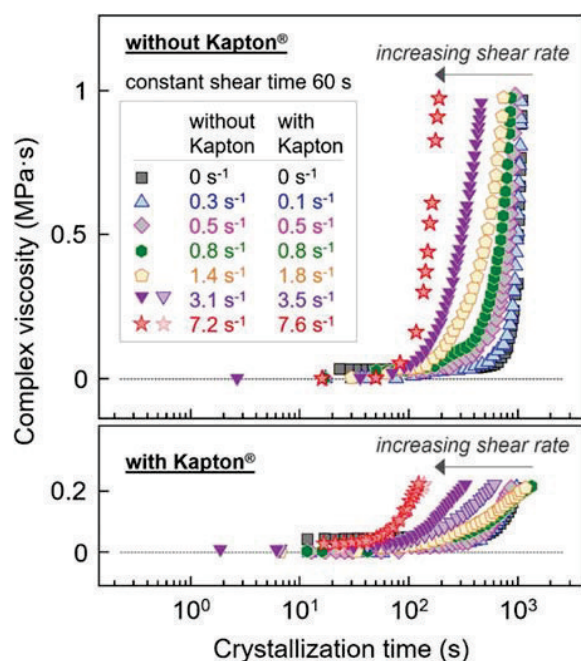


Fig. 2 Viscosity as a function of crystallization time of PA 11 obtained during isothermal crystallization at 180 °C, after shearing the melt at different rates for 60 s. The data of the lower plot were collected using Kapton® films for easy removal of the sample from the instrument after crystallization

of the Kapton® films. Quiescent-melt crystallization of the samples, regardless of the use of Kapton® films, begins after about 1000 s (see black squares), being in agreement with former DSC studies of the crystallization rate (Mollova et al. 2013; Rhoades et al. 2016). When shearing the melt, crystallization shifts to increasingly shorter time with increasing shear rate (see gray arrows), caused by an increase of nuclei density.

Figure 3 shows crystallization onset times as a function of shear rate of PA 11, with black squares and red stars referring to data measured either with or without Kapton®, respectively. Crystallization onset times are defined as intersection of the extrapolated baseline and the estimated highest-slope tangent line of the viscosity curves of Fig. 2. The onset times of crystallization of non-sheared samples are indicated with the corresponding black and red dashed lines, respectively. Regarding non-sheared samples, we observed a slightly lower onset time of crystallization when using Kapton®. In detail, in case of not using Kapton® as a spacer/anti-adhesive, the onset time of crystallization is about 1050 s, while it is about 950 s when using Kapton®, perhaps caused by a nucleating effect of the Kapton® film (Gadzinowska and Piorkowska 2003). The trend of slightly faster crystallization in case of the Kapton®-setup seems to be preserved also in experiments in which samples are subjected to shear despite occasional uncertainties in determination of the crystallization onset time. However, the observed negligible difference of the crystallization rate in case of the two experimental setups has no influence on the discussion of the effect of shear on crystallization.

In fact, regardless of the use of Kapton® films, the crystallization time distinctly decreases on shearing the melt at

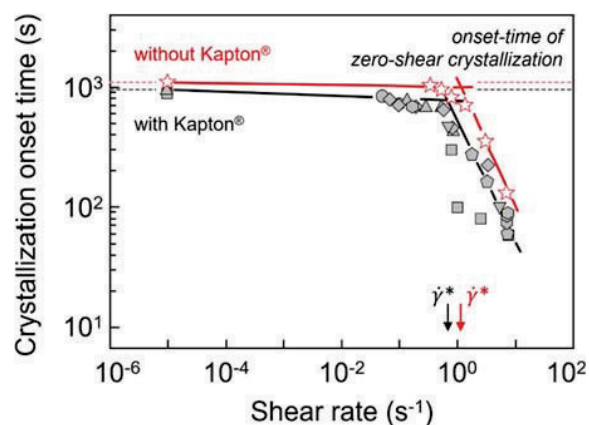


Fig. 3 Crystallization onset times as a function of shear rate of PA 11 samples prepared with and without using Kapton® films (black symbols and red stars, respectively). The crystallization onset times of non-sheared samples are indicated with the corresponding black and red dashed lines, respectively

rates higher than about 0.5 s^{-1} due to formation of additional crystal nuclei. A critical shear rate of around 0.8 to 1 s^{-1} is determined from the intersection of the extrapolated crystallization onset time of the non-sheared samples, and linear fit of onset times observed well above the shear rates where the downturn of the crystallization onset time occurs (Seo et al. 2018)

Figure 4 presents a photograph (left) and POM image (right) of a disk prepared using a shear rate of 7.6 s^{-1} . The images were taken at room temperature after completion of crystallization at $180 \text{ }^\circ\text{C}$ for 1 h. The inner part of the disk in the photograph, where low shear rates are evident, is opaque. In contrast, at large distance from the center, the film appears translucent, with a rather sharp transition from opaque to translucent at a specific radius-value. The change of the optical appearance is interpreted in terms of a critical shear rate, above which crystallization occurs in a different mode. As will be shown below, the crystallinity is independent of the position in the samples, and therefore, the different optical appearance is assumed to be caused by different crystal size and/or superstructure. The POM image at the right-hand side of Fig. 4 additionally reveals with the observed Maltese cross the information that there is orientation of either macromolecules in the amorphous phase and/or of crystals, with the latter described below.

Figure 5 shows micrographs of PA 11 samples taken at room temperature, after shearing the melt at different rates and subsequent isothermal crystallization at $180 \text{ }^\circ\text{C}$ for 1 h. The samples were cut along the radius, from the center to the edge of the disks. Therefore, the flow direction is perpendicular to the cut sections. Higher-magnification micrographs of the sample near the edge of non-sheared and sheared PA 11 (7.6 s^{-1}) are shown to the right in the figure, with the top and bottom images, respectively.

Regarding the images illustrating the structure from the center to the edge (left), the non-sheared sample is shown at the top, while the other images represent the structure

of samples subjected to shear flow before crystallization, with the shear rates indicated at the right-hand side of each thin section. The non-sheared sample shows a space-filled spherulitic structure, with the diameter of the spherulites being $20\text{--}30 \text{ }\mu\text{m}$ (see also right top image), regardless of the position in the disk. In contrast, the sheared PA 11 samples show a gradient structure from the center to the edge due to the increasing shear rates. A critical shear rate for shear-induced formation of nuclei is specified at the position where a distinct change of the semicrystalline superstructure is observed, indicated by yellow circles. The POM micrographs of Fig. 5 confirm consistently in all experiments involving different maximum shear rate the increased nuclei number when the shear rate exceeds about 1 s^{-1} . Worth noting, shearing the melt at a rate above the critical value leads to a tremendous increase of point-like nuclei as well as formation of aligned nuclei as revealed with the bottom-right image.

DSC first-heating scans, measured with a rate of 20 K min^{-1} , of non-sheared (black) and sheared PA 11 at the center (blue) and edge area (red) of the disks are shown in Fig. 6. The purpose of the experiment was to prove the presence of crystals in the edge region of the sheared sample, since POM cannot provide this information (see Fig. 4). However, the melting-peak temperatures and crystallinities of both samples (sheared and non-sheared) and even at different positions (center and edge area) are similar, being about $190 \text{ }^\circ\text{C}$ and 35% , respectively, regardless of the largely different semicrystalline morphology (see the edge structures in the top and bottom thin sections in Fig. 5). Identical melting temperatures are expected since both samples were crystallized at the same temperature of $180 \text{ }^\circ\text{C}$ until completion of the crystallization process.

Figure 7 presents at the top a POM image of a sample sheared at 7.6 s^{-1} for 60 s including information of sampling WAXS patterns as a function of the radius of the disk from the edge (red circle) to the center (blue circle).

Fig. 4 Photograph (left) and POM image (right) of a PA 11 disk crystallized at $180 \text{ }^\circ\text{C}$ for 1 h after shearing the melt at 7.6 s^{-1} for 60 s, taken at room temperature. The orientation of the polarizers is shown at the top right of the POM image

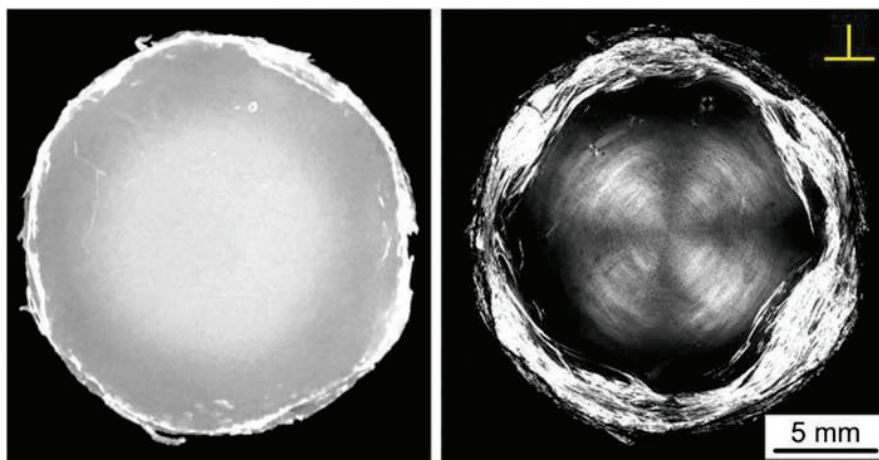
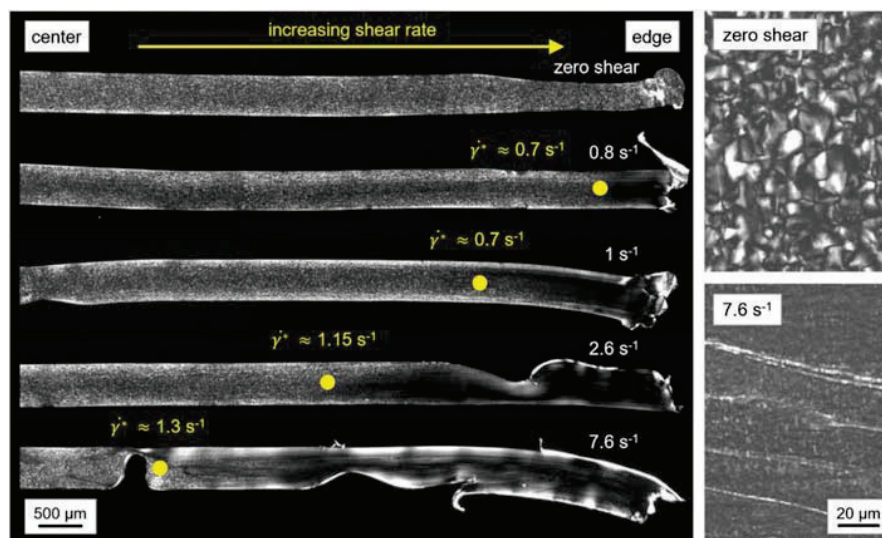


Fig. 5 POM images of PA 11 sections showing the structure from the center to the edge perpendicular to the flow direction, captured at room temperature after shearing the melt at different rates for a constant shear time of 60 s at 190 °C and subsequent isothermal crystallization for 1 h at 180 °C (left). The two images to the right show the structure in the center layer near the edge of non-sheared (top right) and sheared PA 11 (bottom right) at higher magnification



One-dimensional WAXS patterns taken at corresponding positions are shown with the bottom plot in Fig. 7. The scattering patterns collected at the edge and center of the non-sheared sample are indicated with the dashed lines. All samples show three scattering peaks at about 7.4, 20.3, and 23.4 degrees related to the (001), (100), and (010/110) lattice planes, respectively, of the triclinic α -crystals present (Slichter 1959; Kim et al. 1985). As such, the X-ray data consistently confirm that crystallization at 180 °C leads to formation of α -crystals of similar perfection, with the latter indicated by the constant positions of the 100 and 010/110 peaks, regardless of prior shearing.

Figure 8, at the top, shows two-dimensional WAXS patterns in the angular range of the 001 peak of sheared PA

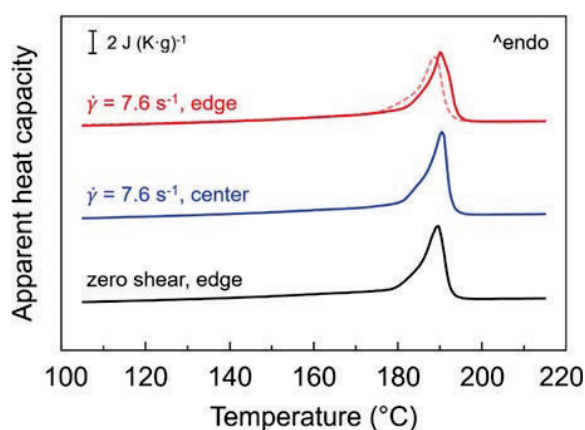


Fig. 6 DSC first-heating scans of non-sheared (black) and sheared PA 11 (blue and red), recorded at 20 K min⁻¹. The red dashed line represents a repetition scan, with the sample taken from a different disk

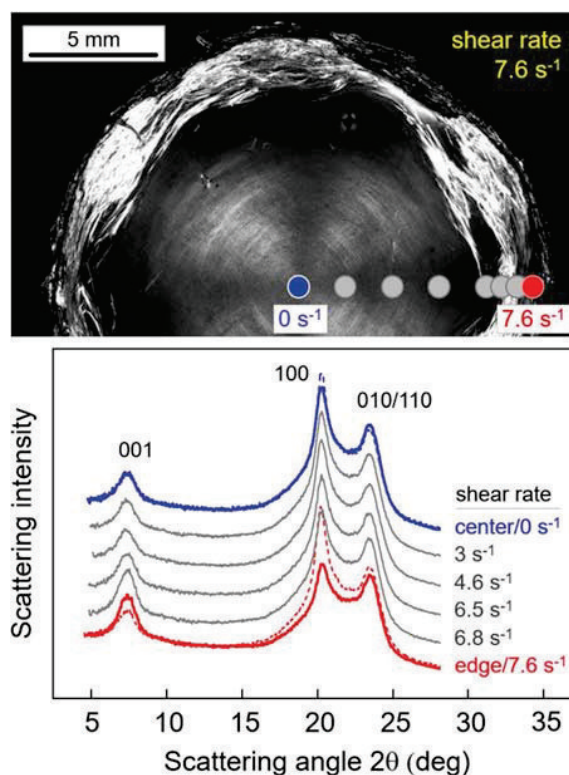


Fig. 7 POM image (top) showing the WAXS-analysis positions from the edge (red) to the center (blue) of the disk, corresponding to different shear rates from 7.6 to 0 s⁻¹, respectively. In the bottom part of the figure are shown WAXS curves taken at the various disk positions with the corresponding shear rates indicated on the right-hand side of the curves. The scattering patterns collected at the edge and center of the non-sheared sample are indicated with the dashed lines

11 (7.6 s^{-1} for 60 s) taken at different distances from the edge (red) to the center of the disk (blue) (see also the POM image in the top part of Fig. 7), while in the bottom plot are shown azimuthal scans of the intensity of the 001 peak. The two-dimensional WAXS patterns served for detection of the crystal orientation along the radius of the sheared disk. Within the analyzed sample plane, the data reveal crystal orientation near the edge, while in the inner part of the disk crystals are randomly oriented. The crystal orientation is clearly detected with the incomplete arc-like Debye-Scherrer ring in the pattern taken at distances lower than 2 mm from the edge. Quantitative information is provided with the azimuthal scans in the bottom plot of Fig. 8, demonstrating, though only weak, increasing crystal orientation toward the edge. Worth noting, despite no crystal orientation was

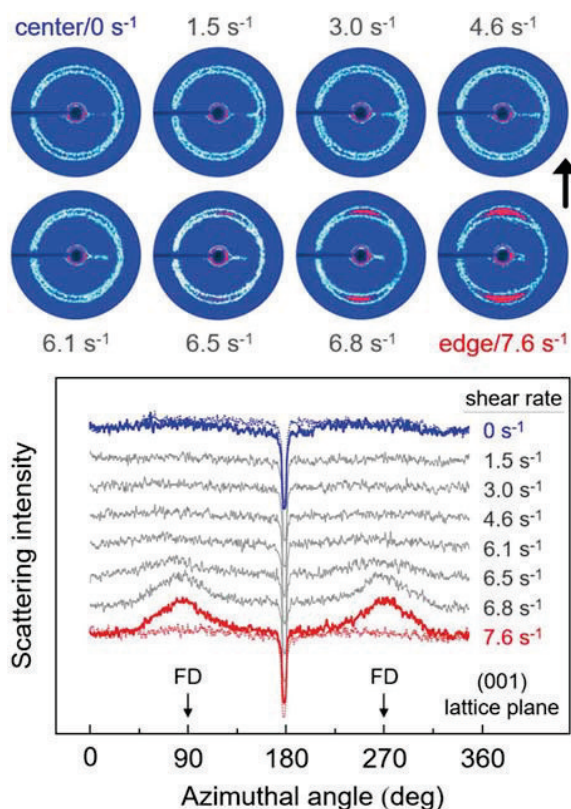


Fig. 8 Two-dimensional scattering patterns in the angular range of the 001-scattering peak of the sheared sample at different positions from the edge to the center of the disk, representing different shear rates (top). The vertical arrow on the right-hand side indicates the flow direction (FD). Scattering intensity as a function of the azimuthal angle at the scattering angle of the 001 peak of the various sample positions (bottom). The data of the non-sheared sample at the edge and center of the disk are presented with the dashed-thin lines. The flow direction (FD) is shown with the arrows at the 90 and 270° positions

detected in the inner part of the disk, the POM image of Fig. 4 (right) revealed with the Maltese cross orientation of molecules which might be related to amorphous-phase orientation, often observed in injection molding or compression molding of amorphous polymers (Rudolph 2009; Meister 2020).

Figure 9 shows POM images of the inner structure of the sheared disk used for WAXS analysis (see Fig. 7). The top image reveals the gradient structure along the radius as discussed above with Fig. 5, while the bottom image shows the structure along the flow direction near the edge, as indicated with the yellow frame in the top image. The yellow circle in the top image emphasizes the radius-position above which there is observed shear-induced crystallization. Note that the observed critical shear rate of 3 s^{-1} of this particular sample is slightly higher than for the samples of Fig. 5, with the mismatch illustrating the uncertainty of the performed experiments. A rough estimation of an average critical shear rate of all samples regardless of the maximum shear rate at the edge reveals a value of $1.4 \pm 0.95 \text{ s}^{-1}$. Again, below this value, there is observed quiescent-like crystallization, while above this value, shear-induced nucleation occurs. If the shear rate is lower than about 5 to 7 s^{-1} , then still spherulitic crystallization is detected, however, with the number of spherulites distinctly increased compared to the center of the disk. In contrast, as demonstrated in the lower image of Fig. 9, at the edge, a qualitatively different morphology evolved, characterized by the presence of long fiber-like objects parallel to the direction of the flow, presumably shish-like structures. Strikingly, only in this part of the sample preferred crystal orientation was measured by WAXS (see Fig. 8).

Regardless of the different morphological features observed as a function of the radius in the sheared disk,

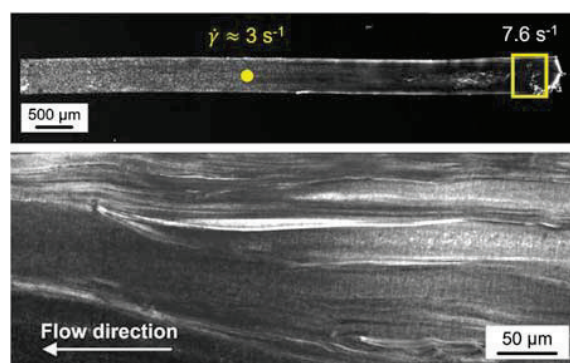


Fig. 9 POM images of sheared PA 11, showing the structure from the center to the edge of the disk (top) and at the edge area (bottom). The direction of flow is perpendicular to the shown section in the top image, while it is indicated with the arrow in the bottom image. The yellow rectangle in the top image illustrates the location represented with the lower image, and the yellow circle indicates the critical shear rate above which the nuclei density increases toward the edge

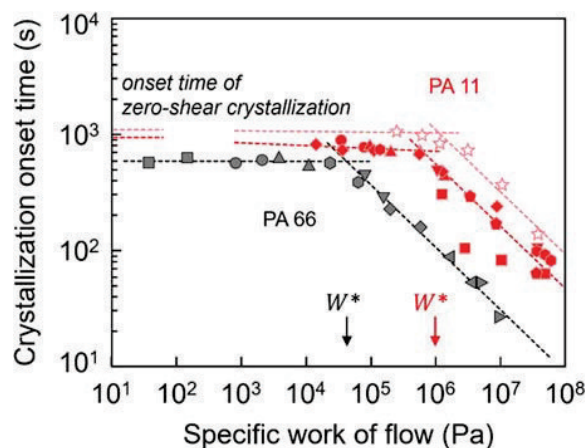


Fig. 10 Crystallization onset time as a function of specific work of flow of PA 11 (red symbols) and PA 66 (black symbols). The data of PA 66 were adapted with permission from Seo et al. 2018, *Macromolecules* 51, 4269–4279. Copyright 2020 American Chemical Society

shearing at rates larger about 1 s^{-1} for 60 s leads to an acceleration of the crystallization process. To accommodate the shearing time, and to permit a comparison with PA 66, crystallization onset times were plotted as a function of the specific work of flow in Fig. 10.

For PA 11 (red symbols), the specific work of flow was calculated from Eq. 1, with the viscosity determined as an average value during the shearing step of the experiments, as proposed in the literature (Mykhaylyk et al. 2008). Information about the specific work of flow of PA 66 (black symbols) was gained from the literature (Seo et al. 2018). The PA 11 samples, collected in this work with (filled symbols) and without using Kapton[®] films (open-star symbols), show a critical specific work of flow of around 1 MPa (see red arrow marked W^*). In contrast, the critical value above which shear-induced nucleation occurs in PA 66 is only about 0.05 MPa (see black arrow), which is distinctly lower than observed for PA 11. In other words, PA 11 requires more work/energy to generate crystal nuclei by shear. We assume that the higher critical specific work of flow is related to the structure of the repeat unit in the chains, that is, the longer aliphatic sequence in PA 11 and lower hydrogen bond density, as these parameters probably affect relaxation times, being important for the stability of shear-induced formed nuclei. The molar mass of both polymers used for the investigations is very similar (17.2 and 22.3 kg mol^{-1} for PA 11 and PA 66, respectively), with both grades having a polydispersity of 2. As such, the different critical specific works of flow cannot be explained by different chain lengths.

Conclusions

In polymer-manufacturing processes such as extrusion or injection molding, crystallization may be induced by normal and shear forces/stress, causing deformation and/or orientation of the molecules in the melt. These features play an important role for shear-induced crystallization implying a possibility to control or tailor the final structure and eventually the properties. Therefore, in the present work, shear-induced formation of nuclei of PA 11 was analyzed using a conventional parallel-plate rheometer. Crystallization of PA 11 after shearing the melt at different rates for 60 s was followed by the evolution of the viscosity. The critical shear rate and specific work of flow above which shear-induced nucleation occurs are around $1\text{--}2 \text{ s}^{-1}$ and 1 MPa, respectively.

Optical microscopy revealed the gradient structure of the sheared disks along the radius, from the center to the edge, identifying ranges of quiescent-like spherulitic crystallization, spherulitic crystallization starting from additional point-like nuclei which were generated by shear, and shear-induced formation of fibrillar structures. WAXS analysis revealed the presence of oriented crystals only in the range of fibrillar crystallization.

This study quantifies for the first time shear-induced crystal nucleation in PA 11 and allows an initial comparison with PA 66. In case of PA 11, the critical specific work of flow is much larger than in case of PA 66, which must be attributed to the different chemical structure, presumably affecting the orientability of molecular segments in the melt and relaxation times. Regarding these parameters, information is not yet available, suggesting further research efforts for explaining the different behaviors of polymers belonging to the polyamide family.

Funding Open Access funding enabled and organized by Projekt DEAL. KJ and RA received financial support from the European Structural and Investment Funds (ESF). This work was supported by the National Science Foundation under grant no. 1653629.

Open Access This article is licensed under a Creative Commons Attribution 4.0 International License, which permits use, sharing, adaptation, distribution and reproduction in any medium or format, as long as you give appropriate credit to the original author(s) and the source, provide a link to the Creative Commons licence, and indicate if changes were made. The images or other third party material in this article are included in the article's Creative Commons licence, unless indicated otherwise in a credit line to the material. If material is not included in the article's Creative Commons licence and your intended use is not permitted by statutory regulation or exceeds the permitted use, you will need to obtain permission directly from the copyright holder. To view a copy of this licence, visit <http://creativecommons.org/licenses/by/4.0/>.

References

- Acierno S, Puyvelde PV (2005) Effect of short chain branching upon the crystallization of model polyamides-11. *Polymer* 46:10331–10338. <https://doi.org/10.1016/j.polymer.2005.07.097>
- Arkema (2020) Polyamide material database. <https://www.extrematerials-arkema.com/en/materials-database/polyamide-material-database/>. Accessed 22 Sep 2020
- Azzurri F, Flores A, Alfonso GC et al (2003) Polymorphism of isotactic polybutene-1 as revealed by microindentation hardness. Part II: correlations to microstructure. *Polymer* 44:1641–1645 [https://doi.org/10.1016/S0032-3861\(02\)00864-9](https://doi.org/10.1016/S0032-3861(02)00864-9)
- Bello JO, Wood RJK (2005) Micro-abrasion of filled and unfilled polyamide 11 coatings. *Wear* 258:294–302. <https://doi.org/10.1016/j.wear.2004.08.008>
- Brill R (1942) Über das Verhalten von Polyamiden beim Erhitzen. *J Für Prakt Chem* 161:49–64. <https://doi.org/10.1002/prac.19421610104>
- Coppola S, Grizzuti N, Maffettone PL (2001) Microrheological modeling of flow-induced crystallization. *Macromolecules* 34:5030–5036. <https://doi.org/10.1021/ma010275e>
- De Santis F, Pantani R, Titomanlio G (2016) Effect of shear flow on spherulitic growth and nucleation rates of polypropylene. *Polymer* 90:102–110. <https://doi.org/10.1016/j.polymer.2016.02.059>
- Dencheva N, Denchev Z, Oliveira MJ, Funari SS (2007) Relationship between crystalline structure and mechanical behavior in isotropic and oriented polyamide 6. *J Appl Polym Sci* 103:2242–2252. <https://doi.org/10.1002/app.25250>
- Fornes TD, Paul DR (2004) Structure and properties of nanocomposites based on nylon-11 and -12 compared with those based on nylon-6. *Macromolecules* 37:7698–7709. <https://doi.org/10.1021/ma048757o>
- Gadzinowska K, Piorkowska E (2003) Influence of sample thickness and surface nucleation on i-PP crystallization kinetics in DSC measurements. *Polimery* 48:790–799. <https://doi.org/10.14314/polimery.2003.790>
- Genas M (1962) Rilsan (Polyamid 11), Synthese und Eigenschaften. *Angew Chem* 74:535–540. <https://doi.org/10.1002/ange.19620741504>
- Gohn AM, Rhoades AM, Okonski D, Androsch R (2018) Effect of melt-memory on the crystal polymorphism in molded isotactic polypropylene. *Macromol Mater Eng* 303:1800148. <https://doi.org/10.1002/mame.201800148>
- Hadinata C, Gabriel C, Ruellmann M et al (2006) Shear-induced crystallization of PB-1 up to processing-relevant shear rates. *Rheol Acta* 45:539–546. <https://doi.org/10.1007/s00397-005-0057-z>
- Halim KAA, Farrell JB, Kennedy JE (2013) Preparation and characterization of polyamide 11/montmorillonite (MMT) nanocomposites for use in angioplasty balloon applications. *Mater Chem Phys* 143:336–348. <https://doi.org/10.1016/j.matchemphys.2013.09.007>
- Iqbal N, Jariyavidyanont K, Rhoades AM, Androsch R (2019) Critical specific work of flow for shear-induced formation of crystal nuclei in poly (L-lactic acid). *Polym Cryst* 2:e10073. <https://doi.org/10.1002/pcr2.10073>
- Janeschitz-Kriegl H, Ratajski E, Stadlbauer M (2003) Flow as an effective promoter of nucleation in polymer melts: a quantitative evaluation. *Rheol Acta* 42:355–364. <https://doi.org/10.1007/s00397-002-0247-x>
- Jariyavidyanont K, Schick C, Androsch R (2019) Nucleation-controlled dual semicrystalline morphology of polyamide 11. *Polym Int* 68:263–270. <https://doi.org/10.1002/pi.5606>
- Jariyavidyanont K, Williams JL, Rhoades AM et al (2018) Crystallization of polyamide 11 during injection molding. *Polym Eng Sci* 58:1053–1061. <https://doi.org/10.1002/pen.24665>
- Keller A, Machin MJ (1967) Oriented crystallization in polymers. *J Macromol Sci Part B* 1:41–91. <https://doi.org/10.1080/00222346708212739>
- Kim KG, Newman BA, Scheinbeim JI (1985) Temperature dependence of the crystal structures of nylon 11. *J Polym Sci Polym Phys Ed* 23:2477–2482. <https://doi.org/10.1002/pol.1985.180231206>
- Kohan MI (1995) Chapter 13 Commercial nylon plastics and their applications. In: Kohan MI (ed) *Nylon plastics handbook*. Hanser Publishers, Munich, pp 487–599
- Kolesov I, Mileva D, Androsch R (2014) Mechanical behavior and optical transparency of polyamide 6 of different morphology formed by variation of the pathway of crystallization. *Polym Bull* 71:581–593. <https://doi.org/10.1007/s00289-013-1079-9>
- Koscher E, Fulchiron R (2002) Influence of shear on polypropylene crystallization: morphology development and kinetics. *Polymer* 43:6931–6942. [https://doi.org/10.1016/S0032-3861\(02\)00628-6](https://doi.org/10.1016/S0032-3861(02)00628-6)
- Lellinger D, Floudas G, Alig I (2003) Shear induced crystallization in poly(ϵ -caprolactone): effect of shear rate. *Polymer* 44:5759–5769. [https://doi.org/10.1016/S0032-3861\(03\)00633-5](https://doi.org/10.1016/S0032-3861(03)00633-5)
- Meister S (2020) Influence of part dimension on ageing of injection moulded thermoplastic materials: exemplary studies on amorphous polycarbonate. *Microsyst Technol*. <https://doi.org/10.1007/s00542-020-05020-3>
- Mezger TG (2006) *The rheology handbook: for users of rotational and oscillatory rheometers*. Vincentz Network GmbH & Co KG
- Mollova A, Androsch R, Mileva D et al (2013) Effect of supercooling on crystallization of polyamide 11. *Macromolecules* 46:828–835. <https://doi.org/10.1021/ma302238r>
- Mykhaylyk OO, Chambon P, Graham RS et al (2008) The specific work of flow as a criterion for orientation in polymer crystallization. *Macromolecules* 41:1901–1904. <https://doi.org/10.1021/ma702603v>
- Ogino Y, Fukushima H, Takahashi N et al (2006) Crystallization of isotactic polypropylene under shear flow observed in a wide spatial scale. *Macromolecules* 39:7617–7625. <https://doi.org/10.1021/ma061254t>
- Pantani R, Coccuro I, Volpe V, Titomanlio G (2010) Shear-induced nucleation and growth in isotactic polypropylene. *Macromolecules* 43:9030–9038. <https://doi.org/10.1021/ma101775h>
- Pepin J, Miri V, Lefebvre J-M (2016) New insights into the Brill transition in polyamide 11 and polyamide 6. *Macromolecules* 49:564–573. <https://doi.org/10.1021/acs.macromol.5b01701>
- Refaa Z, Boutaous M, Siginer DA (2018) PLA crystallization kinetics and morphology development. *Int Polym Process* 33:336–344. <https://doi.org/10.3139/217.3525>
- Rhoades AM, Wonderling N, Schick C, Androsch R (2016) Supercooling-controlled heterogeneous and homogenous crystal nucleation of polyamide 11 and its effect onto the crystal/mesophase polymorphism. *Polymer* 106:29–34. <https://doi.org/10.1016/j.polymer.2016.10.050>
- Rudolph N (2009) *Druckverfestigung amorpher Thermoplaste*. Dissertation, University of Erlangen-Nuremberg
- Schick C, Androsch R (2018) Nucleation-controlled semicrystalline morphology of bulk polymers. *Polym Cryst* 1:e10036. <https://doi.org/10.1002/pcr2.10036>
- Schmidt GF, Stuart HA (1958) Gitterstrukturen mit räumlichen Wasserstoffbrückensystemen und Gitterumwandlungen bei Polyamiden. *Z Für Naturforschung A* 13:222–225. <https://doi.org/10.1515/zna-1958-0308>
- Seo J, Takahashi H, Nazari B et al (2018) Isothermal flow-induced crystallization of polyamide 66 melts. *Macromolecules* 51:4269–4279. <https://doi.org/10.1021/acs.macromol.8b00082>
- Slichter WP (1959) Crystal structures in polyamides made from ω -amino acids. *J Polym Sci* 36:259–266. <https://doi.org/10.1002/pol.1959.1203613020>

- Somani RH, Yang L, Hsiao BS et al (2005) Shear-induced molecular orientation and crystallization in isotactic polypropylene: effects of the deformation rate and strain. *Macromolecules* 38:1244–1255. <https://doi.org/10.1021/ma048285d>
- Spoerer Y, Androsch R, Jehnichen D, Kuehnert I (2020) Process induced skin-core morphology in injection molded polyamide 66. *Polymers* 12:894. <https://doi.org/10.3390/polym12040894>
- Tordjeman Ph, Robert C, Marin G, Gerard P (2001) The effect of α , β crystalline structure on the mechanical properties of polypropylene. *Eur Phys J E* 4:459–465. <https://doi.org/10.1007/s101890170101>
- Zhang C, Hu H, Wang D et al (2005) In situ optical microscope study of the shear-induced crystallization of isotactic polypropylene. *Polymer* 46:8157–8161. <https://doi.org/10.1016/j.polymer.2005.06.074>
- Zhang Q, Mo Z, Liu S, Zhang H (2000) Influence of annealing on structure of nylon 11. *Macromolecules* 33:5999–6005. <https://doi.org/10.1021/ma000298d>

Publisher's note Springer Nature remains neutral with regard to jurisdictional claims in published maps and institutional affiliations.

4.7 Thermal stability and nucleation efficacy of shear-induced pointlike and shishlike crystallization precursors

Katalee Jariyavidyanont¹, Andreas Janke², Muhammad Tariq³, Maria Laura Di Lorenzo⁴, Christoph Schick⁵, René Androsch¹

¹ Interdisciplinary Center for Transfer-oriented Research in Natural Sciences (IWE TFN), Martin Luther University Halle-Wittenberg, 06099 Halle/Saale, Germany.

² Leibniz-Institut für Polymerforschung Dresden e.V., Hohe Str. 6, 01069 Dresden, Germany.

³ Institute of Physics, Martin Luther University Halle-Wittenberg, 06120 Halle, Germany.

⁴ Institute of Polymers, Composites and Biomaterials (CNR), Via Campi Flegrei, 34, 80078 Pozzuoli, Naples, Italy.

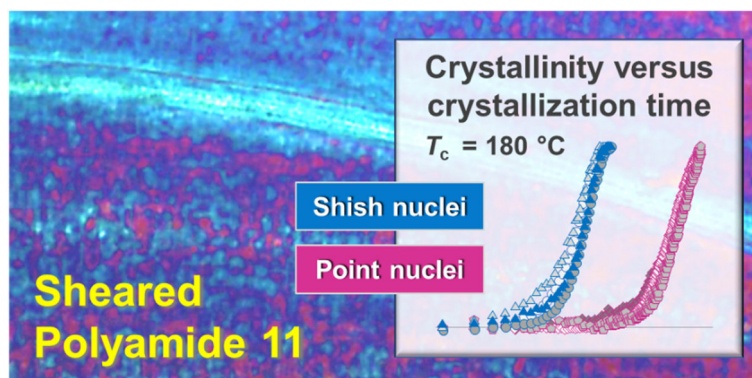
⁵ University of Rostock, Institute of Physics, 18051 Rostock, Germany; Department of Physical Chemistry, Kazan Federal University, Kazan, Russia.

Reprinted with permission from K. Jariyavidyanont, A. Janke, M. Tariq, M.L. Di Lorenzo, C. Schick, R. Androsch. Thermal stability and nucleation efficacy of shear-induced pointlike and shishlike crystallization precursors. *ACS Macro Lett.* 2021, 10, 684–689. Copyright (2021) American Chemical Society.

Research highlights

1. The thermal stability and nucleation efficacy of shear-induced point-like and shish-like precursors located in a single sample spot were analyzed using hot-stage microscopy.
2. The stabilities of both shish-like and point-like nuclei are similar, showing dissolution near the equilibrium melting temperature at about 205 °C.
3. Recrystallization of the shish-like nuclei is faster, in maximum about two order of magnitude, than that of the point-like precursors, because of a) a larger size of the shish-like precursors, b) a more perfect chain conformation serving as a substrate for crystallization, and perhaps c) a higher local orientation of the surrounding melt which reduces the activation energy for crystallization.

Graphical abstract



Thermal Stability and Nucleation Efficacy of Shear-Induced Pointlike and Shishlike Crystallization Precursors

Katalee Jariyavidyanont,* Andreas Janke, Muhammad Tariq, Maria Laura Di Lorenzo, Christoph Schick, and René Androsch*



Cite This: *ACS Macro Lett.* 2021, 10, 684–689



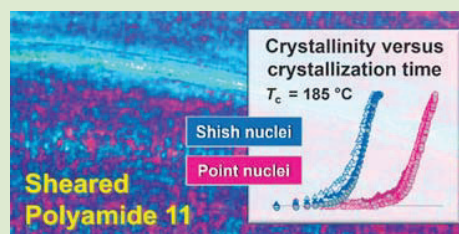
Read Online

ACCESS |

Metrics & More

Article Recommendations

ABSTRACT: The different thermal stabilities of shear-induced pointlike and shishlike crystallization precursors of polyamide 11, generated in a parallel-plate rheometer and coexisting in the same sample, were quantified by hot-stage microscopy, by performing self-seed crystallization experiments. Crystals formed at low supercooling of the melt from these different types of precursors melt at about the same temperature. Annealing of the melt at different temperatures for a predefined time revealed dissolution/disordering of these precursors at 10–15 K higher temperature, near the equilibrium melting point. Despite their similar thermal stabilities, pointlike and shishlike crystallization precursors exhibit distinctly different nucleation efficacies. Under identical crystallization conditions, shishlike precursors cause faster crystallization than pointlike crystal nuclei. The faster crystallization of the shishlike nuclei can be explained, for example, by (a) the larger size of the shishlike precursors, providing numerous nucleation sites; (b) the more perfect chain conformation at the shish surface, which serves as a substrate for crystallization; or perhaps (c) the higher local orientation of the surrounding melt compared with molecular segments near pointlike nuclei, reducing the activation energy for crystallization.



In polymer processing, the melt is subjected to shear flow, often causing deformation and orientation of macromolecules, promoting an increase in the density of nuclei due to a reduction of the energy barrier for their formation. This leads to faster crystallization and a change of the semicrystalline morphology compared with the structure formed during quiescent-melt crystallization,^{1–5} thus affecting the final properties.^{6,7}

As a function of the shearing conditions (i.e., the time and rate of shearing the melt at a specific temperature), beyond pre-existing heterogeneous nuclei, pointlike crystal nuclei, row nuclei, or shishlike nuclei may additionally form and enhance the crystallization process.^{8,9} Only a few studies have reported about the thermal stabilities and nucleation efficacies of the different shear-induced nuclei. It was found that remnants of shish-based crystals survive at higher temperatures in the melt than both self-seed from the kebab lamellar crystals and crystals formed by crystallization of the relaxed melt,^{10–15} even if subjected to long-term annealing.^{12,16} Furthermore, shear-induced nuclei show higher efficacy than nuclei formed from the relaxed melt, though a distinction between different shear-induced nuclei (shishlike vs pointlike nuclei) was not possible by calorimetry.^{14,17} Application of hot-stage polarized-light optical microscopy (POM) suggested that threadlike shishes are more effective than pointlike nuclei for accelerating crystallization.^{15,18} However, a direct comparison of the stabilities and nucleation efficacies of shear-induced pointlike and shishlike nuclei is not available yet.

Therefore, in advance to prior studies, the crystallization behaviors of pointlike versus shishlike precursors are assessed in this study by hot-stage optical microscopy. With the presence of both types of nuclei in a single sample, it is possible to subject them to identical thermal histories, allowing straightforward comparative evaluation of their stabilities and nucleation efficacies.

In order to obtain the desired information, in this work these qualitatively different types of nuclei were generated in polyamide 11 (PA 11) using a parallel-plate rheometer.¹⁹ Pointlike crystal nuclei are observed when the melt is sheared at rates higher than about 1 s^{-1} for 60 s, while fibrillar or shishlike structures form when the shear rate and stress are higher than $5\text{--}6 \text{ s}^{-1}$ and 0.065 MPa , respectively. However, the replacement of pointlike nuclei by shishlike structure is gradual, thus allowing their simultaneous observation in a certain range of shear conditions.

In this work, a molten disk of PA 11 with a radius of 10 mm and a thickness of 0.5 mm was sheared in a Thermo Scientific

Received: February 16, 2021

Accepted: May 5, 2021

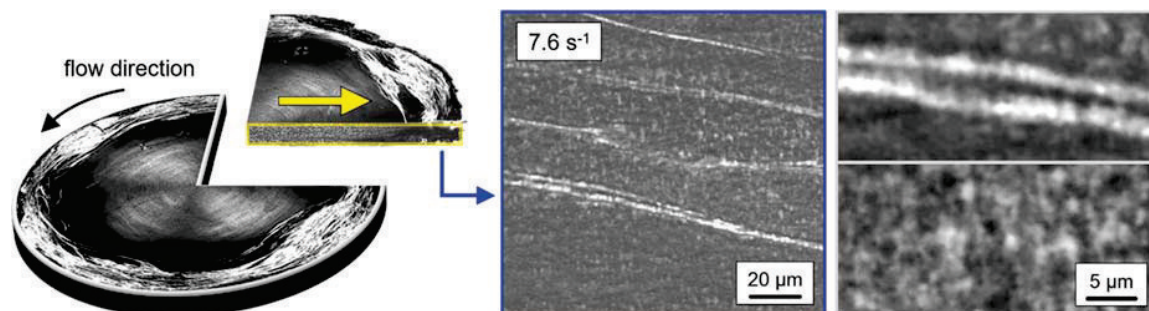


Figure 1. Sheared disk of PA 11 showing the flow direction (black arrow) and sampling position to obtain specimens containing crystals based on shishlike and pointlike nuclei (edge of the disk) (left). The POM images to the right present the structure of such a specimen at low magnification, showing crystals grown from shishlike and pointlike nuclei (left) and, at higher magnification, shish-kebab (right, top) and pointlike structures (right, bottom). From ref 19. CC BY 4.0.

HAAKE RheoStress6000 rheometer at 7.6 s^{-1} for 60 s at $190 \text{ }^\circ\text{C}$ before subsequent isothermal crystallization at $180 \text{ }^\circ\text{C}$ for 1 h. **Figure 1** shows in the left part such a sheared disk with the flow direction indicated by the black arrow. For analysis of the structure as a function of the shear rate, a thin section was taken along the radius as indicated by the yellow arrow. A gradient structure develops as a result of the increasing shear rate, from zero in the center of the disk to 7.6 s^{-1} at the edge (as schematically visualized by the yellow framed sample part), as discussed in detail elsewhere.¹⁹ For hot-stage POM analysis, a specimen was taken near the edge of the disk, where both pointlike and shishlike nuclei are detected, as shown in the left, blue-framed POM image. There are visible long-extended fibrils surrounded by tiny pointlike structures, and the POM images to the right show shish-kebab (top) and pointlike (bottom) structures at higher magnification. It should be noted that the stringlike structures may contain oriented amorphous molecular segments and extended-chain crystals building the shish and folded-chain lamellae building the kebabs, as shown below.

The nanometer-scale structure of sheared PA 11 was furthermore analyzed by atomic force microscopy (AFM) using Dimension FastScan (Bruker-Nano, USA) and NanoWizard 4 (JPK Instruments, Germany) atomic force microscopes, both operated in tapping mode. For the AFM studies, samples were prepared by equilibrating them at $197 \text{ }^\circ\text{C}$ for 3 min using a hot stage to obtain a rather smooth surface.

The stability and efficacy of shear-induced precursors in PA 11 were analyzed using a polarized-light DMRX microscope (Leica, Germany) equipped with a THMS600 hot stage (Linkam, United Kingdom) and operated in transmission mode with the samples placed between crossed polarizers.

Figure 2 shows amplitude (left) and phase AFM images (right) of oriented fibril-like structures (horizontal whitish streaks in the right image), revealing the presence of shish-kebabs, and small spherulites originating from pointlike nuclei, with a few of the latter additionally indicated with the red dots in the left image. Reproducibility was confirmed by using two different AFM devices and analysis of multiple samples.

In a first set of non-isothermal crystallization experiments, samples were heated at 20 K min^{-1} to different maximum temperatures (T_{max}) in a temperature range from above the melting temperature (T_{m}) at around $194\text{--}195 \text{ }^\circ\text{C}$ to above the equilibrium melting temperature ($T_{\text{m},0}$), reported to be 202 or $220 \text{ }^\circ\text{C}$.^{20,21} It should be noted that T_{max} always was chosen to ensure complete melting. The melt was kept for 3 min at each T_{max} before crystallization upon cooling to below the glass

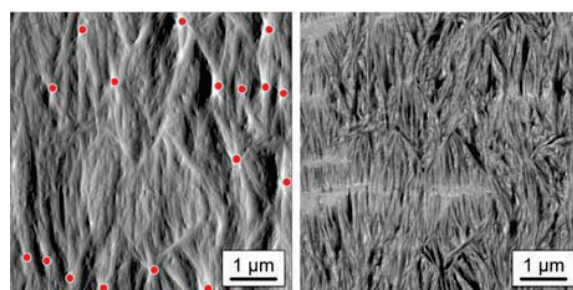


Figure 2. Amplitude (left) and phase AFM images (right) of sheared PA 11 showing shish-kebabs (whitish horizontal streaks in the right image) and small spherulites grown from pointlike nuclei, with the red dots indicating nucleation sites. The images were obtained with a NanoWizard 4 atomic force microscope (JPK Instruments, Germany) using an NSC 15 cantilever (Mikromasch, Bulgaria) (tip radius = 8 nm, spring constant = 40 N m^{-1} , resonance frequency (ω_0) = 325 kHz). The cantilever was operated at an excitation frequency ω less than ω_0 and a free amplitude of 1.6 V .

transition temperature (T_g) of around $45 \text{ }^\circ\text{C}$. It should be noted that cross-linking/degradation within the residence time of 3 min in the melt did not occur, as confirmed in an earlier study.²² The hot stage allowed linear cooling to $80 \text{ }^\circ\text{C}$ at a rate of 20 K min^{-1} . At lower temperatures, cooling turned nonlinear over time for instrumental reasons, but this is unimportant in our experiments since primary crystallization typically occurs at a much higher temperature than $80 \text{ }^\circ\text{C}$ upon cooling at 20 K min^{-1} .²² The experiments were always performed with a new sample when T_{max} was changed or experiments were repeated, in order to ensure reproducibility. Images were captured during cooling the melt to room temperature using a Motic 2300 CCD camera attached to the microscope, and crystallization was evaluated by analysis of the light intensity using NIH ImageJ (version 1.50i).²³

The two graphs at the top of **Figure 3** show the normalized light intensity as a function of temperature during non-isothermal crystallization of nonsheared (left) and sheared PA 11 (right) after melting and heating to different T_{max} , as indicated in the legend of the left plot. At temperatures lower than $197 \text{ }^\circ\text{C}$, melting was incomplete, and such experiments are not considered. Normalization was based on intensity values obtained at $145 \text{ }^\circ\text{C}$, that is, on intensity values obtained after completion of primary crystallization. The POM images in the lower part of **Figure 3** show the evolution of the structure of the

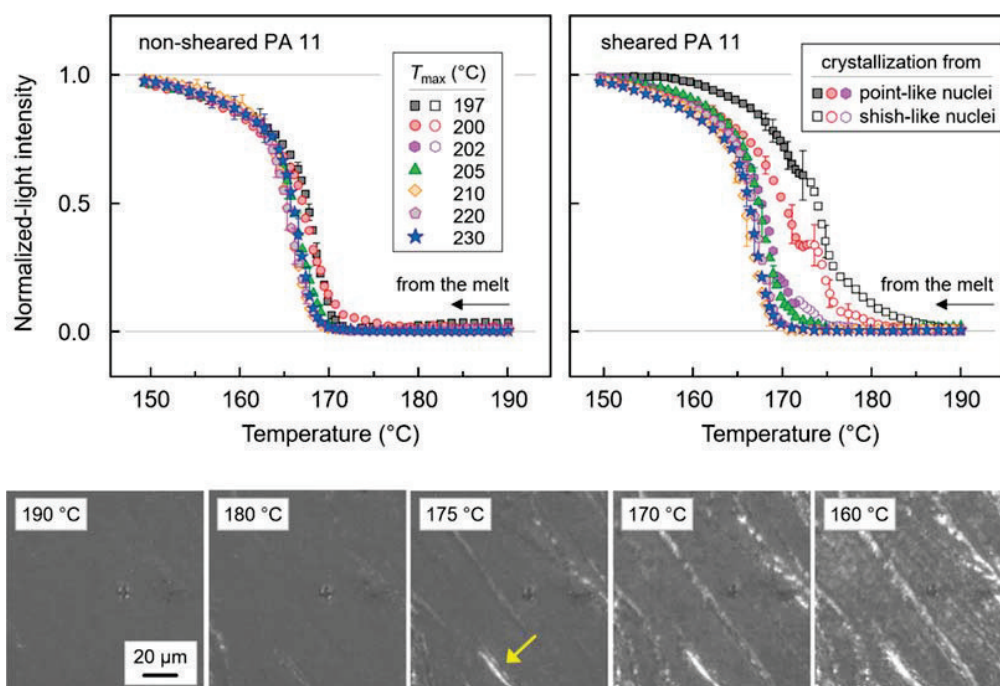


Figure 3. Normalized light intensities (top) obtained during crystallization of nonsheared (left) and sheared PA 11 (right) upon cooling at 20 K min^{-1} from different maximum temperatures T_{max} as indicated in the legend in left plot. Set of POM images (bottom) showing the crystallization of sheared PA 11 from shishlike (yellow arrow) and pointlike nuclei after the melt was heated to $T_{\text{max}} = 200 \text{ }^\circ\text{C}$, which is slightly below $T_{\text{m,0}}$ (reported to be $202 \text{ }^\circ\text{C}^{20}$ or $220 \text{ }^\circ\text{C}^{21}$). It should be noted that greatest care was applied to ensure that crystallization was not affected by preparation-induced constraints of melt deformation, as would be the case if the section were covered with an upper coverslip.

sheared sample during crystallization in the temperature range from 190 to 160 $^\circ\text{C}$, after prior melting at T_{max} of 200 $^\circ\text{C}$.

For nonsheared samples (left plot), crystallization begins at about 170 $^\circ\text{C}$, with only a minor increase in the crystallization temperature when T_{max} is lower than 205 $^\circ\text{C}$. The slight increase in the crystallization temperature is caused by self-nucleation, arising from seeds/remnants of unmolten crystals.^{24,25} It is worth noting that the temperature dependences of the light intensity data reveal a change in the slope at around 160 $^\circ\text{C}$, which is connected with a transition from primary to secondary crystallization upon lowering of the temperature.

In the case of sheared PA 11 (right plot), crystallization after the sample was melted and heated to $T_{\text{max}} = 197 \text{ }^\circ\text{C}$ (black squares), that is, 3 K above its melting temperature, is much faster than in the case of the nonsheared sample, beginning at about 185 $^\circ\text{C}$. Importantly, the light intensity curve shows a distinct discontinuity at a certain temperature, similar to the case of the data observed after heating to $T_{\text{max}} = 200 \text{ }^\circ\text{C}$ (red circles). Close inspection of the POM images in the lower part of Figure 3 reveals that crystallization of shishlike precursors begins at about 180 $^\circ\text{C}$, while pointlike nuclei grow only later into small spherulites at temperatures lower than about 170 $^\circ\text{C}$. Thus, integration of the light intensity over the whole image shows a twofold dependence, that is, the lag of the light intensity is caused by crystallization from two different structures:^{10,11,26} first from shishlike nuclei (open symbols) and second from pointlike nuclei (solid symbols). To confirm this result, isothermal crystallization experiments were performed to better separate the two crystallization events, which might overlap upon cooling at 20 K min^{-1} , as shown below. When T_{max} is

higher than about 205 $^\circ\text{C}$ (green triangles), then the crystallization temperature significantly decreases and becomes similar to that in nonsheared PA 11, and shishlike precursors are not observed. We conclude that heating PA 11, when sheared under the conditions described above, to temperatures higher than 205 $^\circ\text{C}$ leads to complete removal of the shear history.

The nucleation efficacies of the two different types of crystal nuclei were analyzed by isothermal crystallization experiments. Sheared samples were heated to $T_{\text{max}} = 200 \text{ }^\circ\text{C}$, annealed for 3 min, and rapidly cooled at a rate of 50 K min^{-1} to a predefined crystallization temperature of 185 $^\circ\text{C}$. The progress of crystallization was evaluated by analysis of the light intensity of the POM images captured as a function of the crystallization time, as shown in Figure 4. Blue and red coloring of data indicates light intensity analyses performed in sample regions containing pointlike and shishlike nuclei, respectively. The different symbols indicate the evaluation of different samples to ensure reproducibility. Different filling of identical symbols denotes analysis of different areas in a given thin section. Crystallization from the shishlike precursors starts after about 5 s to a few tens of seconds, with the distribution of onset crystallization times perhaps caused by locally different shear histories. In any case, crystallization of pointlike nuclei starts later, beginning after a few hundred seconds.

Figure 5 shows POM images, taken at room temperature, of nonsheared (top row) and sheared PA 11 (bottom row), after cooling from different T_{max} to below T_{g} at a rate of 20 K min^{-1} . In the case of nonsheared PA 11, self-nucleation occurs when T_{max} is lower than about 205 $^\circ\text{C}$, as indicated by the finer structure compared with the case of quiescent-melt crystallization (see,

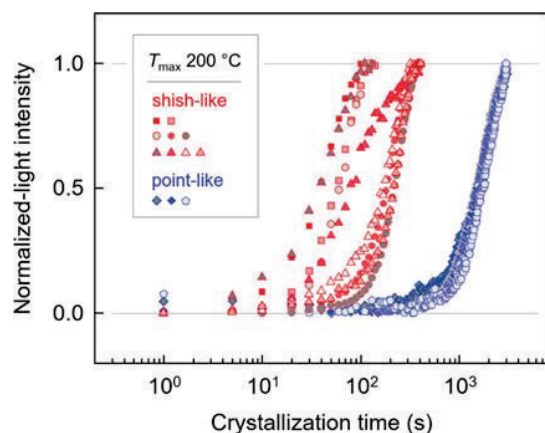


Figure 4. Normalized light intensity as a function of time during crystallization of sheared PA 11 at 185 °C after melting and heating to $T_{\max} = 200$ °C. Blue and red coloring of data denotes light intensity analyses performed in sample regions containing pointlike and shishlike nuclei, respectively. Light intensity was evaluated in different samples and different areas, as described in the text.

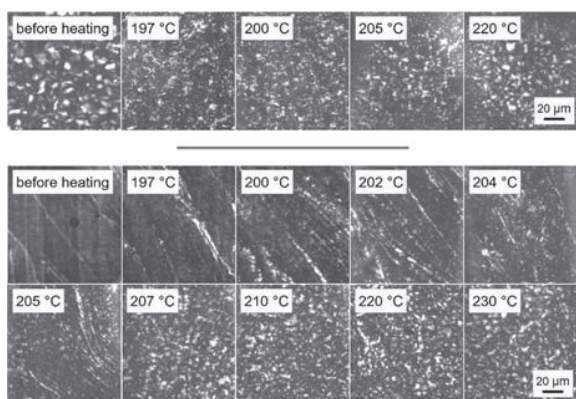


Figure 5. POM micrographs of the final structure of nonsheared (top row) and sheared PA 11 (bottom row) taken at room temperature after non-isothermal crystallization at 20 K min^{-1} from different T_{\max} as indicated in each image.

e.g., the image obtained after heating to 230 °C). Melting nonsheared PA 11 by heating to above 205 °C leads to a decrease in the self-nuclei concentration, thus causing a systematic increase in the spherulite size. Similarly, for sheared PA 11, melting and heating the samples to temperatures up to 205 °C allow neither complete relaxation of the stretched/oriented chain segments in the shishlike structures nor removal of shear-induced pointlike nuclei, leading to faster crystallization than in case of the relaxed melt. However, when the sample is melted and heated to temperatures higher than 205 °C, then both the shishlike and pointlike precursors obviously are destroyed, and crystallization occurs as in the quiescent melt, leading to a space-filled spherulitic morphology. These results are consistent with the light intensity data shown in Figure 3.

The main experimental findings of the above-described experiments are shown in Figure 6. Lamellar crystals (sketched in blue, with the individual blue lines indicating chains), isothermally grown from either shear-induced shishlike or pointlike nuclei at $T_c = 180$ °C, melt upon heating at 20 K min^{-1}

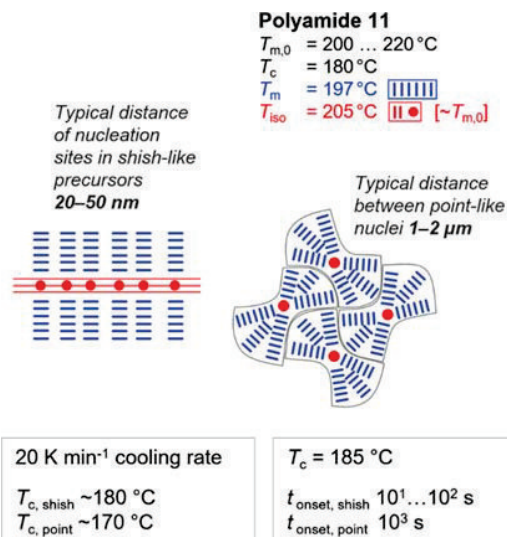


Figure 6. Summary of the experimental findings regarding the melting and isotropization temperatures (T_m and T_{iso} , respectively) of crystals/lamellae (blue) grown from shear-induced nuclei (red), and the crystallization kinetics upon recooling of the melt from $T_{\max} = 200$ °C (see boxes in the lower part of the figure). Estimates of the distance between nuclei in the shish (20–50 nm) and surrounding melt (1–2 μm) are based on the AFM images in Figure 2.

at the same temperature of around 197 °C. This observation fits general knowledge that the melting temperature (for a given crystal structure) mainly is controlled by the crystallization temperature, as studied by, e.g., Hoffman and Weeks.^{27,28} However, as the melting temperature of a crystal also depends on the entropy of melting,²⁸ that is, on the structure of the melt after completed melting of a particular crystal, it is concluded that crystals formed from both point- and shishlike crystal nuclei turn into melts of similar structure/entropy.

Similarly, both types of crystal nuclei, indicated in Figure 6 by the red circles/lines, dissolve at the same temperature of around 205 °C, that is, at a temperature in the vicinity of the equilibrium melting temperature, despite the rather short annealing time of only 3 min applied in this work. A similar nuclei-dissolution/isotropization temperature (T_{iso}) of near $T_{m,0}$ was reported for poly(ether ether ketone)¹³ and polyamide 66,¹⁴ while for isotactic polypropylene shear-induced nuclei survived to much higher temperature than $T_{m,0}$, at least during short-term annealing, for an unknown reason.¹² For PA 11 studied here, $T_{m,0}$ is considered as an upper limit of the stability of (nonforeign) crystal nuclei, regardless their origin and fine structure, including crystal remnants/self-seed,²² shear-induced pointlike nuclei, and shishlike precursors.

Most intriguing is the observation of different nucleation efficacies of shear-induced pointlike nuclei and shishlike precursors, as judged by the different kinetics of both non-isothermal and isothermal crystallization. Crystallization on shishlike precursors in isothermal crystallization experiments at 185 °C is about 10 times faster than crystallization on pointlike nuclei because of the shorter induction time. This difference may be caused by several reasons. Seemingly the volume density of nuclei is tremendously higher in shish regions (as indicated with the red points along the shish in Figure 6), allowing much faster completion of the crystallization process than in regions

containing only few pointlike nuclei, with the latter resulting in spherulitic growth of lamellae over long distances. Furthermore, it may be speculated that the fine structure and/or size of nucleation sites in shishes is different than in the case of pointlike nuclei. Isolated pointlike nuclei are expected to be distinctly smaller (nm scale) than the long shishes containing multiple nucleation points (μm scale). These nucleation points in the shishes, because of the continuous and elongated character of the latter, may provide larger and perhaps even more perfect patches/substrates for secondary nucleation, thus starting to be effective at higher temperature. The higher perfection of the nucleus surface from the point of view of promoting secondary nucleation (growth of kebabs) may easily be caused by the locally higher shear rate in sample regions containing the shishes, leading to enhanced stretching of molecular segments, which eventually lowers the surface free energy and the activation energy for first attachment of molecular segments in the crystal growth step. In addition, molecular nucleation for crystal growth may not be needed because the molecules are part of the shish and the surrounding melt.^{29,30}

In summary, the present work provides a comparison of the thermal stabilities and nucleation efficacies of qualitatively different shear-induced crystallization precursors in PA 11 by selective/space-resolved analysis of melting and crystallization using hot-stage polarized-light optical microscopy. Different types of shear-induced crystallization precursors—pointlike and shishlike nuclei—were generated in a parallel-plate rheometer in such a way as to be simultaneously present in close proximity, permitting a reliable analysis of the melting behaviors of crystals grown from these different types of nuclei and of the recrystallization of the melt subjected to different maximum temperatures. The results lead to the following conclusions:

- (1) The temperatures of melting of crystals grown from shishlike crystallization precursors and pointlike nuclei at the same temperature are identical, suggesting similar stabilities of these crystals. Identical melting temperatures indicate similar size and structure of crystals as well as similar structure/entropy of the melt in regions of former presence of crystals.
- (2) Shishlike crystallization precursors and pointlike nuclei dissolve/disorder upon short-term annealing of the melt at a temperature of about 205 °C, that is, at about $T_{m,0}$. Heating sheared PA 11 to higher temperatures completely erases the shearing history.
- (3) Shishlike crystallization precursors allow for faster completion of crystallization in their neighborhood than is possible in regions containing pointlike nuclei only. Reasons for this are the higher local density, larger size, and lower surface energy of the nuclei along the shish, allowing their growth at higher temperature.

AUTHOR INFORMATION

Corresponding Authors

Katalee Jariyavidyanont – Interdisciplinary Center for Transfer-Oriented Research in Natural Sciences (IWE TFN), Martin Luther University Halle-Wittenberg, 06099 Halle/Saale, Germany; orcid.org/0000-0001-8240-126X; Email: katalee.jariyavidyanont@iw.uni-halle.de

René Androsch – Interdisciplinary Center for Transfer-Oriented Research in Natural Sciences (IWE TFN), Martin Luther University Halle-Wittenberg, 06099 Halle/Saale,

Germany; orcid.org/0000-0002-7924-0159;
Email: rene.androsch@iw.uni-halle.de

Authors

Andreas Janke – Leibniz-Institut für Polymerforschung Dresden e.V., 01069 Dresden, Germany

Muhammad Tariq – Institute of Physics, Martin Luther University Halle-Wittenberg, 06120 Halle, Germany; orcid.org/0000-0002-3078-2459

Maria Laura Di Lorenzo – Institute of Polymers, Composites and Biomaterials (CNR), 80078 Pozzuoli, Naples, Italy

Christoph Schick – Institute of Physics, University of Rostock, 18051 Rostock, Germany; Department of Physical Chemistry, Kazan Federal University, 420008 Kazan, Russia; orcid.org/0000-0001-6736-5491

Complete contact information is available at:

<https://pubs.acs.org/10.1021/acsmacrolett.1c00101>

Notes

The authors declare no competing financial interest.

ACKNOWLEDGMENTS

K.J. and R.A. acknowledge financial support by the European Social Funds (ESF). C.S. acknowledges financial support from the Ministry of Education and Science of the Russian Federation (Grant 14.Y26.31.0019). M.T. acknowledges funding from the Deutsche Forschungsgemeinschaft (DFG, German Research Foundation) (Project ID 189853844-TRR 102). The authors thank Salvatore Mallardo and Pierfrancesco Cerruti (CNR Pozzuoli, Italy) for assistance in shearing experiments.

REFERENCES

- (1) Koscher, E.; Fulchiron, R. Influence of Shear on Polypropylene Crystallization: Morphology Development and Kinetics. *Polymer* **2002**, *43*, 6931–6942.
- (2) Janeschitz-Kriegl, H.; Ratajski, E.; Stadlbauer, M. Flow as an Effective Promotor of Nucleation in Polymer Melts: A Quantitative Evaluation. *Rheol. Acta* **2003**, *42*, 355–364.
- (3) Janeschitz-Kriegl, H. How to Understand Nucleation in Crystallizing Polymer Melts under Real Processing Conditions. *Colloid Polym. Sci.* **2003**, *281*, 1157–1171.
- (4) Lellinger, D.; Floudas, G.; Alig, I. Shear Induced Crystallization in Poly(ϵ -Caprolactone): Effect of Shear Rate. *Polymer* **2003**, *44*, 5759–5769.
- (5) Pantani, R.; Coccorullo, L.; Volpe, V.; Titomanlio, G. Shear-Induced Nucleation and Growth in Isotactic Polypropylene. *Macromolecules* **2010**, *43*, 9030–9038.
- (6) Schrauwen, B. A. G.; Breemen, L. C. A. v.; Spoelstra, A. B.; Govaert, L. E.; Peters, G. W. M.; Meijer, H. E. H. Structure, Deformation, and Failure of Flow-Oriented Semicrystalline Polymers. *Macromolecules* **2004**, *37*, 8618–8633.
- (7) Housmans, J.-W.; Gahleitner, M.; Peters, G. W. M.; Meijer, H. E. H. Structure–Property Relations in Molded, Nucleated Isotactic Polypropylene. *Polymer* **2009**, *50*, 2304–2319.
- (8) Janeschitz-Kriegl, H. *Crystallization Modalities in Polymer Melt Processing*, 2nd ed.; Springer: Wien, 2018.
- (9) Nazari, B.; Tran, H.; Beauregard, B.; Flynn-Hepford, M.; Harrell, D.; Milner, S. T.; Colby, R. H. Two Distinct Morphologies for Semicrystalline Isotactic Polypropylene Crystallized after Shear Flow. *Macromolecules* **2018**, *51*, 4750–4761.
- (10) Somani, R. H.; Yang, L.; Zhu, L.; Hsiao, B. S. Flow-Induced Shish-Kebab Precursor Structures in Entangled Polymer Melts. *Polymer* **2005**, *46*, 8587–8623.
- (11) Zuo, F.; Keum, J. K.; Yang, L.; Somani, R. H.; Hsiao, B. S. Thermal Stability of Shear-Induced Shish-Kebab Precursor Structure

from High Molecular Weight Polyethylene Chains. *Macromolecules* **2006**, *39*, 2209–2218.

(12) Hamad, F. G.; Colby, R. H.; Milner, S. T. Lifetime of Flow-Induced Precursors in Isotactic Polypropylene. *Macromolecules* **2015**, *48*, 7286–7299.

(13) Nazari, B.; Rhoades, A. M.; Schaake, R. P.; Colby, R. H. Flow-Induced Crystallization of PEEK: Isothermal Crystallization Kinetics and Lifetime of Flow-Induced Precursors during Isothermal Annealing. *ACS Macro Lett.* **2016**, *5*, 849–853.

(14) Rhoades, A. M.; Gohn, A. M.; Seo, J.; Androsch, R.; Colby, R. H. Sensitivity of Polymer Crystallization to Shear at Low and High Supercooling of the Melt. *Macromolecules* **2018**, *51*, 2785–2795.

(15) Somani, R. H.; Yang, L.; Sics, I.; Hsiao, B. S.; Pogodina, N. V.; Winter, H. H.; Agarwal, P.; Fruitwala, H.; Tsou, A. Orientation-Induced Crystallization in Isotactic Polypropylene Melt by Shear Deformation. *Macromol. Symp.* **2002**, *185*, 105–117.

(16) Azzurri, F.; Alfonso, G. C. Lifetime of Shear-Induced Crystal Nucleation Precursors. *Macromolecules* **2005**, *38*, 1723–1728.

(17) Gohn, A. M.; Seo, J.; Ferris, T.; Venkatraman, P.; Foster, E. J.; Rhoades, A. M. Quiescent and Flow-Induced Crystallization in Polyamide 12/Cellulose Nanocrystal Composites. *Thermochim. Acta* **2019**, *677*, 99–108.

(18) Liu, K.; Zhang, L.; Liu, H.; Deng, P.; Du, H.; Li, X.; Zhang, J. Recrystallization of Shish-Kebab Structures Induced by Self-Seeding Nucleation. *Mater. Lett.* **2013**, *90*, 145–147.

(19) Jariyavidyanont, K.; Mallardo, S.; Cerruti, P.; Di Lorenzo, M. L.; Boldt, R.; Rhoades, A. M.; Androsch, R. Shear-Induced Crystallization of Polyamide 11. *Rheol. Acta* **2021**, *60*, 231–240.

(20) Zhang, Q.; Mo, Z.; Liu, S.; Zhang, H. Influence of Annealing on Structure of Nylon 11. *Macromolecules* **2000**, *33*, 5999–6005.

(21) Nylon 11 (NYLON11) Heat Capacity, Enthalpy, Entropy, Gibbs Energy. SpringerMaterials, 2014. http://materials.springer.com/polymerthermodynamics/docs/athas_0022 (accessed 2021-01-28).

(22) Jariyavidyanont, K.; Janke, A.; Androsch, R. Crystal Self-Nucleation in Polyamide 11. *Thermochim. Acta* **2019**, *677*, 139–143.

(23) Schneider, C. A.; Rasband, W. S.; Eliceiri, K. W. NIH Image to ImageJ: 25 Years of Image Analysis. *Nat. Methods* **2012**, *9*, 671–675.

(24) Fillon, B.; Wittmann, J. C.; Lotz, B.; Thierry, A. Self-Nucleation and Recrystallization of Isotactic Polypropylene (α Phase) Investigated by Differential Scanning Calorimetry. *J. Polym. Sci., Part B: Polym. Phys.* **1993**, *31*, 1383–1393.

(25) Michell, R. M.; Mugica, A.; Zubitur, M.; Müller, A. J. Self-Nucleation of Crystalline Phases within Homopolymers, Polymer Blends, Copolymers, and Nanocomposites. *Adv. Polym. Sci.* **2015**, *276*, 215–256.

(26) Somani, R. H.; Sics, I.; Hsiao, B. S. Thermal Stability of Shear-Induced Precursor Structures in Isotactic Polypropylene by Rheo-X-Ray Techniques with Couette Flow Geometry. *J. Polym. Sci., Part B: Polym. Phys.* **2006**, *44*, 3553–3570.

(27) Hoffman, J. D.; Weeks, J. J. Melting Process and Equilibrium Melting Temperature of Polychlorotrifluoroethylene. *J. Res. Natl. Bur. Stand., Sect. A* **1962**, *66A*, 13–28.

(28) Wunderlich, B. *Macromolecular Physics: Crystal Melting*; Academic Press: New York, 1980.

(29) Wunderlich, B.; Mehta, A. Macromolecular Nucleation. *J. Polym. Sci., Polym. Phys. Ed.* **1974**, *12*, 255–263.

(30) Wunderlich, B. *Macromolecular Physics: Crystal Nucleation, Growth, Annealing*; Academic Press: New York, 1976.

5. CONCLUSIONS

PA 11 is an important bio-based polymer used in high-performance engineering applications. Application-relevant properties of PA 11 are affected by the semicrystalline morphology including the fraction and structure of crystals, their size, shape and perfection, and their organization in a superstructure, with all these parameters controlled by the crystallization/processing conditions. In polymer melt-processing, crystallization often occurs at rapid cooling and perhaps in presence of shear flow. Knowledge of processing-controlled structure formation in PA 11 is still lacking, which is a main motivation of the presented research, since such knowledge offers the possibility to tailor processing routes for the purpose of controlling structure and properties. Therefore, the aim of this work is to investigate crystallization of PA 11 at processing-relevant cooling rates and in presence of shear.

Quantitative information about quiescent-melt crystallization of PA 11 at processing-relevant cooling conditions were obtained by DSC and FSC on milligram- and nanogram-sized samples, respectively, allowing analysis of crystallization in a wide range of cooling rates. Cooling-rate-controlled structure formation in PA 11 was then evaluated by investigation of the semicrystalline morphology of macroscopic film samples prepared at different cooling histories, demonstrated in **Figure 14**. It can be concluded that crystallization of PA 11 at low cooling rates proceeds via heterogeneous nucleation and spherulitically growing lamellar crystals. In contrast, if cooling the melt at high rates, homogeneous nucleation is dominant, leading to formation of a large number of nanometer-sized mesophase domains. Two crystallization events, initiated via heterogeneous and homogeneous nucleation, causes formation of a dual semicrystalline morphology containing spherulitically grown lamellae formed at high temperature and non-spherulitic arranged mesophase domains formed at low temperature when cooling the melt at rates between 20 and 200 K s^{-1} . Complete vitrification of PA 11 occurs if cooling the melt at rates higher than 1000 K s^{-1} to below the glass transition

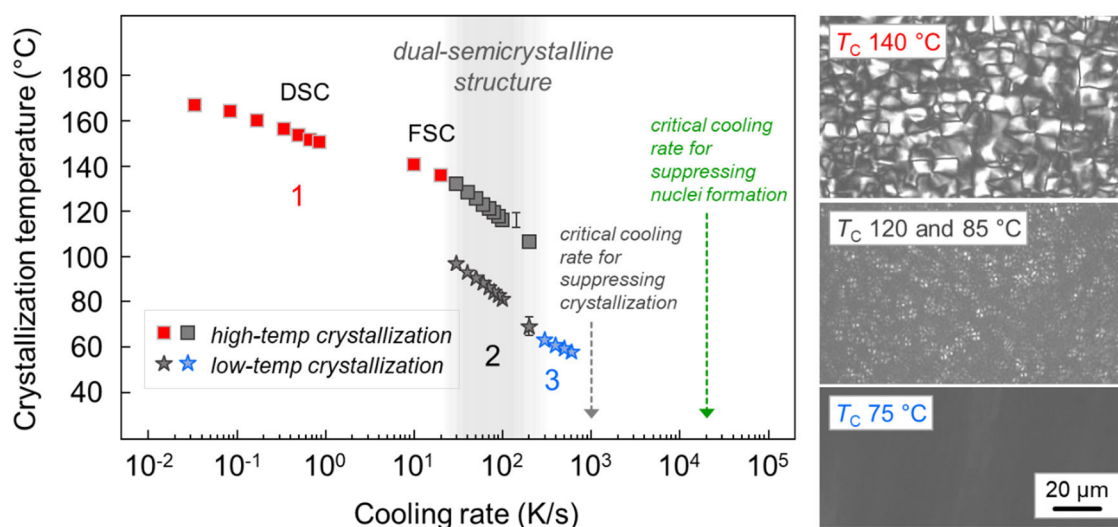


Figure 14: Summary of cooling-rate-controlled crystallization (left) and structure formation in three different cooling-rate ranges in PA 11 (right), reproduced from Ref. [141] with permission from Wiley. The critical cooling rates for suppression of crystallization and formation of crystal nuclei are indicated with gray and green arrows, respectively.

temperature, however, such high rate cannot avoid crystal nucleation during cooling. Formation of homogeneous crystal nuclei on non-isothermal crystallization can only be suppressed if cooling the melt faster than 20,000–30,000 K s⁻¹. The highest nucleation rate of PA 11 is observed at about 60 °C, that is, 10–15 K above its glass transition temperature, and is about one order of magnitude faster than the crystallization rate at identical temperature.

Shear-induced crystallization in PA 11 was studied using a parallel-plate rheometer. Crystallization of PA 11 after shearing the melt at different rates for 60 s was observed by the evolution of the complex viscosity. Since the shear rate increases with the radius of the plate, the sheared samples showed in optical microscopy a gradient structure along the radius. In detail, the structures observed from the center (zero shear condition) to the edge (maximum shear condition) are spherulites like in the quiescent-melt crystallization, finer spherulites due to shear-induced formation of point-like nuclei, and replacement of such point-like structures by shish-kebab structures. In summary, illustrated in **Figure 15**, the critical shear rates, above which shear-induced formation of nuclei and formation of fibrillar structures occur, are around 1 and 5–6 s⁻¹, respectively. The critical specific work of flow of PA 11 was calculated to allow a comparison with PA 66, being of similar chemical structure but having a higher hydrogen bond density. In the case of PA 11, a specific work of flow of about 1 MPa is required for shear-induced formation of nuclei while only 0.05 MPa is sufficient for shear-induced crystallization of PA 66. The difference of the specific work of flow of these two polyamides can be attributed to the different chemical structure, affecting the entropy of the melt and therefore the energy barrier for nucleation and crystallization.¹⁴⁰

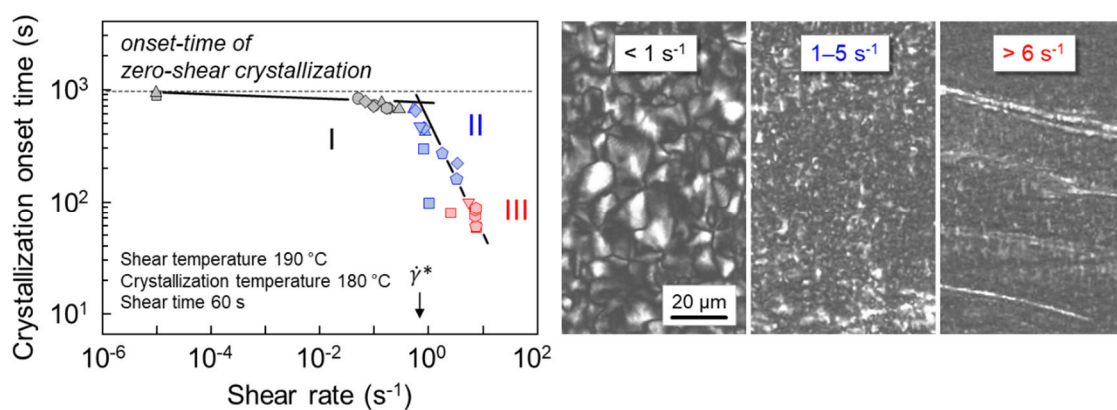


Figure 15: Summary of shear-induced crystallization of PA 11, representing three flow regimes (left) and respective structures (right).¹⁴² The critical shear rate ($\dot{\gamma}^*$) for shear-induced nucleation is about 1 s⁻¹.

The thermal stability of nuclei based on molten crystals formerly grown from the quiescent and sheared melt were analyzed and compared. The stability limit of self-nuclei of PA 11 based on nodular or lamellar crystals grown from the relaxed melt is about 10 or 15 K higher than their melting temperature, respectively. The higher survival-potential and faster melt-recrystallization rate of self-nuclei in PA 11 containing nodular mesophase is suggested being caused by their much lower melting temperature and the higher nuclei density, respectively. Regarding the sheared samples, the stability limit of point-like and shish-like precursors is similar, showing dissolution at about 15 K above the melting temperature of the crystals grown from these precursors. However, if the shear history is not completely removed by heating the

system to a temperature below the stability limit, crystallization of shish-like precursors started earlier than crystallization of the point-like nuclei, at a predefined identical crystallization temperature. The higher nucleation efficiency of the shish-like precursors is suggested being caused by a larger number of nucleation sites along the shishes, a more perfect chain conformation at the shish surface, and/or higher local orientation of the surrounding melt, both supporting secondary crystallization.

The global demand of using bio-based polymers is rising, and the production capacity of the important high-performance bio-based polymer PA 11 is forecasted to be increased. With the knowledge gained in this work, PA 11 crystallization/processing routes, from the points-of-view of thermal profiles and shear deformation, can efficiently be tailored to control the crystallinity, the crystal shape, the higher-order organization of crystals, the formation of specific crystal structures, and the crystal orientation. With these parameters of the structure to be subject of variation, the inherent engineering potential of this important bio-based polymer can further be exploited towards new applications.

References

1. M. Carus. Bio-based Building Blocks and Polymers – Global Capacities, Production and Trends 2020–2025; Short version report; nova-Institute GmbH, **2021**; p 16.
2. Arkema. Rilsan® 70th Anniversary <https://www.extremematerials-arkema.com/en/product-families/rilsan-polyamide-11-family/rilsan-70th-anniversary/> (accessed Feb 2, 2021).
3. Arkema. Polyamide Material Database <https://www.extremematerials-arkema.com/en/materials-database/polyamide-material-database/> (accessed Feb 2, 2021).
4. Arkema. Bio-based Renewable Solutions <https://www.extremematerials-arkema.com/en/product-families/rilsan-polyamide-11-family/bio-based-renewable-solutions/> (accessed Feb 5, 2021).
5. M.I. Kohan. Nylon plastics handbook; Hanser Publishers; Distributed in the USA and in Canada by Hanser/Gardner Publications, Munich, **1995**.
6. Arkema. Arkema increases its specialty polyamides global capacities <https://www.arkema.com/global/en/media/newslit/news/global/corporate/2016/20160906-expansion-of-spec/> (accessed Feb 5, 2021).
7. Arkema has successfully placed its inaugural Green Bond <https://www.arkema.com/global/en/media/newslit/news/global/investorrelations/2020/20201007-arkema-emet-sa-pr/> (accessed Feb 25, 2021).
8. D.S. Ogunniyi. Castor oil: A vital industrial raw material. *Bioresour. Technol.* **2006**, 97, 1086–1091.
9. E.B. Mubofu. Castor oil as a potential renewable resource for the production of functional materials. *Sustain. Chem. Process.* **2016**, 4, 11.
10. S. Gogolewski. Effect of annealing on thermal properties and crystalline structure of polyamides. Nylon 11 (polyundecaneamide). *Colloid Polym. Sci.* **1979**, 257, 811–819.
11. Q. Zhang, Z. Mo, S. Liu, H. Zhang. Influence of annealing on structure of nylon 11. *Macromolecules* **2000**, 33, 5999–6005.
12. E.S. Ong, Y. Kim, H.L. Williams. dynamic mechanical properties of some nylons and their blends. *J. Appl. Polym. Sci.* **1986**, 31, 367–383.
13. T.D. Fornes, D.R. Paul. Structure and properties of nanocomposites based on nylon-11 and -12 compared with those based on nylon-6. *Macromolecules* **2004**, 37, 7698–7709.
14. Arkema. Rilsan® Polyamide 11, a proven legacy, an exciting future. <https://www.extremematerials-arkema.com/export/sites/technicalpolymers/.content/medias/downloads/brochures/rilsan-brochures/Rilsan-Polyamide-11-Brochure-optimized.pdf> (accessed May 11, 2020).
15. W. Romão, E.V.R. Castro, E.A.S. Filho, et al. Ageing of polyamide 11 used in the manufacture of flexible piping. *J. Appl. Polym. Sci.* **2009**, 114, 1777–1783.
16. H. Fiorenza de Lima, M.A. Vaz, M. Ferreira da Costa, A.A. Gomez, G. Lima de Oliveira. Creep behavior of in-service flexible flowline polyamide 11. *Polym. Test.* **2020**, 81, 106205.
17. J.O. Bello, R.J.K. Wood. Micro-abrasion of filled and unfilled polyamide 11 coatings. *Wear* **2005**, 258, 294–302.

18. K.A.A. Halim, J.B. Farrell, J.E. Kennedy. Preparation and characterisation of polyamide 11/montmorillonite (MMT) nanocomposites for use in angioplasty balloon applications. *Mater. Chem. Phys.* **2013**, 143, 336–348.
19. Arkema. Processing Guidelines <https://www.extremematerials-arkema.com/en/product-families/rilsan-polyamide-11-family/processing-guidelines/> (accessed Feb 4, 2021).
20. A.M. Gohn, A.M. Rhoades, D. Okonski, R. Androsch. Effect of melt-memory on the crystal polymorphism in molded isotactic polypropylene. *Macromol. Mater. Eng.* **2018**, 303, 1800148.
21. T.G. Mezger. *The Rheology Handbook*; Vincentz Network, **2012**.
22. S. Bakrani Balani, F. Chabert, V. Nassiet, A. Cantarel. Influence of printing parameters on the stability of deposited beads in fused filament fabrication of poly(lactic) acid. *Addit. Manuf.* **2019**, 25, 112–121.
23. T. Sun, Y. Zhang, G. Han, W. Jiang, R. Zhou. The effect of cooling temperature on the skin-core crystalline structure of β -nucleated polypropylene using finite element analysis. *Results Phys.* **2017**, 7, 2036–2042.
24. K. Krebelj, M. Halilović, N. Mole. The cooling rate dependence of the specific volume in amorphous plastic injection molding. *Int. J. Adv. Manuf. Technol.* **2019**, 103, 1175–1184.
25. K. Krebelj, A. Krebelj, M. Halilović, N. Mole. Modeling injection molding of high-density polyethylene with crystallization in open-source software. *Polymers* **2021**, 13, 138.
26. A.M. Rhoades, J.L. Williams, N. Wonderling, R. Androsch, J. Guo. Skin/core crystallinity of injection-molded poly (butylene terephthalate) as revealed by microfocus X-ray diffraction and fast scanning chip calorimetry. *J. Therm. Anal. Calorim.* **2017**, 127, 939–946.
27. K. Jariyavidyanont, J.L. Williams, A.M. Rhoades, I. Kühnert, W. Focke, R. Androsch. Crystallization of polyamide 11 during injection molding. *Polym. Eng. Sci.* **2018**, 58, 1053–1061.
28. A. D'Amico, A.M. Peterson. An adaptable FEA simulation of material extrusion additive manufacturing heat transfer in 3D. *Addit. Manuf.* **2018**, 21, 422–430.
29. L.C. Sanchez, C.A.G. Beatrice, C. Lotti, J. Marini1, S.H.P. Bettini, L.C. Costa. Rheological approach for an additive manufacturing printer based on material extrusion. *Int. J. Adv. Manuf. Technol.* **2019**, 105, 2403–2414.
30. J.E. Seppala, K.D. Migler. Infrared thermography of welding zones produced by polymer extrusion additive manufacturing. *Addit. Manuf.* **2016**, 12, 71–76.
31. M. Müller, O. Kulikov, K. Hornung, M.H. Wagner. The use of thermoplastic elastomers as polymer processing aids in processing of linear low density polyethylene. *Polym. Sci. Ser. A* **2010**, 52, 1163–1170.
32. M. Härth, A. Dörnhöfer. Film blowing of linear and long-chain branched poly(ethylene terephthalate). *Polymers* **2020**, 12, 1605.
33. D. Drummer, S. Meister. Correlation of processing, inner Structure, and part properties of injection moulded thin-wall parts on example of polyamide 66. *Int. J. Polym. Sci.* **2014**, 2014, 1–8.
34. J.-W. Housmans, M. Gahleitner, G.W.M. Peters, H.E.H. Meijer. Structure–property relations in molded, nucleated isotactic polypropylene. *Polymer* **2009**, 50, 2304–2319.

35. S. Liparoti, V. Speranza, A. Sorrentino, G. Titomanlio. Mechanical properties distribution within polypropylene injection molded samples: Effect of mold temperature under uneven thermal conditions. *Polymers* **2017**, 9, 585.
36. J. Feng, R.-Y. Zhang, J.-J. Wu, W. Yang, M.-B. Yang, J.-M. Feng. Largely enhanced molecular orientation and mechanical property of injection-molded high-density polyethylene parts via the synergistic effect of polyamide 6 in situ microfibrillar and intense shear flow. *Colloid Polym. Sci.* **2014**, 292, 3033–3044.
37. E. Hnatkova, Z. Dvorak. Effect of the skin-core morphology on the mechanical properties of injection-moulded parts. *Mater. Tehnol.* **2016**, 50, 195–198.
38. M.R. Kantz, H.D. Newman, F.H. Stigale. The skin-core morphology and structure–property relationships in injection-molded polypropylene. *J. Appl. Polym. Sci.* **1972**, 16, 1249–1260.
39. C. Fischer, C. Leisen, D. Merken, A. Jungmeier, D. Drummer. The Influence of processing temperature on morphological and tribological properties of injection-moulded microparts. *Adv. Mech. Eng.* **2014**, 6, 218761.
40. C. Fischer, A. Jungmeier, G. Peters, D. Drummer. Influence of a locally variable mold temperature on injection molded thin-wall components. *J. Polym. Eng.* **2018**, 38, 475–481.
41. S. Liparoti, V. Speranza, G. Titomanlio, R. Pantani. Effect of rapid mold heating on the structure and performance of injection-molded polypropylene. *Polymers* **2020**, 12, 341.
42. N.S. Murthy, V.A. Kagan, R.G. Bray. Effect of melt temperature and skin-core morphology on the mechanical performance of nylon 6. *Polym. Eng. Sci.* **2002**, 42, 940–950.
43. R. Čermák, M. Obadal, P. Ponižil, M. Polášková, K. Stoklasa, A. Lengálová. Injection-moulded α - and β -polypropylenes: I. Structure vs. processing parameters. *Eur. Polym. J.* **2005**, 41, 1838–1845.
44. T. Nagaoka, U.S. Ishiaku, T. Tomari, H. Hamada, S. Takashima. Effect of molding parameters on the properties of PP/PP sandwich injection moldings. *Polym. Test.* **2005**, 24, 1062–1070.
45. S. Liparoti, A. Sorrentino, V. Speranza, G. Titomanlio. Mechanical characterization of iPP injection molded samples on multiple length scale. *AIP Conf. Proc.* **2019**, 2055, 070006.
46. D.J. Blundell, A. Keller, A.J. Kovacs. A new self-nucleation phenomenon and its application to the growing of polymer crystals from solution. *J. Polym. Sci. [B]* **1966**, 4, 481–486.
47. B. Fillon, J.C. Wittmann, B. Lotz, A. Thierry. Self-nucleation and recrystallization of isotactic polypropylene (α phase) investigated by differential scanning calorimetry. *J. Polym. Sci. Part B Polym. Phys.* **1993**, 31, 1383–1393.
48. R.M. Michell, A. Mugica, M. Zubitur, A.J. Müller. Self-nucleation of crystalline phases within homopolymers, polymer blends, copolymers, and nanocomposites. In *Polymer Crystallization I: From Chain Microstructure to Processing*; F. Auriemma, G.C. Alfonso, C. de Rosa, Eds.; Advances in Polymer Science; Springer International Publishing, Cham, **2017**; pp 215–256.
49. R. Androsch, M.L.D. Lorenzo, C. Schick. Optical microscopy to study crystal nucleation in polymers using a fast scanning chip calorimeter for precise control of the nucleation pathway. *Macromol. Chem. Phys.* **2018**, 219, 1700479.

50. T.F.J. Pijpers, V.B.F. Mathot, B. Goderis, R.L. Scherrenberg, E.W. van der Vegte. High-speed calorimetry for the study of the kinetics of (de)vitrification, crystallization, and melting of macromolecules. *Macromolecules* **2002**, 35, 3601–3613.
51. G.W.H. Höhne, W. Hemminger, H.-J. Flammersheim. Differential Scanning Calorimetry; G.W.H. Höhne, W. Hemminger, H.-J. Flammersheim, Eds.; Springer-Verlag, Berlin, Heidelberg, **1996**.
52. B. Wunderlich. Thermal Analysis of Polymeric Materials; Springer-Verlag, Berlin Heidelberg, **2005**.
53. V. Mathot, M. Pyda, T. Pijpers, G. Vanden Poel, E. van de Kerkhof. The Flash DSC 1, a power compensation twin-type, chip-based fast scanning calorimeter (FSC): First findings on polymers. *Thermochim. Acta* **2011**, 522, 36–45.
54. S.A. Adamovsky, A.A. Minakov, C. Schick. Scanning microcalorimetry at high cooling rate. *Thermochim. Acta* **2003**, 403, 55–63.
55. F. De Santis, S. Adamovsky, G. Titomanlio, C. Schick. Scanning nanocalorimetry at high cooling rate of isotactic polypropylene. *Macromolecules* **2006**, 39, 2562–2567.
56. R. Androsch, A.M. Rhoades, I. Stolte, C. Schick. Density of heterogeneous and homogeneous crystal nuclei in poly (butylene terephthalate). *Eur. Polym. J.* **2015**, 66, 180–189.
57. A.M. Gohn, A.M. Rhoades, N. Wonderling, T. Tighe, R. Androsch. The effect of supercooling of the melt on the semicrystalline morphology of PA 66. *Thermochim. Acta* **2017**, 655, 313–318.
58. A. Mollova, R. Androsch, D. Mileva, C. Schick, A. Benhamida. Effect of supercooling on crystallization of polyamide 11. *Macromolecules* **2013**, 46, 828–835.
59. F. De Santis, S. Adamovsky, G. Titomanlio, C. Schick. Isothermal nanocalorimetry of isotactic polypropylene. *Macromolecules* **2007**, 40, 9026–9031.
60. C. Silvestre, S. Cimmino, D. Duraccio, C. Schick. Isothermal crystallization of isotactic poly(propylene) studied by superfast calorimetry. *Macromol. Rapid Commun.* **2007**, 28, 875–881.
61. C. Schick. Differential scanning calorimetry (DSC) of semicrystalline polymers. *Anal. Bioanal. Chem.* **2009**, 395, 1589.
62. D. Mileva, J. Wang, M. Gahleitner, K. Jariyavidyanont, R. Androsch. New insights into crystallization of heterophasic isotactic polypropylene by fast scanning chip calorimetry. *Polymers* **2020**, 12, 1683.
63. J.E.K. Schawe, P.A. Vermeulen, M. van Drongelen. A new crystallization process in polypropylene highly filled with calcium carbonate. *Colloid Polym. Sci.* **2015**, 293, 1607–1614.
64. C. Schick, R. Androsch, J.W.P. Schmelzer. Homogeneous crystal nucleation in polymers. *J. Phys. Condens. Matter* **2017**, 29, 453002.
65. J.E.K. Schawe, P.A. Vermeulen, M. van Drongelen. Two processes of α -phase formation in polypropylene at high supercooling. *Thermochim. Acta* **2015**, 616, 87–91.
66. G. Tammann. Number of nuclei in supercooled liquids. *Z. Für Phys. Chem.* **1898**, 25, 441–476.
67. Y. Furushima, S. Kumazawa, H. Umetsu, et al. Crystallization kinetics of poly(butylene terephthalate) and its talc composites. *J. Appl. Polym. Sci.* **2017**, 134, 44739.

68. E. Zhuravlev, J.W.P. Schmelzer, B. Wunderlich, C. Schick. Kinetics of nucleation and crystallization in poly(ϵ -caprolactone) (PCL). *Polymer* **2011**, 52, 1983–1997.
69. K. Nishida, E. Zhuravlev, B. Yang, C. Schick, Y. Shiraishi, T. Kanaya. Vittrification and crystallization of poly(butylene-2,6-naphthalate). *Thermochim. Acta* **2015**, 603, 110–115.
70. I. Stolte, R. Androsch. Kinetics of the melt – Form II phase transition in isotactic random butene-1/ethylene copolymers. *Polymer* **2013**, 54, 7033–7040.
71. I. Kolesov, D. Mileva, R. Androsch, C. Schick. Structure formation of polyamide 6 from the glassy state by fast scanning chip calorimetry. *Polymer* **2011**, 52, 5156–5165.
72. R. Androsch, C. Schick, J.W.P. Schmelzer. Sequence of enthalpy relaxation, homogeneous crystal nucleation and crystal growth in glassy polyamide 6. *Eur. Polym. J.* **2014**, 53, 100–108.
73. R. Androsch, H.M.N. Iqbal, C. Schick. Non-isothermal crystal nucleation of poly (l-lactic acid). *Polymer* **2015**, 81, 151–158.
74. Q. Zia, D. Mileva, R. Androsch. Rigid Amorphous fraction in isotactic polypropylene. *Macromolecules* **2008**, 41, 8095–8102.
75. D. Mileva, R. Androsch, E. Zhuravlev, C. Schick. Morphology of mesophase and crystals of polyamide 6 prepared in a fast scanning chip calorimeter. *Polymer* **2012**, 53, 3994–4001.
76. D.M. Gezovich, P.H. Geil. Morphology of quenched polypropylene. *Polym. Eng. Sci.* **1968**, 8, 202–209.
77. D. Mileva, I. Kolesov, R. Androsch. Morphology of cold-crystallized polyamide 6. *Colloid Polym. Sci.* **2012**, 290, 971–978.
78. J. Grebowicz, S.-F. Lau, B. Wunderlich. The thermal properties of polypropylene. *J. Polym. Sci. Polym. Symp.* **1984**, 71, 19–37.
79. Q. Zia, R. Androsch, H.-J. Radusch, S. Piccarolo. Morphology, reorganization and stability of mesomorphic nanocrystals in isotactic polypropylene. *Polymer* **2006**, 47, 8163–8172.
80. D. Mileva, Q. Zia, R. Androsch, H.-J. Radusch, S. Piccarolo. Mesophase formation in poly(propylene-ran-1-butene) by rapid cooling. *Polymer* **2009**, 50, 5482–5489.
81. S. Piccarolo, M. Saiu, V. Brucato, G. Titomanlio. Crystallization of polymer melts under fast cooling. II. High-purity iPP. *J. Appl. Polym. Sci.* **1992**, 46, 625–634.
82. G. Natta. Progress in the stereospecific polymerization. *Makromol. Chem.* **1960**, 35, 94–131.
83. S. Piccarolo. Morphological changes in isotactic polypropylene as a function of cooling rate. *J. Macromol. Sci. Part B* **1992**, 31, 501–511.
84. I. Coccorullo, R. Pantani, G. Titomanlio. Crystallization kinetics and solidified structure in iPP under high cooling rates. *Polymer* **2003**, 44, 307–318.
85. D. Cavallo, L. Gardella, G.C. Alfonso, et al. Effect of cooling rate on the crystal/mesophase polymorphism of polyamide 6. *Colloid Polym. Sci.* **2011**, 289, 1073–1079.
86. E. Parodi, L.E. Govaert, G.W.M. Peters. Glass transition temperature versus structure of polyamide 6: A flash-DSC study. *Thermochim. Acta* **2017**, 657, 110–122.
87. A.M. Rhoades, N. Wonderling, C. Schick, R. Androsch. Supercooling-controlled heterogeneous and homogenous crystal nucleation of polyamide 11 and its effect onto the crystal/mesophase polymorphism. *Polymer* **2016**, 106, 29–34.
88. N. Hiramatsu, K. Haraguchi, S. Hirakawa. Study of transformations among α , γ and γ' forms in nylon 12 by X-ray and DSC. *Jpn. J. Appl. Phys.* **1983**, 22, 335.

89. C. Fischer, A. Seefried, D. Drummer. Crystallization and component properties of polyamide 12 at processing-relevant cooling conditions. *Polym. Eng. Sci.* **2017**, *57*, 450–457.
90. H. Janeschitz-Kriegl, E. Ratajski, M. Stadlbauer. Flow as an effective promotor of nucleation in polymer melts: a quantitative evaluation. *Rheol. Acta* **2003**, *42*, 355–364.
91. R. Pantani, I. Coccorullo, V. Volpe, G. Titomanlio. Shear-induced nucleation and growth in isotactic polypropylene. *Macromolecules* **2010**, *43*, 9030–9038.
92. S. Coppola, N. Grizzuti, P.L. Maffettone. Microrheological modeling of flow-induced crystallization. *Macromolecules* **2001**, *34*, 5030–5036.
93. H. Janeschitz-Kriegl. How to understand nucleation in crystallizing polymer melts under real processing conditions. *Colloid Polym. Sci.* **2003**, *281*, 1157–1171.
94. E. Koscher, R. Fulchiron. Influence of shear on polypropylene crystallization: morphology development and kinetics. *Polymer* **2002**, *43*, 6931–6942.
95. Z. Wang, Z. Ma, L. Li. Flow-induced crystallization of polymers: molecular and thermodynamic considerations. *Macromolecules* **2016**, *49*, 1505–1517.
96. O.O. Mykhaylyk, P. Chambon, C. Impradice, J.P.A. Fairclough, N.J. Terrill, A.J. Ryan. Control of structural morphology in shear-induced crystallization of polymers. *Macromolecules* **2010**, *43*, 2389–2405.
97. F.G. Hamad, R.H. Colby, S.T. Milner. Onset of flow-induced crystallization kinetics of highly isotactic polypropylene. *Macromolecules* **2015**, *48*, 3725–3738.
98. F.H.M. Swartjes. Stress induced crystallization in elongational flow, Eindhoven University of Technology, Netherlands, **2001**.
99. J.-W. Housmans, R.J.A. Steenbakkers, P.C. Roozmond, G.W.M. Peters, H.E.H. Meijer. Saturation of pointlike nuclei and the transition to oriented structures in flow-induced crystallization of isotactic polypropylene. *Macromolecules* **2009**, *42*, 5728–5740.
100. F.G. Hamad, R.H. Colby, S.T. Milner. Lifetime of flow-induced precursors in isotactic polypropylene. *Macromolecules* **2015**, *48*, 7286–7299.
101. M. Du, K. Jariyavidyanont, I. Kühnert, R. Boldt, R. Androsch. Effect of molar mass on critical specific work of flow for shear-induced crystal nucleation in poly (l-lactic acid). *Polymers* **2021**, *13*, 1266.
102. C. Hadinata, C. Gabriel, M. Ruellmann, N. Kao, H.M. Laun. Shear-induced crystallization of PB-1 up to processing-relevant shear rates. *Rheol. Acta* **2006**, *45*, 539–546.
103. O.O. Mykhaylyk, P. Chambon, R.S. Graham, J.P.A. Fairclough, P.D. Olmsted, A.J. Ryan. The specific work of flow as a criterion for orientation in polymer crystallization. *Macromolecules* **2008**, *41*, 1901–1904.
104. J. Seo, H. Takahashi, B. Nazari, A.M. Rhoades, R.P. Schaake, R.H. Colby. Isothermal flow-induced crystallization of polyamide 66 melts. *Macromolecules* **2018**, *51*, 4269–4279.
105. Z. Refaa, M. Boutaous, D.A. Siginer. PLA crystallization kinetics and morphology development. *Int. Polym. Process.* **2018**, *33*, 336–344.
106. N. Iqbal, K. Jariyavidyanont, A.M. Rhoades, R. Androsch. Critical specific work of flow for shear-induced formation of crystal nuclei in poly (L-lactic acid). *Polym. Cryst.* **2019**, *2*, e10073.
107. H. Janeschitz-Kriegl. Crystallization Modalities in Polymer Melt Processing: Fundamental Aspects of Structure Formation; Springer-Verlag, Wien, **2010**.

108. B. Nazari, H. Tran, B. Beaugard, M. Flynn-Hepford, D. Harrell, S.T. Milner, R.H. Colby. Two distinct morphologies for semicrystalline isotactic polypropylene crystallized after shear flow. *Macromolecules* **2018**, 51, 4750–4761.
109. F.G. Hamad, R.H. Colby, S.T. Milner. Transition in crystal morphology for flow-induced crystallization of isotactic polypropylene. *Macromolecules* **2016**, 49, 5561–5575.
110. J. Seo, D. Parisi, A.M. Gohn, A. Han, L. Song, Y. Liu, R.P. Schaake, A.M. Rhoades, R.H. Colby. Flow-induced crystallization of poly(ether ether ketone): Universal aspects of specific work revealed by corroborative rheology and X-ray scattering studies. *Macromolecules* **2020**, 53, 10040–10050.
111. H. Janeschitz-Kriegl, E. Ratajski. Some fundamental aspects of the kinetics of flow-induced crystallization of polymers. *Colloid Polym. Sci.* **2010**, 288, 1525–1537.
112. D. Lellinger, G. Floudas, I. Alig. Shear induced crystallization in poly(ϵ -caprolactone): Effect of shear rate. *Polymer* **2003**, 44, 5759–5769.
113. B. Nazari, A.M. Rhoades, R.P. Schaake, R.H. Colby. Flow-induced crystallization of peek: Isothermal crystallization kinetics and lifetime of flow-induced precursors during isothermal annealing. *ACS Macro Lett.* **2016**, 5, 849–853.
114. S. Coppola, L. Balzano, E. Gioffredi, P.L. Maffettone, N. Grizzuti. Effects of the degree of undercooling on flow induced crystallization in polymer melts. *Polymer* **2004**, 45, 3249–3256.
115. R.H. Somani, L. Yang, B.S. Hsiao, T. Sun, N.V. Pogodina, A. Lustiger. Shear-induced molecular orientation and crystallization in isotactic polypropylene: effects of the deformation rate and strain. *Macromolecules* **2005**, 38, 1244–1255.
116. R. Massaro, P. Roozmond, M. D’Haese, P.V. Puyvelde. Flow-induced crystallization of polyamide-6. *Int. Polym. Process.* **2018**, 33, 327–335.
117. T.G. Mezger. *The Rheology Handbook: For Users of Rotational and Oscillatory Rheometers*; Vincentz Network GmbH & Co KG, **2006**.
118. R. Pantani, V. Nappo, F.D. Santis, G. Titomanlio. Fibrillar morphology in shear-induced crystallization of polypropylene. *Macromol. Mater. Eng.* **2014**, 299, 1465–1473.
119. F. De Santis, R. Pantani, G. Titomanlio. Effect of shear flow on spherulitic growth and nucleation rates of polypropylene. *Polymer* **2016**, 90, 102–110.
120. A. Keller, M.J. Machin. Oriented crystallization in polymers. *J. Macromol. Sci. Part B* **1967**, 1, 41–91.
121. C. Zhang, H. Hu, D. Wang, S. Yan, C.C. Han. In situ optical microscope study of the shear-induced crystallization of isotactic polypropylene. *Polymer* **2005**, 46, 8157–8161.
122. H. Janeschitz-Kriegl, G. Eder. Shear induced crystallization, a relaxation phenomenon in polymer melts: A re-collection. *J. Macromol. Sci. Part B* **2007**, 46, 591–601.
123. R.H. Somani, L. Yang, L. Zhu, B.S. Hsiao. Flow-induced shish-kebab precursor structures in entangled polymer melts. *Polymer* **2005**, 46, 8587–8623.
124. R.H. Somani, I. Sics, B.S. Hsiao. Thermal stability of shear-induced precursor structures in isotactic polypropylene by rheo-X-ray techniques with couette flow geometry. *J. Polym. Sci. Part B Polym. Phys.* **2006**, 44, 3553–3570.
125. D. Cavallo, F. Azzurri, L. Balzano, S.S. Funari, G.C. Alfonso. Flow memory and stability of shear-induced nucleation precursors in isotactic polypropylene. *Macromolecules* **2010**, 43, 9394–9400.

126. A.M. Rhoades, A.M. Gohn, J. Seo, R. Androsch, R.H. Colby. Sensitivity of polymer crystallization to shear at low and high supercooling of the melt. *Macromolecules* **2018**, 51, 2785–2795.
127. F. Azzurri, G.C. Alfonso. Lifetime of shear-induced crystal nucleation precursors. *Macromolecules* **2005**, 38, 1723–1728.
128. A.T. Lorenzo, M.L. Arnal, J.J. Sánchez, A.J. Müller. Effect of annealing time on the self-nucleation behavior of semicrystalline polymers. *J. Polym. Sci. Part B Polym. Phys.* **2006**, 44, 1738–1750.
129. R. Androsch, R. Zhang, C. Schick. Melt-recrystallization of poly (l-lactic acid) initially containing α' -crystals. *Polymer* **2019**, 176, 227–235.
130. A.M. Gohn, J. Seo, T. Ferris, P. Venkatraman, E.J. Foster, A.M. Rhoades. Quiescent and flow-induced crystallization in polyamide 12/cellulose nanocrystal composites. *Thermochim. Acta* **2019**, 677, 99–108.
131. K.L. Kearns, J. Scherzer, M. Chyasnovichyus, D. Monaenkova, J. Moore, R.L. Sammler, T. Fielitz, D.A. Nicholson, M. Andreev, G.C. Rutledge. Measuring flow-induced crystallization kinetics of polyethylene after processing. *Macromolecules* **2021**, 54, 2101–2112.
132. K.G. Kim, B.A. Newman, J.I. Scheinbeim. Temperature dependence of the crystal structures of nylon 11. *J. Polym. Sci. Polym. Phys. Ed.* **1985**, 23, 2477–2482.
133. S.S. Nair, C. Ramesh, K. Tashiro. Polymorphism in nylon-11: Characterization using HTWAXS and HTFTIR. *Macromol. Symp.* **2006**, 242, 216–226.
134. Q. Zhang, Z. Mo, H. Zhang, S. Liu, S.Z.D. Cheng. Crystal transitions of Nylon 11 under drawing and annealing. *Polymer* **2001**, 42, 5543–5547.
135. Y.S. Choi, S.K. Kim, M. Smith, F. Williams, M.E. Vickers, J.A. Elliott, S. Kar-Narayan. Unprecedented dipole alignment in α -phase nylon-11 nanowires for high-performance energy-harvesting applications. *Sci. Adv.* **2020**, 6, eaay5065.
136. R. Brill. Beziehungen zwischen Wasserstoffbindung und einigen Eigenschaften von Polyamiden. *Makromol. Chem.* **1956**, 18, 294–309.
137. J. Pepin, V. Miri, J.-M. Lefebvre. New insights into the Brill transition in polyamide 11 and polyamide 6. *Macromolecules* **2016**, 49, 564–573.
138. S. Acierno, P.V. Puyvelde. Effect of short chain branching upon the crystallization of model polyamides-11. *Polymer* **2005**, 46, 10331–10338.
139. K. Jariyavidyanont, W. Focke, R. Androsch. Crystallization kinetics of polyamide 11 in the presence of sepiolite and montmorillonite nanofillers. *Colloid Polym. Sci.* **2016**, 294, 1143–1151.
140. R. Zhang, K. Jariyavidyanont, M. Du, E. Zhuravlev, C. Schick, R. Androsch. Nucleation and crystallization kinetics of polyamide 12 investigated by fast scanning calorimetry. *J. Polym. Sci.* (Accepted Dec 10, 2021).
141. K. Jariyavidyanont, C. Schick, R. Androsch. Nucleation-controlled dual semicrystalline morphology of polyamide 11. *Polym. Int.* **2019**, 68, 263–270.
142. K. Jariyavidyanont, S. Mallardo, P. Cerruti, M.L. Di Lorenzo, R. Boldt, A.M. Rhoades, R. Androsch. Shear-induced crystallization of polyamide 11. *Rheol. Acta* **2021**, 60, 231–240.

List of abbreviations

ABS	Acrylonitrile butadiene styrene
AFM	Atomic force microscopy
DSC	Differential scanning calorimetry
FSC	Fast scanning chip calorimetry
h	Sample thickness
HDPE	High density polyethylene
iPB-1	Isotactic polybutene-1
iPP	Isotactic polypropylene
LDPE	Low density polyethylene
LLDPE	Linear low density polyethylene
PA 11	Polyamide 11
PA 6	Polyamide 6
PA 66	Polyamide 66
PA 12	Polyamide 12
PBN	Poly(butylene-2,6-naphthalate)
PBT	Poly(butylene terephthalate)
PCL	Poly(ϵ -caprolactone)
PEEK	Poly(ether ether ketone)
PET	Poly(ethylene terephthalate)
PLA	Poly(lactic acid)
PLLA	Poly(L-lactic acid)
POM	Polarized-light optical microscopy
r	Sample radius
T_{Brill}	Brill transition temperature
T_g	Glass transition temperature
T_m	Melting temperature
t_s	Shear time
T_s	Shear temperature
W	Specific work of flow
WAXS	Wide-angle X-ray scattering
XRD	X-ray diffraction
$\dot{\gamma}$	Shear rate
$\dot{\gamma}^*$	Critical shear rate
ω	Angular velocity
η	Viscosity
τ_r	Reptation time
τ_R	Rouse time

List of figures and tables

Figure 1:	Timeline of history and development of Rilsan [®] PA 11.....	2
Figure 2:	Production steps, from left to right, to obtain bio-based PA 11 (top) and repeating unit of the PA 11 macromolecule (bottom).....	3
Figure 3:	Simulated shear-rate distribution (top, left) and temperature distribution (bottom) over the cross section of a polypropylene tensile-test bar (top, right, black area), taken at the center of the bar. The time scale starts after 0.8 s which corresponds the time of half mold filling; mold filling is completed after 1.77 s.....	4
Figure 4:	Elastic modulus as a function of the distance along the thickness of an injection-molded bar of iPP, shown with the top POM-image. The flow direction is indicated by the yellow arrow. The three images at the bottom show the structure at different positions observed by AFM.....	5
Figure 5:	Characteristic time of crystallization of iPP in a wide range of temperatures between 0 and 140 °C, proceeding via heterogeneous (filled and unfilled symbols in light-blue and light-gray colors, at temperatures above about 55 °C) and homogeneous nucleation (dark-blue and dark-gray filled symbols), obtained by FSC (filled symbols) and DSC (unfilled symbols).....	7
Figure 6:	Crystallization peak-temperature of iPP as a function of cooling rate, obtained by DSC ($\leq 1 \text{ K s}^{-1}$, open squares) and by FSC cooling experiments ($>10 \text{ K s}^{-1}$, filled squares).....	8
Figure 7:	AFM images of iPP, PA 6, and PA 66, (from left to right), obtained by crystallization at high (top row) and at low supercooling of the melt (bottom row). The yellow circles in the bottom-right image indicate two heterogeneous nuclei where the crystal growth started	9
Figure 8:	POM images of the structure of 100 μm thick iPP films, prepared by cooling the melt at different rates, as indicated in each image. The scale bar of 30 μm applies to all images	10
Figure 9:	WAXS patterns of iPP, obtained from film samples prepared by cooling the melt at different rates (left) and basal planes of the unit cell of monoclinic α -crystals and pseudo-hexagonal mesophase (right).....	11
Figure 10:	Crystallization time as a function of shear rate, allowing to distinguish three crystallization regimes: zero-shear or quiescent-melt crystallization (Regime I, black), shear-induced formation of point-like nuclei (Regime II, blue), and shear-induced formation of fibrillar structure (Regime III, red). The POM images on the top show iPP structures formed after crystallization in different regimes. ⁹⁸ The flow direction is indicated with the yellow arrow.....	13

Figure 11: Sketch of the sample compartment of a parallel-plate rheometer (top). The lower part shows the increase of the shear rate with radius of the disc-like sample.....	14
Figure 12: POM image showing the structure of a sheared PLLA disc ($\dot{\gamma} = 2.5 \text{ s}^{-1}$, $t_s = 10 \text{ s}$, $T_s = 135 \text{ }^\circ\text{C}$), crystallized at $135 \text{ }^\circ\text{C}$ for 4 min, along the radius. The specific work of flow values indicated in the figure are obtained by calculation using Eq. (1), demonstrating the maximum specific work of flow at the edge of about 1.7 MPa.....	15
Figure 13: Schematic about the cooling-rate controlled crystal polymorphism and semicrystalline morphologies of PA 11 crystallized from the quiescent melt (left), with fast and slow cooling routes represented in the red and blue colors, respectively. Basal planes of the unit cells of pseudo-hexagonal δ' -crystal (top) and the triclinic α -crystal (bottom) are shown in the right part of the figure.....	16
Figure 14: Summary of cooling-rate-controlled crystallization (left) and structure formation in three different cooling-rate ranges in PA 11 (right). The critical cooling rates for suppressing crystallization and nucleation are indicated with gray and green arrows, respectively.....	77
Figure 15: Summary of shear-induced crystallization of PA 11, representing three flow regimes (left) and respective structure formation (right). The critical shear rate ($\dot{\gamma}^*$) for shear-induced nucleation is about 1 s^{-1}	78
Table 1: Examples of shear and cooling rates in melt processing of polymers using different manufacture technologies. The table serves for demonstration of the order of magnitude of cooling rates and shear rates only; detailed information about specific processing conditions, part geometries, etc. is available in the provided references.....	4
Table 2: Examples of critical cooling rates for suppression of crystallization and homogeneous crystal nucleation.....	9
Table 3: Supercooling-controlled crystal polymorphism of various polymers.....	11
Table 4: Specific work of flow of various homopolymers.....	14

Acknowledgements

I would like to express my sincere gratitude and appreciation to the following people who contribute in helping me to shape this piece of work.

I would like to express my deeply thankfulness to my doctoral supervisor, Prof. Dr. René Androsch, who gave me this great opportunity to perform my PhD work in his group. Thank you very much for your constant guidance, encouragement, and for always supporting me for many opportunities, either participation in international conferences or collaboration in different research groups, with all these experiences having built my confidence in working independently and improving my professional skills.

I would like to gratefully acknowledge the European Social Fund (ESF) for the three-year scholarship of my PhD project.

I would like to extend my sincere thanks to Prof. Dr. Christoph Schick and Dr. Evgeny Zhuravlev from the Institute of Physics, University of Rostock, for the kind support in super-fast scanning calorimetry and always fruitful discussions.

I would like to acknowledge my colleagues from the Institute of Polymers, Composites and Biomaterials (CNR), Pozzuoli, Naples, Italy. Dr. Maria Laura Di Lorenzo, thank you very much for your warm welcome and giving me a great opportunity to perform rheological experiments in your group. Salvatore Mallardo and Dr. Pierfrancesco Cerruti, big thanks to both of you for the kind help and guidance throughout all steps of rheological experiments.

Many thanks go to Andreas Janke, Dr. Regine Boldt, Dr. Ines Kühnert, and Yvonne Spörer from Leibniz-Institut für Polymerforschung Dresden e.V. (IPF), Dresden, for their support and kind collaboration in atomic force microscopy, X-ray diffraction, and injection molding.

I would also like to thank my colleagues from School of Engineering, Penn State Behrend, Dr. Alicyn Rhoades, for always kind collaboration and useful discussions. My thanks also go to Anne Gohn, my PhD buddy, for the encouragement and discussion throughout our PhD time.

I am also thankful to Muhammad Tariq, from the Institute of Physics, Martin Luther University Halle-Wittenberg, for assistance in atomic force microscopy.

I am also grateful my best friends, Witoon Purahong, Kantida Juncheed, and Benjawan Tanunchai, for friendship, encouragement, support, and joyfulness during my stay in Halle.

At the end, I would like to say the biggest gratitude to my parents, Chansak and Maneewan Jariyavidyanont. Without your tremendous understanding, encouragement, and the belief in me toward my journey to pursue my PhD degree, it would be impossible for me to complete my study. I am also deeply thankful to my uncle and my aunt, Ditmar and Katharos Krüger, for all supports and encouragement during my stay in Germany. Last but not least, I am grateful to my beloved sister and brother, Pawimonkarn and Poramet Jariyavidyanont.

Declaration of authorship

I hereby declare that this dissertation represents my own work and has been written with the revision of my supervisor, Prof. Dr. René Androsch. The usages of other sources and scientific ideas from literature are indicated in the citations correctly. Furthermore, I declare that this dissertation has not been submitted to another faculty.

City, Date

(Katalee Jariyavidyanont)

Curriculum Vitae

Katalee Jariyavidyanont

PERSONAL DATA

Date of birth: 6th August 1986
Place of birth: Ubon Ratchathani, Thailand
Nationality: Thai
Email: katalee.jariyavidyanont@iw.uni-halle.de

EDUCATION

Aug 2013 M.Sc. in Polymer Materials Science, Martin Luther University Halle-Wittenberg.
Mar 2009 B.Sc. in Petrochemical Technology, King Mongkut's Institute of Technology
Ladkrabang, Thailand.

ACADEMIC EXPERIENCES

Since Jul 2017 Ph.D. candidate, Martin Luther University Halle-Wittenberg.
Jul 2015–Jun 2017 Research assistant, Interdisciplinary center for transfer-oriented
research in natural sciences, Martin Luther University Halle-
Wittenberg.
May 2013–Oct 2014 Research assistant, Helmholtz Centre for Environmental Research-
UFZ, Halle.
Sep 2011 Research assistant, Martin Luther University Halle-Wittenberg.

ACADEMIC ACTIVITIES

Dec 2021 Flash meeting, Oral presentation (online), Switzerland.
Oct 2019 11th International discussion meeting on polymer crystallization (IDMPC19),
Poster presentation (Poster prize), San Sebastian, Spain.
Sep 2018 4th International conference on bio-based polymers and composites, Oral
presentation, Balatonfüred, Hungary.
Sep 2016 9th ECNP International conference on nanostructures and nanocomposites,
Poster presentation, Rome, Italy.
Dec 2015 GEFTA-Fortbildungskurs "Kalorimetrie für Einsteiger-Schwerpunkt DSC".
Jan 2009 26th Annual Conference of the Microscopy Society of Thailand (MST26),
Poster presentation, Chiangmai, Thailand.
Mar–Apr 2008 Practical training, Gas Separation Plant (Quality control division), Rayong,
Thailand.

PUBLICATIONS

K. Jariyavidyanont, A. Janke, M. Tariq, M. L. Di Lorenzo, C. Schick, R. Androsch, Thermal stability and nucleation efficacy of shear-induced pointlike and shishlike crystallization precursors. *ACS Macro Lett.* **2021**, 10, 684–689.
K. Jariyavidyanont, S. Mallardo, P. Cerruti, M. L. Di Lorenzo, R. Boldt, A. M. Rhoades, R. Androsch, Shear-induced crystallization of polyamide 11. *Rheol. Acta* **2021**, 60, 231–240.

- M. Du, K. Jariyavidyanont, I. Kühnert, R. Boldt, R. Androsch, Effect of molar mass on critical specific work of flow for shear-induced crystal nucleation in poly(L-lactic acid). *Polymers* **2021**, 13, 1266.
- K. Jariyavidyanont, E. Zhuravlev, C. Schick, R. Androsch, Kinetics of homogeneous crystal nucleation of polyamide 11 near the glass transition temperature. *Polym. Cryst.* **2020**, e10149.
- K. Jariyavidyanont, A. Janke, R. Androsch, Crystal self-nucleation in polyamide 11 of different semicrystalline morphology. *Polymer* **2019**, 184, 121864.
- R. Androsch, K. Jariyavidyanont, C. Schick, Enthalpy relaxation of polyamide 11 of different morphology far below the glass transition temperature. *Entropy* **2019**, 21, 984.
- K. Jariyavidyanont, W. Focke, R. Androsch, Thermal properties of biobased polyamide 11, In *Thermal Properties of Bio-based Polymers*. Eds.; M.L. Di Lorenzo, R. Androsch, Springer, Cham, 2019, 143–187.
- N. Iqbal, K. Jariyavidyanont, A.M. Rhoades, R. Androsch, Critical specific work of flow for shear-induced formation of crystal nuclei in poly(L-lactic acid). *Polym. Cryst.* **2019**, 2, e10073.
- K. Jariyavidyanont, A. Janke, R. Androsch, Crystal self-nucleation in polyamide 11. *Thermochim. Acta* **2019**, 677, 139–143.
- K. Jariyavidyanont, A. Abdelaziz, R. Androsch, C. Schick, Experimental analysis of lateral thermal inhomogeneity of a specific chip-calorimeter sensor. *Thermochim. Acta* **2019**, 674, 95–99.
- K Jariyavidyanont, R Androsch, C Schick, Nucleation-controlled dual semicrystalline morphology of polyamide 11. *Polym. Int.* **2018**, 68, 263–270
- K Jariyavidyanont, J. Williams, A.M. Rhoades, I Kühnert, W Focke, R Androsch, Crystallization of polyamide 11 during injection molding. *Polym. Eng. Sci.* **2018**, 58, 1053–1061.
- K Jariyavidyanont, R Androsch, C Schick, Crystal reorganization of poly(butylene terephthalate). *Polymer* **2017**, 124, 274–283.
- K Jariyavidyanont, W Focke, R Androsch, Crystallization kinetics of polyamide 11 in the presence of sepiolite and montmorillonite nanofillers. *Colloid Polym. Sci.* **2016**, 294, 1391.

TECHNICAL AND RELEVANT SKILLS

Professional skills	Optical microscopy, Differential scanning calorimetry, Fast scanning chip calorimetry, Dynamic mechanical analysis, Rheology.
Language	Thai (Mother language), English (Reading, writing and speaking fluently), German (Basic knowledge).

City, Date

(Katalee Jariyavidyanont)